Theoretische Physik

Universität Bielefeld

Kondensierte Materie

Escape Processes far from Thermal Equilibrium: Path Integrals and Force Spectroscopy

Dissertation
zur Erlangung des Doktorgrades
an der Fakultät für Physik
der Universität Bielefeld

vorgelegt von

Sebastian Getfert

begutachtet durch

Prof. Dr. Peter Reimann
Prof. Dr. Dario Anselmetti

vorgelegt am

6. Juli 2009

Printed on paper ∞ ISO 9706

Contents

List of Symbols

$\mathcal{C} \approx 0.577$	Euler's constant
α	dissociation length divided by the thermal energy
ϵ	force-free barrier height in units of the thermal energy
$\delta(t)$	Dirac's delta function
$\Delta\, g$	pulse strength of the fluctuating temperature
$\Delta V,\ \Delta U$	height of a potential barrier
$\Delta x_{s,u}(t)$	deviation of the optimizing path from the stable or unstable orbit
η	friction coefficient
$\Gamma(t)$	instantaneous escape rate in a fast modulated force field
κ	relevant total elasticity of cantilever, linker molecules, receptor, and ligand
λ	logarithm of the force-free dissociation rate
$\lambda_{s,u}$	Lyapunov coefficients of the stable and unstable orbit
$\boldsymbol{\mu}$	model parameters
$\boldsymbol{\mu}_0$	true model parameters
$\boldsymbol{\mu}^*$	maximum likelihood estimate of the model parameters
$\omega(f)$	attempt frequency for an instantaneous force f
ω	frequency of a periodic driving force
Φ^*	action of the optimizing path
$\Psi(t_1)$	first passage time density
$\rho(x, t \mid \dots)$	conditional probability density for a Browninan particle
σ^2	standard deviation of a probability distribution
$\Theta(\cdot)$	Heaviside step function
τ	pulse length of the fluctuating temperature
τ_R	relaxation time
$\xi(t)$	Gaussian white noise of strength $D = 1$
$\tilde{\xi}(t)$	Gaussian white noise of strength $2D$
$\mathcal{A}(t)$	basin of attraction of a force field
c	spring constant of the cantilever

D_{N_c}	maximum deviation between a theoretical and an empirical survival probability
$\mathcal{D}_{x,p}(t)$	deviation from the optimizing path for small changes of the boundary conditions
$E_{\mathrm{b}}(f)$	potential barrier for an instantaneous force f
$F\,(x,t)$	time-dependent force field
f_{c}	critical force at which an energy barrier vanishes
F_d	friction or damping force
$f_{\min}$	threshold force below which rupture events cannot be distinguished from thermal fluctuations
$F(s)$	force-extension curve
$j(x,t \mid \dots)$	flux of probability
$k_B = 1.38 \cdot 10^{-23} J/K$	Boltzmann's constant
$L(x,\dot{x},t)$	Lagrangian
$n_i(t)$	(accumulated) probability to find a system in a metastable state i, also survival probability
$\mathcal{N}(\mu,\sigma^2)$	Normal distribution with mean μ and variance σ^2
$n_{eq,i}$	quasi equilibrium probability to find a system in a metastable state i
$p(\mathbf{f} \mid \boldsymbol{\mu},\mathbf{v})$	joint probability to observe N rupture forces
$p_1(f \mid \dots)$	distribution of rupture forces
$p^*(t)$	generalized momentum of the optimizing path
Q^*	prefactor in the saddle point approximation
q_i	position where two parabolas in a piecewise parabolic potential are jointed
r	loading rate
s	distance of the surface from the rest position of the cantilever
$s(\boldsymbol{\mu})$	limit of s_N for $N \to \infty$
s_c	deflection of the cantilever
s_d	distance of the tip from the surface
$s_N(\mathbf{f},\boldsymbol{\mu},\mathbf{v})$	logarithm of the likelihood p divided by $-N$
$S[x(t)]$	Onsager-Machlup functional
T	temperature
t	time
$\mathcal{T}$	period of an external force-field
t_d	dwell time
$U(x)$	static potential for the (reaction) coordinate
$V(x,t)$	metastable potential function for the (reaction) coordinate

v	pulling velocity
$W(t)$	Wiener process
m	mass of a particle or a degree of freedom
x	(reaction) coordinate
$X_{t_1}(t)$	solution of the deterministic equation of motion
$x^*(t)$	coordinate of the optimizing path
$v = \dot{x}$	velocity of a particle or a degree of freedom
$\ddot{x}$	acceleration of a particle or a degree of freedom
$x_{\max}(t)$	instantaneous maximum of a potential
$x_{\min}(t)$	instantaneous minimum of a potential
$x_s(t)$	stable orbit
$x_u(t)$	unstable orbit
Z^*	derivative of the prefactor in the saddle point approximation with respect to the final coordinate

List of Figures

Part I

General introduction and concepts

1 Introduction

Thermally activated escape over a potential barrier is ubiquitous in physical, biological, chemical, and technical processes and its understanding of paramount importance [HTB90]. Examples arise in the context of chemical and biological bonds [Mer01], folding and unfolding of polymers [LOR$^+$01, BS05], molecular motors [Rei02], friction at the atomic scale [RGB$^+$03], and phase jumps in Josephson junctions [Kur72, FD74], to name only a few.

In the last decades elaborate experimental techniques have not only allowed to observe systems at the nano-scale where thermal noise is particular important, but also to directly manipulate them in a well defined manner, leading to *far from thermal equilibrium* conditions which are theoretically particularly challenging. Thermally activated escape from a metastable state under these far from thermal equilibrium conditions is the main topic of this work.

Historically, Arrhenius may be considered as the father of reaction rate theory. He investigated the dependence of the rate k of a chemical reaction on the temperature T. Following a previous work of van't Hoff, he proposed in 1889 a proportionality $k \propto \exp(-A/T)$ with a constant A that was later identified with E_b/k_B. Here E_b denotes the minimal energy needed before the reaction can occur and k_B Boltzmann's constant. In the following half a century a lot of efforts have been spent on calculating the escape rate, leading to concepts like the transition state method [HTB90, PT05], but it took until 1940 that an expression for the rate could be derived from microscopic physics principles by Kramers in his seminal paper [Kra40]. To this aim he described thermally activated escape from a metastable state as Brownian motion of a fictitious particle along a reaction coordinate in a (static) field of force. The theoretical modeling of this Brownian motion goes, amongst others, back to Einstein [Ein05] and can be described in two different ways. On the one hand, single realizations of the dynamics can be considered. This results in a stochastic differential equation, the *Langevin equation* [Lan08]. On the other hand, one may consider the probability distribution of particles. The temporal evolution of this distribution is governed by the *Fokker-Planck equation* [Fok14, Smo15, Ris89]. Starting from the latter one, Kramers showed that, for small noise strengths, meaning that E_b is much larger than the thermal energy k_BT, the escape rate is of the form proposed by Arrhenius and derived expressions for the prefactor in the case of weak, intermediate, and strong damping. In the subsequent decades Kramers' rate theory was generalized in various important directions [HTB90], but for a long time all of these works were restricted to the case of time-independent force fields and time-independent heat baths. Some of the concepts relevant for the theoretical description of Brownian motion and Kramers' rate theory will be outlined in chapter 2.

From a theoretical point of view, systems far from thermal equilibrium are particularly interesting for the following reason: In the equilibrium case, the probability distribution of particles always resembles a Boltzmann form, and the second law of thermodynamics sets strict restrictions to the behavior of the system. In the non-equilibrium case, the probability distribution can strongly deviate from the Boltzmann form. The possible behavior of the system is much more versatile, and important, partly counterintuitive effects can occur. Extensively studied effects are the absolute negative mobility [ERCdB05], stochastic resonance [GHJM98], or the rectification of noise in ratchets and Brownian motors [Rei02]. The required non-equilibrium conditions are achieved by applying time-dependent external perturbations either directly to the system, leading to time-dependent potentials, or to its thermal environment, resulting in time-dependent temperatures or damping coefficients. In fact, the invention of experimental techniques like optical tweezers [ADBC86] or the atomic force microscope [BQG86] made it possible to exert quickly varying perturbations like forces on nano-sized objects and thus to experimentally study the proposed effects.

The escape rate of a particle from a metastable state in the presence of time-dependent perturbations is, in general, also time-dependent, and a relevant and important question is how this escape rate can be calculated. Here two different cases can be distinguished. If the external driving is much slower than all internal relaxation processes, the escape rate can at any time be approximated by the escape rate in the frozen system. This situation has been extensively studied in many theoretical and experimental works, e.g., [ER97]. However, if the perturbation of the system occurs on the same time scale as the internal relaxation processes, the situation is much more involved, and, despite its importance, this situation has been studied much less extensively than the first one. Approximations to the time-dependent escape rate were only derived for rather special cases. In this thesis examples for both cases will be considered. In general, these examples refer to bio-chemical reactions or to the escape of nano- or micro-sized particles from metastable potentials in an aqueous environment. As pointed out by Astumian [Ast06], for these systems it is nearly impossible to achieve a situation in which the system is not near *mechanical equilibrium*. That means, the damping is strong so that the inertia term in the equations of motion can be neglected. The viscous drag is then equal to the net force, but with opposite sign. Throughout this work we will restrict our discussions to this *overdamped* case.

In part II of this thesis we consider (dynamic) *single-molecule force spectroscopy* experiments [Mer01, Rit06] which allow to observe the chemical dissociation of two biomolecules at the single-molecule level. These experiments can, for example, be conducted with an atomic force microscope (AFM) by connecting one binding partner via a suitable linker to the tip of the AFM and the other one to the surface. When retracting the tip from the surface at a constant speed, a steadily increasing force on the pico-Newton scale acts on the complex. The main quantity of interest is the magnitude, or to be more precise the distribution, of the force at the moment when the bond breaks, i.e., the *rupture force*. It has been proposed by Evans and Ritchie [ER97] that this forced single-molecule dissociation process can be viewed as a thermally activated escape of a reaction coordinate over a potential barrier and that the dissociation/escape rate can at any time be very well approximated by the Kramers rate from a frozen, tilted potential. From a biological point of view, the perhaps most important applications of single-molecule force spectroscopy arise in the context of *molecular recognition*. This concept refers to the ability of biomolecules to recognize their target molecules with an astonishing high precision. As most biological functions rely on this highly selective recognition, its importance can hardly be overestimated. Consequently, single-molecule force spectroscopy, being one of the few experimental techniques allowing to study molecular recognition at the single-molecule level, has been applied to a remarkable range of interactions: from the binding of complex biological molecules like antibodies [HBG+96, RSA+98] and protein-DNA interactions [BBA+03, KCB+04, BBA+05] to small bio-organic or organic compounds like peptides [EWB+05] and supramolecular systems [AdJM+04]. The basic principles of single-molecule force spectroscopy will be presented in chapter 3. However, the theoretical interpretation of the experimental data is still very challenging. In this thesis several important questions in this context will be addressed.

The model introduced by Evans and Ritchie predicts the rupture force distribution starting from a given potential landscape. But for a real experiment one usually faces the inverse problem. The distribution of rupture forces is known, and one wants to gain information about the energy landscape of the bond. Although the knowledge of this distribution allows to calculate the dissociation rate for a given instantaneously applied force, it is well known that one cannot uniquely reconstruct the full potential landscape [ISB+97]. Hence, one usually starts from some model potential landscape and tries to infer its parameters from the experimental data. In chapter 4 we will discuss how this can be done in the optimal way. We will then demonstrate that the proposed method is in fact superior to the commonly used methods. However, by "simulating" an idealized experiment on the computer, we will also demonstrate that only some global features of the kinetics and of the potential landscape can be reliably reconstructed from single-molecule force spectroscopy experiments while others, like the height E_b of the potential barrier of the unperturbed bond, depend critically on the a priori choice for the functional form of the potential landscape. Quite different potential landscapes with completely different values for the barrier height lead to nearly identical rupture force distributions.

In chapter 5 we turn to real experimental data. It was shown in [REB+06] that these data are often incompatible to the basic assumptions which are usually employed when theoretically modeling these experiments. A heterogenous bond model has been introduced in which it has been proposed that some properties of the bond are subjected to random variations upon repeating the single experiment. Here, this Ansatz will be put forward and the microscopic physical origin of the proposed heterogeneity will be discussed. In fact, there are, for example, direct experimental hints for variations in the pulling geometry which result in a natural way in a randomization of the angle between the applied force and the direction of the reaction coordinate which might explain the experimental observations. However, we will also discuss alternatives to this model. For example, very similar distributions of rupture forces might be obtained if the bond can exist in different metastable states and if the initial probabilities for the states differ from the equilibrium ones. The results from this part of the work might also be useful for various other experimental systems like friction at the atomic scale [RGB$^+$03] which is modeled within the very same theoretical framework.

While it can be assumed for single-molecule force spectroscopy experiments that the time-dependent escape rate is at any time very well approximated by the Kramers rate from the frozen potential, in part III of this thesis the technically much more challenging case of largely arbitrarily modulated potentials and temperatures will be considered. As for the derivation of the Kramers rate, it will be assumed that the thermal energy is small compared to the relevant potential barrier. Some approximations to the time-dependent or the time-averaged escape rate are known for periodically modulated potentials [SDG99, LRH00b, MS01, BG05, RD05], resulting in a renormalization of E_b which depends in a very complicated manner on details of the model. But each of these approximations is usually limited to just one of the following cases: weak, slow, fast, or moderately fast and moderately strong driving. In chapter 6 we employ the technique of path integration to develop an approximation to the instantaneous escape rate that applies to arbitrary modulation frequencies and the whole range of modulation strengths, from no modulation to moderately strong modulation. After discussing some properties of the approximation, we will show that it unifies and extends several of the previously known approximations. For example, for small noise strengths and adiabatically slowly modulated potentials or temperatures it simply reduces to the Kramers rate. A comparison to high precision numerical results will show for a number of fairly general modulations and potentials that the approximation is in fact very good.

Employing this new approximation scheme, we will consider systems with several metastable states in chapter 7. While the potentials are static, we allow for time-dependent temperatures. In thermal equilibrium, the probability distribution of particles in a confining potential is of the Boltzmann form, and for small, constant noise strengths always the energetically lowest metastable state is preferentially occupied. We will show that this situation may considerably change in systems far from thermal equilibrium. Even more interestingly, the effective escape rate from a potential with several metastable states may *decrease* upon temporally *increasing* the temperature. Indeed, given that thermal noise is indispensable to escape, one would expect that an "extra dose" of noise should always enhance escape. As far as we know, these effects have not yet been studied experimentally. But it is very likely that the emerging possibilities of nanotechnology will make it possible soon.

2 Basic concepts of stochastic modeling and rate theory

This chapter outlines the basic stochastic modeling concepts. The motion of a Brownian particle in a potential will be discussed and then generalized to the dynamics of a general reaction coordinate. Particular attention will be paid to methods allowing to calculate the escape rate from a domain of attraction. These concepts provide the basis for the discussions in the following chapters. As all of these concepts and methods are well known, the line of reasoning will at some points be kept on a rather heuristic level. At these points we will refer to mathematically more rigorous approaches. General overviews over this topic are given, e.g., in [Ris89, HTB90, Rei02].

2.1 The Langevin equation with Gaussian white noise

In this section we consider the motion of a Brownian particle in a fluid under the action of an external conservative force. As already discussed in the introduction, there exist different approaches to describe this motion. Here we will focus on Langevin's approach which is based on Newton's equation of motion [Lan08, LG97]. In Langevin's own words this approach is "infinitely more simple" than Einstein's [Ein05].

Let us consider the simplest possible case, namely that of a one-dimensional particle with coordinate $x(t)$ at time t and with mass m. For a moment we will assume that no external force acts on the particle. Then the motion of the particle is governed by Newton's equation of motion $m\ddot{x}(t) = F(\dot{x}(t), x(t), t)$.[1] Here F is the sum of a friction force F_d and a fluctuation force $\tilde{\xi}$. In the simplest case, the friction force is given by Stokes' law:

$$F_d(\dot{x}(t), x(t), t) = -\eta\dot{x}(t) \; , \tag{2.1}$$

where η is the friction coefficient. The physical mechanism behind this friction force is that the Brownian particle collides with molecules of the fluid. Through these collisions the momentum of the particle is transferred to the molecules of the fluid, i.e., the kinetic energy is dissipated to the thermal environment. On the other hand, these very same collisions result in an additional fluctuating force $\tilde{\xi}(t)$ which acts on the particle and causes the observed erratic Brownian motion.

---

[1] Throughout this work the usual convention to denote the derivative with respect to the time by a dot and the derivative with respect to a coordinate by a prime will be used.

Assuming that the environment is in thermal equilibrium, the fluctuating force can in many physical problems be modeled as a Gaussian noise with mean and correlation:

$$\begin{aligned} \langle \tilde{\xi}(t) \rangle &= 0 \,, & (2.2) \\ \langle \tilde{\xi}(t)\tilde{\xi}(t') \rangle &= 2D\delta(t-t') \,. & (2.3) \end{aligned}$$

Here $\delta(t)$ is Dirac's delta function, $\langle\,\rangle$ refers to an average over an ensemble of single realizations, and $2D$ denotes the noise strength which depends for a given temperature T solely on the friction coefficient η and is given by

$$D = \eta k_B T \,, \tag{2.4}$$

with k_B the Boltzmann constant. This relation, together with equation (2.3), is termed the *fluctuation-dissipation relation* [CW51] and reflects that both effects of the thermal environment, energy dissipation and thermal fluctuations, have the same origin. The friction coefficient η hence determines the coupling strength of the Brownian particle to the thermal environment.[2]

The spectral density of a fluctuation force with delta correlation (2.4) is independent of the frequency. Therefore, such a fluctuation force is called (Gaussian) *white noise*. It is a mathematical idealization and formally defined as the derivative of a Wiener process[3] [FW98, RY99]. From a physical point of view, modeling the effects of the thermal environment by an energy dissipation mechanism of the form (2.1) and the fluctuation force by a Gaussian white noise (2.2-2.4) means that the correlation time, which is at least as large as the typical duration τ_0 of the collisions between the Brownian particle and the molecules of the fluid, is much smaller than all other relevant time scales of the problem.

Let us now consider the dynamics of a Brownian particle in a potential $V(x,t)$. The existence of such a potential does not change the statistical properties of the fluctuation force. The dynamics of the system is hence given by the *Langevin equation*:

$$m\ddot{x}(t) + V'(x(t),t) = -\eta\dot{x}(t) + \sqrt{2\eta k_B T}\xi(t) \,, \tag{2.5}$$

where we have defined $\xi(t) := \tilde{\xi}(t)/\sqrt{2\eta k_B T}$. Here, $\xi(t)$ is a Gaussian white noise with zero mean and correlation:

$$\langle \xi(t)\xi(t') \rangle = \delta(t-t') \,. \tag{2.6}$$

Again, the right-hand side of equation (2.5) models all effects of the thermal environment while the left-hand side accounts for the deterministic part of the dynamics.

---

[2] It can indeed be shown that the statistical properties (2.2,2.3) of the fluctuation force are already fixed by the *Ansatz* (2.1) for the dissipation mechanism (see [Rei01]).

[3] A Wiener process $W(t)$ is characterized by the following three properties:

- $W(0) = 0$.
- $W(t)$ is almost surely continuous.
- $W(t)$ has independent increments with distribution $W(t) - W(s) \sim \mathcal{N}(0, t-s)$ for all $0 \le s \le t$.

Here, $W(t) - W(s) \sim \mathcal{N}(0, t-s)$ means that $W(t) - W(s)$ is drawn from a normal distribution with zero mean and variance $t - s$.

A particularly important case is the overdamped motion, where the mass is small and/or the damping strong so that the term $m\ddot{x}(t)$ in equation (2.5) can be dropped. This equation then reduces to the *overdamped Langevin equation*:

$$\eta\dot{x}(t) = -V'\left(x(t), t\right) + \sqrt{2\eta k_B T}\xi(t) \, . \tag{2.7}$$

This case typically arises when dealing with very small objects. For a macroscopic sphere with radius r, the friction coefficient η is according to Stokes' law, for example, proportional to the radius while its mass is proportional to r^3. In the limit $r \to 0$, the term $m\ddot{x}(t)$ in equation (2.5) is hence negligible. On the other hand, in the opposite limit of very large objects the fluctuating force can be neglected.

2.2 Equation of motion for a general reaction coordinate

So far we have considered the dynamics of a one-dimensional particle in a thermal environment which could be described by equations (2.5) and (2.7), respectively. However, such a modeling approach is also applicable to the dynamics of various other physical systems in contact with a heat bath. Examples include the polarization reversal in nanomagnets [WOH+97], friction at the atomic scale [RGB+03, SJF05, ESJ+06], phase jumps in Josephson junctions [Kur72, FD74], the dynamics of the geometrical configurations of polymers [LOR+01, BS05], and the rupture of bonds between two or more biomolecules [ER97, Mer01]. In these systems, x refers to some collective degree of freedom in the high dimensional phase space of the system. The dynamics of this degree of freedom shall be slow compared to the other degrees of freedom. Therefore, x is referred to as a *slow reaction coordinate*.

One may, for example, consider the interaction of two biomolecules in an aqueous environment which serves as a heat bath (cf. Part II). For sufficiently low temperatures the transition from an initially bound state to the unbound state occurs practically always along the same *most probable escape path* $\Phi^*(x)$ in the high-dimensional phase space of the system (cf. also chapter 6). This path is parameterized by a single parameter x, the reaction coordinate. Then, all relevant states of the system are characterized by the position on this escape path, i.e., by the value of x. In many cases, the relative distance between the centers of mass of the two biomolecules is a "good reaction coordinate" meaning that this quantity uniquely characterizes the position on the most probable escape path. But for other systems, it may be possible that one cannot find a reaction coordinate with such a simple interpretation.

Concerning the temporal evolution of the reaction coordinate, for many systems it has proven fruitful to assume a stochastic dynamics of the form (2.5) or (2.7). In most cases, this is a priori just a phenomenological modeling approach which can be justified only a posteriori by the success of the resulting predictions.

There is a long-standing discussion whether such a stochastic dynamics for the reaction coordinate can alternatively also be deduced from the microscopic dynamics of the system which is governed by the Hamiltonian equations of motion or equivalently by the Euler-Lagrange equations [Kuy97, GPS02]. Quite some progress in this direction has been made, resulting in Langevin type equations of motion for the reaction coordinate [Gre52, Zwa61, GHT80, Mil83, Rei02]. However, at the very end one is left with postulating some ad hoc Ansatz for the properties of the noise and the dissipation terms [cf. equation (2.1)] in these equations. We, therefore, restrict ourselves to a brief and mathematically not very rigorous sketch of some ideas of these approaches and refer for further details to the above mentioned references, in particular to [GHT80]. We will, furthermore, restrict our discussion to the interaction of two biomolecules which is of great importance for the present work. For the other examples mentioned at the beginning of this section a completely analogous argumentation applies.

On a microscopic level, the state of the system at time t_0 is given by a point $\mathbf{\Phi}_0$ in the high-dimensional phase space. In general, this point is defined by the set of positions $\mathbf{q} = (q_1, \dots q_f)$ and momenta $\mathbf{p} = (p_1, \dots p_f)$ of the atoms of the two biomolecules and of the surrounding fluid, hence $\mathbf{\Phi}(t_0) = \mathbf{\Phi}_0 = (\mathbf{q}_0, \mathbf{p}_0)$. Together with the Hamiltonian $H = H(\mathbf{q}, \mathbf{p}, t)$, this gives the state $\mathbf{\Phi}(t)$ of the system at any time t as the solution of Hamilton's equations of motion. However, because the phase space is of very high dimension, it is neither possible to simultaneously measure the positions and momenta of all the particles, nor is it possible to prepare the system in a given state $\mathbf{\Phi}_0$. Now we assume that there exists a single slow degree of freedom $x(t)$ which can be identified with the value of a given, not explicitly time-dependent phase space function X, hence $X(\mathbf{\Phi}(t)) = x(t)$ (the relative distance between the centers of mass of the two biomolecules is such a phase space function). Then, also $\dot{x}(t)$ is connected to a phase space function, namely $d/dt\, X(\mathbf{\Phi}(t)) = \{X(\mathbf{\Phi}(t)), H(\mathbf{\Phi}(t))\} = \dot{x}(t)$ where $\{\cdot, \cdot\}$ denotes the Poisson brackets. To any given values $(x, \dot{x})$ there exists a whole hypersurface $S(x, \dot{x})$ on which the functions X and $d/dt\, X$ assume the same values. Let us denote by $\mathbf{\Omega}_{x,\dot{x}}$ a point on the hypersurface $S(x, \dot{x})$. Then the microscopic state $\mathbf{\Phi}$ of the system can also be characterized by the values $X(\mathbf{\Phi}) = x$, $d/dt\, X(\mathbf{\Phi}) = \dot{x}$ and the point on the corresponding hypersurface, i.e., $\mathbf{\Phi} = (x, \dot{x}, \mathbf{\Omega}_{x,\dot{x}})$. The preparation of the system is assumed to be such that $X(\mathbf{\Phi}(t_0)) = x_0$ and $d/dt\, X(\mathbf{\Phi}(t_0)) = \dot{x}_0$ are exactly given, while $\mathbf{\Omega}_{x_0,\dot{x}_0}(t_0)$ is randomly sampled from some distribution. Next, the temporal evolution of $x(t) = X(\mathbf{\Phi}(t))$ can be considered. As our knowledge about the initial state is limited to the values of the phase space functions X and $d/dt\, X$, while $\mathbf{\Omega}_{x_0,\dot{x}_0}(t_0)$ is unknown, this dynamics is of stochastic nature. Nevertheless, one can formally split the rate of change of $\dot{x}(t)$ at a given time t into three parts: A systematic part which depends solely on the instantaneous value $x = x(t)$ and thus defining the effective potential, a dissipative term depending on $\dot{x}(t)$, and a "random" part which on the average over all initial conditions $\mathbf{\Omega}_{x_0,\dot{x}_0}(t_0)$ leading to $(x(t), \dot{x}(t))$ is zero. The result is a Langevin type equation for the reaction coordinate $x(t)$. However, the single terms (like the properties of the noise term) appearing in this equation depend on the microscopic dynamics in a complicated way. The applicability to a given system is, thus, rather limited. Furthermore, the effective heat bath, which enters the equation of motion for $x(t)$ via the dissipative term and the noise term, in general contains memory. Then, the dynamics of the reaction coordinate is non-Markovian. Finally, one is still left with postulating an Ansatz for the stochastic dynamics of the reaction coordinate. One can, for example, make a Markovian approximation to the dynamics which can be justified by the assumption that $x(t)$ is the only slow coordinate. In this case, the dissipation term in the Langevin equation is of the form (2.1) which fixes the statistical properties of the noise according to equations (2.2,2.3) [see [Rei01] for a proof].

We will restrict our discussion to the overdamped dynamics (2.7) from now on. Furthermore, the term "Brownian particle" may also refer to a general reaction coordinate.

2.3 Fokker-Planck equation

In the previous two sections 2.1 and 2.2, we have described Brownian motion in the form of single realizations of the stochastic dynamics (2.5,2.7). Next, a completely equivalent description will be discussed. Here we will restrict ourselves to the one-dimensional overdamped motion (2.7).

In this approach the conditional probability density

$$\rho(x,t|t_0,x_0) := \langle \delta(x - x(t)) \rangle \ , \tag{2.8}$$

to find the particle at time t at position x will be considered. The notation $\rho(\ldots|x_0,t_0)$ refers to the initial condition $\rho(x,t_0|x_0,t_0) = \delta(x-x_0)$. The time-evolution of this quantity is governed by a deterministic partial differential equation, called the *Fokker-Planck equation* . Without giving any proof, it was proposed by Fokker in 1914 [Fok14] and discussed by Planck in 1918. A mathematically rigorous derivation of this equation, as well as a discussion of methods for its solution, can be found in [Ris89].

The time-evolution of the probability density $\rho(x,t|x_0,t_0)$ is given by[4]:

$$\frac{\partial}{\partial t}\rho(x,t|x_0,t_0) = \frac{\partial}{\partial x}\left(\frac{V'(x,t)}{\eta} + \frac{k_BT}{\eta}\frac{\partial}{\partial x}\right)\rho(x,t|x_0,t_0) =: \hat{L}_{\mathrm{FP}}\rho(x,t|x_0,t_0) \ , \tag{2.9}$$

where the linear differential operator $\hat{L}_{\mathrm{FP}}$ is termed the *Fokker-Planck operator*. This equation was also proposed by Smoluchowski in 1915 [Smo15] and is, therefore, also called *Smoluchowski equation*. In this work Smoluchowski gave a nice heuristic argument for its validity. He considered the continuity equation for the probability density

$$\frac{\partial}{\partial t}\rho(x,t|x_0,t_0) = -\frac{\partial}{\partial x}j(x,t|x_0,t_0) \ , \tag{2.10}$$

where $j(x,t|x_0,t_0)$ is the flux of probability. This quantity has a contribution $-\frac{k_BT}{\eta}\frac{\partial}{\partial x}\rho(x,t|x_0,t_0)$ from the diffusion and a contribution $-\frac{V'(x,t)}{\eta}\rho(x,t|x_0,t_0)$ from

---

[4] One may, of course, choose any other initial condition $\rho(x,t_0) = \rho_0(x)$. Then, due to the linearity of the Fokker-Planck equation, the probability density at time t reads: $\rho(x,t) = \int dx_0 \ \rho_0(x_0)\rho(x,t|x_0,t_0)$.

the convective flow. The total flux $j(x,t|x_0,t_0)$ is the sum of these contributions, yielding together with equation (2.10) the Fokker-Planck equation (2.9).

In the absence of an external potential this equation reduces to the well known diffusion equation:

$$\frac{\partial}{\partial t}\rho(x,t|x_0,t_0) = \frac{k_BT}{\eta}\frac{\partial^2}{\partial x^2}\rho(x,t|x_0,t_0)\ , \tag{2.11}$$

with diffusion coefficient k_BT/η in accordance with Einstein's 1905 result [Ein05], henceforth also called the Einstein relation.

2.4 Escape from a static potential

Let us now consider the thermally activated escape from a metastable, static potential, like that depicted in figure 2.1. As discussed in section 2.2, the coordinate x does not necessarily refer to the position of a particle, but can be a general reaction coordinate. Consequently, the escape over the potential barrier at $x_{\max}$ can also describe the decay of some metastable state. This can be, e.g., the unfolding of a protein or rupture of a bond which will be discussed in detail in chapter 3. Having this in mind, we will for simplicity refer to this problem as the escape of a Brownian particle from a metastable state.

In the absence of a fluctuation force, the dynamics of the particle is given by equation (2.7) with temperature $T = 0$. If the particle is in the metastable state $x \leq x_{\max}$ at some time t_0, it will stay there forever and relax to the minimum of the potential at $x_{\min}$ on a time scale approximately given by $\tau_R = \eta/V''(x_{\min})$. The situation changes for a finite temperature T. Then the particle will almost surely cross the barrier for sufficiently large times. In this work, we are mainly interested in the case of small noise strengths so that $k_BT \ll \Delta V := V(x_{\max}) - V(x_{\min})$.

In order to characterize this escape process, we first have to define the boundary conditions for the problem. Here we will assume that the potential $V(x)$ is monotonically decreasing for $x < x_{\min}$ and has an absorbing boundary at $x_a > x_{\max}$. That means, particles that cross this boundary will be “removed infinitely fast". A particle shall be injected into the potential in the vicinity of the minium at time t_0. Then, for sufficiently large times t, the probability density $\rho(x,t) = \rho(x,t|x_0,t_0)$ will become independent of the initial conditions. Next, we can consider the survival probability of the state, i.e., the probability that the particle has not crossed the boundary until time t:

$$n(t) := \int_{-\infty}^{x_a} dx\ \rho(x,t)\ . \tag{2.12}$$

The relative change of this probability becomes independent of time after a short equilibration and defines the *escape rate*:

$$k := -\dot{n}(t)/n(t)\ . \tag{2.13}$$

This quantity can also be expressed in two different ways. Firstly, we make use of the Fokker-Planck equation (2.9) and insert it into equation (2.13) which yields

$$k = -\frac{1}{n(t)} \frac{k_B T}{\eta} \frac{\partial}{\partial x} \rho(x_a, t) \ . \tag{2.14}$$

Alternatively, one may assume that a constant flux j of particles is injected into the potential at some point $x_+ < x_{\min}$. Then the system will relax into a quasi-steady state where $\partial/\partial t\, \rho(x,t) = 0$ and $j(x,t) = j$ for all $x > x_+$ (see figure 2.1), and one can define:

$$k := \frac{j}{n} \ , \tag{2.15}$$

where n is the stationary probability to find the particle inside the domain of attraction. Often equation (2.15) is used to define the escape rate. However, the formulation (2.13) has the advantage that it can be directly generalized to the case of time-dependent force fields which will be discussed in chapter 6.

The approach (2.15) is termed the flux-over-population method and was used by Kramers in 1940 to derive his famous result [Kra40] (see next section). There exist also other approaches to this problem which are extensively discussed in [HTB90]. Among them are concepts like the mean first passage time or the method of the lowest eigenvalue. In the former, one studies the distribution of times which a random walker, starting near the minimum of the potential, needs to pass the boundary $x_{\max}$ for the first time. The expectation value of this distribution is termed the *mean first passage time*. This concept is commonly used in the mathematical literature. In the method of the lowest eigenvalue, the escape rate is identified with the lowest non-vanishing eigenvalue of the Fokker-Planck operator $\hat{L}_{\mathrm{FP}}$. In the limit of small noise strengths ($\Delta V/(k_B T) \gg 1$) all these approaches yield identical results [Ris89, HTB90].

2.5 Kramers rate

For low temperatures, i.e., small noise strengths, the escape rate (2.15) can be very accurately approximated by a simple formula, called the Kramers rate. It depends only on a few properties of the potential. In order to derive this approximation, we will closely follow Kramers' original line of reasoning [Kra40].

Let us consider the situation discussed above equation (2.15), namely that a constant flux j of particles is injected into the potential at some point $x_+ < x_{\min}$. Considering only positions $x > x_+$, in the stationary state the probability density obeys, according to equations (2.9,2.10), the differential equation:

$$\frac{V'(x)}{\eta} \rho(x,t) + \frac{k_B T}{\eta} \frac{\partial}{\partial x} \rho(x,t) = -j \ . \tag{2.16}$$

For the boundary condition $\rho(x_a, t) = 0$, its solution reads:

$$\rho(x,t) = \frac{\eta j}{k_B T} \exp\left(-\frac{V(x)}{k_B T}\right) \int_x^{x_a} dy \ \exp\left(\frac{V(y)}{k_B T}\right) \ . \tag{2.17}$$

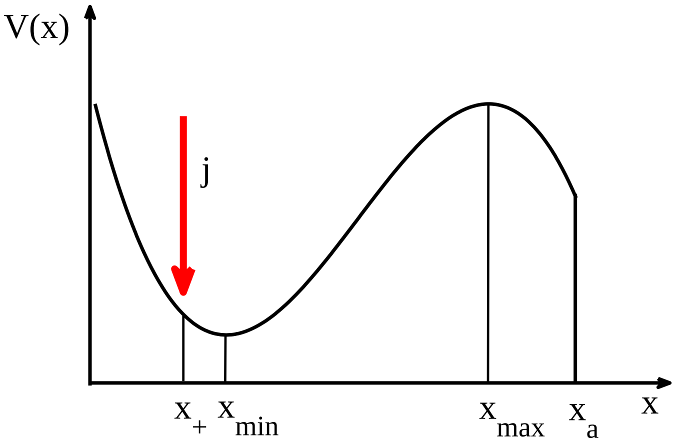

Figure 2.1: Illustration of the escape problem from a metastable potential. An absorbing boundary is placed at x_a. Particles are injected at x_+ at a constant rate j.

Using equation (2.12) and equation (2.15), we get the following expression for the escape rate:[5]

$$\frac{1}{k} = \int_{-\infty}^{x_a} dx \, \frac{\eta}{k_B T} \exp\left(-\frac{V(x)}{k_B T}\right) \int_{x}^{x_a} dy \, \exp\left(\frac{V(y)}{k_B T}\right) \, . \tag{2.18}$$

The main contribution to the first integral stems from the x values in close vicinity to the minimum of the potential at x_{min} (the remaining contributions are exponentially suppressed). For these values, the second integral is approximately constant with its main contribution stemming from the y values near the maximum x_{max} of the potential. Hence, both integrals can be approximated by the Laplace or Gaussian steepest-descent method, yielding the Kramers rate

$$k = \frac{\sqrt{|V''(x_{\mathrm{max}})| V''(x_{\mathrm{min}})}}{2\pi\eta} \exp\left(-\frac{\Delta V}{k_B T}\right) \, . \tag{2.19}$$

The inverse of this rate is called the Kramers time t_K and characterizes the typical survival time of the metastable state.

---

[5] Here we have implicitly assumed that x_+ is sufficiently small so that the probability to find the particle at a point $x < x_+$ is negligible. However, equation (2.19) remains valid for all $x_+ < x_{\mathrm{min}}$.

Part II

Single-molecule force spectroscopy: Theory and evaluation of experimental data

3 Principle and theory of single-molecule force spectroscopy

This chapter introduces the basic principles of single-molecule force spectroscopy. After a short introduction to the interactions between biomolecules, we turn to the experimental techniques used for these kinds of measurements. Particular attention will be paid to the atomic force microscope. The chapter ends with a review of the theoretical models which are commonly used in order to interprete the experimental data.

3.1 Introduction

Many biological functions rely on the ability of biomolecules to recognize their target molecules with an astonishingly high precision. Examples include the recognition of viruses by the receptors of the immune system or the specific binding of proteins to DNA. The latter is of fundamental importance for all aspects of transcription. Due to its importance for biological functions, *molecular recognition* is the subject of many scientific studies.

Biomolecules, like proteins or DNA, are macromolecules which can consist of several thousands (in general covalently bound) atoms. Despite their size, biomolecules are built up of a relatively small number of fundamental building blocks. For example, proteins are chains of amino acids. Each amino acid is linked to its neighbors via covalent peptide bonds. There are no more than 20 types of amino acids in proteins of all life-forms, from bacterium to human. Determined by the sequence of the amino acids in the chain, the protein folds to a complex and well-defined three-dimensional structure. This results in a remarkable variety of structurally complex and functionally sophisticated proteins [Str95, AJL$^+$08]. Likewise, DNA consists of two polynucleotide chains, each of them being built up of four types of nucleotide subunits.

The binding between two or more biomolecules as well as the folding of proteins relies on the cooperative effect of many non-covalent bonds. These interactions can roughly be divided into four groups: electrostatic interactions, van der Waals attractions, hydrogen bonds, and hydrophobic effects. The latter of these interactions is mediated by the water molecules of the surrounding medium. In water the strength of all these interactions is of the order of the thermal energy k_BT at room temperature and, therefore, by a factor of approximately 100 weaker than the covalent bonds [Str95, AJL$^+$08]. Hence, no non-covalent interaction can separately result in a stable bond between two biomolecules (cf. section 2.5). The formation of a *specific bond* requires that the two biomolecules possess topologically as well as chemically complementary surfaces so that many non-covalent bonds can simultaneously form [PD40]. This condition is a form of the key-lock principle which has already been proposed by Fischer in 1894 [Fis94]. The typical strength of the resulting specific bonds is of the order of $10k_BT$ and therefore still much lower than that of covalent bonds. However, the requirement that the two binding partners must possess complementary surfaces is the basis of the high specificity of the biomolecular interactions.

Single-molecule force spectroscopy provides a possibility to study these bonds and, in particular, to gain information about binding motifs and positions, as well as informations about the properties of the bond like the binding strength and dissociation rate. It is, therefore, a valuable tool to study the molecular basis of many biological functions.

3.2 Single-molecule force spectroscopy with the AFM

3.2.1 Atomic force microscope

A ground-breaking step towards studying matter on the atomic scale was the invention of the *scanning tunneling microscope (STM)* by Binnig and Rohrer in 1981 [BRGW82, BR82]. This technique makes use of the vacuum tunneling current of electrons between a sharp conducting tip and a conducting surface. Scanning such a tip against the surface, while regulating the distance between tip and surface such that the tunneling current is constant, allows to image the surface at an atomistic scale (for a review see [Wie94]).

Already in 1986 Binnig and Rohrer were rewarded with the Nobel price in physics which demonstrates the impact the STM had on surface science. In the same year Binnig invented another imaging technique, the *atomic force microscope (AFM)*, also called scanning force microscope [BQG86]. A schematic sketch of an atomic force microscope is shown in figure 3.1. The key feature of this apparatus is a tiny force sensor consisting of a tip with a diameter of typically a few 10 nm which is mounted on a soft cantilever. If this tip approaches the surface, different forces act between the single atoms of the tip and the surface, among them electrostatic and magnetic forces, van der Waals forces, and at very short distances quantum-mechanical repulsive forces (for details see [Wie94, Gie03]). These forces cause a deflection of the cantilever which behaves approximately like a Hookean spring. While in Binnig's prototype of an AFM the deflection was measured by a STM, in most modern AFMs optical methods are employed [MA88]. A focused laser beam is reflected off the rear side of the cantilever which is often metal coated to guarantee high reflectivity. The reflected beam is sensed by a (quadrant) photodiode. The signal of this detector is used by a feedback loop to control the vertical distance between tip and sample which is mounted on a piezoelectric device. Similarly as for the STM, the surface can be scanned while keeping, e.g., the force between tip and surface constant. The result is a topographic image of the sample surface with a sub-Å resolution. Different imaging modes exist.

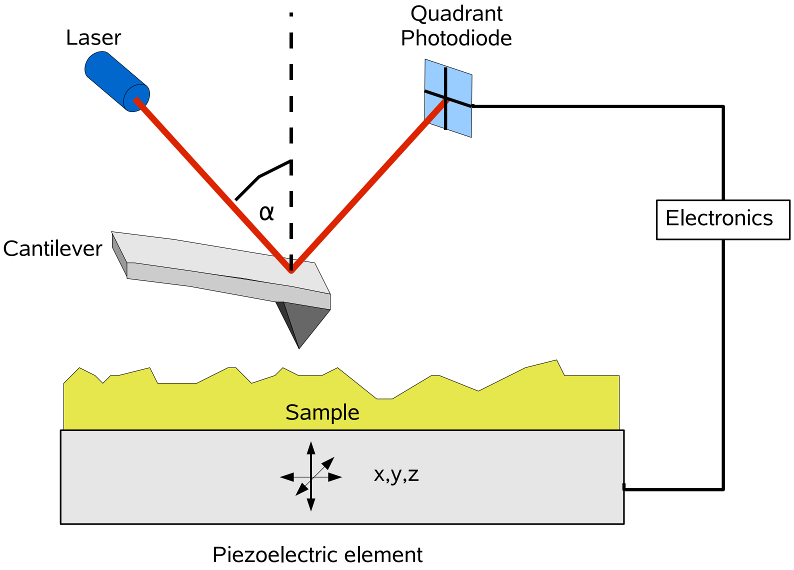

Figure 3.1: Schematic sketch of an atomic force microscope.

For details we refer to [Gie03].

The advantage of AFM over STM is that also measurements on non-conducting samples are possible. No vacuum is required, and experiments can be conducted in aqueous solution which is particularly interesting when studying biological systems.

3.2.2 Force spectroscopy

The atomic force microscope as an imaging device makes use of the forces F acting between the sharp tip and the surface atoms. These forces are connected to the experimentally accessible deflection s_c of the cantilever over a wide range of forces via Hooke's law:

$$F = c\, s_c \,, \tag{3.1}$$

with c the spring constant of the cantilever. Hence, AFM provides the possibility to quantitatively determine forces acting on the cantilever tip, provided that the spring constant is known. This quantity can be determined in different ways, e.g., by measuring the thermal fluctuations of the cantilever [HB93] or by connecting it to the geometry of the cantilever [Gie03]. Typical spring constants lie in the region of 10-100 pN/nm, allowing to determine the forces with an accuracy of a few pN [HD06].

The basic idea of *(local) force spectroscopy* is to determine the force versus distance curve at a particular point on the sample surface, i.e., for fixed x, y coordinates. The quantity which can be experimentally controlled is the z coordinate, that means, the

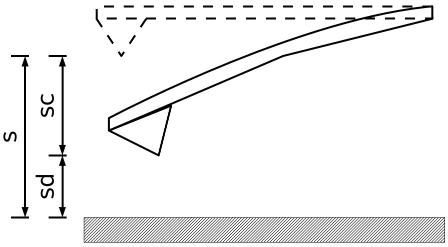

Figure 3.2: Deflection of the AFM cantilever. The distance s can be experimentally controlled.

relative distance s of the surface from the rest position of the cantilever. If elastic deformations of tip and surface can be neglected, this is the sum of the deflection s_c of the cantilever and the absolute distance s_d of the tip from the surface (see figure 3.2):

$$s = s_c + s_d \; . \tag{3.2}$$

In force spectroscopy experiments, the AFM tip or the surface is cycled up and down while measuring the force acting on the cantilever, yielding the so called *force distance curves* $F(s)$ which will be discussed in more detail in section 3.2.3.

In *single-molecule force spectroscopy* experiments, specific ligand-receptor interactions can be probed. A typical experimental setup is sketched in figure 3.3. It is basically the same as that for local force spectroscopy, but in addition one binding partner is connected to the cantilever tip, and the other is bound to the surface. The ligand, the receptor-molecules, or both are linked via polymeric tethers to the tip and to the surface, respectively [HBG$^+$96, RSA$^+$98]. Typical choices for these polymeric tethers are poly(ethylene glycol) (PEG) linkers. Usually, at least one of the linkers is long (about 30 nm) compared to the molecular length scales. This guarantees that intermolecular interactions can be distinguished from the tip-sample interactions in the force distance curves. The surface density of bound molecules is chosen such that only in a small fraction of force distance curves (approximately 10%) a bond between the ligand and the receptor-molecules can be observed. Then the probability for multiple parallel bonds is assumed to be negligible [ZLCB02].

From the force distance curves, rupture or unbinding forces can be analyzed for various pulling velocities. This yields information about the properties of the molecular interaction and will be discussed in detail in section 3.3 .

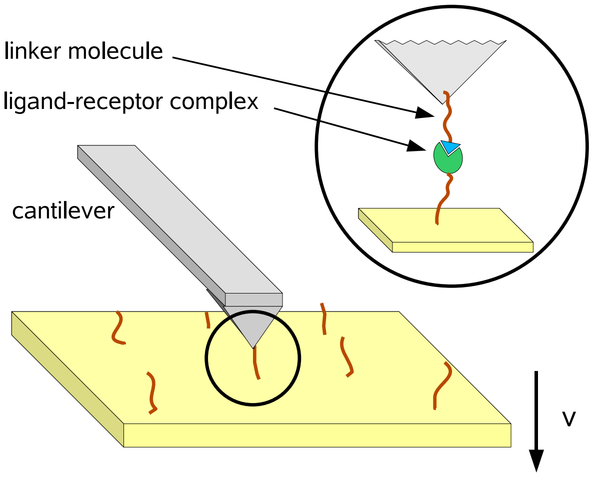

Figure 3.3: Schematic illustration of a dynamic force spectroscopy experiment. The receptor is immobilized on the surface, and the ligand is connected via a linker to the tip of an AFM cantilever which serves as a force transducer. The distance between surface and tip can be controlled with a piezoelectric element. When the surface is pulled down at a constant speed v, monotonically increasing forces act on the ligand-receptor complex.

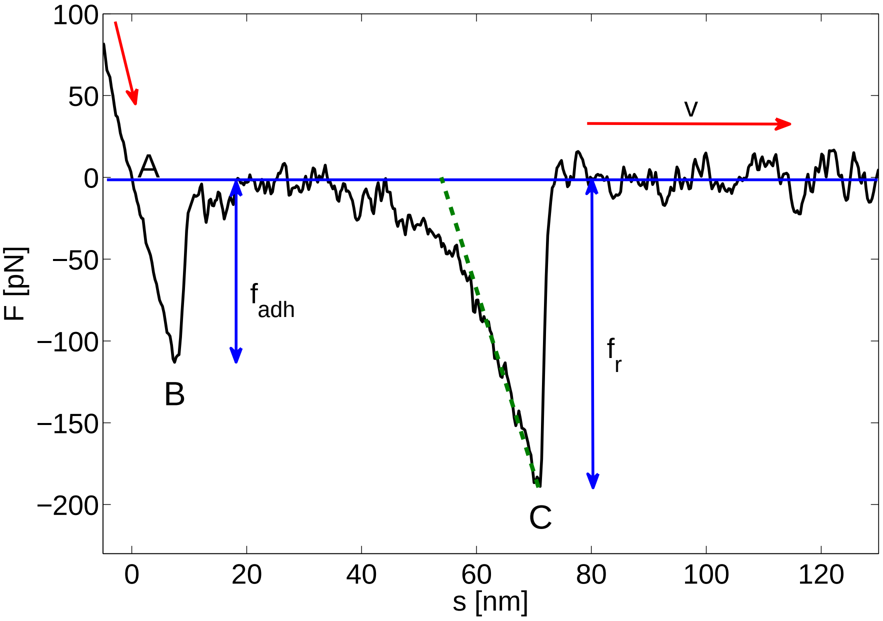

Figure 3.4: Retracting part of a "typical" force distance curve $F(s)$ measured by AFM for the protein-DNA interaction studied in [BMF$^+$07]. The surface is pulled down at a constant speed v in the direction indicated by the red arrows. The adhesion force between tip and surface is denoted by f_{adh} and the rupture force of the protein-DNA complex by f_r. The part of the force distance curve after the rupture of the bond at point C is used to fit the so called baseline (blue) which corresponds to a vanishing force acting on the tip. More details are given in the main text.

3.2.3 Force distance curves

The retracting part of a typical force distance curve measured by AFM is shown in figure 3.4. The curve starts when the tip is pressed on the surface so that the cantilever is bended upwards which causes a positive force signal. Then, the surface is pulled down at a constant speed. The force decreases, and at point A the attractive and repulsive forces cancel each other, resulting in a vanishing net interaction. At this point the cantilever is not deflected and hence $s_c = 0$. Upon further motion of the surface, the attractive force regime is entered where tip and sample adhere to each other (see section 3.2.1 and [Wie94, Gie03]). At point B an instability occurs. The tip jumps off the surface into the unbent position of the cantilever. This jump can be identified with the transition from one energy minimum of a bistable potential to another minimum. The force at which this jump occurs is termed the adhesion force $-f_{adh}$. Amongst others, it depends on the material of surface and tip and on the temperature [KT04, SPA$^+$07]. From B on, the complex composed of cantilever, linkers, and the ligand-receptor molecules is stretched until the bond breaks at point C. The part of the force distance curve between B and C is called the *force-extension curve*. Although a number of different models describing the mechanical response of idealized polymeric chains in terms of microscopic parameters like contour and Kuhn length exist (e.g. the freely jointed chain or the worm-like chain model, as reviewed, e.g., in [Mer01]), the exact functional form of this part of the force distance curve $F(s)$ is quite complicated. Since the total elastic entity is composed of cantilever, linkers, and ligand-receptor molecules, no simple realistic model exists to describe the relevant force-extension curve $F(s)$. However, because this curve is approximately linear over a wide range of loading forces, it is often approximated by a straight line (cf. green dashed line in figure 3.4) in order to quantitatively evaluate single-molecule force spectroscopy experiments. After the rupture of the specific bond at point C, the measured force fluctuates around zero. This part of the force distance curve is used to determine the baseline (blue solid line in figure 3.4) where no force acts on the tip. All forces are measured with respect to this offset, and the rupture force f_r is defined as the distance to this value at point C.

In typical experiments, many thousands of force distance cycles are measured for each pulling velocity. Only a small fraction of them shows specific rupture events. In the other curves only the adhesion signal is visible. It is, therefore, highly desirable to automatically process the force distance curves [KJHM05]. Among others, this was the aim of our work [FAR$^+$08]. We will come back to this point in section 5.4.

3.2.4 Force spectroscopy with other techniques

Besides the atomic force microscope a number of other experimental techniques exist to perform single-molecule force spectroscopy experiments, for a review see, e.g., [Mer01, LLA$^+$02, Rit06]. Most of these techniques have in common that a small force sensor (like the cantilever of the AFM) is functionalized with one of the molecules which shall be studied while the binding partner of this molecule is immobilized.

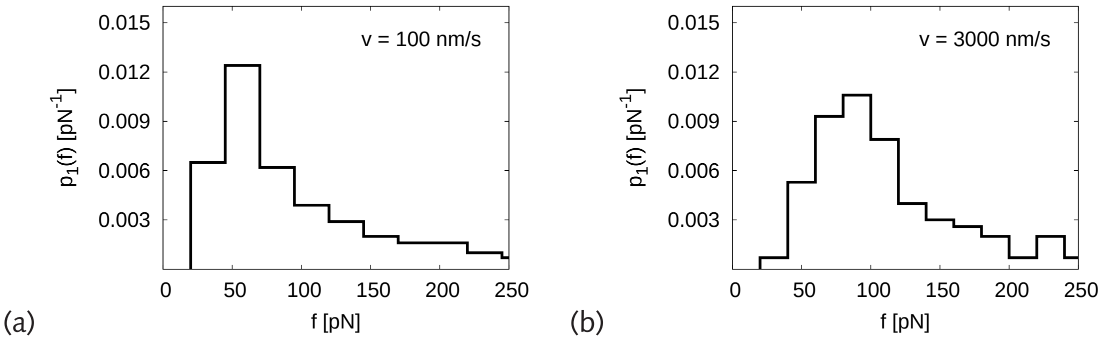

Figure 3.5: Typical distributions of rupture forces measured by Eckel et al. with the AFM for the dissociation of the PhoB peptide from the DNA target sequence [EWB$^+$05]. The pulling velocity in (a) was $v = 100$ nm/s and that in (b) $v = 3000$ nm/s.

Prominent examples, which also allow a detection of rupture forces on the pico-Newton scale, are the *biomembrane force probe (PFP)* [MNL$^+$99, NDKM03, HO07], *laser optical tweezers (LOTs)* [VSWS05, MWS07], *magnetic tweezers (MTs)* [SL07], and magnetic biochips [PKRB05]. The theory that will be reviewed in the next section, in principle, applies to all these techniques.

3.3 Theoretical modeling of bond rupture

As discussed in the previous section, single-molecule force spectroscopy experiments yield a set of N rupture forces $\mathbf{f} = \{f_i\}_{i=1}^N$ measured at pulling velocities $\mathbf{v} = \{v_i\}_{i=1}^N$. Usually, for each pulling velocity several rupture forces are sampled, i.e., many of the v_i are identical. Figure 3.5 shows two rupture force distributions for a typical experiment, here the dissociation of a peptide from its DNA target sequence studied by Eckel et al. [EWB$^+$05]. For each fixed pulling velocity, the rupture forces are found to be distributed over a wide range, and with increasing velocity these distributions shift towards higher forces. This observation is in contrast to the expectation for a purely mechanical breaking of a compound object which should rupture at some “critical” force. Hence, the theoretical interpretation of single-molecule pulling experiments is a non-trivial task. Major steps towards theoretically modeling these experiments are due to Evans and Ritchie [ER97]. Following a previous work of Bell [Bel78], they proposed that a forced bond rupture event is a thermally activated decay of a metastable state that can be described within the framework introduced in chapter 2. Several extensions of this theory exist, all relying on this basic picture of a thermally activated decay, see, e.g., [HG00, Sei00, Eva01, Wil03, BDA02, DFKU03, HS03, DBA04, HK06, SR06, ML06, DHS06, HP08].

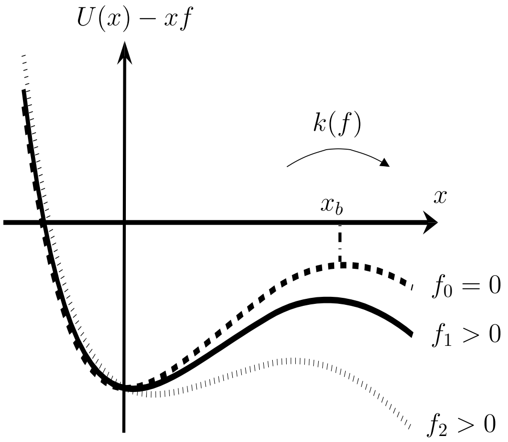

Figure 3.6: Schematic illustration of the total relevant potential energy landscape $U(x) - xf$ of a receptor-ligand bond as a function of the reaction coordinate x without and with externally applied bias forces $f_1 < f_2$. For low forces, the main effect is that the energy barrier $E_\mathrm{b}(f)$ is lowered by an amount $\Delta E_\mathrm{b} \simeq x_\mathrm{b} f$, where x_b is the distance between potential well and barrier at zero force. For larger forces this distance decreases.

3.3.1 Bond rupture as thermally activated decay of a metastable state

Following Evans and Ritchie [ER97, Mer01], a single-molecule dissociation process is viewed as a thermally activated escape of a reaction coordinate x over a potential barrier, see figure 3.6. According to our discussion in chapter 2, the dynamics of this reaction coordinate can be described by the one-dimensional overdamped Langevin equation (2.7) with delta-correlated white noise.[1]

In single-molecule force spectroscopy experiments a steadily increasing force is applied to the bond, resulting in a time-dependent potential (cf. figure 3.6)

$$V(x,t) = U(x) - f(t)x \ , \tag{3.3}$$

where $f(t) = \cos(\varphi)F(t)$ is the *projection of the instantaneous force* onto the direction of the reaction coordinate and $U(x)$ the potential landscape of the unperturbed bond. It is usually assumed that $f(t)$ agrees with the measured force $F(t)$. That means that the direction of pulling is identically to the direction of the reaction coordinate or that the angle φ between these two directions is always the same so that the factor $\cos(\varphi)$ can be included in the reaction coordinate.[2]

---

[1] As already discussed in section 2.2, this is an ad hoc Ansatz which cannot be derived systematically. Since the true phase space of this system is high-dimensional, projecting the dynamics to just one relevant reaction coordinate will, in general, result in a noise term with memory. We, hence, implicitly assume that the correlation time of this noise is much shorter than all other relevant time scales of the system, in particular, much shorter than the relaxation time τ_R.

[2] In Ansatz (3.3) it is also implicitly assumed that the relative distance of the centers of mass of the

Given the one-dimensional potential landscape along the reaction coordinate, the dissociation rate $k(f)$ for a static force $f(t) = f$ is given by the Kramers rate (2.19)

$$k(f) = \omega(f)\, \exp(-E_{\rm b}(f)/k_B T). \tag{3.4}$$

In comparison to equation (2.19), the pre-exponential factor depending on the curvature of the potential at the extrema and on the friction coefficient has been abbreviated by $\omega(f)$ and is sometimes also referred to as an "attempt frequency". The exponentially leading Boltzmann-Arrhenius factor contains the relevant potential barrier $E_{\rm b}(f)$ against escape:

$$E_{\rm b}(f) := V(x_{\rm max}(t(f)), t(f)) - V(x_{\rm min}(t(f)), t(f)) \ , \tag{3.5}$$

where $x_{\rm min,max}(t)$ are the instantaneous minimum and maximum of $V(x,t)$.

Exploiting the fact that, under experimentally realistic conditions, the force increases on a time scale much larger than all other relevant molecular relaxation times, the instantaneous escape rate is at any time very well approximated by equation (3.4) (cf. chapter 6). Due to this separation of time scales [HTB90], the reaction kinetics can be very accurately approximated by a one-step rate equation:

$$\frac{dn(t)}{dt} = -k\left(f(t)\right) n(t) \ , \tag{3.6}$$

where $n(t)$ denotes the survival probability of the bond up to time t and $k(f(t))$ is the accompanying dissociation rate (3.4) at an instantaneous external force $f(t)$.

Employing equation (3.6), the experimentally established survival probability $n(t)$ (for a given fixed pulling velocity) can be used to reconstruct the force-dependent escape rate $k(f)$. From this knowledge information about the underlying potential landscape, i.e., potential energy vs. the reaction coordinate, cf. figure 3.6, shall be gained. As the escape rate in equation (3.4) depends only on the energy *difference* at two force-dependent extrema (and via the prefactor on the curvature at these extrema), the full potential landscape cannot be uniquely reconstructed [ISB$^+$97].

One therefore usually starts with some model energy landscape and tries to deduce its global features, such as barrier height in the absence of the force and dissociation length (the distance between potential well and barrier without bias force, cf. figure 3.6). This introduces some specific functional form for the escape rate (3.4) involving several parameters $\boldsymbol{\mu}$, which are then determined by fitting the experimental data.

3.3.2 Distribution of rupture forces

A key assumption for a quantitative analysis of single-molecule force spectroscopy experiments is that the instantaneous force $f(t)$ depends solely on the total instantaneous extension $s = s(t)$ of all elastic components of the complex (cantilever, linker,

---

molecules is a "good" reaction coordinate. Otherwise, application of force would result in a more complicated effect on the metastable potential than assumed in equation (3.3).

receptor, and ligand). In other words, there exists a common force-extension curve $F(s)$ such that

$$f(t) = F(s(t)) \tag{3.7}$$

for all the pulling experiments under consideration, independently of any further details (pulling speed, linker properties, etc.) of the single repetitions of the experiment [FAR+08].

We restrict ourselves to the usual case that the surface is retracted at constant velocity v, i.e.,

$$s(t) = vt \ , \tag{3.8}$$

and without loss of generality we choose the time offset such that $t = 0$ when pulling starts. Applying furthermore the usual assumption of a linear force-extension characteristics (cf. section 3.2.3 and figure 3.4), the instantaneous force at time t is given by

$$f(t) = \kappa vt \ , \tag{3.9}$$

where κ is the relevant total elasticity of cantilever, linker molecules, receptor, and ligand (slope of green dashed line in figure 3.4).

We can formally solve equation (3.6) for a given velocity v and a given force-dependence of the escape rate $k(f) = k(f|\boldsymbol{\mu})$ which is characterized by a set of model parameters $\boldsymbol{\mu}$. Changing to f as independent variable by employing (3.9) yields the probability density of escape events at the force value f:

$$p_1(f|\boldsymbol{\mu}, v) = -\frac{dn(f|\boldsymbol{\mu}, v)}{df} = \frac{k(f|\boldsymbol{\mu})}{\kappa v} e^{-g(f|\boldsymbol{\mu})/\kappa v} \ , \tag{3.10}$$

$$g(f|\boldsymbol{\mu}) := \int_0^f df' k(f'|\boldsymbol{\mu}) \ . \tag{3.11}$$

For later convenience, the rupture force distribution (3.10) is written as a conditional probability, conditioned on the values of the model parameters $\boldsymbol{\mu}$ and the pulling velocity v. While, in practice, the latter is directly accessible from the measurement, the model parameters $\boldsymbol{\mu}$ have to be inferred from the distribution of rupture forces (see chapter 4).

3.3.3 Rate Ansatz

For any functional form of the rate $k(f|\boldsymbol{\mu})$, the integral (3.11) can be evaluated numerically or by employing efficient approximations [HG00, Evs08]. In what follows, we focus on two prominent rate approximations which allow to evaluate the integral from equation (3.11) analytically.

Bell's model

The first common approximation, originally due to Bell [Bel78], and later also employed by Evans and Ritchie [ER97], consists in the linearization of the force dependent potential barrier (3.5) according to

$$E_{\mathrm{b}}(f) = E_{\mathrm{b}}(0) - x_{\mathrm{b}} f \ . \tag{3.12}$$

The *dissociation length* x_{b} is defined as the distance between potential well and barrier of the unperturbed potential $U(x)$, i.e., $x_{\mathrm{b}} := x_{\max}(t=0) - x_{\min}(t=0)$ [cf. figure 3.6]. Furthermore, the force dependence of the pre-exponential factor $\omega(f)$ in the Kramers rate (3.4) is neglected, resulting in

$$k(f|\boldsymbol{\mu}) = k_0 \exp\left(\frac{x_{\mathrm{b}} f}{k_{\mathrm{B}} T}\right) =: \exp(\lambda + \alpha f) \ , \tag{3.13}$$

where $k_0 := \omega(0)\exp(-E_{\mathrm{b}}(0)/k_{\mathrm{B}}T)$ is the force-free dissociation rate and $\lambda := \ln k_0$, $\alpha := x_{\mathrm{b}}/k_{\mathrm{B}}T$ are convenient abbreviations.

Substituting equation (3.13) into (3.10,3.11), a straightforward calculation yields the survival probability and the probability density of rupture events for Bell's model:

$$n(f|\boldsymbol{\mu}, v) = \exp\left(-\frac{e^{\lambda}}{\kappa v}\frac{e^{\alpha f}-1}{\alpha}\right) \ , \tag{3.14}$$

$$p_1(f|\boldsymbol{\mu}, v) = \frac{e^{\lambda+\alpha f}}{\kappa v}\exp\left(-\frac{e^{\lambda}}{\kappa v}\frac{e^{\alpha f}-1}{\alpha}\right) \ . \tag{3.15}$$

In this approximation the survival probability (3.14) and the rupture force density (3.15) are conditioned on $\boldsymbol{\mu} = (\lambda, \alpha)$ and v. The remaining parameter κ, appearing on the right-hand sides of (3.14,3.15), is assumed to be exactly known from the force-extension curves.

For pulling velocities larger than $k_0/(\alpha\kappa)$, the rupture force density (3.15) has a maximum at

$$f^* = \frac{1}{\alpha}\ln\left(\frac{\alpha\kappa v}{e^{\lambda}}\right) \ , \tag{3.16}$$

otherwise it is a monotonically decreasing function of the force f. As discussed in more detail in section 4.2.2, relation (3.16) is often employed to estimate the model parameters from a single-molecule force spectroscopy experiment. A similar relation can be derived for the mean rupture force $\langle f \rangle$ as, for example, done in appendix A.2.

Extension of Bell's model

As can be seen from figure 3.6, a linearization (3.12) of the force dependent potential barrier $E_{\mathrm{b}}(f)$ is relatively good for small forces. For a larger force, the distance between the potential extrema decreases, leading to a weaker sensitivity of the barrier height to force variations upon further pulling than in equation (3.12).

Models including this effect, in general, rely on some assumptions concerning the shape of the energy landscape. Typical choices are Morse potentials, harmonic potentials with a cusp barrier, two parabolas at the potential extrema joined at a midpoint, and linear-cubic potentials [DFKU03, HS03, HK06, ML06, DHS06, HK06, HP08]. It has been suggested in [DHS06] that for sufficiently high barriers, i.e., forces substantially smaller than the critical force, the dissociation rate can be written in a unique form:

$$k(f|\boldsymbol{\mu}) = (1-\gamma\alpha f/\epsilon)^{1/\gamma-1}\, e^{\lambda+\epsilon[1-(1-\gamma\alpha f/\epsilon)^{1/\gamma}]}\ , \tag{3.17}$$

with three model parameters $\boldsymbol{\mu} = (\lambda, \alpha, \epsilon)$ and fixed exponent $1/\gamma$. Here λ and α have the same physical meaning as in equation (3.13), and $\epsilon := E_{\mathrm{b}}(0)/k_{\mathrm{B}}T$ stands for the force-free activation energy barrier in units of the thermal energy $k_{\mathrm{B}}T$.

The extra parameter γ controls the manner in which the barrier height decreases with the applied force. We note that, physically, this parameter should be in the range $\gamma \in (0, 1]$ since $\gamma \leq 0$ would imply a positive barrier for all $f > 0$. On the other hand, the first derivative of the barrier height equals minus the distance between the potential extrema corresponding to a given force value. Since we expect this distance to decrease with the force, we conclude that the second force derivative of the barrier height must be positive, excluding γ-values greater than 1. Specifically, for $\gamma = 1$ the parameter ϵ drops out and one recovers Bell's model (3.13), $\gamma = 2/3$ reproduces the Kramers rate for a cubic reaction potential, and $\gamma = 1/2$ corresponds to a parabolic potential well with a cusp barrier.

Substituting equation (3.17) into (3.6) and employing equation (3.9), one derives the survival probability and the rupture force density of the bond:

$$n(f|\boldsymbol{\mu}, v) = \exp\left(-\frac{e^{\lambda}}{\kappa v}\frac{e^{\epsilon[1-(1-\gamma\alpha f/\epsilon)^{1/\gamma}]}-1}{\alpha}\right)\ , \tag{3.18}$$

$$p_1(f|\boldsymbol{\mu}, v) = \frac{k(f|\boldsymbol{\mu})}{\kappa v} n(f|\boldsymbol{\mu}, v)\ . \tag{3.19}$$

We mention that, like for Bell's model, approximate formulas for the mean and most probable rupture force can be derived [Gar95, Evs08].

As already mentioned, the application of Kramers' reaction rate theory requires that the potential barrier $E_{\mathrm{b}}(f)$ is sufficiently high compared to the thermal energy $k_{\mathrm{B}}T$ (cf. section 2.5). Thus, all approximations are only valid for forces substantially smaller than the critical force at which the barrier vanishes, $f_{\mathrm{c}} = \epsilon/(\gamma\alpha)$. On the other hand, if the exponent $1/\gamma$ in equation (3.17) is known, i.e., if it is known how the potential barrier decreases with increasing force, one should, in principle, be able to estimate the force-free potential barrier $E_{\mathrm{b}}(0)$ from single-molecule force spectroscopy data. How accurate these estimates are, will be discussed in the next chapter. We will furthermore deal with the question whether the exponent $1/\gamma$ itself can be determined by performing such experiments.

4 Evaluation of single-molecule force spectroscopy experiments

Let us assume that a specific model and thus the particular form of the probability density p_1 in (3.10) is given. Then, the remaining task is to estimate the model parameters $\boldsymbol{\mu}$ from a given set of N rupture forces $\mathbf{f} = \{f_i\}_{i=1}^N$ and pulling velocities $\mathbf{v} = \{v_i\}_{i=1}^N$. There exist different "recipes" for doing this, called estimators. Each of them can be formally represented by some function $\tilde{\boldsymbol{\mu}}(\mathbf{f})$, indicating that the estimate, being a function of the random variables $\mathbf{f}$, is a random variable itself. Now, the main question is: what is the optimal estimate of the model parameters that can be extracted from the given set of N rupture forces? Stated differently: which recipe yields estimates $\tilde{\boldsymbol{\mu}}(\mathbf{f})$ of the model parameters which are *on average* over many data sets $\mathbf{f}$ closest to the *"true" model parameters*?

Questions of this kind have been extensively discussed in the mathematical literature, and it has been shown that in many cases the so-called maximum likelihood estimator is the "best possible recipe" [Cra46, CT91]. In this chapter, we briefly review the main results and work out a rather simple, new derivation under the specific conditions given in single-molecule pulling experiments, namely the availability of quite large data sets of measured rupture forces for several different pulling velocities. We will show that, under realistic experimental conditions, indeed no estimator $\tilde{\boldsymbol{\mu}}(\mathbf{f})$ outperforms the maximum likelihood estimator. After that, we apply the method to the two specific models discussed in section 3.3.3. For Bell's model explicit expressions for the statistical errors will be derived. The main purpose for discussing the generalization of Bell's model is to examine whether all of the model parameters, in particular the force-free activation barrier height, can be estimated reliably from the experimental data.

The main parts of this chapter are taken from our publications [GR07, GER09]. All numerical and most of the analytical calculations as well as writing main parts of the manuscripts have been done by the present author.

4.1 Parameter estimation: Properties of the maximum likelihood estimator

4.1.1 Maximum likelihood estimator

Our starting point is the probability p to observe a given set of N rupture forces $\mathbf{f} = \{f_i\}_{i=1}^N$ measured at pulling velocities $\mathbf{v} = \{v_i\}_{i=1}^N$. Since the f_i are statistically independent, this probability reads:

$$p(\mathbf{f}|\boldsymbol{\mu},\mathbf{v}) = \prod_{i=1}^{N} p_1(f_i|\boldsymbol{\mu},v_i)\ . \tag{4.1}$$

The proceeding consists in simply maximizing (4.1) with respect to $\boldsymbol{\mu}$ [GR07, DMS+07]; usually, this has to be done numerically. For any given $\mathbf{f}$ and $\mathbf{v}$ the corresponding set of parameters $\boldsymbol{\mu}^* = \boldsymbol{\mu}^*(\mathbf{f},\mathbf{v})$ is called the *maximum likelihood estimate*.

Intuitively, the properties of this estimator are most easily understood within the framework of Bayesian inference [JB03, D'A03, Dos03]. The quantity in (4.1) is called *likelihood* and plays a central role in the Bayesian approach. Extending the notion of "probability" in the sense of "degree of belief" to the model parameters $\boldsymbol{\mu}$, the joint probability $p(\mathbf{f},\boldsymbol{\mu},\mathbf{v})$ can be written in terms of conditional probabilities $p(...|...)$ either in the form $p(\boldsymbol{\mu}|\mathbf{f},\mathbf{v})\,p(\mathbf{f},\mathbf{v})$ or in the form $p(\mathbf{f}|\boldsymbol{\mu},\mathbf{v})\,p(\boldsymbol{\mu},\mathbf{v})$, yielding Bayes' theorem:

$$p(\boldsymbol{\mu}|\mathbf{f},\mathbf{v}) = p(\mathbf{f}|\boldsymbol{\mu},\mathbf{v})\,p(\boldsymbol{\mu},\mathbf{v})\,[p(\mathbf{f},\mathbf{v})]^{-1}\ . \tag{4.2}$$

The left-hand side represents the "likeliness" of $\boldsymbol{\mu}$, given the data $\mathbf{f}$, $\mathbf{v}$, and hence is clearly of central interest for our purposes. Considering also the right-hand side as a function of $\boldsymbol{\mu}$, it is equal to the likelihood from (4.1) times the so called *prior probability* $p(\boldsymbol{\mu},\mathbf{v})$, encapsulating all our knowledge about $\boldsymbol{\mu}$ before the measurement, times a $\boldsymbol{\mu}$-independent factor. Thus, determining $p(\boldsymbol{\mu}|\mathbf{f},\mathbf{v})$ by means of the right-hand side of (4.2) provides the central "recipe of learning" within the Bayesian approach [D'A03, Dos03].

Regarding actual practical application of Bayesian inference, the determination of the prior probability is the most problematic point. Different recipes for selecting an appropriate prior exist [JB03]. Common choices are distributions which are uniform in the parameters or the logarithms of the parameters. Rigorous justifications are in general not possible and one is left with postulating some heuristic ad hoc Ansatz.

However, dynamic force spectroscopy usually provides large data sets, i.e., large N. Then the likelihood (4.1) develops a narrow peak in the region of its maximum $\boldsymbol{\mu}^*$ (see next section), and the prior $p(\boldsymbol{\mu},\mathbf{v})$ in (4.2), though usually unknown in detail, can be considered as approximately constant, i.e., $p(\boldsymbol{\mu}|\mathbf{f},\mathbf{v}) \propto p(\mathbf{f}|\boldsymbol{\mu},\mathbf{v})$. Given $\mathbf{f}$ and $\mathbf{v}$, the likelihood (4.1) thus quantifies the "likeliness" that the "true" model parameters are $\boldsymbol{\mu}$.

The upshot of the above intuitive considerations is that maximizing (4.1) with respect to $\boldsymbol{\mu}$ should yield the best possible guess for the unknown true parameters. Furthermore, the statistical uncertainties of this estimate should be somehow related to the width of the likelihood. In the following subsection, we leave this intuitive level and turn to a more rigorous discussion of the asymptotic properties of the maximum likelihood estimator.[1]

---

[1] In this work Bayesian inference is only used to motivated the choice of the maximum likelihood estimator for parameter inference. From a mathematical point of view, Bayesian inference is a com-

4.1.2 Asymptotic properties

Let us assume that the rupture forces f_i have been sampled according to the "true" distribution $p_1(f_i|\boldsymbol{\mu}_0, v_i)$ with unknown, *"true" model parameters* $\boldsymbol{\mu}_0$. For a given set of rupture forces $\mathbf{f}$ and pulling velocities $\mathbf{v}$ the maximum likelihood estimate can then be determined as described above. Upon repeating the entire set of N pulling experiments with the same set of pulling velocities $\mathbf{v}$, a different set of rupture data $\mathbf{f}$ will be sampled, yielding a different maximum likelihood estimate $\boldsymbol{\mu}^*$. While the probability distribution of $\mathbf{f}$ is given by (4.1) with $\boldsymbol{\mu} = \boldsymbol{\mu}_0$, what can we say about the distribution of the maximum likelihood estimates $\boldsymbol{\mu}^*$?

To answer this question, we first exploit the fact that in typical single-molecule pulling experiments for each pulling velocity several hundred rupture forces are measured. The resulting set of rupture force data $\mathbf{f}$ is thus quite large, and it is convenient to rewrite the likelihood (4.1) as

$$\begin{aligned} p(\mathbf{f}|\boldsymbol{\mu}, \mathbf{v}) &= \exp\{-N\, s_N(\mathbf{f}, \boldsymbol{\mu}, \mathbf{v})\} \ , && (4.3)\\ s_N(\mathbf{f}, \boldsymbol{\mu}, \mathbf{v}) &:= -N^{-1} \sum_{i=1}^{N} \ln p_1(f_i|\boldsymbol{\mu}, v_i) \ . && (4.4) \end{aligned}$$

Furthermore, we assume that rupture forces have been measured at Z different pulling velocities v_β, $\beta = 1, ..., Z$, and that the relative frequency with which the different pulling velocities v are sampled, converges towards a well defined limit $\rho(v) = \sum_{\beta=1}^{Z} \rho_\beta \delta(v - v_\beta)$ for $N \to \infty$. Then it follows from the law of large numbers [CT91] that

$$s_N(\mathbf{f}, \boldsymbol{\mu}, \mathbf{v}) \quad \to \quad s(\boldsymbol{\mu}) := -\langle \ln p_1(f|\boldsymbol{\mu}, v)\rangle_1 \tag{4.5}$$

for $N \to \infty$, where $\langle \cdots \rangle_1$ indicates an average over f and v with weight $p_1(f|\boldsymbol{\mu}_0, v)\, \rho(v)$. Hence, s_N is an intensive, entropy-like quantity. Observing that $s(\boldsymbol{\mu}) - s(\boldsymbol{\mu}_0)$ is a relative entropy of the form $\langle \ln(p_1(f|\boldsymbol{\mu}_0, v)/p_1(f|\boldsymbol{\mu}, v))\rangle_1$, and using the fact that $p_1(f|\boldsymbol{\mu}, v)$ is normalized with respect to f for every choice of the parameters $\boldsymbol{\mu}$, we obtain

$$s(\boldsymbol{\mu}) - s(\boldsymbol{\mu}_0) = \int dv\ \rho(v) \int df\ p_1(f|\boldsymbol{\mu}, v)\, [R \ln R - R + 1] \ , \tag{4.6}$$

with $R := p_1(f|\boldsymbol{\mu}_0, v)/p_1(f|\boldsymbol{\mu}, v)$. Finally, using the inequality

$$0 \le \int_1^R dx\ \ln x = R \ln R - R + 1 \quad \forall R \ , \tag{4.7}$$

we see that $s(\boldsymbol{\mu}) - s(\boldsymbol{\mu}_0) \ge 0$ and that $s(\boldsymbol{\mu}) - s(\boldsymbol{\mu}_0) = 0$ if the expression in the square brackets on the right-hand side of (4.6) vanishes for all f. Thus, $s(\boldsymbol{\mu})$ has a

---

pletely different approach to parameter inference than maximum likelihood estimation. The latter is a method from the "frequentists" approach to probability theory. Even "probability" has a different meaning within these two frameworks. We do not discuss this rather "philosophical" point in more detail here and refer to the references [Siv96, JB03]. We mention, however, that in our case of large data sets both frameworks yield the same estimates.

unique absolute minimum at $\boldsymbol{\mu} = \boldsymbol{\mu}_0$ [CT91]. Since s_N converges for large N toward s according to (4.5), also the minimum $\boldsymbol{\mu}^*$ of the former converges to the minimum $\boldsymbol{\mu}_0$ of the latter, i.e., the maximum likelihood estimate is a so-called consistent estimate [Cra46].

For large, but finite N values, $\boldsymbol{\mu}$ will be close to $\boldsymbol{\mu}^*$. Consequently, we can expand $s_N(\mathbf{f}, \boldsymbol{\mu}, \mathbf{v})$ up to second order about its minimum at $\boldsymbol{\mu}^*$, and neglecting terms of order $\mathcal{O}(1/\sqrt{N})$, the Hessian matrix of $s_N(\mathbf{f}, \boldsymbol{\mu}^*, \mathbf{v})$ can be replaced by the Hessian $H = H(\boldsymbol{\mu}_0)$ of $s(\boldsymbol{\mu}_0)$, which is generically positive definite, i.e.,

$$s_N(\mathbf{f}, \boldsymbol{\mu}^* + \boldsymbol{\Delta}, \mathbf{v}) \;\; = \;\; s_N(\mathbf{f}, \boldsymbol{\mu}^*, \mathbf{v}) + \boldsymbol{\Delta}^\dagger H \boldsymbol{\Delta}/2 \; . \tag{4.8}$$

For large N this is a very good approximation for all $\boldsymbol{\mu}$-values, and $p(\mathbf{f}|\boldsymbol{\mu}, \mathbf{v})$ approaches a very sharply peaked Gaussian about $\boldsymbol{\mu}^*$,

$$p(\mathbf{f}|\boldsymbol{\mu}, \mathbf{v}) \propto \exp\{-N(\boldsymbol{\mu} - \boldsymbol{\mu}^*)^\dagger H(\boldsymbol{\mu} - \boldsymbol{\mu}^*)/2\} \; . \tag{4.9}$$

We can now determine the first moments of the distribution of the maximum likelihood estimate $\boldsymbol{\mu}^*$ (upon many repetitions of the same experiment). Differentiating (4.8) and choosing $\boldsymbol{\Delta} = \boldsymbol{\mu}_0 - \boldsymbol{\mu}^*$ results in

$$\boldsymbol{\mu}^* - \boldsymbol{\mu}_0 = -H^{-1}\partial s_N(\mathbf{f}, \boldsymbol{\mu}_0, \mathbf{v})/\partial\boldsymbol{\mu} \; . \tag{4.10}$$

Averaging over $\mathbf{f}$ yields zero on the right-hand side, as can be inferred from (4.4,4.5) and the fact that $\boldsymbol{\mu}_0$ is the minimum of s. Hence,

$$\langle \boldsymbol{\mu}^* \rangle = \boldsymbol{\mu}_0 \; , \tag{4.11}$$

where $\langle \cdots \rangle$ indicates an average over $\mathbf{f}$ with weight $p(\mathbf{f}|\boldsymbol{\mu}_\mathbf{0}, \mathbf{v})$ for a given set of pulling velocities $\mathbf{v}$. Equation (4.11) thus shows that the maximum likelihood estimate is "unbiased" for large N.

With (4.10) the determination of the second moments is straightforward. Using

$$\left\langle \frac{\partial}{\partial \mu_i} s_N(\mathbf{f}, \boldsymbol{\mu}_0, \mathbf{v}) \frac{\partial}{\partial \mu_j} s_N(\mathbf{f}, \boldsymbol{\mu}_0, \mathbf{v}) \right\rangle = \frac{1}{N} H_{ij} \; , \tag{4.12}$$

gives the covariance matrix for the maximum likelihood estimate:

$$\langle [\boldsymbol{\mu}^* - \boldsymbol{\mu}_0] \, [\boldsymbol{\mu}^* - \boldsymbol{\mu}_0]^\dagger \rangle = (N\, H)^{-1} \; . \tag{4.13}$$

Observing that $(N\, H)^{-1}$ is also the covariance matrix of the distribution from (4.9), we arrive at our

First main conclusion: For any given, sufficiently large data set $\mathbf{f}$, the expected deviation of the concomitant maximum likelihood estimate $\boldsymbol{\mu}^*$ from the "true" parameters $\boldsymbol{\mu}_0$ immediately follows from the "peak-width" of likelihood (4.1), considered as a function of $\boldsymbol{\mu}$.

Similarly, using the central limit theorem, one can show (see appendix A.1) that $\boldsymbol{\mu}^*$ is Gaussian distributed, yielding with (4.9) our

Second main conclusion: Apart from the peak position and a normalization factor, the likelihood (4.1) for one given data set $\mathbf{f}$ looks practically the same as the distribution of the maximum likelihood estimates $\boldsymbol{\mu}^*$ from many repetitions of the N pulling experiments.

4.1.3 Cramér-Rao bound

It should be noted that, in order to derive the above two main conclusions, we did not make any use of the Bayesian formalism (4.2) at all. The latter only served to acquire an intuitive idea about the meaning of the likelihood (4.1). At this intuitive level, we have seen that the left-hand side of (4.2) is very well approximated by the sharply peaked Gaussian in (4.9), and hence it is reasonable to expect that its maximum $\boldsymbol{\mu}^*$ should be the best possible guess for the unknown, true parameters $\boldsymbol{\mu}_0$ that possibly can be inferred from a given set of data $\mathbf{f}$. A more rigorous line of reasoning starts with an arbitrary "recipe" $\tilde{\boldsymbol{\mu}}(\mathbf{f})$ of estimating the true parameters $\boldsymbol{\mu}_0$ from a given data set $\mathbf{f}$. The only assumption is that this recipe is unbiased, i.e., upon repeating the same experiment many times, the "true" parameters are recovered on average, $\langle\tilde{\boldsymbol{\mu}}(\mathbf{f})\rangle = \boldsymbol{\mu}_0$. By generalizing the well known Cramér-Rao inequality [CT91], which in turn is basically a descendant of the Cauchy-Schwarz inequality, one can show [Cra46] for any such "recipe" $\tilde{\boldsymbol{\mu}}(\mathbf{f})$ that

$$\langle [\tilde{\boldsymbol{\mu}} - \boldsymbol{\mu}_0]\, [\tilde{\boldsymbol{\mu}} - \boldsymbol{\mu}_0]^\dagger \rangle - (N\, H)^{-1} \geq 0 \,, \tag{4.14}$$

i.e., the matrix on the left-hand side is non-negative definite. Comparison with (4.13) yields our

Third main conclusion: There is no unbiased estimator $\tilde{\boldsymbol{\mu}}$ of the true parameters $\boldsymbol{\mu}_0$ which on the average outperforms the maximum likelihood estimate $\boldsymbol{\mu}^*$.

The remaining possibility that a biased estimator may be even better is rather subtle to treat rigorously, but intuitively this seems quite unlikely. Furthermore, in the above conclusion we exploited the relation (4.13) which is strictly correct only for asymptotically large N. Finally, also the criterion of minimizing the left-hand side of equation (4.14) itself is in principle debatable, but hardly in practice.

4.1.4 Parameter inference: Main steps for the practical application

We now briefly summarize the main steps of the maximum likelihood method for evaluating single-molecule pulling experiments. The first step consists in specifying the dependence of the rupture force probability $p_1(f|\boldsymbol{\mu}, v)$ on the model parameters $\boldsymbol{\mu}$ and the pulling velocity v within a given theoretical description. Then, for the set of rupture forces $\mathbf{f} = \{f_i\}_{i=1}^N$ and corresponding pulling velocities $\mathbf{v} = \{v_i\}_{i=1}^N$ the logarithm of the likelihood (4.3)

$$-\, N s_N(\mathbf{f}, \boldsymbol{\mu}, \mathbf{v}) = \sum_{i=1}^{N} \ln p_1(f_i|\boldsymbol{\mu}, v_i) \tag{4.15}$$

is maximized with respect to the model parameters $\boldsymbol{\mu}$. Usually, this step has to be accomplished numerically. The position of the maximum defines the most probable parameters $\boldsymbol{\mu}^*$ which are on average closer to the true model parameters than any other estimate. The statistical uncertainties of the parameters can then be estimated as

$$\langle [\boldsymbol{\mu}^* - \boldsymbol{\mu}_0]\,[\boldsymbol{\mu}^* - \boldsymbol{\mu}_0]^\dagger \rangle \approx (N\,H_N)^{-1}\;, \tag{4.16}$$

where H_N denotes the Hessian matrix of s_N evaluated at the most probable parameters $\boldsymbol{\mu}^*$ and $\boldsymbol{\mu}_0$ the true model parameters. Moreover, the distribution of the maximum likelihood estimate is Gaussian with mean $\boldsymbol{\mu}_0$.

4.2 Application to Bell's model

By numerically solving the integral in the formal solution (3.10,3.11) for the rupture force density, one can apply the maximum likelihood approach from the previous section to deduce the rate parameters for any functional form of the escape rate. In what follows, however, we will focus on the two rate approximations discussed in section 3.3.3, which allowed us to evaluate the integral from equation (3.11) analytically.

4.2.1 Statistical uncertainties of Bell's model

For Bell's model, the probability density for the rupture forces is given by equation (3.15):

$$p_1(f|\boldsymbol{\mu}, v) = \frac{e^{\lambda+\alpha f}}{\kappa v} \exp\left(-\frac{e^{\lambda}}{\kappa v} \frac{e^{\alpha f} - 1}{\alpha} \right)\;. \tag{4.17}$$

This density is conditioned on the two unknown parameters $\boldsymbol{\mu} = (\lambda, \alpha)$ which shall be extracted from the rupture force data.

For this model we can calculate $s(\boldsymbol{\mu}) = -\langle \ln p_1(f|\boldsymbol{\mu}, v)\rangle_1$, as defined in (4.5), analytically if the dimensionless quantity $\tau_\beta := e^{\lambda_0}/(\kappa v_\beta \alpha_0)$ is small for all pulling velocities, i.e., $\tau_\beta \ll 1$. In fact, $\tau_\beta < 1$ is equivalent to the assumption that the distribution of rupture events $p_1(f|\boldsymbol{\mu}_0, v_\beta)$ has a maximum at some force $f_\beta^* > 0$ [cf. equation (3.16)]. Details of the calculations are given in appendix A.2, resulting in

$$\begin{aligned} s(\boldsymbol{\mu}) \quad &= \quad -\lambda + \sum_{\beta=1}^{Z} \rho_\beta s_\beta(\boldsymbol{\mu}) + \mathcal{O}(\tau_\beta)\;, \qquad (4.18)\\ s_\beta(\boldsymbol{\mu}) \quad &:= \quad \ln(\kappa v_\beta) + \eta(\mathcal{C} + \ln \tau_\beta) + \frac{e^{\lambda}\,\Gamma\,(\eta+1)}{\kappa v_\beta \alpha\,[\tau_\beta]^\eta}\;, \end{aligned}$$

with $\eta := \alpha/\alpha_0$, $\mathcal{C} \approx 0.577$ Euler's constant, and $\Gamma(\cdot)$ the Gamma function. Differentiating (4.18) twice with respect to the model parameters, a straightforward calculation yields the Hessian $H = H(\boldsymbol{\mu}_0)$ of $s(\boldsymbol{\mu}_0)$. Finally, inverting this (2×2) matrix, we obtain the variance of the maximum likelihood estimate of the two parameters:

$$\langle(\alpha^* - \alpha_0)^2\rangle \approx \frac{\alpha_0^2}{N} \frac{1}{\frac{\pi^2}{6} + \sigma^2(\ln(r))} \,, \tag{4.19}$$

$$\langle(\lambda^* - \lambda_0)^2\rangle \approx \frac{1}{N} \frac{\sum\limits_{\beta=1}^{Z} \frac{N_\beta}{N} \left(\alpha_0^2 \langle f_\beta \rangle^2 + \frac{\pi^2}{6} \right)}{\frac{\pi^2}{6} + \sigma^2(\ln(r))} \,, \tag{4.20}$$

where

$$\sigma^2(\ln(r)) = \sum_{\beta=1}^{Z} \rho_\beta \ln^2(r_\beta) - \left(\sum_{\beta=1}^{Z} \rho_\beta \ln(r_\beta) \right)^2 \tag{4.21}$$

is the variance of the logarithm of the loading rate $r := \kappa v$ and

$$\langle f_\beta \rangle = -1/\alpha_0(\mathcal{C} + \ln(e^{\lambda_0}/(r_\beta \alpha_0))) \tag{4.22}$$

the expected rupture force at loading rate r_β (again neglecting terms of order $\mathcal{O}(\tau_\beta)$). For practical application of equations (4.19,4.20), the true model parameters $\boldsymbol{\mu}_0$ on the right-hand sides of the equations have to be replaced by the concomitant maximum likelihood estimate $\boldsymbol{\mu}^*$. For large N this is a very good approximation.

In single-molecule pulling experiments, only a limited range of pulling velocities v is accessible, i.e., $v_\beta \in [v_{\min}, v_{\max}]$. Now the question arises: for which distribution of pulling velocities $\rho(v)$ do the statistical uncertainties (4.19,4.20) of the estimated parameters become minimal? Recognizing that the variance of the maximum likelihood estimate of α depends on the distribution of the pulling velocities solely via the term $\sigma^2(\ln(r))$ in the denominator of (4.19), while this distribution enters into the expression for the statistical uncertainties of λ^* also via the terms $\langle f_\beta \rangle$ in the numerator of (4.20), we see that it is, in general, not possible to simultaneously minimize the two uncertainties. Given a fixed number N of pulling experiments, the minimization of the variance $\langle(\alpha^* - \alpha_0)^2\rangle$ of α^* is equivalent to a maximization of $\sigma^2(\ln(r))$. Under the constraint $v_\beta \in [v_{\min}, v_{\max}]$ for all pulling velocities v_β, this maximum is obviously reached if half of the rupture forces have been sampled at a pulling velocity as large as possible, i.e., $v_{\max}$, and the other half at a pulling velocity as small as possible, i.e., $v_{\min}$. This result is independent of the values of the true model parameters $\boldsymbol{\mu}_0$. Regarding the distribution of λ^*, the situation is more complicated. Given the analytic expression (4.20) for the error, the calculation is straightforward, but not shown here for the following two reasons. The "best" choice consists again in sampling just at the two extreme pulling velocities $v_{\min}$ and $v_{\max}$. The relative number of pulling experiments for each of the two pulling velocities is, however, non-trivial and depends on the values of the true model parameters $\boldsymbol{\mu}_0$. It is, therefore (in contrast to the result for α^*), only of limited use for a real experiment.

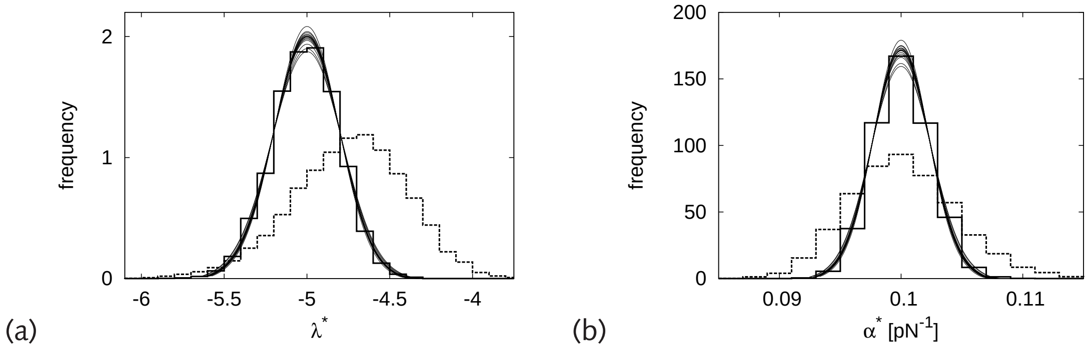

Figure 4.1: Solid histogram: Distributions of the (a) first and (b) second components of the maxima $\boldsymbol{\mu}^* = (\lambda^*, \alpha^*)$ of the likelihood (4.1) for 10000 "computer experiments". For each of them, $N = 400$ rupture forces f were sampled according to (4.17), 100 for each of the 4 loading rates $\kappa v = 50$, 200, 1000, 5000 pN/s and with "true" parameters $\lambda_0 = -5$ and $\alpha_0 = 0.1$ pN^{-1}. These are typical numbers in "real experiments" [Mer01]. For sake of better visibility the bin-width of the histograms is much larger than the optimal bin-width for a Gaussian distribution (appendix A.3). Thin lines: Likelihood (4.1) for the first 15 of the 10000 experiments after integrating over the other component, shifting the maximum to $\mu_{i,0}$, and normalizing (some are almost indistinguishable). Dotted histogram: Distribution of the estimates for λ and α according to the "standard method", as described in the main text.

4.2.2 Illustration for computer generated data

We now illustrate the findings from sections 4.1.2 and 4.1.3. To avoid uncontrollable experimental inaccuracies and uncertainties regarding the "true" model and the "true" model parameters $\boldsymbol{\mu}_0$, we numerically generated synthetic rupture data $\mathbf{f}$ by "simulating" an idealized experiment on the computer according to the probabilistic "law" (4.17) with given parameters $\boldsymbol{\mu} = \boldsymbol{\mu}_0$. Hence, all remaining uncertainties are statistical finite N effects. Figure 4.1 shows the results for 10000 repetitions of a computer experiment, each sampling $N = 400$ rupture forces $\mathbf{f}$ according to (4.17) with experimentally realistic parameter values $\alpha_0 = 0.1\,\text{pN}^{-1}$ and $\lambda_0 = -5$. Since two-dimensional distributions are difficult to compare graphically, we focus on the marginal distributions. For each of the 10000 experiments, the maximum $\boldsymbol{\mu}^* = (\lambda^*, \alpha^*)$ of the likelihood (4.1), considered as a function of $\boldsymbol{\mu}$, was determined numerically. The distribution of the resulting λ^*- and α^*-values are depicted as histograms in figure 4.1. The standard deviations of the maximum likelihood estimate for λ and α, determined from the 10000 experiments, are $s(\lambda^*) = 0.20$ and $s(\alpha^*) = 0.0023\,\text{pN}^{-1}$, respectively. These values coincide with those obtained from the analytical approximations (4.19-4.22), when rounded up to the above shown decimal places. Replacing the parameters $\boldsymbol{\mu}_0$ on the right-hand side of (4.19,4.20) by the maximum likelihood estimate $\boldsymbol{\mu}^*$ for one given data set thus provides reliable estimates for the statistical uncertainties.

Furthermore, for the first 15 of the 10000 experiments, after integrating over the other parameter in the likelihood (4.1), shifting the peak position from μ_i^* to $\mu_{i,0}$, and normalizing, the resulting marginal distributions were plotted in figure 4.1. They closely agree with the histograms. These observations illustrate very convincingly our two conclusions from section 4.1.2. In particular, finite-N corrections are apparently very small for the typical parameter values used in this example. Also the practically perfect Gaussianity of the distributions is as expected, cf. (4.9).

Let us finally compare the performance of the maximum likelihood estimate with that of the most widely used "recipe" of parameter estimation in the field of single-molecule pulling experiments. This consist of the following steps: (i) Fit a Gaussian to the observed rupture force distribution for a fixed pulling velocity v and approximate the most probable rupture force f^* by the maximum of that Gaussian. (ii) Plot f^* for different v versus $\ln(v)$ and fit the resulting points by a straight line. (iii) Assume that the model (4.17) is applicable and employ equation (3.16) to deduce its model parameters $\boldsymbol{\mu} = (\lambda, \alpha)$ from the slope and the axis intercept of the straight line as detailed, e.g., in [ER97, MNL$^+$99, SOS$^+$00, Mer01, ER03]. We have applied this procedure to each of the 10000 experiments in figure 4.1 and plotted the distribution of the resulting estimates for λ and α in figure 4.1. The systematic bias of the estimate for λ can be traced back to fitting a Gaussian, which is symmetric about its maximum, to the asymmetric "true" distribution (4.17) [ER03], while the suboptimal variance of the estimate for both λ and α signals that quite some information is lost by only considering the most probable rupture forces f^*. Hence, the maximum likelihood estimate represents a substantial improvement compared to the so far "standard method" of data evaluation in this field. This is in agreement with our conclusion from section

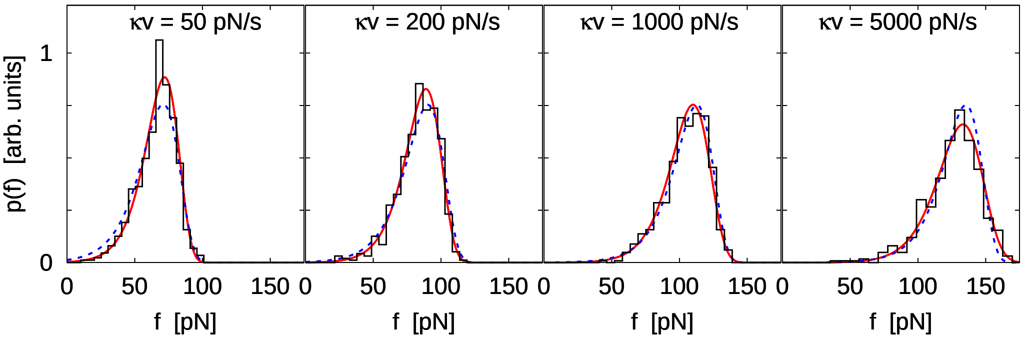

Figure 4.2: Rupture force distributions for different loading rates κv. Histograms: numerically generated rupture forces according to (3.17-3.19) with $\gamma = 2/3$, $\lambda_0 = -5$, $\alpha_0 = 0.1$ pN^{-1}, $\epsilon_0 = 15$. For each κv, we sampled 500 forces, i.e., $N = 2000$. The bin-width is chosen according to equation (A.15). The maximum likelihood fits $p_1(f|\boldsymbol{\mu}^*, v)$ according to (3.17-3.19) for $\gamma = 1/2$ and $\gamma = 2/3$ (red solid) are not distinguishable within the line width in this plot. For $\gamma = 1/2$, the fit parameters have the following values: $\lambda^* = -5.37$, $\alpha^* = 0.110$ pN^{-1} , and $\epsilon^* = 17.2$. For $\gamma = 2/3$, the fit results are slightly closer to the true parameter values, namely, $\lambda^* = -5.20$, $\alpha^* = 0.104$ pN^{-1}, and $\epsilon^* = 14.64$. Blue dashed distribution: same for Bell's Ansatz $\gamma = 1$, with fit results $\lambda^* = -3.81$ and $\alpha^* = 0.072$ pN^{-1}. Upon repeating the entire "numerical experiment", the resulting plots always look practically the same.

4.1.3. We have also directly compared the maximum likelihood estimate with other known "recipes" of evaluating single-molecule rupture data, e.g., [ER03]. In all cases we found that the maximum likelihood method was superior.

4.3 Extension of Bell's model

Our second example is the extension of Bell's model discussed in section 3.3.3. In this model the barrier height was not assumed to decrease linearly according to equation (3.12), but rather as

$$E_\mathrm{b}(f) = E_\mathrm{b}(0)(1 - f/f_c)^{1/\gamma} = E_\mathrm{b}(0)(1 - \gamma\alpha f/\epsilon)^{1/\gamma} \ . \tag{4.23}$$

Assuming a similar scaling for the prefactor in (3.4), the rate could be written in the form (3.17), and an analytical expression for the probability density of rupture events p_1 could be derived. For a known value of γ, this model involves the three unknown parameters $\boldsymbol{\mu} = (\lambda, \alpha, \epsilon)$.

This suggests that, for escape processes over a single activation barrier, single-molecule force spectroscopy should, in principle, provide the possibility not only to

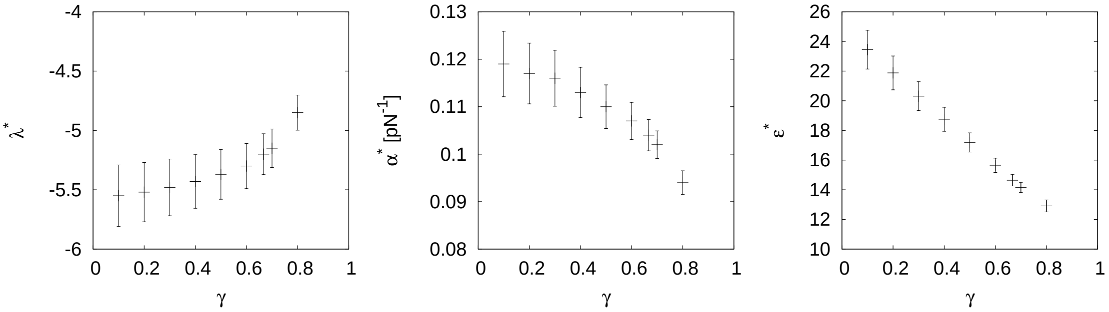

Figure 4.3: Maximum likelihood fit values for the data set from figure 4.2 fitted with the rupture force distribution (3.17-3.19). Each data point was obtained by fitting the same data set, but assuming a different value of the parameter γ.

determine the force-free dissociation rate $k_0 = \exp(\lambda)$ and the dissociation length x_b (as in Bell's model), but also the height $E_\mathrm{b}(0) = \epsilon k_\mathrm{B} T$ of the barrier. Naturally, the question arises how accurate these estimates will be, and whether the inferred values critically depend on the chosen theoretical model, in particular on the value of the parameter γ. These questions will be addressed next.

There is an ongoing debate in literature about which of the three exponents, i.e., $\gamma = 1$, $\gamma = 2/3$, or $\gamma = 1/2$, is most appropriate to use when evaluating experimental rupture data [DFKU03, HS03, SO03, ML06, DHS06, HK06]. Taking for granted that one of the three models approximates the "truth" satisfactorily, choosing $\boldsymbol{\mu} = \boldsymbol{\mu}^*$ is – according to our above conclusions – the closest one can get to the "full truth" on the basis of one given data set $\mathbf{f}$. In case of disagreement about the "true" γ-value, a fully objective selection criterion seems unavailable in principle. In practice, the usual criterion is the comparison with the basic "true" quantity observed experimentally, namely the distribution of rupture forces.

For the example shown in figure 4.2, we sampled $N = 2000$ rupture forces $\mathbf{f}$ according to the distribution (3.17-3.19). In the simulations, we have taken $\gamma = 2/3$ and realistic parameter values $\lambda_0 = -5$, $\alpha_0 = 0.1$ pN^{-1}, $\epsilon_0 = 15$.

In order to test the maximum likelihood method, for the resulting data set we determined the estimate $\boldsymbol{\mu}^*$ for several possible γ-values. Since in a real experiment, the value of the exponent γ is not known a priori, also during the fitting, the γ-values used were not necessarily coincident with the "true" value used for data generation. The bin-width of the histograms in figure 4.2 was chosen as $h_\beta = 2.83 s_{N_\beta} N_\beta^{-1/3}$, where s_{N_β} is the standard deviation of the rupture forces measured at pulling velocity v_β. As discussed in appendix A.3, this is the optimal choice of the bin-width for Bell's model; although this model is in fact not the true one in our numerical experiment, this choice of the bin-width remains suitable, as every distribution can separately be very well fitted with equation (3.15).

Comparing in figure 4.2 the resulting distributions $p_1(f|\boldsymbol{\mu}^*, v)$ for three different γ

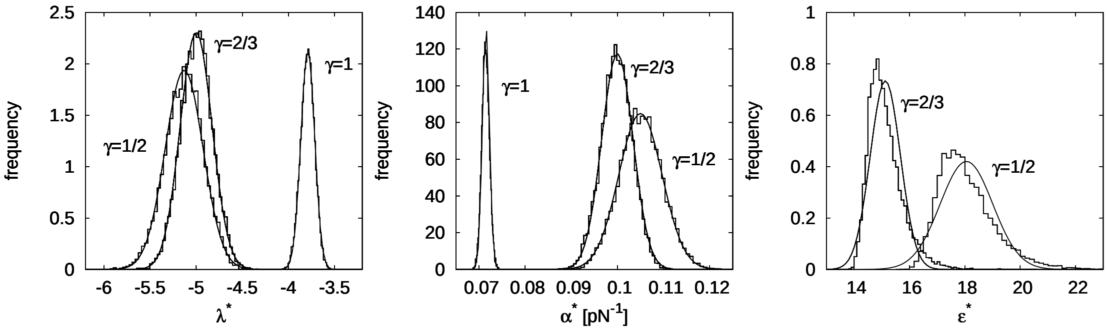

Figure 4.4: Histograms: Numerically determined distribution of the single components of the maxima $\boldsymbol{\mu}^* = (\lambda^*, \alpha^*, \epsilon^*)$ of the likelihood (4.1,3.17-3.19) with $\gamma = 1/2$, $\gamma = 2/3$, and $\gamma = 1$ for 10000 "computer experiments". For all data sets the rupture forces were generated numerically according to (3.17-3.19) with $\gamma = 2/3$, $\lambda_0 = -5$, $\alpha_0 = 0.1$ pN^{-1}, $\epsilon_0 = 15$. For each κv, we sampled 500 forces, i.e., $N = 2000$. The bin-width of the histograms is $h_\beta = 3.49 s_{N_\beta} N_\beta^{-1/3}$ (see appendix A.3). Solid lines: Gaussian approximations to the distributions with covariance matrices (4.13). They have been shifted so that their maximum coincides with the mean of the empirically determined distributions. For sake of better visibility the distributions for $\gamma = 1$ have been rescaled by an appropriate value.

values, we observe the following. Already the two-parametric Bell's Ansatz ($\gamma = 1$) reproduces the experimental distribution of rupture forces with reasonable accuracy, see the dotted line in figure 4.2. However, if one increases the number of fit parameters to three, one obtains the fit distributions notably different from the Bell's curves, see the solid lines corresponding to $\gamma = 1/2$ and $\gamma = 2/3$. We also note that the difference between the curves corresponding to these two values of γ is smaller than the line thickness. This means that if one treats the exponent γ as a fourth fit parameter, then its precise value cannot be determined by fitting the experimental rupture force distribution. With respect to the three remaining fit parameters, their values are rather close to each other for the fits with $\gamma = 1/2$ and $\gamma = 2/3$, with the largest discrepancy between the fit values of the force-free barrier height (see the caption in figure 4.2).

When fitting the real experimental data, one does not know a priori the true value of the exponent γ. It is therefore of interest to find out, how the remaining fit parameter values depend on the assumption with respect to this quantity. Figure 4.3 shows the fit results obtained for different assumed values of γ within the physically meaningful range. All of the fitting curves obtained for the different γ-values from figure 4.3 coincided within the line thickness. We observe that the resulting fit values of the force-free escape rate e^{λ} and the dissociation length $k_{\mathrm{B}}T\alpha$ are not very sensitive to the choice of the exponent γ. At the same time, the force-free barrier height value inferred from the fit depends approximately linearly on the choice of this parameter, and can assume values differing by as much as a factor of 2 at extreme γ-values. This means that when fitting the experimental data, the value of the force-free barrier height will be determined with the least accuracy.

In view of these observations, an interesting question arises: are the approximations (4.13) and (4.19-4.22) for the statistical uncertainties of the model parameters still valid for those models, about which we (in our case) *know* that they are not true? To study this point, we have repeated the above described procedure for 10000 data sets, each generated in the same way and with same "true" parameters as the data set shown in figure 4.2. The distributions of the inferred parameters $\boldsymbol{\mu}^*$ for the three different γ-values are depicted in Fig. 4.4 as histograms. Following section 4.1.2, they should be bell-shaped with variance given by equation (4.13). We have evaluated this expression at the mean values of the inferred parameters $\boldsymbol{\mu}^*$ for each of the three γ-values, respectively. For $\gamma = 2/3$ and $\gamma = 1/2$ this had to be done numerically, whereas for $\gamma = 1$, equations (4.19-4.22) could be employed. The resulting distributions, centered about the mean value of the inferred parameters, are shown in figure 4.4 as solid lines. For λ and α they closely agree to the histograms. With respect to the parameter ϵ, the approximated variance agrees very well with the empirically determined, but finite-N corrections to the full distributions, which are not symmetric about their centers, are apparent.

In conclusion, although the models for $\gamma = 1$ and $\gamma = 1/2$ are not the true models, equation (4.13) still yields very good approximations for the statistical uncertainties of the parameters, i.e., for their distribution upon repeating the same experiment many times. Nevertheless, comparing these distributions to the distribution of the parameters for the "true" gamma-value $\gamma = 2/3$, we see, that by choosing the wrong model, the systematic deviations to the parameters are much larger than the statistical uncertainties. As one will, in general, be unsure about the true underlying energy landscape, and thus about the "true" γ-value, this point is essential if one wishes to use the inferred parameter values in another context than the interpretation of single-molecule pulling experiments.

We would like to mention that the deviations between the distributions resulting from the different γ values increase with the pulling velocity [DHS06]. Hence, by increasing the range of accessible pulling velocities $[v_{\min}, v_{\max}]$, a clearer distinction between the models is possible. However, for precise measurements with the AFM the loading rate κv is limited to a few orders of magnitude, comparable with our values.

4.4 Discussion

In this chapter (and in our works [GR07, GER09]) we have shown that the maximum likelihood approach is an extremely simple, general, and powerful method for parameter estimation in the context of single-molecule force spectroscopy. For large data sets it outperforms all other estimates. Furthermore, approximations to the statistical uncertainties of the parameters are available once the parameters are estimated. In the case of the standard Bell model we were able to derive an analytical expression for these uncertainties in terms of the model parameters and the distribution of the applied loading rates. For more general models, the uncertainties can be determined numerically.

When fitting the experimental data, one usually assumes some functional form of the force-dependent escape rate involving several fit parameters. By means of a numerical example, we have demonstrated for potentials with a single activation barrier that the largest number of such parameters that can be determined from the experiment is three. These parameters are related to the force-free value of the rate, the dissociation length, and the barrier height in the absence of the force. Furthermore, when fitting the experimental rupture force distributions, one needs to make an additional assumption about the manner in which the escape rate decreases with the applied force. While the fit values of the force-free escape rate and the dissociation length depend only weakly on this assumption, the value of the force-free barrier height can be determined much less reliably. We have shown that, even if the model adopted for the description of the experiment is not the true one, but predicts distributions of rupture forces similar to the measured distribution, the statistical uncertainties found from the maximum likelihood method very well approximate the dispersion of the estimated parameters upon repeating the same experiment many times. Often these uncertainties are much smaller than the systematic error resulting from choosing the "wrong" model.

5 Incompatibilities between experiment and theory – theoretical assumptions under critical inspection

Having introduced the basic stochastic modeling concepts in the field of single-molecule force spectroscopy (chapter 3) and a general method for parameter estimation (chapter 4), we will now turn to real experimental data.

In the previous chapter we have demonstrated that, given a dissociation kinetics in the form of a one-step rate equation (3.6), a number of different models for the force-dependence of the dissociation rate $k(f)$ can explain the "experimental" findings equally well, even under idealized conditions (no experimental error, force distance curve linear with fixed and known κ, etc.). For real single-molecule pulling experiments, it turns out that the rupture force data can, in most cases, *not* be explained by a one-step rate description (3.6), e.g., [SSHM99, MSL+05, NAPG06]. This incompatibility between experimental findings and theoretical assumptions was rigorously demonstrated in [RER+04, IP04]. It is particularly astonishing in view of the fact that, for a number of closely related systems, like the unfolding of polymers [CVLL+03], opening of DNA hairpins [HZV+07], nanopore unzipping of DNA hairpins [MVV+04], and disruption of a DNA-protein complex by unzipping DNA [KW03], which are theoretically described by the very same formalism, the experimental data is in good agreement with the theory.

In [REB+06], Raible et al. introduced a model based on the heterogeneity of chemical bonds. In this model the heterogeneity was introduced in form of an ad hoc Ansatz, by postulating a randomization of one of the model parameters. This resulted in an excellent agreement between experiment and theory for all studied data sets. However, the exact physical origin of this heterogeneity remained unclear.

After briefly reviewing the heterogeneous bond model, we will critically reconsider the theoretical assumptions on which the modeling in section 3.3 was based. Then we will discuss some physical mechanisms which can naturally result in a randomization of one or more model parameters, as well as alternatives to this proposed randomization.

5.1 Revealing incompatibilities between experiment and theory

Let us for an example consider the dissociation of the PhoB peptide from the DNA target sequence studied by Eckel et al. [EWB+05]. The distributions of rupture forces measured at five different pulling velocities are shown in figure 5.1 (b)-(f). We will now check whether any of the models discussed in the previous chapters is applicable to these data.

A minor theoretical challenge constitutes the fact that one cannot reliably determine arbitrarily small rupture forces in the experiment. These cannot be distinguished from the noise in the force distance curves. For an evaluation of the experiment one therefore only uses those rupture forces larger than a threshold force $f_{\min}$. This threshold should be larger than the thermal fluctuations so that one can assume that all rupture forces above this value can be determined. Typically for AFM measurements, $f_{\min}$ has a value of a few ten pN. For the example shown in figure 5.1, $f_{\min} = 20$pN was chosen. In order to compare the experimentally measured rupture force distribution to the theoretical distribution, one has to normalize the theoretical density according to

$$p_1(f|\boldsymbol{\mu}, v, f_{\min}) := p_1(f|\boldsymbol{\mu}, v)/n(f_{\min}|\boldsymbol{\mu}, v) \ , \tag{5.1}$$

where $p_1(f|\boldsymbol{\mu}, v, f_{\min})$ denotes the rupture force density for a given value of $f_{\min}$ and $p_1(f|\boldsymbol{\mu}, v)$ that for $f_{\min} = 0$. The same notation is used for the survival probability $n(f|\dots)$.

Figure 5.1 (a) shows the most probable rupture force f^* (the maximum of the rupture force distribution determined from a Gaussian fit, see section 4.2.2) in dependence of the loading rate κv. It is obvious that f^* increases approximately linearly with $\ln(\kappa v)$. As this relationship is also predicted by Bell's model (3.16), this observation is often seen as a hint that Bell's model is in fact applicable to the evaluation of single-molecule pulling experiments [MNL+99, Eva01, NDKM03, BKB+05, EWB+05]. Fitting on the semi-logarithmic scale a straight line to the data, assuming an (average) total net elasticity $\kappa = 3$pN/nm of the complex composed of cantilever, linker molecules, peptide, and DNA sequence [c.f. section 3.2.3)], and applying equation (3.16) yields the model parameters $\lambda = -3.93$ and $\alpha = 0.133$ pN^{-1}.[1]

Comparing in figure 5.1 the resulting distributions (3.15,5.1) to the experimentally determined ones reveals a great discrepancy. Except the positions of the maxima (which have been used for fitting the data) both distributions are completely different. The fitted distributions according to Bell's model are, in particular, much too small and have the wrong skewness. Furthermore, other methods for parameter estimation (like the maximum likelihood method from the previous chapter) yield completely different parameter values and distributions which are quite different from those obtained from the f^* vs. $\ln(\kappa v)$ plot and which are also in complete disagreement with the experimentally measured distributions (data not shown). In the same way, the extension of Bell's model (3.10,3.17) yields similarly unsatisfying results [cf. blue solid lines in figure 5.1 (b)-(f)]. In summary, none of the previously discussed models can explain the experimental findings from [EWB+05]. For other experiments similar conclusions

---

[1] The value $\kappa = 3$pN/nm is taken from [REB+06]. It is a typical value for single-molecule pulling experiments measured by AFM. However, if one just wants to check whether any model based on the one-step rate description (3.6) with $f(t) = \kappa t$ is applicable, the precise value of κ is irrelevant. The net elasticity enters the distribution of rupture forces only in the combination e^{λ}/κ.

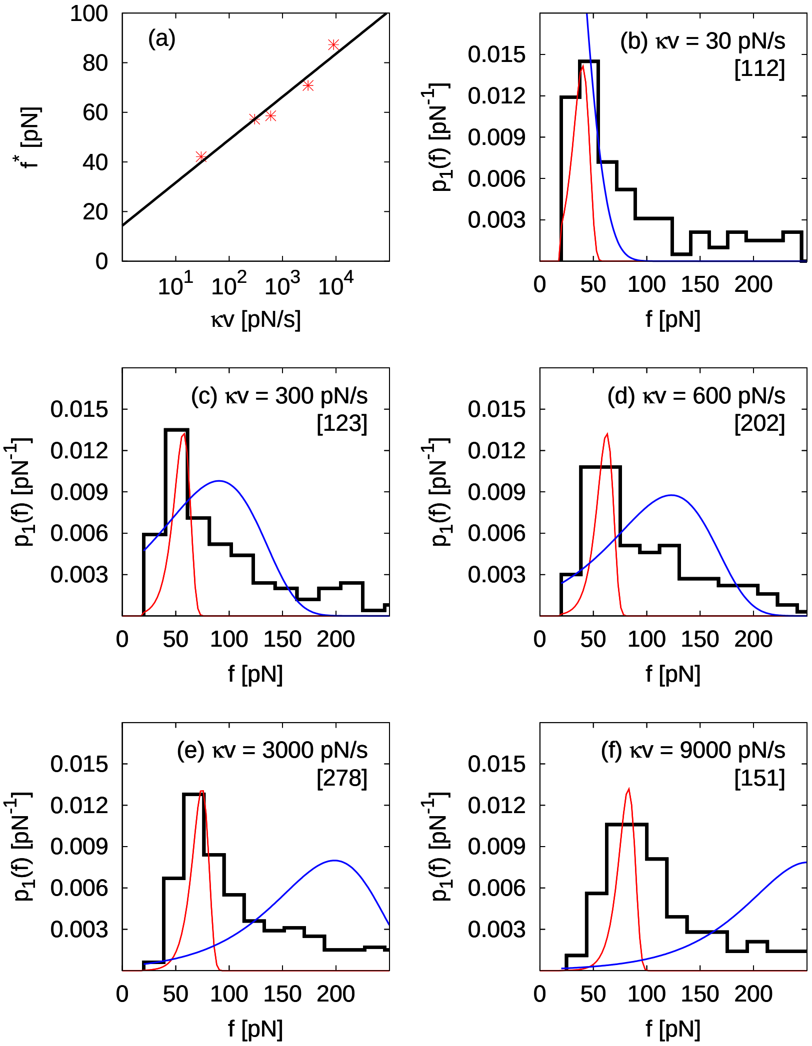

Figure 5.1: Dissociation of the PhoB peptide from the DNA target sequence measured by Eckel et al. [EWB+05]. (a) The experimentally determined most probable rupture force f^* as a function of the loading rate κv is depicted by the points. The solid line corresponds to the least squares fit according to equation (3.16) with fit parameters $\lambda = -3.93$ and $\alpha = 0.133$ pN^{-1}. (b)-(f) show the distributions of rupture forces measured at five different pulling velocities. The number of rupture forces at each pulling velocity is indicated in brackets. The experimental data is shown by the black histograms, the Bell's model (3.15) with parameters obtained from the force spectrum (a) and for sake of better visibility rescaled by an appropriate value by the red lines. The maximum likelihood fits $p_1(f|\boldsymbol{\mu}^*, v)$ of the extension of Bell's model (3.17-3.19) with exponent $\gamma = 2/3$ are shown by the blue lines. The fit parameters have the following values: $\lambda^* = -1.18$, $\alpha^* = 0.0215$ pN^{-1}, and $\epsilon^* = 134.19$. A force threshold of $f_{\min} = 20$pN and a net elasticity $\kappa = 3$pN/nm were used.

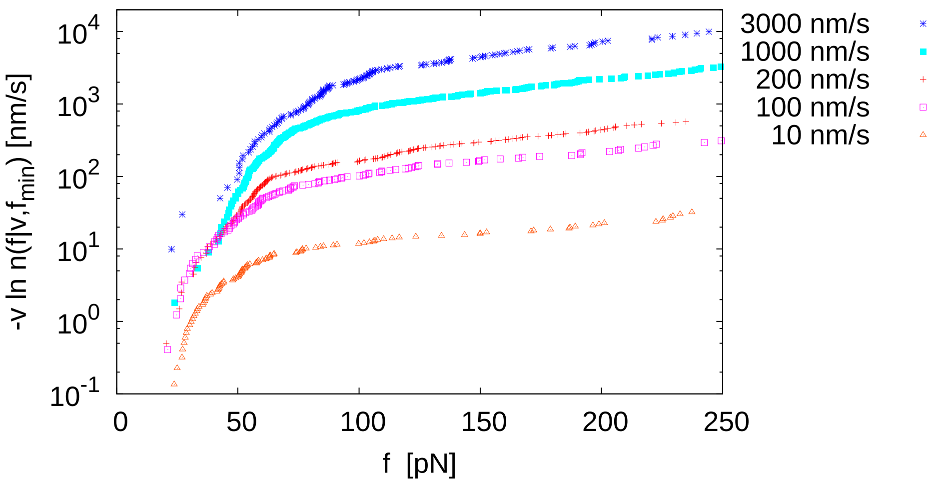

Figure 5.2: Experimentally reconstructed functions $-v\ln(n(f|v)$ for the same data as in figure 5.1. A few large forces are omitted for sake of better visibility.

were drawn [SSHM99, MSL+05, NAPG06].

Following [RER+04, IP04] one can rigorously demonstrate that the experimental rupture force data are in fact incompatible to the basic assumptions from section 3.3.1, namely:

- *Assumption 1*: The reaction kinetics is given by the first-order differential equation:
$$\dot{n}(t) = -k(f(t))n(t) \; . \tag{5.2}$$
- *Assumption 2*: There exists a common, monotonically increasing force-extension curve $F(s)$ such that
$$f(t) = F(s(t)) \tag{5.3}$$
for all the pulling experiments under consideration, independently of any further details (pulling speed, linker properties, etc.) of the single repetitions of the experiment.

Using that $s(t) = vt$ can be experimentally controlled with great accuracy and combining equations (5.1-5.3), we obtain in analogy to equations (3.10,3.11)

$$n(f|v, f_{\text{min}}) = \exp\left(-\frac{1}{v}g(f|f_{\text{min}})\right) \; , \tag{5.4}$$

$$g(f|f_{\text{min}}) := \int_{f_{min}}^{f} df' \frac{k(f')}{F'(F^{-1}(f'))} \; . \tag{5.5}$$

Hence, given that the above two assumptions are valid, $g(f|f_{\text{min}}) = -v\ln(n(f|v, f_{\text{min}}))$ should not depend on the pulling velocity. This observation is independent of the exact force-dependence of the rate $k(f)$ and independent of the exact form of the force-extension curve $F(s)$.

Given N_v experimentally measured rupture forces f_i, $i = 1, ..., N_v$, measured at a pulling velocity v, the survival probability of the bond can be approximated by $\tilde{n}(f|v, f_{\min}) = N_v^{-1} \sum_{i=1}^{N_v} \Theta(f_i - f)$ with the Heaviside step function $\Theta(\cdot)$. For the same data as in figure 5.1, these functions are shown in 5.2. The functions corresponding to the different pulling velocities clearly do not collapse on a single curve. One can therefore conclude that at least one of the above two assumptions (5.2,5.3) does not apply to the experiment [EWB$^+$05]. The same discrepancy was found by us and Raible for a number of other experimental data sets [BBA$^+$03, NDKM03, BBA$^+$05, BMF$^+$07, FSA$^+$09].

5.2 Heterogeneous bond model

A possible explanation for this discrepancy is given in [REB$^+$06] in the form of a heterogeneous bond model. The basic idea of this model is that the two assumptions (5.2,5.3) are in fact valid for each single repetition of the experiment. But in each repetition one actually deals with a slightly different system composed of ligand, receptor, linker molecules, cantilever, and thermal environment, leading to a different force-dependence of the escape rate $k(f)$. Possible physical reasons leading to such a heterogeneity are: there might exist different conformations of the ligand-receptor complex [SSHM99, NSK$^+$03, TNELG04]; variations of the local environment of the complex, e.g., in the form of fluctuations of the pH-value, electric fields and ionic strength [VL01]; multiple binding sites of the receptor for the ligand [SSHM99]; and geometrical variations of the microscopic configuration upon repeating the experiment, as illustrated and discussed in figure 5.3, and observed in experiments and computer simulations for the unfolding of proteins [BPZ$^+$03, DBBR06, BPHD08]. Furthermore, in a small fraction of experiments one might be pulling apart multiple parallel bonds [EPNS08, GRK$^+$08] or unspecific bonds [RRL$^+$06]. A cooperative rupture of multiple bonds or that of an unspecific bond cannot (or only hardly) be distinguished from the rupture of a single specific bond in the force distance curves (cf. section 5.4).[2]

In order to formalize this, one assumes that there exists a parametric form of the force-dependent escape rate $k(f) = k(f|\boldsymbol{\theta})$ with parameters $\boldsymbol{\theta}$. Now the variations of the force-dependence of the escape rate are modeled such that the functional form of the escape rate is the same for each repetition of the experiment, but the parameters $\boldsymbol{\theta}$ assume different values. That means, they are drawn from some distribution $\rho(\boldsymbol{\theta}|\boldsymbol{\mu})$ depending on the ultimate model parameters $\boldsymbol{\mu}$. Under these assumptions the survival

---

[2] The fraction of unspecific rupture events can be estimated by performing "control experiments" in which the specific binding site is blocked.

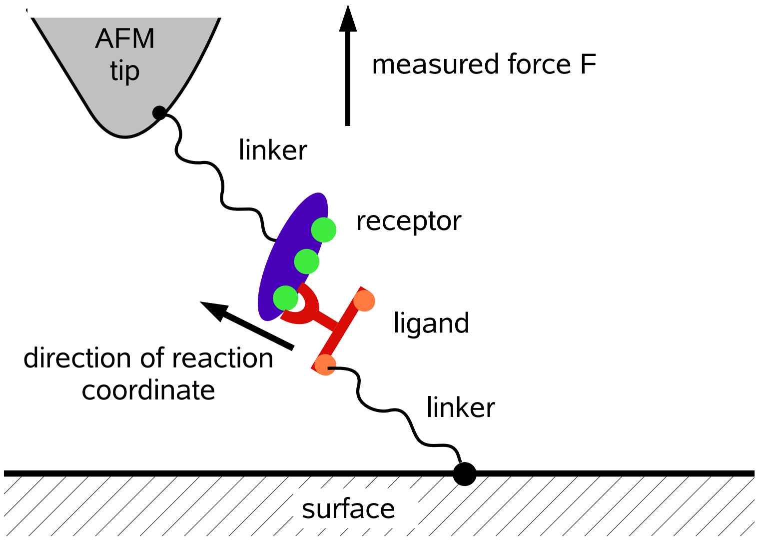

Figure 5.3: Schematic illustration of some random geometrical variations in single-molecule pulling experiments. The green and orange dots indicate possible binding sites between ligand and receptor, and between ligand and linker, respectively. The binding sites between receptor and ligand are omitted for sake of better visibility. The black dots indicate the points where the linkers are connected to the tip and to the surface. Depending on the choice of the green and orange binding sites and on the positions of the immobilization points, which cannot be controlled experimentally, the force acting along the relevant reaction coordinate can significantly differ from the measured normal component of the force F. Furthermore, the escape rate $k(f)$, itself, can depend on the direction of the applied force [BPZ$^+$03, DBBR06, BPHD08], and the lateral component of the force can influence the deflection of the laser beam from the cantilever, see figure 3.1, and hence the "measured" force in a complicated manner [KEG06].

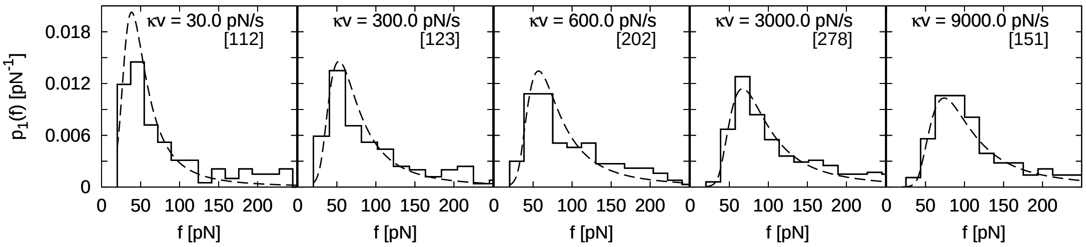

Figure 5.4: Solid histograms: Same as figure 5.1(b)-(f). Dashed lines: Maximum likelihood fits $\hat{p}_1(f|\boldsymbol{\mu}^*, v, f_{\min})$ according to equations (5.6,5.7,3.14). The fit parameters have the following values: $\lambda^* = -4.905$, $\alpha_m^* = 0.103$pN^{-1}, and $\sigma^* = 0.0663$pN^{-1}.

probability of the bond is given by

$$\hat{n}(f|\boldsymbol{\mu}, v, f_{\min}) = \frac{\int d\boldsymbol{\theta}\; n(f|\boldsymbol{\theta}, v)\rho(\boldsymbol{\theta}|\boldsymbol{\mu})}{\int d\boldsymbol{\theta}\; n(f_{min}|\boldsymbol{\theta}, v)\; \rho(\boldsymbol{\theta}|\boldsymbol{\mu})}\;, \tag{5.6}$$

where $n(f|\boldsymbol{\theta}, v)$ is the survival probability according to equations (5.2-5.5). The hat in equation (5.6) refers to the fact that $\hat{n}(f|\boldsymbol{\mu}, v, f_{\min})$ corresponds to a different model than $n(f|\boldsymbol{\theta}, v)$. Finally, the rupture force density $\hat{p}_1(f|\boldsymbol{\mu}, v, f_{\min}) = -d/df\; \hat{n}(f|\boldsymbol{\mu}, v, f_{\min})$ follows directly from equation (5.6).

It should be noted that the basic models discussed in section 3.3 are special cases of the heterogeneous bond model corresponding to a delta distribution $\rho(\boldsymbol{\theta}|\boldsymbol{\mu}) = \delta(\boldsymbol{\theta} - \boldsymbol{\mu})$.

Now the remaining task is to find an appropriate model for the force-dependent escape rate $k(f) = k(f|\boldsymbol{\theta})$ and for the force-extension curve $F(s)$. Here we follow [REB$^+$06] and make the same choices as in section 3.3.3 for Bell's model. Hence, the survival probability $n(f|\boldsymbol{\theta}, v)$ of the basic model is again given by equation (3.14) and the corresponding model parameters are $\boldsymbol{\theta} = (\tilde{\lambda}, \tilde{\alpha})$. Furthermore, as done in [REB$^+$06], we assume for the present that $\tilde{\alpha}$ is Gaussian distributed with mean α_m and variance σ^2, while $\tilde{\lambda} = \lambda$ is fixed. This assumption can (in part) be justified by the role of the random geometrical variations (figure 5.3) as the angle between the applied force and the direction of the relevant reaction coordinate has been implicitly included in the parameter $\tilde{\alpha}$, cf. discussion below equation (3.3) and section 5.6. Hence, the distribution of the parameters is

$$\rho(\boldsymbol{\theta}|\boldsymbol{\mu}) \propto \exp\left(-\frac{1}{2}\frac{(\tilde{\alpha} - \alpha_m)^2}{\sigma^2}\right)\Theta(\tilde{\alpha})\delta(\lambda - \tilde{\lambda})\;, \tag{5.7}$$

with model parameters $\boldsymbol{\mu} = (\lambda, \alpha_m, \sigma)$.

Let us again consider the data from [EWB$^+$05]. The maximum likelihood estimates of the parameters of the model specified by (5.6,5.7,3.14) are $\lambda^* = -4.905$, $\alpha_m^* =$

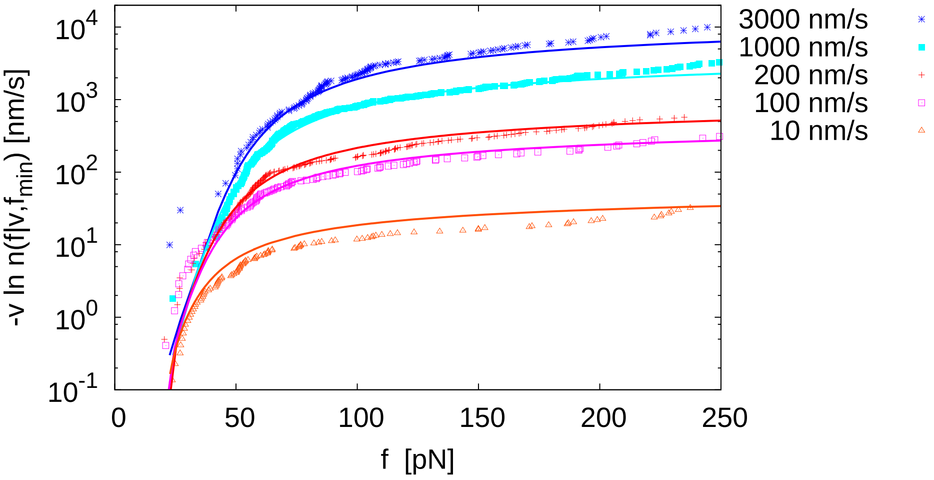

Figure 5.5: Same as figure 5.2. The solid lines correspond to the theoretical distribution (5.6) supplemented with equations (3.14,5.7) and with fit parameters $\boldsymbol{\mu}^*$ as in figure 5.4.

0.103pN^{-1}, and $\sigma^* = 0.0663$pN^{-1}. In figure 5.4 the resulting distributions of rupture forces $\hat{p}_1(f|\boldsymbol{\mu}^*, v, f_{\min})$ are compared to the experimentally determined histograms for the different pulling velocities. The corresponding f vs. $-v \ln \hat{n}(f|\boldsymbol{\mu}^*, v, f_{\min})$ plots are shown in figure 5.5. Within the statistical uncertainties, the agreement between the experimental and theoretical distributions is quite good, especially when compared to figure 5.1(b)-(f). Considering the statistical uncertainties of the estimated model parameters, we can proceed as detailed in section 4.1 and apply equation (4.16). Here, the Hessian matrix has to be evaluated numerically at the most probable parameters $\boldsymbol{\mu}^*$. The resulting uncertainties are: $s(\lambda^*) = 0.516$, $s(\alpha_m^*) = 0.008$pN^{-1}, and $s(\sigma^*) = 0.005$pN^{-1}. By applying parametric bootstrap methods [ET93] in analogy to our numerical experiments in sections 4.2 and 4.3, we have verified for different examples that these estimates and the corresponding confidence intervals are again very good and that finite N corrections are rather small.

The agreement between the theoretical and experimental distributions of rupture forces is similarly good for the other data sets [BBA$^+$03, NDKM03, BBA$^+$05, BMF$^+$07, FSA$^+$09] studied by Raible and us. A somewhat similar model has been proposed independently in [LOYI06] to explain the occurrence of so-called “catch bonds” under the application of a constant force [ZLM05, PPF$^+$05].

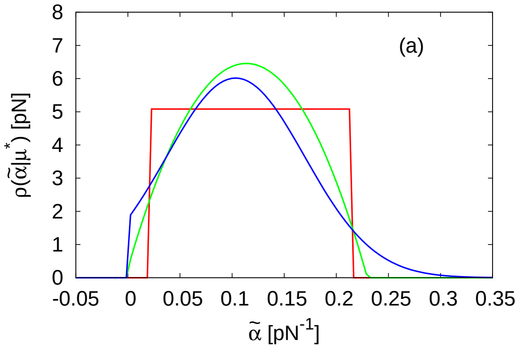

Figure 5.6: Fitted distributions $\rho(\tilde{\alpha}|\boldsymbol{\mu}^*)$ for the same data as in figure 5.4. They are obtained from $\rho(\boldsymbol{\theta}|\boldsymbol{\mu}^*)$ by integrating over the remaining parameter $\tilde{\lambda}$. The parameters of the distribution as well as the estimated value for λ can be taken from the main text. (a) blue: Gaussian distribution (5.7), green: parabolic distribution (5.8), and red: uniform distribution (5.9). (b) red: linear distribution (5.10), blue: Gamma distribution (5.11), and green: Beta distribution (5.12).

5.3 Influence of the parametric Ansatz for the rate distribution

Next, we want to check the influence of the parametric Ansatz for the distribution of the model parameters $\rho(\tilde{\alpha}|\boldsymbol{\mu})$. In section 5.3.1 we will assume, as in equation (5.7), that only the parameter $\tilde{\alpha}$ is subjected to random variations while $\tilde{\lambda} = \lambda$ is the same for all repetitions of the experiment. We will investigate how strong the quality of the fitted distributions, as well as the value of λ, depend on this Ansatz. In section 5.3.2 the opposite situation, i.e., only $\tilde{\lambda}$ is subjected to random variations while $\tilde{\alpha} = \alpha$ is fixed, will be considered. Throughout this section we will restrict our discussion to the data from [EWB+05]. However, similar conclusions can be drawn for other data sets.

5.3.1 Other distributions of α

Let us first study two other distributions which are – as the Gaussian distribution (5.7) – symmetric about some value:[3]

- *Parabolic distribution*

$$\rho(\boldsymbol{\theta}|\boldsymbol{\mu}) \propto (\tilde{\alpha}-\alpha_{\min})(\alpha_{\max}-\tilde{\alpha})\Theta(\tilde{\alpha}-\alpha_{\min})\Theta(\alpha_{\max}-\tilde{\alpha})\Theta(\tilde{\alpha})\delta(\lambda-\tilde{\lambda}) \ , \qquad (5.8)$$

---

[3] Except the cutoff at $\tilde{\alpha} = 0$.

with model parameters $\boldsymbol{\mu} = (\lambda, \alpha_{\mathrm{min}}, \alpha_{\mathrm{max}})$. Employing the maximum likelihood method to determine the most probable parameters as well as the concomitant statistical uncertainties yields: $\lambda^* = -4.853 \pm 0.439$, $\alpha^*_{\mathrm{min}} = -2.569 \cdot 10^{-3} \pm 5.036 \cdot 10^{-3}$ pN^{-1}, and $\alpha^*_{\mathrm{max}} = 2.298 \cdot 10^{-1} \pm 0.128 \cdot 10^{-1}$ pN^{-1}.

- *Uniform distribution*

$$\rho(\boldsymbol{\theta}|\boldsymbol{\mu}) \propto \Theta(\tilde{\alpha} - \alpha_{\mathrm{min}})\Theta(\alpha_{\mathrm{max}} - \tilde{\alpha})\Theta(\tilde{\alpha})\delta(\lambda - \tilde{\lambda}) \ , \tag{5.9}$$

with most probable parameters $\lambda^* = -5.219 \pm 0.428$, $\alpha^*_{\mathrm{min}} = 1.932 \cdot 10^{-2} \pm 0.193 \cdot 10^{-2}$ pN^{-1}, and $\alpha^*_{\mathrm{max}} = 2.160 \cdot 10^{-1} \pm 0.119 \cdot 10^{-1}$ pN^{-1}.

The marginal distributions $\rho(\tilde{\alpha}|\boldsymbol{\mu}^*)$, obtained from $\rho(\boldsymbol{\theta}|\boldsymbol{\mu}^*)$ by integrating over the remaining parameter $\tilde{\lambda}$, are shown in figure 5.6 (a) together with the corresponding Gaussian distribution (5.7). The mean values, the dispersions about these values, as well as the inferred values for λ are very similar for all three distributions. This observation is in full agreement with [REB$^+$06] where the same parametric forms have been applied to the data from [BBA$^+$03].

However, the three distributions (5.7-5.9) employed so far have in common that they are, in absence of the cutoff at $\tilde{\alpha} = 0$, symmetric about their mean values. We now consider other distributions which do not possess such a symmetry:

- *Linear distribution*

$$\rho(\boldsymbol{\theta}|\boldsymbol{\mu}) \propto (\tilde{\alpha} - \alpha_{\mathrm{min}})\Theta(\tilde{\alpha} - \alpha_{\mathrm{min}})\Theta(\alpha_{\mathrm{max}} - \tilde{\alpha})\Theta(\tilde{\alpha})\delta(\lambda - \tilde{\lambda}) \ , \tag{5.10}$$

with $\lambda^* = -3.524 \pm 0.339$, $\alpha^*_{\mathrm{min}} = -2.305 \cdot 10^{-1} \pm 1.111 \cdot 10^{-1}$ pN^{-1}, and $\alpha^*_{\mathrm{max}} = 1.672 \cdot 10^{-1} \pm 0.078 \cdot 10^{-1}$ pN^{-1}.

- *Gamma distribution*

$$\rho(\boldsymbol{\theta}|\boldsymbol{\mu}) \propto \left(\frac{\tilde{\alpha}}{\bar{\alpha}}\right)^m \exp\left(-\frac{\tilde{\alpha}}{\bar{\alpha}}\right) \Theta(\tilde{\alpha})\delta(\lambda - \tilde{\lambda}) \ , \tag{5.11}$$

with $\lambda^* = -7.863 \pm 1.209$, $\bar{\alpha}^* = 5.098 \cdot 10^{-2} \pm 0.606 \cdot 10^{-2}$ pN^{-1}, and $m^* = 2.093 \pm 0.156$.

- *Beta distribution*

$$\rho(\boldsymbol{\theta}|\boldsymbol{\mu}) \propto \left(\frac{\tilde{\alpha}}{\alpha_{\mathrm{max}}}\right)^m \left(1.0 - \frac{\tilde{\alpha}}{\alpha_{\mathrm{max}}}\right)^s \Theta(\alpha_{\mathrm{max}} - \tilde{\alpha})\Theta(\tilde{\alpha})\delta(\lambda - \tilde{\lambda}) \ , \tag{5.12}$$

with $\lambda^* = -7.684$, $\alpha^*_{\mathrm{max}} = 3.395$pN^{-1}, $m^* = 1.997$, and $s = 62.01$.

The corresponding distributions $\rho(\tilde{\alpha}|\boldsymbol{\mu}^*)$ are shown in 5.6 (b). Particularly interesting is the fact that the fitted Gamma distribution (5.11) and the Beta distribution (5.12) are nearly identical. This can also be seen directly by comparing equations (5.11) and (5.12) and by making use of the well known approximation $(1.0 - \tilde{\alpha}/\alpha_{\mathrm{max}})^s \approx$

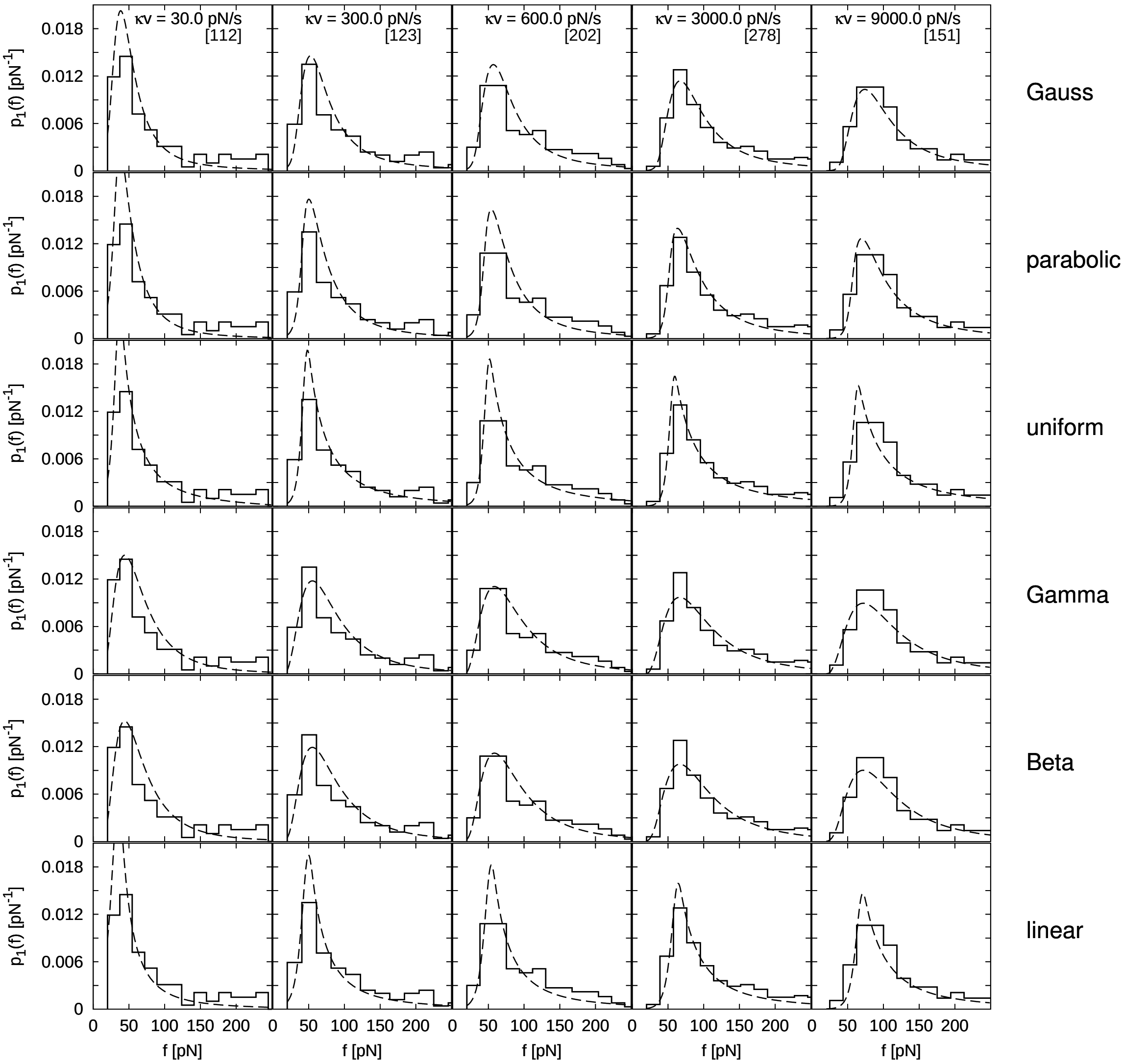

Figure 5.7: Same comparison between experimental and fitted rupture force distributions as in figure 5.4, but for the different distributions (5.7-5.12) of the parameter $\tilde{\alpha}$ shown in figure 5.6. The explicit values of the model parameters can be taken from the main text. The bin-width of the histograms was chosen according to equation (A.12) (see Appendix A.3), supplemented with the concomitant maximum likelihood estimates.

$\exp(-\tilde{\alpha}s/\alpha_{\max})$ for $s \gg 1$. Hence, $\bar{\alpha}^* = 0.051$pN^{-1} in equation (5.11) has to be compared to $\alpha^*_{\max}/s^* = 0.055$pN^{-1} in equation (5.12). These values are obviously close to each other. The most probable parameters of the Beta distribution are therefore found in a region where the Beta distribution approaches the Gamma distribution and depends on $\alpha_{\max}$ and s only via their ratio.[4] Consequently, our assumption from chapter 4, that the likelihood as a function of the model parameters develops a sharp maximum, does not apply here, and we cannot estimate the statistical uncertainties of the model parameters in the usual way.

Except the positions of the maxima, the distributions $\rho(\tilde{\alpha}|\boldsymbol{\mu}^*)$ shown in figure 5.6 (b) differ considerably from each other and from those shown in figure 5.6 (a). In particular, the skewness and asymptotics for large $\tilde{\alpha}$ values is completely different. In figure 5.7 the corresponding distributions of rupture forces are compared to the experimentally determined ones. For this comparison, the bin-width of the histograms was chosen following the procedure described in Appendix A.3. Here, however, no analytic expression for the optimal bin-width could be derived. Instead, equation (A.12) with $\hat{p}_1(f|\boldsymbol{\mu}^*, v, f_{\min})$ from (5.6,5.11,3.14) was solved numerically. Although the six distributions $\rho(\tilde{\alpha}|\boldsymbol{\mu}^*)$ of model parameters are quite different, each of them explains the experimental findings satisfactorily, with the seemingly best agreement for the Gamma/Beta and for the Gaussian distribution. Hence, it seems that the distribution of rupture forces (5.6) depends only weakly on details of the underlying distribution $\rho(\boldsymbol{\theta}|\boldsymbol{\mu})$, as long as the mean values and the dispersions about these values are comparable.

The parameter λ has the same physical meaning for all so far applied distributions $\rho(\boldsymbol{\theta}|\boldsymbol{\mu}^*)$. Namely, it denotes the logarithm of the force-free dissociation rate which is assumed to be the same for all repetitions of the experiment. While it has been assumed in [REB$^+$06] that the inferred value for this parameter does not significantly depend on the distribution of $\tilde{\alpha}$, which is indeed the case for the three symmetric distributions (5.7-5.9), we find here that this value depends considerably on the parametric Ansatz for the asymmetric distributions (5.10-5.12). For example, the most probable force-free dissociation rate $k_0^* = \exp(\lambda^*)$ is for the linear distribution approximately two orders of magnitude larger than for the Gamma distribution. This "systematic" difference is much larger than the statistical uncertainties of the inferred parameter value, cf. the statistical uncertainties of λ. This situation is comparable to our discussions in section 4.3, where the estimated energy barrier height ϵ in the extension of Bell's model was found to depend strongly on the Ansatz for the exponent γ.

Next, the comparison between experimental and theoretical distributions shall be further quantified. For this purpose, different statistical tests for hypotheses testing can be used. Here we employ a particular simple test, namely the Kolmogorov-Smirnov test [Jam06]. This test provides a possibility to check whether a given set

---

[4] The inferred set of parameters $\boldsymbol{\mu}^*$, obtained by numerically maximizing the likelihood, is not unique and depends strongly on the initial guess. However, within the numerical accuracy λ^*, m^*, and $\alpha^*_{\max}/s^*$ can be uniquely determined.

test set		**$\tilde{\alpha}$, Gauss (5.7)**		**$\tilde{\alpha}$, Gamma (5.11)**		**$\tilde{\lambda}$, Gamma (5.14)**	
v_c (nm/s)	N_c	D_{N_c}	$\sqrt{N_c}D_{N_c}$	D_{N_c}	$\sqrt{N_c}D_{N_c}$	D_{N_c}	$\sqrt{N_c}D_{N_c}$
10	112	0.266	2.82	0.171	1.87	0.083	0.88
100	123	0.074	0.82	0.088	0.98	0.069	0.76
200	202	0.121	1.72	0.094	1.34	0.081	1.16
1000	278	0.095	1.58	0.068	1.13	0.049	0.81
3000	151	0.114	1.40	0.093	1.14	0.087	1.07

Table 5.1: Maximum deviation D_{N_c} of the empirical survival probability of the test data set $\{f_i|v_i = v_c\}_{i=1}^{N}$ of size N_c from the theoretical survival probability (5.6,3.14) supplemented with a Gaussian (5.7) and a Gamma (5.11) distribution of the parameter $\tilde{\alpha}$ and with a Gamma distribution (5.14) for the parameter $\tilde{\lambda}$. Indicated in red are the deviations for which the hypothesis has to be rejected on the basis of a Kolmogorov-Smirnov test with a significance level of 0.05. More details are given in the main text.

of rupture forces is compatible to a proposed theoretical distribution. However, in our case this distribution depends on the maximum likelihood estimate of the model parameters and thus on the set of rupture forces. As a consequence, the Kolmogorov-Smirnov test cannot be applied directly. One possibility to circumvent this problem consists in splitting the full data sets into two subsets. One of them is used to obtain an estimate $\boldsymbol{\mu}^*$ of the model parameters. Then it can be checked whether the model, together with these parameters, is consistent with the distribution of rupture forces in the other subset. The latter is from now on called the test set.

For simplicity, the test set used here consists of all N_c rupture forces measured at a pulling velocity v_c, i.e., $\{f_i|v_i = v_c\}_{i=1}^{N}$. In the Kolmogorov-Smirnov test the maximum deviation of the empirical survival probability $\tilde{n}(f|v_c, f_{\min})$ from the theoretical survival probability $\hat{n}(f|\boldsymbol{\mu}^*, v_c, f_{\min})$ is considered, i.e.,

$$D_{N_c} := \max_f |\tilde{n}(f|v_c, f_{\min}) - \hat{n}(f|\boldsymbol{\mu}^*, v_c, f_{\min})| \ . \tag{5.13}$$

It can be shown [Jam06] that, given that the rupture forces have been sampled from the distribution $\hat{p}_1(f|\boldsymbol{\mu}^*, v_c, f_{\min}) = -d/df\, \hat{n}(f|\boldsymbol{\mu}^*, v_c, f_{\min})$, the distribution of $\sqrt{N_c}D_{N_c}$ (upon repeating the experiment many times) is independent of the functional form of $\hat{p}_1(f|\boldsymbol{\mu}^*, v_c, f_{\min})$. On a significance level of 0.05, $\sqrt{N_c}D_{N_c}$ should not exceed 1.36. That means, given that the N_c forces have been sampled according to $\hat{p}_1(f|\boldsymbol{\mu}^*, v_c, f_{\min})$, then on the average only in one out of 20 cases, $\sqrt{N_c}D_{N_c}$ should be larger than 1.36.

We restrict our comparison between the experimental and theoretical distributions to the Gaussian and Gamma distribution of parameters (5.7,5.11) for which the apparently best agreement was found. The procedure described above has been applied to each of the five different pulling velocities used for the data in figure 5.6. The

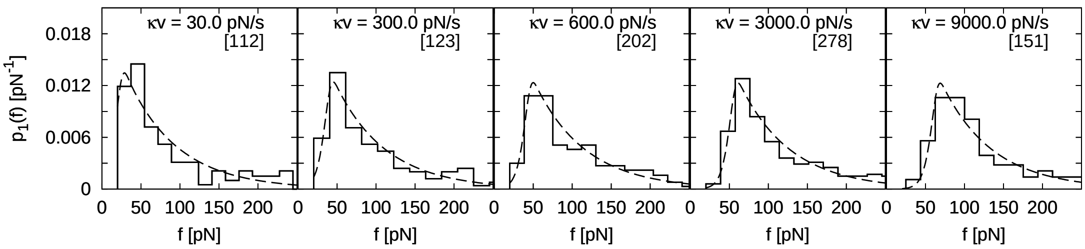

Figure 5.8: Solid histograms: Same as figure 5.1(b)-(f). Dashed lines: Maximum likelihood fits $\hat{p}_1(f|\boldsymbol{\mu}^*, v, f_{\min})$ according to equations (5.6,5.14,3.14).

resulting maximum deviations D_{N_c} are given in table 5.1. While for the Gamma distribution only in one case the critical value for $\sqrt{N_c}D_{N_c}$ is exceeded, this threshold is exceeded for the Gaussian distribution for four out of the five test sets. Hence, the Gamma distribution seems to explain the experimental findings better. A closer inspection reveals that for the Gaussian distribution and large pulling velocities, the largest deviation between the empirical and theoretical survival probabilities is found in the large force regime. This can be traced back to the fact that $\rho(\tilde{\alpha}|\boldsymbol{\mu}^*)$ does not vanish as $\tilde{\alpha} \to 0$. As a consequence, the theoretical distributions $\hat{p}_1(f|\boldsymbol{\mu}^*, v, f_{\min})$ have a long large force tail.

Although a fully objective statement is impossible, the results from table 5.1 indicate that there are still some small systematic deviations from the experimentally observed distribution (for the Gamma distribution and $v_c = 200$nm/s, the renormalized deviation $\sqrt{N_c}D_{N_c}$ is also close to the critical value). However, these small deviations will probably vanish by a further fine-tuning of the distribution of model parameters or when including the effect of the experimental noise in the evaluation which has so far not been done. In addition, modeling the force-dependence of the rate as in the extension of Bell's model (3.17) might also improve the results.

5.3.2 Variation of λ

Up to now we have always considered the situation that only $\tilde{\alpha}$ was allowed to vary from one repetition of the experiment to the next while $\tilde{\lambda}$ always assumed the same value. Next, the opposite situation will be considered. This means, $\tilde{\lambda}$ changes upon repeating the experiment while $\tilde{\alpha}$ is always the same. Remembering that the force-free dissociation rate and the energy barrier height are connected to $\tilde{\lambda}$ via $e^{\tilde{\lambda}} = \tilde{k}_0 = \omega(0)\exp(-E_b(0)/k_BT)$, we see that the randomization of the latter quantity is equivalent to a randomization of one of the former quantities.

As in the previous section, we have to make an Ansatz for the functional form of the distribution of the model parameters. Let us assume that the energy barrier height is drawn from a Gamma distribution. Then obviously:

$$\rho(\boldsymbol{\theta}|\boldsymbol{\mu}) \propto (\lambda_{\max} - \tilde{\lambda})^m \exp\left(\frac{\tilde{\lambda}}{\bar{\lambda}}\right) \Theta(\lambda_{\max} - \tilde{\lambda}) \delta(\alpha - \tilde{\alpha}) \ . \tag{5.14}$$

Further assuming that $m \geq 0$, the most probable parameters are found to be $\alpha^* = 0.143\text{pN}^{-1}$, $\lambda^*_{\max} = -1.39$, $\bar{\lambda}^* = 9.37$, and $m^* = 0.0$. Figure 5.8 shows that the agreement of the maximum likelihood fit with the experiment is excellent. This is also confirmed by the Kolomorogov-Smirnov test. Proceeding in the same way as detailed in the previous section, the results of this test for the different test sets are summarized in table 5.1. Rather surprisingly, this test indicates that a randomization of $\tilde{\lambda}$ fits the experimental data even better than a randomization of $\tilde{\alpha}$. Similar results were found for the four parameter Beta distribution

$$\rho(\boldsymbol{\theta}|\boldsymbol{\mu}) \propto \left(\frac{\tilde{\lambda}}{\lambda_{\min}} - 1.0\right)^m \left(1.0 - \frac{\tilde{\lambda}}{\lambda_{\max}}\right)^s \Theta(\lambda_{\max} - \tilde{\lambda}) \Theta(\tilde{\lambda} - \lambda_{\min}) \delta(\alpha - \tilde{\alpha}) \ , \tag{5.15}$$

which has shown to be sufficiently general to fit all other studied data sets, e.g., [BBA$^+$03, NDKM03].

However, for Bell's model the transformation $\tilde{\lambda} \to \tilde{\lambda} + \tilde{\lambda}'$ results in a shift of the rupture force distribution (3.15) towards lower forces (by $\Delta f = \tilde{\lambda}'/\alpha$). As a consequence, changing the skewness of the distribution of $\tilde{\lambda}$, in general, results in rupture force distributions with opposite skewness. Stated differently, for a given, experimentally established rupture force distribution, the possible functional forms of the distribution of $\tilde{\lambda}$ are limited to those functions which allow the correct skewness. This is in contrast to a randomization of $\tilde{\alpha}$, cf. figures 5.6 and 5.7.

Considering the Gamma distribution (5.14) fitted to the data from [EWB$^+$05], we see that the distribution has a "cutoff" at the maximum value $\lambda^*_{\max} = -1.39$ and falls off exponentially towards the lower $\tilde{\lambda}$ values, on a scale given by $\bar{\lambda}^* = 9.37$. Hence, rather small $\tilde{\lambda}$ values, down to values of $\tilde{\lambda} \approx -20$, are needed to satisfactorily explain the experimental rupture force distribution. This corresponds to a variation of the energy barrier height of approximately $20 k_B T$. In view of the fact that the typical strength of a specific bond is of the order of just $10 k_B T$ (compare section 3.1) and in view of the restrictions concerning the skewness of the distribution, interpreting the randomization of the relevant energy barrier height as the physical origin of the heterogeneity of the bonds might appear rather unlikely.

However, most of the possible physical sources of the heterogeneity of chemical bonds discussed in [REB$^+$06] and reviewed in section 5.2 are likely to effect the energy barrier height (and thus $\tilde{\lambda}$) as well as $\tilde{\alpha}$. For example, it has been shown in [DBBR06, BPHD08] that the unfolding kinetics of proteins can critically depend on the pulling geometry. Depending on the direction of the applied force, completely different dissociation/unfolding pathways may be sampled which is visualized in figure 5.9 for a two dimensional model potential landscape. While in absence of an applied force practically always pathway I with the lowest energy barrier is taken,

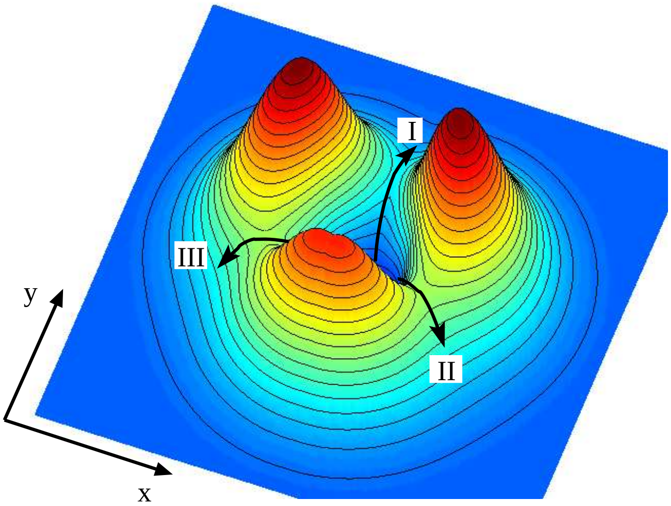

Figure 5.9: Model of a two dimensional potential landscape. In absence of a force, thermally activated escape practically always occurs along pathway I. Under application of force, also the other pathways (II and III) may be sampled, depending on the direction of the applied force.

under application of force, also the other pathways with higher energy barriers may be sampled. It is possible that such a system may still be described approximately by Bell's model, but with parameter values $(\tilde{\lambda}, \tilde{\alpha})$ now depending on the direction of the applied force. As illustrated and discussed in figure 5.3, in single-molecule pulling experiments the microscopic configuration of the system is subjected to random variations of this pulling geometry. Considering also other possible reasons for the heterogeneity, like variations in the local environment or a small fraction of multiple or of unspecific bonds, the proposed randomization of the parameter $\tilde{\lambda}$ upon repeating the experiment is not as unlikely as it might be suggested at the first glance.

The upshot of this section is that it is sufficient to randomize just one of the two parameters in Bell's model to explain the experimental findings. But from the experimental data alone, no conclusions can be drawn which parameter in fact changes from one repetition of the experiment to the next. Most likely, both parameters will change simultaneously. It is clear that allowing such a simultaneous randomization of both parameters in the Ansatz for the distribution $\rho(\boldsymbol{\theta}|\boldsymbol{\mu})$ of model parameters would result in an even better agreement between experimental and theoretical distributions. However, quite different distributions of just one of the model parameters, with significantly different values of the remaining parameter, can explain the experimental findings equally well. In view of this fact, a simultaneous randomization of both parameters seems to be of little use. Again, the inferred values for the model parameters can only be roughly connected to physical quantities if no further information about the system (for example from specially designed experiments) is available.

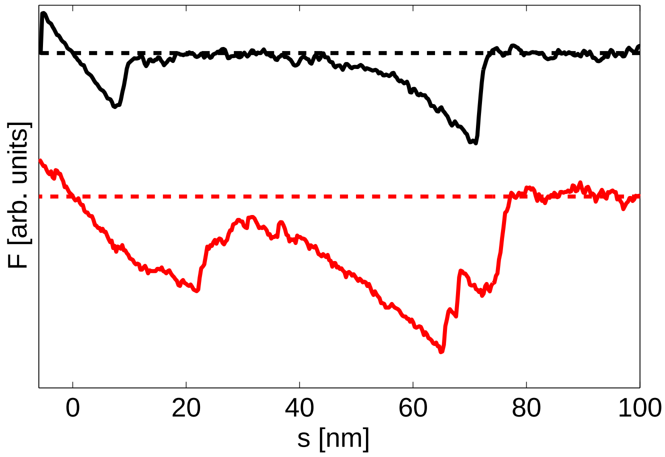

Figure 5.10: Solid lines: Retracting part of two force distance curves measured by AFM for the protein-DNA interaction studied by Bartels et al. [BMF$^+$07]. Dashed lines: Baselines of the two measurements corresponding to a vanishing force acting on the AFM tip. All forces are measured with respect to these lines.

5.4 Preprocessing the data: Experimental hints for a heterogeneity of bonds

Together with Alexander Fuhrmann and Robert Ros from the experimental biophysics group of Dario Anselmetti, we have reanalyzed already published data to check whether there are any direct experimental hints for variations of the number of bonds, the local environment, or of the microscopic pulling geometry which were possible physical sources of the proposed heterogeneity of the bonds. For this purpose we have, in a first step, considered the full force distance curves of the single measurements, and not only the rupture forces. The rupture force data correspond to the dissociation of a protein from a 285bp long DNA fragment and was measured by Bartels et al. [BMF$^+$07].

A basic assumption in nearly all theoretical models for the interpretation of single-molecule pulling experiments is that there exits a unique force-extension curve $F(s)$ which is the same for all repetitions of the experiment (cf. section 5.1). As the cantilever is always the same (at least for a huge subset of data) and as the linker molecules employed for the experiment possess a very sharp distribution of length, this assumption seems reasonable. Even if different binding motifs between ligand and receptor exist, one would not expect that the force-extension curve is influenced by details of the bond between ligand and receptor.

Figure 5.10 shows two examples of measured force-extension curves. The black curve has, as expected, an adhesion signal at a low distance s and a single rupture event at a larger distance. In both cases, after the tip jumps off the surface and after the rupture of the bond, the force immediately fluctuates around the baseline corresponding to a vanishing force acting on the cantilever. However, in a non-negligible fraction of force distance curves, like the red curve in figure 5.10, this behavior is different. The force signal does not immediately "jump back" to the baseline, but to some finite value. Especially the behavior of the red curve in figure 5.10 after the rupture of the bond at $s \approx 60$nm might be hint that one is, in this measurement, not pulling apart a single bond, but multiple parallel bonds. Curves which show such multiple rupture events are excluded from the further analysis.[5] Furthermore, in all theoretical models, it is assumed that all bonds have formed at forces not larger than the threshold force $f_{\min}$. Therefore, in addition only those measurements have been used for a further evaluation for which the force acting on the bond is smaller than $f_{\min}$ after the tip jumps off the surface (adhesion signal).

In [FAR$^+$08] we have shown that, for "not too small" $f_{\min}$, the remaining force-extension curves can be very well fitted with a second-degree polynomial in the whole force interval $[f_{\min}, f_r]$ with f_r the rupture force, but not with a straight line as usually assumed. Details of the exact numerical algorithm are given in [FAR$^+$08]. For other data sets more complicated functions than low order polynomials might be necessary. For example, in [RBA07] the freely jointed chain model and the worm-like chain model have been employed. It has been shown that the simple approximation of a linear force-extension curve results in small but systematic errors in the estimated model parameters. Realizing, however, that the parameterization of the curve is only an intermediate step in the evaluation, any function which describes the force-extension characteristic satisfactorily over the full range of pulling forces, may be used. For all data sets studied by us second-degree polynomials were sufficient.

After aligning the curves such that $F(s = 0) = f_{\min} = 32$pN, all these resulting polynomials for the data from [BMF$^+$07] and a pulling velocity $v = 2000$nm/s are shown in figure 5.11(a). Clearly, these curves do not collapse to a single universal force-extention curve as expected, but show rather large deviations. Hence, the basic assumption 2 from section 5.1 [equation (5.3)] is in fact not true.

In principle, this finding may have different physical reasons, e.g., a dispersion of linker lengths, a fraction of multiple bonds, or variations of the pulling geometry. We will now briefly discuss whether any of these points might explain the findings from figure 5.11(a) quantitatively. The effect of the dispersion of linker lengths has been discussed in detail in [FWKG03, KCB$^+$04]. In the experiment [BMF$^+$07], rather soft cantilevers (with spring constant $c \approx 10$pN/nm) have been used. As a consequence, differences in the force distance curves due to a dispersion of the linker length can be expected to occur mainly in the low extension/low force part of the curves. This is in contrast to the observed behavior of the force-extension curves from figure 5.11(a). Furthermore, in the experiment [BMF$^+$07] the proteins were immobilized on the surface via short linker molecules, and the DNA fragment was linked via an approximately

---

[5] This has in fact already been done previously when evaluating the experiments.

35nm long PEG linker to the tip. Both linkers had a very sharp length distribution [FW]. The dispersion of linker lengths should thus play a minor role. A similar conclusion can be drawn for multiple parallel bonds. Again, the differences should be mainly visible in the low force regime. Furthermore, as only in approximately 10% of all trials a rupture event in the force distance curves is visible, it is very unlikely that a large fraction of those curves with a rupture event corresponds to the rupture of multiple parallel bonds (cf. discussion in chapter 3.2.2). On the other hand, the observed splitting of the curves might be a hint for variations of the pulling geometry. That these variations occur is likely in view of the fact that the rather stiff DNA fragment is, with approximately 97nm, long compared to the linker molecules. This effect might even be amplified by the fact that the protein, which binds to the DNA fragment, is linked to the surface with a very short linker of only a few nm. As a consequence, the direction of the force acting on the cantilever is, in general, not normal to the surface. This speculation is confirmed by the typical force distance curves shown in figure 5.10. Subtracting the deflection s_c of the cantilever at the point of rupture, we see that the distance of the tip from the surface at this point is approximately $s_d = 60$nm (cf. figure 3.2). Compared to sum of the length of the DNA fragment and of the PEG linker, $L = L_{\mathrm{DNA}} + L_{\mathrm{PEG}} \approx 130$nm, this distance is short, indicating that the complex is in these cases stretched under a large angle (with respect to the normal direction of the surface). As demonstrated in [KEG06], the tangential component of the force can influence the deflection of the laser beam from the cantilever, see figure 3.1, and hence the "measured" force in a complicated manner. Because only the distance s of the cantilever from the surface is experimentally controlled, variations of the pulling geometry also result in different rates at which the linker molecules are stretched. Another possible reason for the observed behavior of the force distance curves is that the compound object does not simply consist of the protein, the DNA fragment, and the two linkers, but that a whole network of linkers participates. There are experimental hints – the location of the rupture event in the force distance curves is incompatible to the single lengths of the molecules – that this might happen [FW].

Next, we have put forward a selection procedure of rupture events such that the initial discrepancy between theory and experiment is remedied by construction. For this purpose we have considered (for one pulling velocity) the data pairs (f_i, f_i') with f_i the rupture force and f_i' the slope of the (fitted) force-extension curve prior to the rupture. This data has been binned to a histogram, and the data points in the neighborhood of the maximum of this histogram have been selected, resulting in a subset of typically 20 data points. Then a second degree polynomial has been fitted to the force distance curves of this subset by a least squares fit. This curve can be assumed to be the most characteristic force-extension curve of the present data set and is called the fitted universal force-extension curve $F_u(s)$. In a second step, all force-extension curves for *all pulling velocities* are compared with $F_u(s)$, and only those which are "sufficiently close" to this curve are accepted for the final evaluation. This selection procedure is controlled by two parameters (δ_1, δ_2). The first of them sets the maximum relative deviation of the slope f_i' at the rupture point from the slope of

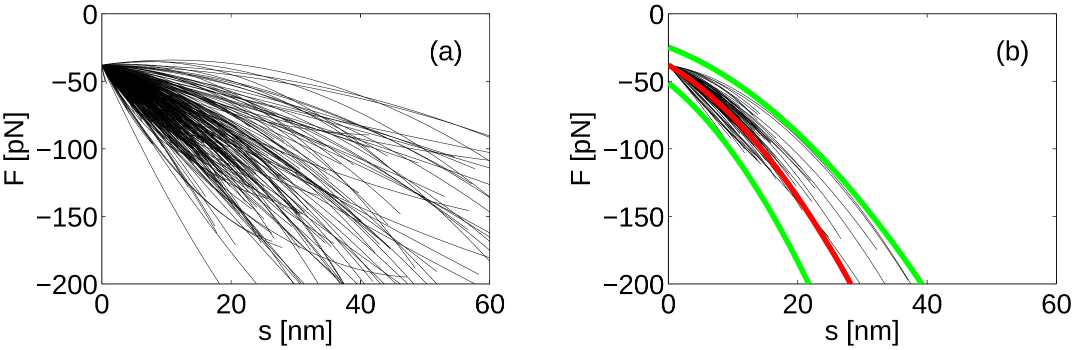

Figure 5.11: Force-extension curves measured for the protein-DNA interaction [BMF$^+$07] at a pulling velocity $v = 2000$nm/s. (a) All fitted force-extension curves with just one rupture event and maximum force $\max(F(s)) > -f_{\min} = 32$pN after appropriate aligning. (b) The fitted universal force-extension curve $F_u(s)$ is shown in red. All accepted curves (black) lie entirely between the two green lines which set the maximum allowed deviation from $F_u(s)$. More details are given in the text.

the universal force extension curve at this point. The second defines an interval around $F_u(s)$, limiting the maximum relative deviations [cf. green lines in figure 5.11(b)].

The result of this filtering procedure with $(\delta_1 = 0.2, \delta_2 = 0.35)$ is shown in figure 5.11(b) for the force-extension curves measured at $v = 2000$nm/s. However, the distributions of the rupture forces before and after this filtering procedure differ within their intrinsic statistical uncertainties from each other only slightly. The same was found for all other analyzed data sets. Even going to smaller tolerance levels (δ_1, δ_2) does not change this finding, implying that the distribution of rupture forces does not critically depend on details of the force-extension characteristic. Furthermore, the f vs. $-v \ln n(f|v, f_{\min})$ plots in figure 5.12 reveal the same discrepancy between standard models and experimental data as in figure 5.2, while the heterogeneous bond model again fits the data very well (data not shown).

Although the data processing described above did not result in a significantly improved agreement between experimental data and the standard theories, it suggests that there are in fact variations in the experimental conditions, e.g., in the microscopic configuration, from one repetition of the experiment to the next which might effectively be described by a randomization of the model parameters. The differences in the force-extension curves can be a result of geometrical variations, but also other reasons are possible. For example, a whole network of linkers might somehow interact with the tip. This is suggested by some experiments [FW], but the physical and chemical origin of this proposed interaction is still unclear. On the other hand, looking on individual force-extension curves, one sees that in some repetitions of the experiment one is pulling apart multiple parallel bonds. In a small but not negligible

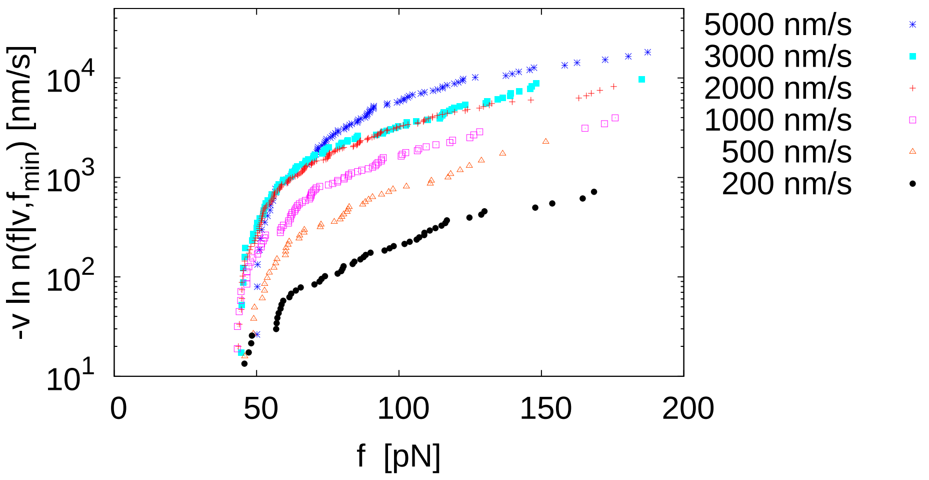

Figure 5.12: The functions $-v \ln n(f|v, f_{\mathrm{min}})$ for the experimental rupture force data from [BMF+07]. A unique threshold force $f_{min} = 42$ pN has been used for all pulling velocities. Only events with a force-extension characteristic similar to the constructed universal force-extension curve $F_u(s)$ have been taken into account. The number N_v of experimental data points for the six different velocities are $N_{200\text{nm/sec}} = 54$, $N_{500\text{nm/sec}} = 48$, $N_{1000\text{nm/sec}} = 80$, $N_{2000\text{nm/sec}} = 151$, $N_{3000\text{nm/sec}} = 87$, and $N_{5000\text{nm/sec}} = 95$. A few large rupture forces are omitted for sake of better visibility.

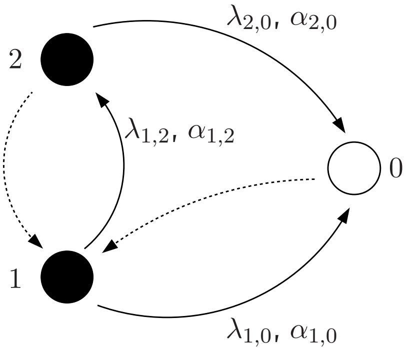

Figure 5.13: Schematic representation of a chemical bond that can exist in the two different metastable states 1 and 2. The dissociation into the unbound state 0 can proceed along different pathways indicated by the solid arrows.

fraction, these bonds might rupture nearly simultaneously so that the multiple rupture event cannot or only hardly (red curve in figure 5.11) be resolved.[6] As discussed above these events cannot be removed by the proposed filtering procedure, but will influence the distribution of rupture forces [GRK$^+$08]. This will be discussed in some more detail in section 5.6.

5.5 Effects of non-equilibrium initial distributions

We will now discuss a possible alternative explanation for the observed incompatibility between the experimental data and the theoretical models based on a one-step rate description. Some recent experiments have provided an indication that – after formation – the bond relaxes relatively slowly via some metastable states [PH05, LYZL06, BBLD07, FSA$^+$09]. For example, it has been observed in [PH05, LYZL06, FSA$^+$09] that the average rupture force $\langle f \rangle$ at a given pulling velocity increases with the dwell time t_d, i.e., the time the tip is pressed onto the surface before it is again pulled away. In these works, it has been proposed that for too short dwell times t_d the system has not always reached the deepest energy minimum, i.e., the initial distribution between these metastable states is *not* the equilibrium distribution. We will now investigate whether these non-equilibrium effects can result in rupture force distributions similar to the observed ones.

Let us consider the simple two-state model which is schematically represented in figure 5.13. We assume that the formation of the bond always occurs via the metastable state 1. Then the bond can either relax to the ground state 2 or dissociate to the unbound state 0. For simplicity, we will further assume that, once the ground

---

[6] This has been supplemented by numerical experiments by simulating the force-extension curves of two parallel bonds with linkers attached at different positions on the tip.

state is reached, the system cannot return to state 1, but only directly dissociate. The reaction kinetics is hence given by the following master equation:

$$\begin{aligned}\dot{n}_1(t|\boldsymbol{\mu},v) &= -(k_{1,2}(f(t|v)|\boldsymbol{\mu})+k_{1,0}(f(t|v)|\boldsymbol{\mu}))n_1(t|\boldsymbol{\mu},v)\ , && (5.16)\\ \dot{n}_2(t|\boldsymbol{\mu},v) &= -k_{2,0}(f(t|v)|\boldsymbol{\mu})n_2(t|\boldsymbol{\mu},v)+k_{1,2}(f(t|v)|\boldsymbol{\mu})n_1(t|\boldsymbol{\mu},v)\ , && (5.17)\end{aligned}$$

with force-dependent rates as in Bell's model (3.13). That means, each force-dependent dissociation rate is specified by two parameters $(\lambda_{i,j},\alpha_{i,j})$.

Models of this kind have been studied in various publications, e.g., [BDA02, RER$^+$04, IP04]. While the initial distribution between the two states is usually assumed to be given (in general the equilibrium distribution), we will proceed differently and explicitely consider the equilibration process. For this purpose, we reconsider the experimental conditions: The tip is pressed onto the surface for the time t_d. During this time a bond between the ligand and receptor can form. Dealing with the dynamics of tethered molecules, modeling the association process is a highly complicated and unsolved problem [JWK$^+$01]. We therefore simply assume that the bond can form at any time, while the tip is pressed onto the surface, with equal probability. Then the tip is pulled away. This, however, does not immediately result in a force acting on the bond. First the complex of linker-molecules, receptor, and ligand has to be stretched (cf. sections 3.2.3 and 5.4 and figure 5.10). Here we will assume that no force acts on the bond up to a distance $s = L$ of the cantilever from the surface, followed by a linearly increasing force in analogy to Bell's model. We will, hence, choose the time offset such that $t = 0$ at the moment the bond has formed. Then, the time-dependence of the force is given by

$$f(t|v) = \kappa\begin{cases}0 & \text{if } t < t_{eq}+L/v\ ,\\ t-(t_{eq}+L/v) & \text{else}\ ,\end{cases} \tag{5.18}$$

with t_{eq} uniformly distributed in $[0;t_d]$. The time the bond has to equilibrate, before a force is applied to it, thus depends on the pulling velocity.

Next, the dynamics according to equations (5.16-5.18) with $n_1(t=0|\boldsymbol{\mu},v)=1$, $n_2(t=0|\boldsymbol{\mu},v)=0$ shall be numerically simulated. For this purpose, we choose experimentally realistic values $t_d = 0.4$s, $L = 60$nm and rate parameters $\alpha_{1,2} = -0.001$pN^{-1}, $e^{\lambda_{1,2}}/\kappa$=1s^{-1}, $\alpha_{1,0} = 0.09$pN^{-1}, $e^{\lambda_{1,0}}/\kappa$=0.3s^{-1}, $\alpha_{2,0} = 0.05$pN^{-1}, $e^{\lambda_{2,0}}/\kappa$=0.1s^{-1}. For six different pulling velocities between $v = 200$nm/s and $v = 5000$nm/s, 200 rupture forces have been generated according to the probabilistic laws (5.16-5.18), using the so-called Gillespie algorithm. In order to make a comparison to the experiment more realistic, we added a Gaussian distributed error Δf with standard deviation $\sigma_f = 15$pN to the resulting rupture forces and kept only those above a threshold force $f_{\min} = 42$pN. The error Δf is assumed to contain all experimental uncertainties, like instrumental noise or variations in the pulling geometry. The result of this computer experiment is shown in figure 5.14(a) in the form of the f vs. $-v\ln n(f|\boldsymbol{\mu},v,f_{\min})$ plots. Comparing them to figure 5.12 for the experimental data from [BMF$^+$07] shows that both are very similar. The same can be seen by directly comparing the histograms of rupture forces.

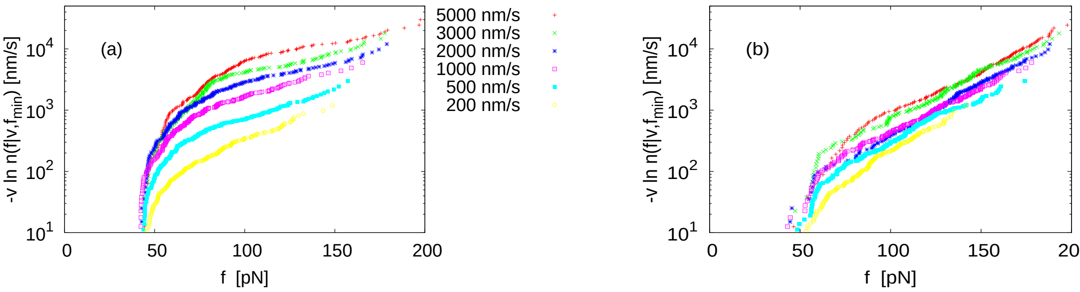

Figure 5.14: The functions $-v \ln n(f|v, f_{\text{min}})$ for two numerical experiments with reaction kinetics from figure 5.13 and time-dependent force (5.18) with total length $L = 60$nm. The transition rates according to Bell's model are specified by the parameter values: $\alpha_{1,2} = -0.001$pN^{-1}, $e^{\lambda_{1,2}}/\kappa$=1s^{-1}, $\alpha_{1,0} = 0.09$pN^{-1}, $e^{\lambda_{1,0}}/\kappa$=0.3s^{-1}, $\alpha_{2,0} = 0.05$pN^{-1}, $e^{\lambda_{2,0}}/\kappa$=0.1s^{-1}. In (a) a dwell time $t_d = 0.4$s was used and in (b) $t_d = 20$s. For each velocity 200 rupture events have been simulated, and an additive experimental error with $\sigma_f = 15$pN has been assumed. The threshold force was $f_{\text{min}} = 42$pN.

We can therefore conclude that, at least in principle, multiple state models with non-equilibrium initial distributions can result in rupture force distributions similar to the observed ones. However, a relevant question is: Is it also probable that these models can explain all experimental data sets which are apparently incompatible to the theory? To study this point we will first consider the situation that we start from an equilibrium distribution. For various networks of metastable states and allowed transitions between them, it has been demonstrated by Raible et al. [RER$^+$04] that (except for very complicated networks involving many metastable states) the experimental findings cannot be reproduced satisfactorily, when starting from an equilibrium initial distribution. For our example, this can be confirmed by increasing the dwell time t_d. The results for t_d =20s are shown in 5.14(b). The reconstructed $-v \ln n(f|\boldsymbol{\mu}, v, f_{\text{min}})$ functions nearly collapse on a single curve, as predicted by the basic models based on a one-step rate equation, and are qualitatively very different from those in (a) and thus also from the experimental data. To the best of our knowledge such a behavior could not be observed in any of the experiments where the average rupture force was found to depend on the dwell time. One may furthermore ask whether the velocity dependence of the $-v \ln n(f|v, f_{\text{min}})$ functions is typical for the two-state model with non-equilibrium initial conditions. The answer to this question is "no"; The details of the distribution, like the skewness, depend critically on the model parameters as well as the range of pulling velocities. In fact, the "typical" rupture force distribution according to the two state model has two peaks, each of them similar to the distribution of rupture forces in Bell's model. Even including the backward transition from state 2 to state 1 does not change this finding. In contrast to this, the experimentally measured $-v \ln n(f|\boldsymbol{\mu}, v, f_{\min})$ functions almost always show a velocity dependence as in figure 5.12 and 5.14(a), respectively.

In summary, in some cases non-equilibrium effects in multiple state models may explain the experimental findings. It is, however, rather unlikely that they are the only reason for the apparent discrepancy between experiment and theory.

5.6 Concluding discussion

In this part of the present work, we have demonstrated that the evaluation and interpretation of single-molecule force spectroscopy data is still very challenging. The reverse problem of connecting the measured rupture force data to the physical properties of the chemical bond is hard to tackle, even under idealized conditions (chapter 4). Some properties of the dissociation process and of the underlying potential landscape, like the force-free dissociation rate and the distance between potential well and barrier, can be reliably estimated, while the determination of other quantities, like the barrier height, requires further information.

The situation is even more complicated for real experimental data. We have shown that the data are in most cases incompatible with the basic assumptions (5.2,5.3) which are usually employed when evaluating these experiments. Different explanations have been discussed, and it has been shown that different models may explain the findings. The most general and promising explanation has been introduced by Raible [REB$^+$06] in the form of a heterogeneous bond model. We have shown that quite different distributions of model parameters result in nearly the same rupture force distributions. On the one hand, this shows that the extracted parameters are just model parameters. Although they have, in principle, a physical interpretation, it is not clear how to connect them to the true physical quantities of the bond if the data can be fitted with completely different values, or even distributions, of the single parameters. On the other hand, this insensitivity of the rupture force distribution on details of the distribution of model parameters argues for the heterogeneous bond model. Any changes of the experimental conditions from one repetition of the experiment to the next, which can be described effectively by a randomization of the model parameter α, causes qualitatively the same distribution of rupture forces (skewness) and the same velocity dependence of the $-v \ln n(f|v, f_{\min})$ functions as experimentally observed.

It has been argued that one possible source of the heterogeneity of the bonds are variations of the pulling geometry which are likely to occur at least in some of the experiments studied. These variations can cause a randomization of the model parameters in two different ways. First, the AFM cantilever "measures" only the component of the force normal to the surface. This can differ from the force acting along the direction of the relevant reaction coordinate, cf. figure 5.3. This effect can be included in the parameter α via $\alpha \to \cos(\varphi)\alpha$, where φ is the "random" angle between the two forces.[7] Second, the dissociation pathway, and hence both parameters α and λ, may depend on the direction of the applied force, as illustrated in figure 5.9, and therefore on the pulling geometry. Another possible reason is that in a fraction of trials one is pulling apart multiple parallel bonds. We have discussed in section 5.4 that the force-extension curves corresponding to these events can, in many cases, not be distinguished from those of single rupture events. It has been shown in [GRK$^+$08] that, if the force is unequally distributed along the single bonds (caused, for example, by different immobilization points on the cantilever tip), this can result in similar rupture force distributions as in the heterogeneous bond model. This is, however, not surprising. The force acting on bond i at time t is $f_i(t) = c_i(f(t))f(t)$, $0 \leq c_i(f) \leq 1$. In the relevant rage of forces, $c_i(f)$ depends only weakly on the force, so that we can approximate $c_i(f) = c_i$. The simultaneous rupture of the bonds occurs, in general, at the moment at which the bond with the largest force $f_{\max} = c_{\max} f$ ruptures. This force is then distributed over the other bonds and leads finally to their rupture. It is therefore very likely that the reaction kinetics can again be described effectively by a Bell type model with $\tilde{\alpha} = c_{\max}\alpha$. Because $c_{\max}$ changes from one repetition of the experiment to the next, the multiple bond model is effectively a special case of the heterogeneous bond model. Although the multiple bond model is based on a nice physical picture, it is rather unlikely that it is consistent with the experiments discussed in this chapter. In [GRK$^+$08] a large fraction of all rupture events had to correspond to the simultaneous rupture of multiple parallel bonds. There is, however, no experimental evidence that this is the case for the experimental data studied by us. Only in very few force distance curves, multiple rupture events could be resolved. Furthermore, in only about 10% of all trials at least one bond has formed. As the number of bonds should roughly follow a Poissonian statistics, the occurrence of a large fraction of multiple bonds is very unlikely.

Specially designed experiments are needed in order to gain further insight into the physical mechanisms underlying the forced rupture of bonds in single-molecule force spectroscopy experiments. From a theoretical point of view, it would be interesting to study model systems where both, the receptor and the ligand, are "small" molecules and possess just one binding site for the linker-molecules. Both, the receptor and ligand, should then be linked via long linkers to the tip and to a flat surface, respectively. In this way, the influence of geometrical variations should be reduced to a minimum. Furthermore, surface charges should play no role. Then dwell times, concentrations of immobilized molecules, and other parameters of the experiment can be systematically varied. Measurements on such a system, where both binding partners were immobilized via long PEG linkers, were performed in [MBZ$^+$07], resulting in one of the few data sets which are compatible to a one-step rate description.

---

[7] In addition, there can occur other measurement errors, cf. figure 5.3.

Part III

Escape rates of overdamped Brownian particles far from thermal equilibrium

6 A unified approach to the approximation of escape rates

6.1 Introduction

In part II of this work we have considered the forced rupture of chemical bonds as experimentally studied in single-molecule pulling experiments. This rupture is modeled as a thermally activated escape of a Brownian particle from a metastable potential under application of a steadily increasing force. The rate at which this force increases is, however, much slower than all relevant molecular relaxation processes. In this context one speaks of an adiabatically slowly modulated potential $V(x,t) = U(x) - f(t)x$, and the relevant probability density closely resembles the Boltzmann form. As a consequence, the escape rate out of such a slowly modulated potential can at any time be very well approximated by the Kramers rate (2.19).

In this part of the work, we consider the particularly challenging situation that the system is far from thermal equilibrium. This can either be the result of fast and strong modulations of the potential or of the thermal bath, e.g., in form of time-dependent temperatures. In this case, the probability density strongly deviates from the Boltzmann form, and the instantaneous escape rate can no longer be approximated by the Kramers rate [LRH00b]. Important for conceptual reasons as well as for a number of experiments are periodically modulated potentials. The escape from such systems has been studied in a number of works [Jun93, MS96a, SDG99, Tal99, LRH00a, LRH00b, MS01, BG04, BG05, RD05, RD06], but each of these approaches is limited to just one of the following cases: weak, slow, fast, or moderately fast and moderately strong driving. Furthermore, the non-periodic case can be treated by none of these approximations.

In this chapter we put forward a new path integral approximation for the instantaneous escape rate which unifies and extends several of the previous approximations [CCR81, Jun93, MS96a, Shn97, BDKA99, SDG99, Tal99, LRH00a, LRH00b, MS01, SSLM01, BG04, BG05, RD05, RD06] and which is not limited to just one of the above mentioned cases. The escape from periodically as well as from non-periodically modulated systems can be treated, and the modulation can occur on any time scale. Only very strong driving cannot be treated within this formalism.

The focus of this chapter lies on the derivation of the approximation and on the discussion of some of its properties. Then, the approximation will be applied to some model systems and compared to very accurate numerical results. While these examples will be for time-dependent potentials and static temperatures, we will in the following chapter 7 consider the complementary case of static potentials and time-dependent temperatures and illustrate some interesting effects which can occur in these systems.

6.2 General formulation of the problem

6.2.1 Model

In this chapter we again consider the overdamped one-dimensional motion of a Brownian particle or of a general reaction coordinate (see sections 2.1, 2.2). For a spatially homogeneous white noise, the general equation of motion reads:

$$\eta(t)\dot{x}(t) = F\left(x(t),t\right) + \sqrt{2D(t)}\xi(t)\ , \tag{6.1}$$

$$\langle \xi(t) \rangle = 0, \quad \langle \xi(t)\xi(t') \rangle = \delta(t-t')\ . \tag{6.2}$$

In contrast to equation (2.7) the friction coefficient $\eta(t)$ as well as the noise strength $D(t)$ are allowed to be time-dependent. Both situations can experimentally be realized. For example, the dynamics of a Browninan particle in a solvent containing anisotropic molecules (i.e., a lyotropic liquid), which can be oriented by a time-dependent external magnetic field, can be described by equation (6.1) with a time-dependent friction coefficient [HH05]. Short laser pulses, temporarily heating the environment of the Brownian particle, on the other hand, result in a time-dependent noise strength.

Without loss of generality the friction coefficient can be assumed to be constant [divide both sides of equation (6.1) by $\eta(t)$]. Furthermore, using dimensionless units (see, e.g., [Rei02]), we can appropriately rescale time and set $\eta(t) = 1$. Hence, equation (6.1) reduces to

$$\dot{x}(t) = F\left(x(t),t\right) + \sqrt{2D(t)}\xi(t)\ . \tag{6.3}$$

The time-dependence of the force field $F\left(x,t\right)$ can be completely arbitrary. The most often studied case is that of a time-periodic force field with period $\mathcal{T}$, so that

$$F\left(x,t\right) = F\left(x,t+\mathcal{T}\right)\ . \tag{6.4}$$

However, this assumption is not necessary for the theory that will be developed in sections 6.3 and 6.4. But for reasons of simplicity we will restrict our discussions at some points to this case.

We will further assume that the deterministic dynamics

$$\dot{x}(t) = F\left(x(t),t\right) \tag{6.5}$$

exhibits exactly one bounded *stable orbit* $x_s(t)$ (attractor) and one bounded *unstable orbit* $x_u(t)$ (repeller) with the following properties:

$$\lambda_s \ := \lim_{t\to\infty} \tfrac{1}{t} \textstyle\int_0^t dt'\ \lambda_s(t') < 0\ , \quad \lim_{t\to\infty} \frac{1}{t} \int_0^{-t} dt'\ \lambda_s(t') > 0\ , \tag{6.6}$$

$$\lambda_u \ := \lim_{t\to\infty} \tfrac{1}{t} \textstyle\int_0^t dt'\ \lambda_u(t') > 0\ , \quad \lim_{t\to\infty} \frac{1}{t} \int_0^{-t} dt'\ \lambda_u(t') < 0\ , \tag{6.7}$$

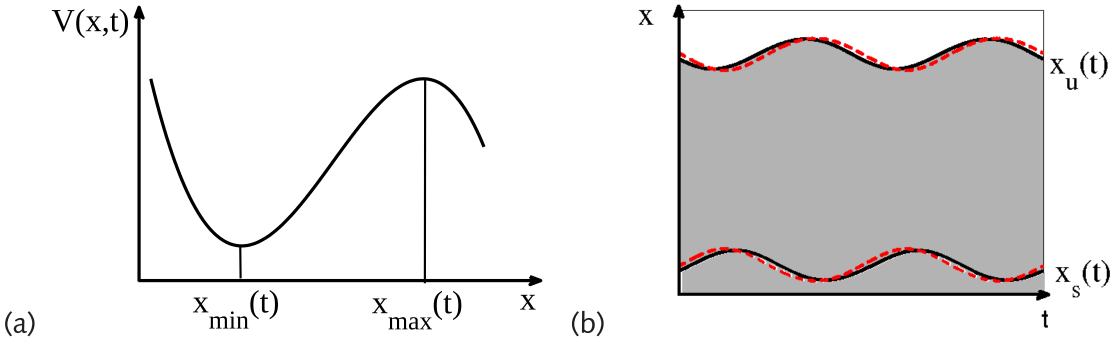

Figure 6.1: (a) The cubic potential $V(x,t) = -a/3\,x^3 + b/2\,x^2 - A\sin(\omega t)x$ used in section 6.6.4 with parameters $a = 1.78$ and $b = 2.67$ at time $t = 0$. The instantaneous minimum is denoted as $x_{\min}(t)$ and the maximum as $x_{\max}(t)$. (b) The stable and unstable orbits (solid lines) as a function of time. They follow $x_{\min}(t)$ and $x_{\max}(t)$ (red dashed lines), respectively, with some phase shift. The basin of attraction $\mathcal{A}(t)$ is shown as the grey shaded region.

where

$$\lambda_{s,u}(t) := F'(x_{s,u}(t), t)\ . \tag{6.8}$$

The quantities $\lambda_{s,u}$ are also termed *Lyapunov coefficients*.[1] Here we assume that $x_s(t) < x_u(t)$ for all times. The analogous case $x_s(t) > x_u(t)$ can be treated in the same way. Hence, *every* solution of equation (6.5) in the long-time limit converges to $x_s(t)$ if $x(t_0) < x_u(t_0)$ for some time t_0 and diverges to $x = \infty$ if $x(t_0) > x_u(t_0)$.

For our standard example of a time-periodic force field (6.4) the orbits become periodic functions, too:

$$x_s(t) = x_s(t + \mathcal{T}), \quad x_u(t) = x_u(t + \mathcal{T})\ . \tag{6.9}$$

The force field $F\,(x,t)$ is connected to a potential $V(x,t)$ via $F\,(x,t) = -V'(x,t)$. We denote by $x_{\min}(t)$ the instantaneous minimum of $V(x,t)$ and by $x_{\max}(t)$ the instantaneous maximum [cf. figure 6.1(a)]. The stable and unstable orbit agree with these functions only for an adiabatically slow modulation of the potential. Usually, they follow $x_{\min}(t)$ and $x_{\max}(t)$, respectively, with some phase shift [and smaller amplitude, see Fig. 6.1(b)] [BG02].

6.2.2 Definition of the instantaneous escape rate

In section 2.4 it was shown that the escape rate k from a static metastable potential can be defined as the flux of probability over an absorbing boundary x_a. In some works this definition is also used in the case of fast driven systems, e.g., [RD05]. In these systems the so-defined escape rate is also time-dependent, and the explicit value

---

[1] The conditions (6.6,6.7) are sufficient, but not necessary for stable and unstable orbits, respectively.

at a given time will ultimately depend on the position of the absorbing boundary x_a. Here, we use a different definition of the instantaneous escape rate [LRH00a, LRH00b] which is very similar to our original definition (2.13) where the escape rate was defined as the relative change of the survival probability of a metastable state. This definition seems to be more natural and is, in particular, independent of the (arbitrary) choice of the absorbing boundary. In order to avoid any confusion with the escape rate k defined in section 2.4, we will denote the instantaneous escape rate defined in equation (6.10) by $\Gamma(t)$.

Let us consider the deterministic motion (6.5). According to our assumptions about the stable and unstable orbits $x_{s,u}(t)$, we can define a time-dependent basin of attraction $\mathcal{A}(t) = \{x \in \mathbb{R} \mid x < x_u(t)\}$ [gray shaded region in figure 6.1(b)]. Every particle that is in this region at some time t_0 will stay there forever.

This situation changes for a non-vanishing noise strength $D(t)$. Then, the particle will leave the basin of attraction with probability one as $t \to \infty$. Let us consider a particle starting at some point $x_0 \in \mathcal{A}(t_0)$ at time t_0. We denote by $n(t|t_0, x_0)$ the probability that the particle has not left the basin of attraction until time t, i.e., the survival probability. The instantaneous escape rate $\Gamma(t)$ is defined as the relative change of probability:

$$\Gamma(t) := -\frac{\frac{d}{dt} n(t|t_0, x_0)}{n(t|t_0, x_0)} \ . \tag{6.10}$$

For static potentials this definition is equivalent to the usual definition (2.13) of the escape rate. It should be noted that the escape rate (6.10) depends on the chosen initial condition $x(t_0) = x_0$. However, in the following we will restrict ourselves to small noise strengths $D(t)$ so that the typical time needed to escape from the basin of attraction (the Kramers time t_K) is much larger than all relevant time scales τ_R of the deterministic motion. Then, for times $t - t_0$ much larger than τ_R the definition (6.10) becomes independent of t_0 and x_0, and we may choose $x(t_0) = x_s(t_0)$. If at the same time $t - t_0 \ll t_K$, the denominator in equation (6.10) can be approximated by 1.

The instantaneous escape rate $\Gamma(t)$ can also be expressed in terms of the probability density $\rho(x, t|x_0, t_0)$. Its time evolution is given by the Fokker-Planck equation (cf. section 2.3). For the dynamics (6.2,6.3) this equation reads [Ris89, HTB90]:

$$\frac{\partial}{\partial t} \rho(x, t|x_0, t_0) = \frac{\partial}{\partial x} \left(-F(x, t) + D(t) \frac{\partial}{\partial x} \right) \rho(x, t|x_0, t_0) \ . \tag{6.11}$$

Expressed in terms of this quantity, the probability to find the particle within the basin of attraction is

$$n(t|t_0, x_0) = \int_{-\infty}^{x_u(t)} dx \ \rho(x, t|x_0, t_0) \ . \tag{6.12}$$

Substituting equation (6.12) into equation (6.10), approximating $n(t|t_0, x_0) = 1$, and making use of equation (6.11), one readily finds (cf. equation (2.14))

$$\Gamma(t) = -D(t) \frac{\partial}{\partial x_u(t)} \rho(x_u(t), t|x_0, t_0) \ . \tag{6.13}$$

As already discussed at the beginning of this section, definition (6.10) of the instantaneous escape rate $\Gamma(t)$ differs from that used by some other authors, e.g., [RD05]. But when considering the time-averaged escape rate[2]

$$\bar{\Gamma} := \lim_{t\to\infty} \frac{1}{t} \int_0^t dt\, \Gamma(t) \; , \tag{6.14}$$

both definitions of $\Gamma(t)$ yield the same $\bar{\Gamma}$. Therefore, as long as only the time-averaged escape rate is experimentally accessible (which is the usual case), both definition can be used equivalently.

6.2.3 Time transformation

We will now show that we can, without loss of generality, assume that the noise strength $D(t)$ in the Langevin equation (6.3) is time-independent.

Let us for this purpose write the noise strength in the form:

$$\begin{aligned} D(t) \quad &=: \quad Dg(t) \; , & (6.15)\\ \lim_{t\to\infty} \frac{1}{t} \int_0^t dt\, g(t) \quad &= \quad 1, \quad g(t) > 0 \; . & (6.16) \end{aligned}$$

Using the fact that $g(t)$ is strictly positive allows us to define an auxiliary time $\hat{t}(t)$ via [Rei02]

$$\hat{t}(t) := \int_0^t dt'\, g(t') \; . \tag{6.17}$$

Now the Langevin equation (6.3) can be written in terms of $\tilde{x}(\hat{t}) := x(t(\hat{t}))$, yielding

$$\dot{\tilde{x}}(\hat{t}) = \tilde{F}\left(\tilde{x}(\hat{t}), \hat{t}\right) + \sqrt{2D}\xi(\hat{t}) \; , \tag{6.18}$$

with $\xi(\hat{t})$ a Gaussian white noise with correlations as in equation (6.2) and

$$\tilde{F}\left(\tilde{x}(\hat{t}), \hat{t}\right) := F(x(t(\hat{t})), t(\hat{t}))/g(t(\hat{t})) \; . \tag{6.19}$$

The problem of an overdamped particle in a time-dependent temperature field can thus be mapped to the case of an overdamped particle in an effective (time-dependent) force field with a time-independent temperature. Hence, from now on we will assume that the noise strength is time-independent. Once we have approximated the instantaneous escape rate $\tilde{\Gamma}(\hat{t})$ for this problem, we can make use of $\tilde{n}(\tilde{t}) = n(t(\tilde{t}))$ so that the escape rate in the original time t immediately follows as

$$\Gamma(t) = \frac{d\hat{t}}{dt} \tilde{\Gamma}(\hat{t}(t)) = g(t)\tilde{\Gamma}(\hat{t}(t)) \; . \tag{6.20}$$

We will come back to the case of time-dependent noise strengths in section 6.7.

---

[2] For time-periodic forces or noise strengths, $\bar{\Gamma}$ is defined as the average over one period $\mathcal{T}$.

6.3 Theoretical framework

The technique of path integration is well developed in the physical [CCR81, Sch81, LRT82, BDKA99, LRH00b, BML$^+$05] and the mathematical literature [Lud75, FW98].[3] In this section we briefly outline the main ingredients of this formalism for the calculation of the transition probability density $\rho(x, t|x_0, t_0)$. We refer to the above mentioned references for further details. In the subsequent sections these concepts will be used to derive approximations for the escape rate.

6.3.1 Notation

In the following, it will often be necessary to explicitly state the dependence of a quantity A or of a function $B(t)$ on the boundary conditions, that means, on the initial and final times and positions. The following notations will be used equally for this purpose:

$$A_{t_0}(t_f) = A_{t_0}(x_f, t_f) = A(x_f, t_f|x_0, t_0) , \tag{6.21}$$

$$B(t) = B_{t_0}(t) = B(t|x_f, t_f, x_0, t_0) . \tag{6.22}$$

The time-average of such a function is defined as

$$\bar{B} := \lim_{t\to\infty} \frac{1}{t} \int_0^t dt'\ B(t') \tag{6.23}$$

for non-periodic force fields and as

$$\bar{B} := \frac{1}{\mathcal{T}} \int_0^{\mathcal{T}} dt'\ B(t') \tag{6.24}$$

for periodic ones.

6.3.2 Path integrals for the transition probability density

The solution of equation (6.11) with initial condition $\rho(x, t_0|x_0, t_0) = \delta(x - x_0)$ and $D(t) = D$ can be formally written as [CCR81, FW98]

$$\rho(x_f, t_f|x_0, t_0) = \int\limits_{\substack{x(t_0)=x_0,\\ x(t_f)=x_f}} \mathfrak{D}x(t)\ e^{-S[x(t)]/D} , \tag{6.25}$$

---

[3] It is interesting to note that it was indeed *not* Feynman who proposed the path integral method first. Gregor Wentzel used a very similar concept in a 1924 paper [Wen24, AL98]. The value of these ideas was not recognized at that time, and the paper was forgotten. Wentzel himself never came back to this idea.

where the integral has to be taken over all paths with $x(t_0) = x_0$ and $x(t_f) = x_f$, and where $\mathfrak{D}x(t)$ denotes the integration measure. In equation (6.25) $S[x(t)]$ denotes the action of the path $x(t)$ (also called the *Onsager-Machlup functional*) and is defined as

$$S[x(t)] := \int_{t_0}^{t_f} dt \; L(x(t), \dot{x}(t), t) \; , \tag{6.26}$$

with Lagrangian

$$L(x, \dot{x}, t) = \frac{1}{4} \left[\dot{x} - F(x,t)\right]^2 \; . \tag{6.27}$$

It should be noted that the path integral (6.25) is mathematically well defined only as a limiting case of the time-discretized dynamics (6.3) with $t_i = t_0 + i\Delta t, i = 1, \ldots, N$ (for details see, e.g., [BDKA99, LRH00b]). In this case, equation (6.25) is a high dimensional integral with appropriately discretized versions of the action (6.26,6.27), and with integration measure $\prod_{i=1}^{N} dx_i (4\pi D \Delta t)^{-N/2}$.[4]

We now consider the case of a small noise strength D. Then, the main contribution to the integral in equation (6.25) stems from those paths that minimize the action. Let us for a moment assume that there exists only one path $x^*(t)$ that globally minimizes S. The more general case will be discussed in section 6.3.3. Paths with a higher action are exponentially suppressed. Therefore, with decreasing noise strength D, transitions become exponentially less probable (unless $S[x^*(t)] = 0$). But, given that the particle reaches x_f at time t_f, it is most likely that it has moved in close vicinity to $x^*(t)$.

As is well known from classical mechanics, the path that extremizes the action satisfies the Euler-Lagrange equation, or equivalently the Hamilton equations [Kuy97, GPS02]:

$$\begin{aligned} \dot{x}^*(t) &= 2p^*(t) + F(x^*(t), t) \; , && (6.28) \\ \dot{p}^*(t) &= -p^*(t) F'(x^*(t), t) \; , && (6.29) \end{aligned}$$

with boundary conditions:

$$x^*(t_0) = x_0, \quad x^*(t_f) = x_f \; . \tag{6.30}$$

Here, $p^*(t)$ can be understood as a generalized momentum and is formally defined via equation (6.28). Exploiting equations (6.26,6.27,6.28), we see that the action of the optimizing path is given by

$$\Phi^*(x_f, t_f | x_0, t_0) := S[x^*(t)] = \int_{t_0}^{t_f} dt \; p^*(t)^2 \; . \tag{6.31}$$

Because the main contribution to the path integral (6.25) stems from trajectories in the vicinity of the optimizing path $x^*(t)$, we can expand the action around this

---

[4] In fact, as discussed in section 2.1, the Gaussian white noise $\xi(t)$ is a mathematical idealization. The Langevin equation (6.3) itself has a tangible meaning only in the limiting case of the time-discretized dynamics.

path and keep only contributions up to second order in $y(t) = x^*(t) - x(t)$. This results in a Gaussian integral which can be easily solved, and we finally end up with [CCR81, LRH00b]

$$\rho(x_f, t_f|x_0, t_0) = \frac{e^{-\Phi^*(x_f,t_f|x_0,t_0)/D}}{\sqrt{4\pi D Q^*(x_f, t_f|x_0, t_0)}} \left[1 + \mathcal{O}(D)\right] . \tag{6.32}$$

This approximation is also called (functional) *saddle point approximation*. The most challenging task consists in finding the appropriate prefactor $Q^*(x_f, t_f|x_0, t_0)$. In [LRH00b] it was shown that $Q^*(x_f, t_f|x_0, t_0) = Q^*(t_f)$ is given by the solution $Q^*(t)$ of the second order linear differential equation:

$$\ddot{Q}^*(t) = 2\frac{d}{dt}\left[Q^*(t)F'(x^*(t), t)\right] - 2Q^*(t)p^*(t)F''(x^*(t), t) , \tag{6.33}$$

with initial condition

$$Q^*(t_0) = 0, \quad \dot{Q}^*(t_0) = 1 . \tag{6.34}$$

It should be noticed that $Q^*(t)$ in equations (6.33,6.34) has to be understood in the sense of $Q^*(t|x_f, t_f, x_0, t_0)$. The initial and final positions enter via the optimizing path in the differential equation (6.33).

In order to calculate the instantaneous escape rate $\Gamma(t)$ according to equation (6.13), we do not only need the transition probability density, but also its derivative with respect to the final coordinate x_f. Therefore, we will now discuss the corresponding derivatives of the action $\Phi^*(x_f, t_f|x_0, t_0)$ and of the prefactor $Q^*(x_f, t_f|x_0, t_0)$ which appear in the saddle point approximation (6.32) of the transition probability density.

In full analogy to classical mechanics one obtains [Kuy97, GPS02]

$$\frac{\partial}{\partial x_f} S\left[x^*(t)\right] = p^*(t_f) . \tag{6.35}$$

The determination of $\partial/\partial x_f Q^*(x_f, t_f|x_0, t_0)$ is slightly more involved. To start with, we consider the path $x^*(t)$ that minimizes the action (6.26,6.27) for the boundary conditions $x^*(t_0) = x_0$ and $x^*(t_f) = x_f$. Analogously, we denote by $\tilde{x}^*(t)$ the optimizing path corresponding to $\tilde{x}^*(t_0) = x_0$ and $\tilde{x}^*(t_f) = x_f + dx_f$, where in comparison to $x^*(t)$ the final position is shifted by an amount dx_f, while both, the initial time and position and the final time, are kept fixed. For sufficiently small dx_f both paths will be in close vicinity to each other for all $t \in [t_0; t_f]$, and we write

$$\tilde{x}^*(t) \quad =: \quad x^*(t) + dx_f \mathcal{D}_x(t) , \tag{6.36}$$

$$\tilde{p}^*(t) \quad =: \quad p^*(t) + dx_f \mathcal{D}_p(t) , \tag{6.37}$$

where $p^*(t)$ and $\tilde{p}^*(t)$ are the momenta corresponding to $x^*(t)$ and $\tilde{x}^*(t)$, respectively. Expanding the force $F\left(\tilde{x}^*(t), t\right)$ and its derivative $F'\left(\tilde{x}^*(t), t\right)$ around $x^*(t)$, i.e.,

$$F\left(\tilde{x}^*(t), t\right) \quad = \quad F\left(x^*(t), t\right) + dx_f \mathcal{D}_x(t) F'\left(x^*(t), t\right) , \tag{6.38}$$

$$F'\left(\tilde{x}^*(t), t\right) \quad = \quad F'\left(x^*(t), t\right) + dx_f \mathcal{D}_x(t) F''\left(x^*(t), t\right) , \tag{6.39}$$

and inserting equations (6.36-6.39) into equations (6.28,6.29) for the optimizing path, one sees that $\mathcal{D}_x(t), \mathcal{D}_p(t)$ solve a set of two coupled first order linear differential equations:

$$\begin{aligned} \dot{\mathcal{D}}_x(t) &= F'(t)\mathcal{D}_x(t) + 2\mathcal{D}_p(t) \ , && (6.40) \\ \dot{\mathcal{D}}_p(t) &= -p^*(t)F''(t)\mathcal{D}_x(t) - F'(t)\mathcal{D}_p(t) \ . && (6.41) \end{aligned}$$

Here we have used the abbreviation $F'(t) := F'\left(x^*(t), t\right)$ and similarly for the higher derivatives. The boundary conditions for this problem are given by $\mathcal{D}_x(t_0) = 0$ and $\mathcal{D}_x(t_f) = 1$. However, as the linear differential equations (6.40,6.41) are homogeneous, one may integrate them with any initial conditions $\mathcal{D}_x(t_0) = 0$ and $\mathcal{D}_p(t_0) = p_0 \neq 0$ and divide the solution by the final value $\mathcal{D}_x(t_f)$. The quantity $\mathcal{D}_p(t_f)$ equals the derivative of the momentum $p^*(t_f)$ with respect to the final position x_f. Hence, we have together with equation (6.35):

$$\frac{\partial^2}{\partial x_f^2} S\left[x^*(t)\right] = \frac{\partial}{\partial x_f} p^*(t_f) = \mathcal{D}_p(t_f) \ . \tag{6.42}$$

In the same line, we can expand $\tilde{Q}^*(t) = \tilde{Q}^*(t|x_f + dx_f, t_f, x_0, t_0)$ in powers of dx_f. To first order we have

$$\tilde{Q}^*(t) = Q^*(t) + dx_f Z^*(t) + \mathcal{O}(dx_f^2) \ . \tag{6.43}$$

Proceeding in the same way for all quantities appearing in the differential equation (6.33) for the prefactor, one finds that $Z^*(t)$ satisfies an inhomogeneous second order linear differential equation. Using the usual abbreviations, this is

$$\frac{1}{2}\ddot{Z}^*(t) - \frac{d}{dt}\left[F'(t)Z^*(t)\right] + p^*(t)F''(t)Z^*(t) = H(t) \ , \tag{6.44}$$

with

$$H(t) = \frac{d}{dt}\left[F''(t)Q^*(t)\mathcal{D}_x(t)\right] - F''(t)Q^*(t)\mathcal{D}_p(t) - p^*(t)F'''(t)Q^*(t)\mathcal{D}_x(t) \ , \tag{6.45}$$

and with initial conditions

$$Z^*(t_0) = 0, \quad \dot{Z}^*(t_0) = 0 \ . \tag{6.46}$$

From (6.43) one can infer that

$$\frac{\partial}{\partial x_f} Q^*(x_f, t_f|x_0, t_0) = Z^*(t_f) \ , \tag{6.47}$$

i.e., once the optimal path $x^*(t)$ is determined via equations (6.28,6.29), one can solve the set of differential equations (6.33,6.40,6.41,6.44) and obtain explicit values for the prefactor and its derivative.

6.3.3 Optimizing paths and limitations

The approximation of the transition probability density, presented in the previous section, in principle applies to arbitrary initial and final positions. Therefore, one might in particular choose $x_f = x_u(t_f)$ and $x_0 = x_s(t_0)$, and approximate $\rho(x_u(t), t|x_0, t_0)$, appearing in equation (6.13) for the instantaneous escape rate, by equation (6.32). This was the basic idea for the approximation in [LRH00a, LRH00b]. However, this approach is limited to moderately strong and moderately fast driving. The reason for this is most easily understood when considering the optimizing paths. As this discussion is necessary in order to motivate and understand our proceeding in section 6.4, we review the main points in the following paragraphs, although they are not new [Col79, WH80, CCR81, BDKA99, LRH00b, BG05, RD06].

Let us first consider our standard example (6.4,6.9): the thermally activated escape from a metastable state in a periodically modulated force field where the modulation is moderately strong and moderately fast. Then there exist, in general, many solutions $x_i^*(t)$ of equations (6.28,6.29), i.e., many paths that (locally) minimize the action functional. For a particular example with finite $t_f - t_0$, figure 6.2(a) shows all optimizing paths. These paths are "typical" for the thermally activated escape in periodically modulated systems [LRH00b, RD06]. They start on the stable orbit $x_s(t)$ at time t_0 and follow it for some time. Then, in a relatively short time window Δt the paths cross to the unstable orbit $x_u(t)$ and stay in its vicinity until time t_f. It is obvious from equations (6.26,6.27) that the deterministic motion does not generate any action. Hence, also the parts of the optimizing path in close vicinity to the periodic orbits contribute little to S. Nearly the whole action is accumulated in the short time Δt in which the particle travels from the stable to the unstable orbit. For not too large driving frequencies $\omega = 2\pi/\mathcal{T}$, this transition strongly synchronizes with the modulation and appears when the energy barrier is lowest, i.e., once per period. All the paths can be characterized with respect to the time at which they travel into the vicinity of the unstable orbit. To be more precise, we can choose some intermediate level x_1 and enumerate the paths in the sequence they cross this level for the first time. We denote these times by t_1^i and use the convention that $x_1^*(t)$ is the optimizing path that travels to $x_u(t)$ at the latest possible time [see figure 6.2(a)].

Summing up the contributions from all paths, a first main result from [LRH00b] was the following approximation of the instantaneous escape rate:

$$\Gamma(t_f) = \sum_i \frac{p_i^*(t_f) e^{-\Phi_i^*(x_f, t_f|x_0, t_0)/D}}{\sqrt{4\pi D Q_i^*(x_f, t_f|x_0, t_0)}} \left[1 + \mathcal{O}(D)\right] , \tag{6.48}$$

where equations (6.13,6.32,6.35) have been used and all contributions of order D are neglected. For any finite $t_f - t_0$ there will be, in general, only one path that globally minimizes the action S. Then, for small noise strengths D, this path will mainly contribute to the sum in equation (6.48). However, in the small noise limit, escape is a rare event so that usually the case $t_f - t_0 \gg \max(\mathcal{T}, \Delta t)$ is considered. One can show that for large indices i, two "neighboring" optimizing path are connected

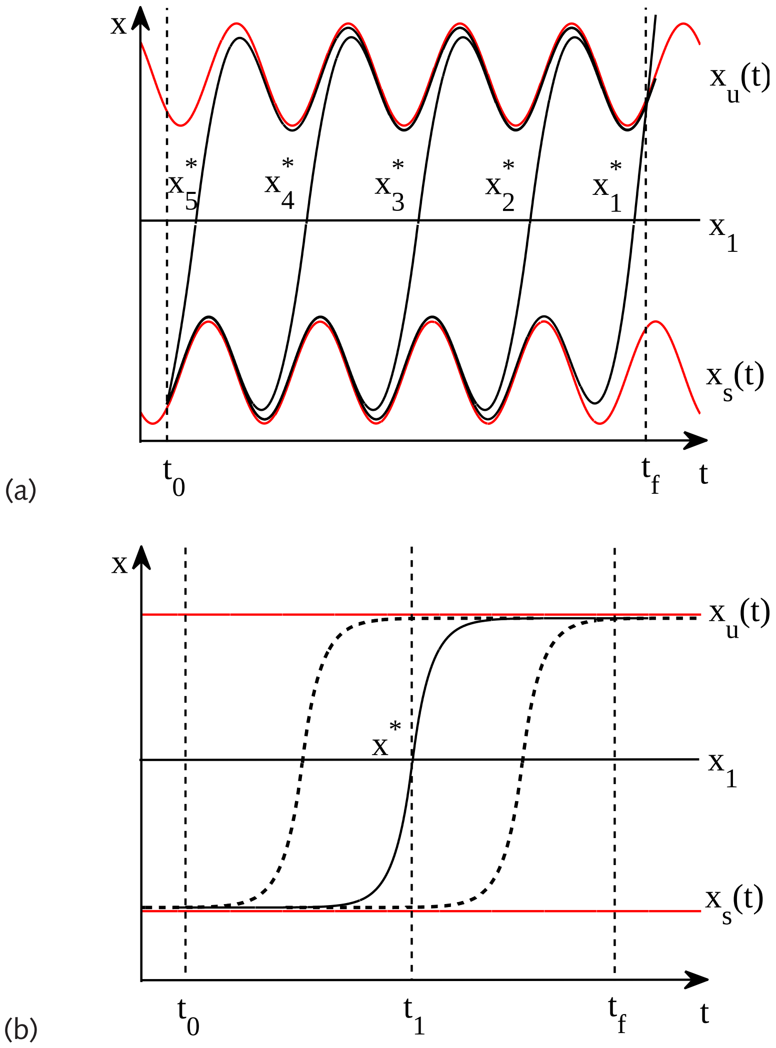

Figure 6.2: (a) Illustration of the escape from a periodically modulated potential. The particle starts on the stable orbit $x_s(t)$ at time t_0 and crosses the unstable orbit $x_u(t)$ at time t_f. The periodic orbits are depicted by the red solid lines and are shifted by a small number for reasons of better visibility. For these boundary conditions, 5 different solutions $x_i^*(t)$, $i = 1, \ldots, 5$ of equations (6.28,6.29) exist (one for each period of the driving). They correspond to local minima of the action (6.26) and are shown as black solid lines. For this illustration the piecewise parabolic potential $U(x)$ from equation (6.157) with an additive sinusoidal driving force $f(t) = A\sin(\omega t)$ has been used. For the same potential $U(x)$ and the same initial and final times, (b) shows the case of a vanishing driving force $f(t) = 0$. Only one optimizing path $x^*(t)$ (black solid line) exists. The dashed lines are approximate solutions of equations (6.28,6.29) which arise from $x^*(t)$ by a translation in time.

by a translation in time by $\mathcal{T}$, i.e., $x_i^*(t) = x_{i+1}^*(t - \mathcal{T})$ for $i \to \infty$. Without going into details, we note that this fact has been used in [LRH00b] in order to further approximate $\Gamma(t_f)$ in (6.48).

Let us now turn to the case of a static force field $F(x,t) = F(x)$ which is discussed in [WH80, CCR81] (see also section 6.5). As shown for an example in figure 6.2(b), in general, a unique optimizing path $x^*(t)$ exists. Qualitatively it is very similar to the optimizing paths from figure 6.2(a). Usually, one refers to such a trajectory as an *instanton*. For a constant force, equations (6.28,6.29) simplify to $d/dt[\dot{x}^*(t)^2 + F(x^*(t))^2] = 0$. In the limit $t_f - t_0 \to \infty$ the only solution of this equation is given by $\dot{x}^*(t) = -F(x^*(t))$, i.e., the optimizing path is the time-reversed deterministic motion. Exploiting the fact that equations (6.28,6.29) are invariant under a time translation, we see that for any τ the trajectory $x^*(t+\tau)$ [dashed lines in figure 6.2(b)] is an optimizing path, too. Given that $t_f - (t_1 + \tau)$ is large, it satisfies the same boundary conditions as $x^*(t)$, up to exponentially small corrections [CCR81] (see also section 6.4.3). However, again all the paths arising from $x^*(t)$ by a time translation can be uniquely characterized by the time t_1 at which they cross the intermediate level x_1. As a consequence of this continuous time translation symmetry, the Gaussian approximation to the full path integral (6.25) breaks down (the order D corrections become very large) so that no approximation of the form (6.48) applies to the escape rate in this case. The same is true for adiabatically slow, very fast, or very weak modulations [LRH00b].

Hence, approximation (6.48) applies only to a limited interval of modulation frequencies ω, whereas a completely different treatment is necessary for other frequencies. A further complication is that the interval of frequencies, for which equation (6.48) can be used, is usually not known. In the following section we develop an approximation to the rate which can be applied to the whole range of modulation frequencies from zero to ∞. This approximation can be considered as a generalization of the the result from [LRH00b]. The sum over the contributions to the path integral (6.25) is replaced by an integral over the time at which an intermediate level is crossed for the first time. A motivation, that this proceeding is reasonable, is our above observation: In periodically modulated systems as well as in static systems the main contributions to the path integral (that with lowest action) can be characterized by this time.

Before continuing, we point out that the appearance of the continuous time translation symmetry results from the fact that both, the initial and the final coordinate, lie on the stable or on the unstable orbit, and that the movement in close vicinity to these orbits does not accumulate any action, as can be inferred from equations (6.26,6.27). In contrast, if the initial or/and final coordinate does not lie on such an orbit, the symmetry breaks down and the saddle point approximation applies.

6.4 A new path integral approach to the escape problem

We now come to the central section of this chapter and introduce an approximation for the instantaneous escape rate that applies to arbitrary modulation frequencies[5] ω and to the whole range of modulation strength, from no modulation to moderately strong modulation. Only the case of very strong driving has to be excluded. In section 6.4.2 the term "moderately strong" will be quantified.

6.4.1 Renewal approach

Let us again consider the Langevin equation (6.3) and (6.18), respectively, for our present problem. For every realization of the noise $\xi(t)$ and every initial condition $x(t_0) = x_0$ the solution of this equation is continuous. That means, a particle starting at x_0 at time t_0 and reaching the position x_f at time t_f, has crossed every level x_1 with $x_0 < x_1 < x_f$ at least one time. We denote by R_1 the time at which the level is crossed for the first time, or to be more specific $R_1 := \inf(\{t\}|x(t) = x_1)$. The corresponding probability density $\Psi(x_1, t_1|x_0, t_0)$ is called *first passage time density*, so that

$$\text{Prob}\,(R_1 \in [t_1\,;\, t_1 + dt]) = \Psi(x_1, t_1|x_0, t_0)dt \tag{6.49}$$

is the probability that the level x_1 is crossed in an interval dt around t_1 for the first time [Red01].

We know from the Markovian nature of our problem that the probability that the particle reaches x_f at time t_f, provided that it was at position x_1 at time t_1, depends solely on the initial and final times and positions, but not on the history of the process. This allows us to rewrite the transition probability $\rho(x_f, t_f|x_0, t_0)$ as

$$\rho(x_f, t_f|x_0, t_0) = \int_{t_0}^{t_f} dt_1\ \Psi(x_1, t_1|x_0, t_0)\rho(x_f, t_f|x_1, t_1)\ , \tag{6.50}$$

with $x_0 < x_1 < x_f$ a priori arbitrary.

From now on we will always denote by x_0 an initial position on the stable orbit and by x_f a final position on the unstable orbit, i.e.,

$$x_0 = x(t_0) = x_s(t_0), \quad x_f = x(t_f) = x_u(t_f)\ . \tag{6.51}$$

Using equations (6.13,6.50), we get

$$\Gamma(t_f) = -D \int_{t_0}^{t_f} dt_1\ \Psi(x_1, t_1|x_0, t_0)\frac{\partial\rho(x_f, t_f|x_1, t_1)}{\partial x_f}\ . \tag{6.52}$$

For any $x_0 < x_1 < x_f$ this is still an exact equation for the instantaneous escape rate. Now the main idea of our proceeding is to approximate both, $\Psi(x_1, t_1|x_0, t_0)$ and $\partial/\partial x_f \rho(x_f, t_f|x_1, t_1)$, in terms of the optimizing paths with the corresponding

---

[5] That means, the force field is allowed to have contributions of arbitrary frequency.

boundary conditions. As we have already discussed at the end of section 6.3.3, for not too strong modulations, in general, a unique path exists that globally minimizes the action S, provided that x_1 is for all times "sufficiently" far away from the stable and unstable orbit.[6]

For such a level x_1 we can use approximation (6.32) together with equations (6.35,6.47) and get

$$\frac{\partial}{\partial x_f}\rho(x_f,t_f|x_1,t_1) = \left(p^*_{t_1}(t_f) + \frac{DZ^*_{t_1}(t_f)}{2Q^*_{t_1}(t_f)}\right)\frac{e^{-\Phi^*_{t_1}(t_f)/D}}{\sqrt{4\pi DQ^*_{t_1}(t_f)}}\left[1+\mathcal{O}(D)\right] \tag{6.53}$$

and hence

$$\begin{aligned}
\Gamma(t_f) &= \Gamma_0(t_f) + \Gamma_1(t_f) + \Gamma_0(t_f) * \mathcal{O}(D)\ , &(6.54)\\
\Gamma_0(t_f) &= \int_{t_0}^{t_f} dt_1\ \Psi_{t_0}(x_1,t_1)\frac{p^*_{t_1}(t_f)e^{-\Phi^*_{t_1}(t_f)/D}}{\sqrt{4\pi DQ^*_{t_1}(t_f)}}\ , &(6.55)\\
\Gamma_1(t_f) &= \int_{t_0}^{t_f} dt_1\ \Psi_{t_0}(x_1,t_1)\frac{DZ^*_{t_1}(t_f)e^{-\Phi^*_{t_1}(t_f)/D}}{2Q^*_{t_1}(t_f)\sqrt{4\pi DQ^*_{t_1}(t_f)}}\ , &(6.56)
\end{aligned}$$

where the notation introduced in section 6.3.1 has been used. Here, the neglected terms of order D arise from the saddle point approximation (6.32). The integrand of $\Gamma_1(t_f)$ is of the same order in the noise strength D. However, we will show in section 6.4.4 that, for any finite noise strength, $DZ^*_{t_1}(t_f)/Q^*_{t_1}(t_f)$ becomes large compared to the final momentum $p^*_{t_1}(t_f)$ for some t_1 appearing in the integral. Including the first correction $\Gamma_1(t_f)$, thus improves approximation (6.54), in general. This will later be discussed and demonstrated. In the next section, we derive an approximation for the first passage time density $\Psi_{t_0}(x_1,t_1)$. As all other quantities can be calculated as described in section 6.3.2, equations (6.54,6.55,6.56) provide an approximation for the instantaneous escape rate which can be applied to a wide range of modulation strengths and the whole range of driving frequencies, provided that the noise strength is small. These equations are the first main result of this chapter.

We note that in [BG04], Berglund and Gentz have used a similar renewal approach to derive an approximation for the instantaneous escape rate. However, their approach was limited to a pulsed, piecewise parabolic potential and was not based on the path integral formalism. Furthermore, their main aim was to mathematically rigorously approximate the escape rate for moderately strong and moderately fast driving as it was done in [LRH00b]. Hence, this work goes beyond the results of [BG04] and has a different aim, namely, to find an approximation to the rate which works for arbitrary modulation frequencies.

---

[6] For very strong *and* fast modulation several optimizing paths can exist. Then one has to sum over their contributions.

6.4.2 Approximation of the first passage time density

The problem of finding analytical expressions for the first passage time density $\Psi_{t_0}(x_1, t_1)$ is an unsolved problem, even for simple stochastic processes, like the Ornstein-Uhlenbeck process, if time-dependent forces and absorbing boundaries are involved. A great deal of work has already been done to find approximations to this quantity for various different systems [Dur85, DW92, STH04, STH05]. However, to the best of our knowledge none of them can be applied to arbitrary time-dependent force fields. Here we propose an approximation scheme which can be applied under the same conditions as the saddle point approximation (6.32).

The first passage time density $\Psi_{t_0}(x_1, t_1)$ can be obtained by solving the Fokker-Planck equation (6.11) for an absorbing boundary at x_1. Then, $\Psi_{t_0}(x_1, t_1)$ is the flux of probability over this boundary. However, in general equation (6.11) cannot be solved in closed form for others than free boundary conditions. Thus, casting the problem to one with free boundary conditions, would be a great simplification.

Equation (6.50) provides one possibility for such an approach. Let us consider this equation for $y = x_1 + \epsilon$ with $\epsilon > 0$ small:

$$\rho(y, t|x_0, t_0) = \int_{t_0}^{t} dt_1 \; \Psi_{t_0}(x_1, t_1)\rho(y, t|x_1, t_1) \; . \tag{6.57}$$

This is an integral equation for $\Psi_{t_0}(x_1, t_1)$. Following the discussion in the previous section, the left-hand side of this equation can be approximated by the saddle point approximation (6.32). Next, let us look at the propagator $\rho(y, t|x_1, t_1)$. This can be calculated by solving the Langevin equation (6.3) with $x(t_1) = x_1$ (or equivalently by solving the corresponding Fokker-Planck equation). We denote by $X_{t_1}(t)$ the solution of the corresponding deterministic equation (6.5) for the same initial condition $X_{t_1}(t_1) = x_1$. Intuitively, it is clear that for small ϵ the transition probability as a function of $t - t_1$ (and fixed t) will at first rapidly grow. Then, with further increasing $t - t_1$, the particle will most likely follow $X_{t_1}(t)$ and relax to the stable orbit so that transitions to $y = x_1 + \epsilon$ become less and less probable. For $t - t_1 \gtrsim \tau_R$ we finally have $\rho(y, t|x_1, t_1) \approx \rho(y, t|x_0, t_0)$. Contributions from these times will be neglected in the following.[7] Hence, the lower integration limit in (6.57) can be replaced by $t - \tau_R$. Because the largest contributions to (6.57) stem from times t_1 near t, we can, furthermore, approximate $\rho(y, t|x_1, t_1)$ by a short-time propagator. One possible technique for finding approximate propagators for the case of small noise strengths (which we are dealing with) was suggested by van Kampen [Kam03]. It consists in introducing a new variable $\vartheta(t)$ via

$$x(t) = X_{t_1}(t) + \sqrt{D}\vartheta(t), \quad \vartheta(t_1) = 0 \; . \tag{6.58}$$

---

[7] The paths that cross x_1 at some time t_1 for the first time and reach $x_1 + \epsilon$ at time $t \gg t_1$ have an action much larger than the action of the paths that spend most of the time in close vicinity to the stable orbit and then directly travel to $x_1 + \epsilon$. Thus, their contribution to the path integral (6.25) is exponentially suppressed, for small noise strengths D.

For this variable the Langevin equation reads

$$\dot{\vartheta}(t) = a(t)\vartheta(t) + \sqrt{2}\xi(t), \quad a(t) := F'(X_{t_1}(t), t)\ , \tag{6.59}$$

where terms of order $D^{1/2}$ are neglected. We assume $a(t) \leq 0$ for all $t > t_1$ to guarantee stability of the solution. The Fokker-Planck equation corresponding to (6.59) is that of an Ornstein-Uhlenbeck process:

$$\frac{\partial}{\partial t}\tilde{\rho}(\vartheta, t|0, t_1) = \frac{\partial}{\partial \vartheta}\left(-a(t)\vartheta + \frac{\partial}{\partial \vartheta}\right)\tilde{\rho}(\vartheta, t|0, t_1)\ . \tag{6.60}$$

Its solution is readily found to be Gaussian with zero mean and standard deviation:

$$\sigma^2_{t_1}(t) \;=\; 2\int_{t_1}^{t} dt'\; e^{2L(t,t')}\ , \tag{6.61}$$

$$L(t, t') \;=\; \int_{t'}^{t} dt''\; a(t'')\ . \tag{6.62}$$

As ϑ is connected to our original variable x via the deterministic equation (6.58), the approximation for the desired transition probability follows as

$$\rho(y, t|x_1, t_1) \approx \left|\frac{d\vartheta}{dx}\right| \tilde{\rho}(\vartheta, t|0, t_1) = \frac{1}{\sqrt{2\pi D\sigma^2_{t_1}(t)}} \exp\left(-\frac{(y - X_{t_1}(t))^2}{2D\sigma^2_{t_1}(t)}\right)\ . \tag{6.63}$$

In [GW93] it was shown that this approximation is usually good for sufficiently small times and noise strengths. We note that more involved approximations for the short time propagator exist, e.g., [Dro95]. These, however, often do not apply to explicitly time-dependent force fields, or have to be adjusted to every force field separately. We, therefore, use the simple approximation (6.63) which is usually good enough for our purposes.

We now replace the left-hand side of equation (6.57) by the saddle point approximation (6.32) and the propagator under the integral on the right-hand side by equation (6.63), thus:

$$\frac{e^{-\Phi^*_{t_0}(y,t)/D}}{\sqrt{4\pi D Q^*_{t_0}(y, t)}} = \int\limits_{t-\tau_R}^{t} dt_1\; \Psi_{t_0}(x_1, t_1) \frac{\exp\left(-\frac{(y - X_{t_1}(t))^2}{2D\sigma^2_{t_1}(t)}\right)}{\sqrt{2\pi D\sigma^2_{t_1}(t)}}\ . \tag{6.64}$$

This equality only holds approximately, but should be very good for small noise strengths. Closely following the proceeding in [DW92], we apply the operator $-D\partial/\partial y$ to both sides of equation (6.64) with the result:

$$LHS \;=\; \frac{p^*_{t_0}(y, t)e^{-\Phi^*_{t_0}(y,t)/D}}{\sqrt{4\pi D Q^*_{t_0}(y, t)}}\ , \tag{6.65}$$

$$RHS \;=\; \int\limits_{t-\tau_R}^{t} dt_1\; \Psi_{t_0}(x_1, t_1) \frac{y - X_{t_1}(t)}{\sigma^2_{t_1}(t)} \frac{e^{-\frac{(y - X_{t_1}(t))^2}{2D\sigma^2_{t_1}(t)}}}{\sqrt{2\pi D\sigma^2_{t_1}(t)}}\ , \tag{6.66}$$

where LHS stands for the left-hand side of the resulting equation and RHS for the right-hand side, respectively. On the left-hand side the term proportional to $DZ^*_{t_0}(y,t)/Q^*_{t_0}(y,t)$ has been neglected. It is clear that this can be done for small noise strengths D if $Z^*_{t_0}(y,t)/Q^*_{t_0}(y,t)$ is bounded. This will be discussed in more detail in sections 6.4.3 and 6.4.4.

We next consider the limit $y \to x_1$. As all quantities appearing on the left-hand side are continuous in y, it obviously follows

$$\lim_{y \searrow x_1} LHS = \frac{p^*_{t_0}(x_1,t)e^{-\Phi^*_{t_0}(x_1,t)/D}}{\sqrt{4\pi D Q^*_{t_0}(x_1,t)}} = p^*_{t_0}(x_1,t)\rho(x_1,t|x_0,t_0) \; . \tag{6.67}$$

Taking the corresponding limit of the right-hand side is much more involved. The argument of the exponential function in equation (6.66) converges for $t_1 \to t$ towards zero, if $y = x_1$, whereas it diverges to $-\infty$ for every $y \neq x_1$. Hence, equation (6.66) is only valid for $y > x_1$. For $y = x_1$ integration and differentiation do not commute in this simple way, and we have to be more careful when considering the limit $y \to x_1$. In full analogy to the appendix of [DW92] we first split the integral in (6.66) into two parts:

$$RHS = \int_{t-\tau_R}^{t-\delta} dt_1 \; \cdots + \int_{t-\delta}^{t} dt_1 \; \cdots := I_1(y,\delta) + I_2(y,\delta) \; . \tag{6.68}$$

For every $\delta > 0$ all quantities under the integral $I_1(y,\delta)$ remain finite in the limit $y \to x_1$. Hence,

$$\lim_{\delta \searrow 0} \lim_{y \searrow x_1} I_1(y,\delta) = \int\limits_{t-\tau_R}^{t} dt_1 \; \Psi_{t_0}(x_1,t_1) \frac{x_1 - X_{t_1}(t)}{\sigma^2_{t_1}(t)} \frac{e^{-\frac{(x_1 - X_{t_1}(t))^2}{2D\sigma^2_{t_1}(t)}}}{\sqrt{2\pi D \sigma^2_{t_1}(t)}} \; . \tag{6.69}$$

Turning to the integral $I_2(y,\delta)$, we first note that

$$\sigma^2_{t_1}(t) = 2(t - t_1) + \mathcal{O}(\delta^2) \; . \tag{6.70}$$

Because δ can be chosen arbitrarily small, terms of order δ^2 are neglected without loss of generality. Substituting $s = 2Dt_1$ and defining $t' = 2Dt$ and $\delta' = 2D\delta$, we arrive at

$$I_2(y,\delta) = \frac{1}{2} \int\limits_{t'-\delta'}^{t'} ds \; \tilde{\Psi}_{t_0}(x_1,s) \frac{y - \tilde{X}_s(t')}{t' - s} \frac{e^{-\frac{(y - \tilde{X}_s(t'))^2}{2(t'-s)}}}{\sqrt{2\pi(t'-s)}} \; , \tag{6.71}$$

with $\tilde{\Psi}_{t_0}(x_1,s) := \Psi_{t_0}(x_1,s/2D)$ and $\tilde{X}_s(t') := X_{s/2D}(t'/2D)$. One can show that the limit $\delta \to 0$, $y \to x_1$ of $I_2(y,\delta)$ exists and is given by (details are given in appendix B.1, see also [DW92])

$$\lim_{\delta \searrow 0} \lim_{y \searrow x_1} I_2(y,\delta) = \frac{1}{2}\Psi_{t_0}(x_1,t) \; . \tag{6.72}$$

We can now combine equations (6.64-6.69,6.72) with the result:

$$p^*_{t_0}(t)\rho(x_1,t|x_0,t_0) = \frac{1}{2}\Psi_{t_0}(x_1,t) + \int\limits_{t-\tau_R}^{t} dt_1\ \Psi_{t_0}(x_1,t_1)\frac{x_1 - X_{t_1}(t)}{\sigma^2_{t_1}(t)}\frac{e^{-\frac{(x_1-X_{t_1}(t))^2}{2D\sigma^2_{t_1}(t)}}}{\sqrt{2\pi D\sigma^2_{t_1}(t)}}\ . \quad (6.73)$$

Bringing the integral in equation (6.73) to the left-hand side, multiplying by 2, and adding a zero in the form $F\rho - F\rho$, we finally arrive at

$$\Psi_{t_0}(x_1,t) \ = \ \dot{x}^*_{t_0}(t)\rho(x_1,t|x_0,t_0) \ + \ \Psi^{rest}_{t_0}(x_1,t)\ , \quad (6.74)$$

$$\Psi^{rest}_{t_0}(x_1,t) \ = \ \int\limits_{t-\tau_R}^{t} dt_1\ \Psi_{t_0}(x_1,t_1)\left[\frac{2(X_{t_1}(t)-x_1)}{\sigma^2_{t_1}(t)} - F(x_1,t)\right]\frac{e^{-\frac{(x_1-X_{t_1}(t))^2}{2D\sigma^2_{t_1}(t)}}}{\sqrt{2\pi D\sigma^2_{t_1}(t)}}\ , \quad (6.75)$$

where $\dot{x}^*_{t_0}(t) = 2p^*_{t_0}(t) + F(x_1,t)$ is the velocity of a particle following the optimal path at the moment it crosses the level x_1. This equation allows to determine the first passage time density $\Psi_{t_0}(x_1,t)$ iteratively:

$$\Psi_{t_0}(x_1,t) = \dot{x}^*_{t_0}(t)\rho(x_1,t|x_0,t_0) + \sum_{i=1}^{\infty}\Psi^i_{t_0}(x_1,t)\ . \quad (6.76)$$

Up to small errors, which result from the approximations (6.32,6.63) and should become negligible in the small noise limit, this equation is exact (provided that the series converges). We will now discuss that, for a continuous and not too strong modulation of the force field, already the zeroth order approximation

$$\Psi_{t_0}(x_1,t) \approx \dot{x}^*_{t_0}(t)\rho(x_1,t|x_0,t_0) \quad (6.77)$$

is very good. To see this, we consider the first correction to $\Psi_{t_0}(x_1,t)$, namely

$$\Psi^1_{t_0}(x_1,t) = \int\limits_{t-\tau_R}^{t} dt_1\ \dot{x}^*_{t_0}(t_1)\rho(x_1,t_1|x_0,t_0)\left[\frac{2(X_{t_1}(t)-x_1)}{\sigma^2_{t_1}(t)} - F(x_1,t)\right]\frac{e^{-\frac{(x_1-X_{t_1}(t))^2}{2D\sigma^2_{t_1}(t)}}}{\sqrt{2\pi D\sigma^2_{t_1}(t)}}\ . \quad (6.78)$$

If we assume that $Q^*_{t_0}(x_1,t)$ in equation (6.67) is bounded from below by $Q^*_{t_0,min} > 0$ and from above by $Q^*_{t_0,max}$, we can estimate[8]

$$\rho(x_1,t_1|x_0,t_0) \le \sqrt{\frac{Q^*_{t_0,max}}{Q^*_{t_0,min}}}e^{\Delta\Phi^*(t,t_1)/D}\rho(x_1,t|x_0,t_0)\ , \quad (6.79)$$

---

[8] In fact, a negative prefactor would imply that the solution $x^*(t), p^*(t)$ of equations (6.28,6.29) does not minimize the action S, but rather corresponds to a saddle point or a maximum. In this case, the saddle point approximation itself is not applicable. Our discussions in sections 6.4.3 and 6.4.4 will show that the prefactor is usually also bounded from above.

where $\Delta\Phi^*(t,t_1) = \Phi^*_{t_0}(x_1,t) - \Phi^*_{t_0}(x_1,t_1)$ is the difference of the action. Because, usually, $\dot{x}^*_{t_0}(t_1)$ will also be bounded, one can conclude that the first correction is small compared to the zeroth order approximation (6.77) if the following integral is small:

$$\int\limits_{t-\tau_R}^{t} dt_1 \, \left[\frac{2(X_{t_1}(t)-x_1)}{\sigma^2_{t_1}(t)} - F(x_1,t)\right] \frac{\exp\left(-\frac{1}{D}\left[\frac{(x_1-X_{t_1}(t))^2}{2\sigma^2_{t_1}(t)} - \Delta\Phi^*(t,t_1)\right]\right)}{\sqrt{2\pi D\sigma^2_{t_1}(t)}} \,. \tag{6.80}$$

For not too strong modulations, the argument of the exponential function is a monotonically decreasing function of $t-t_1$. The main contribution to the integral, thus, stems from times t_1 near the upper bound t. At the same time, the term in the squared brackets in front of the exponential function vanishes at $t_1 = t$ and increases approximately linearly for small $t-t_1$. Hence, the zeroth order approximation will be, in general, very good for small noise strengths and not too strong driving. In appendix B.2 a more rigorous result will be derived under some additional constraints for a piecewise linear potential. Employing some further assumptions about the modulation strength, it can be shown that for this potential already the first order correction is of the same order in D as the terms neglected in the saddle point approximation (6.32) which has been used in order to obtain approximation (6.74) for the first passage time density. A similar behavior can be expected for other potentials, although a rigorous proof is at the moment not available.

From a practical point of view, the easiest possibility to check whether the zeroth order approximation is sufficient, is to evaluate the integral (6.78) and to compare it to the zeroth order approximation. An explicit example is shown in figure 6.3. For a cubic potential with additive sinusoidal driving, equations (6.77) and (6.78) are evaluated for various modulation frequencies. In all cases the zeroth order approximation is very good. In fact, the first correction (6.78) improves the approximation only for large modulation frequencies. The reason for this behavior should be that the errors, resulting from the two approximations in (6.64), are of the same order of magnitude as $\Psi^1_{t_0}(x_1,t)$. For all studied cases the zeroth order approximation indeed converges to the exact result for $D \to 0$.

We finish this section with some remarks. Firstly, for static potentials approximation (6.77) reproduces a well known result from transition state theory [HTB90]. This case will be discussed in more detail in section 6.5. Secondly, it should be noticed that equation (6.77) is intuitively clear. The flux of probability over the boundary x_1 equals the density of particles at this level, times a "characteristic" velocity. However, as we have seen, the proof of this intuitive result is rather involved. Equations (6.74,6.77) are the second main result of this chapter. Together with equations (6.54-6.56) they allow us to approximate the instantaneous escape rate $\Gamma(t)$ for arbitrary modulation frequencies. Finally, if there exist more than one optimizing path, one has to sum over their contributions in approximation (6.77).

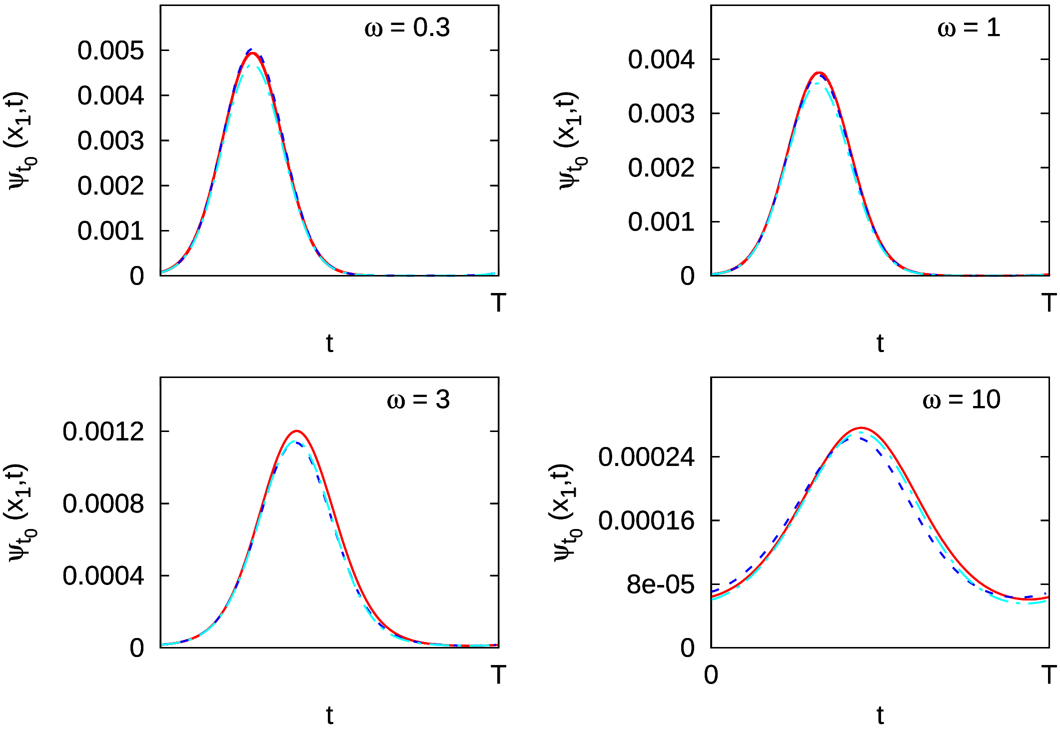

Figure 6.3: First passage time density for the modulated cubic potential $V(x,t) = -a/3\,x^3 + b/2\,x^2 - A\sin(\omega t)x$ which is also used in section 6.6.4. All shown curves were obtained for the parameters: $a = 1.78$, $b = 2.67$, $A = 0.3$, and $D = 0.05$. The absorbing boundary was placed at $x_1 = 0.75$ (the inflection point of the un-modulated potential), and the driving frequency was varied from $\omega = 0.3$ (top left figure) to $\omega = 10.0$ (bottom right figure). The zeroth order approximation (6.77) is shown as the blue dashed line, the approximation including the first order correction (6.78) as the green dashed-dotted line, whereas the red solid line shows the first passage time density obtained from numerically solving the Fokker-Planck equation (6.11) with appropriate boundary conditions.

6.4.3 Behavior of the optimizing paths in vicinity of the stable and unstable orbit

In the previous sections we have derived equations for all quantities appearing in approximation (6.54-6.56) for the escape rate. Next, we want to discuss how these quantities depend on t_1 for a fixed final time t_f and a fixed reference level x_1. For this purpose, we first have to consider the behavior of the optimizing paths in the vicinity of the stable and unstable orbit. In this region we can expand the force around these orbits:

$$F(x^*(t),t) = F(x_{s,u}(t),t) + \lambda_{s,u}(t)\Delta x_{s,u}(t) \ , \tag{6.81}$$

with $\lambda_{s,u}(t)$ defined in equation (6.8). Here and in the following we set

$$\Delta x_{s,u}(t) := x^*(t) - x_{s,u}(t) \ . \tag{6.82}$$

The derivatives of the force field are expanded in the same way.

In this approximation the Hamiltonian equations (6.28,6.29) for the optimizing paths become

$$\begin{aligned} \Delta\dot{x}_{s,u}(t) &= 2p^*(t) + \lambda_{s,u}(t)\Delta x_{s,u}(t) \ , &(6.83)\\ \dot{p}^*(t) &= -\lambda_{s,u}(t)p^*(t) \ . &(6.84) \end{aligned}$$

These equations are equivalent to equations (6.40,6.41) for two infinitesimally neighboring paths. However, as the momentum of a particle following exactly one of the orbits vanishes, the term proportional to $F''(x_{s,u}(t),t)$ is dropped out. The solutions of equations (6.83,6.84) are

$$\begin{aligned} \Delta x_{s,u}(t) &= \Delta x_{s,u}(\tilde{t})e^{\Lambda_{s,u}(t,\tilde{t})} + p^*(t)I_{s,u}(t,\tilde{t}) \ , &(6.85)\\ p^*(t) &= p^*(\tilde{t})e^{-\Lambda_{s,u}(t,\tilde{t})} \ , &(6.86) \end{aligned}$$

with

$$\begin{aligned} \Lambda_{s,u}(t,\tilde{t}) &:= \int_{\tilde{t}}^{t} dt' \ \lambda_{s,u}(t') \ , &(6.87)\\ I_{s,u}(t,\tilde{t}) &:= 2\int_{\tilde{t}}^{t} dt' \ e^{2\Lambda_{s,u}(t,t')} \ , &(6.88) \end{aligned}$$

and with $\tilde{t}$ an arbitrary reference time. It is not surprising that the expressions in (6.87,6.88) are equivalent to those in (6.61,6.62). In both cases a particle in a quadratic potential was considered.

Turning to the movement in the vicinity of the unstable orbit, equations (6.85,6.86) determine the full solution in terms of the two parameters $\Delta x_u(\tilde{t})$ and $p^*(\tilde{t})$. We can use the boundary condition $x^*(t_f) = x_u(t_f)$ to eliminate one of them. As the reference time $\tilde{t}$ is arbitrary, we can choose $\tilde{t} = t_f$ with the result:

$$\Delta x_u(t) = p^*(t)I_u(t,t_f) = p^*(t_f)e^{-\Lambda_u(t,t_f)}I_u(t,t_f) \ . \tag{6.89}$$

This equation is valid for all $t \leq t_f$ for which the optimal path is close to the unstable orbit. Let us denote by t_u the time at which the particle enters the neighborhood of this orbit so that equations (6.83,6.84) apply for all $t_u \leq t \leq t_f$. Then, by dividing (6.89) by the same identity evaluated at t_u, we arrive at

$$\Delta x_u(t) = \Delta x_u(t_u) e^{-\Lambda_u(t,t_u)} \frac{I_u(t,t_f)}{I_u(t_u,t_f)} , \tag{6.90}$$

$$p^*(t) = \Delta x_u(t_u) e^{-\Lambda_u(t,t_u)} \frac{1}{I_u(t_u,t_f)} . \tag{6.91}$$

One can infer from assumptions (6.7,6.8) that $\Lambda_u(t,t_u)$ is, for a fixed time t_u and sufficiently large $t - t_u$, a monotonically increasing function of t and can be approximated by

$$\Lambda_u(t,t_u) \approx \lambda_u(t - t_u) . \tag{6.92}$$

From this behavior one readily sees that $I_u(t_u,t_f)$ converges for $t_f \to \infty$ towards a finite value

$$I_u(t_u) := -\lim_{t_f \to \infty} I_u(t_u,t_f) > 0 . \tag{6.93}$$

For a periodically modulated force field, $I_u(t_u)$ is also periodic in t_u with period $\mathcal{T}$. Hence, we see from equations (6.90,6.91) that both, $|\Delta x_u(t)|$ and $p^*(t)$, decrease exponentially with the time the particle spends in the neighborhood of the unstable orbit. In the case of $\Delta x_u(t)$ this is of course only true as long as also $t_f - t$ is large.

In full analogy one finds for the movement in vicinity of the stable orbit

$$\Delta x_s(t) = \Delta x_s(t_s) e^{-\Lambda_s(t,t_s)} \frac{I_s(t,t_0)}{I_s(t_s,t_0)} , \tag{6.94}$$

$$p^*(t) = \Delta x_s(t_s) e^{-\Lambda_s(t,t_s)} \frac{1}{I_s(t_s,t_0)} , \tag{6.95}$$

where t_s denotes the time at which the neighborhood of the stable orbit is left. Here $I_s(t_s,t_0)$ converges for $t_0 \to -\infty$ towards

$$I_s(t_s) := \lim_{t_0 \to -\infty} I_s(t_s,t_0) . \tag{6.96}$$

Again, for periodic force fields this quantity becomes periodic in t_s. Analogously to equation (6.92) we have $\Lambda_s(t,t_s) \approx -\lambda_s(t_s - t)$ for large $t_s - t$. Hence, equations (6.94,6.95) are dominated by exponentially increasing factors $\exp(\lambda_s(t_s - t))$.

6.4.4 Asymptotics of the integrand

In this section we discuss the asymptotical behavior of the quantities in the approximation (6.54-6.56) for the rate in the case of periodically modulated force fields. For other force fields the asymptotical behavior will be qualitatively the same, but for rigorous estimates more assumptions about the force field, than applied in section 6.2.1, are necessary.

For periodically modulated systems it is clear that in the considered limit $t_0 \to -\infty$ the first passage time density $\Psi_{t_0}(x_1, t_1)$ becomes a periodic function of t_1. Also the action of the path, starting at x_1 at time t_1, and crossing the unstable orbit at time t_f, is invariant under a translation of time by $\mathcal{T}$, i.e.,

$$\Phi^*_{t_1}(t_f) = \Phi^*_{t_1+\mathcal{T}}(t_f + \mathcal{T}) \; . \tag{6.97}$$

It is further well known that for a fixed time t_1 the action of the globally minimizing path is a monotonically decreasing function of the final time t_f.[9] Together with equation (6.97) and the fact that the action is always positive, it follows that also $\Phi^*_{t_1}(t_f)$ converges to a t_1 periodic function

$$\Phi^\infty(t_1) := \lim_{(t_f - t_1)\to\infty} \Phi^*_{t_1}(t_f) \; . \tag{6.98}$$

Turning to the momentum $p^*_{t_1}(t_f)$ of the optimizing path at the moment it crosses the unstable orbit, we can infer from equations (6.91) and (6.93) that it is an exponentially decreasing function of the time $t_f - t_u$, the path spends in the vicinity of the unstable orbit. As the time needed to travel from the reference level x_1 into the vicinity of the unstable orbit is negligible for large $t_f - t_1$, it follows that

$$p^*_{t_1}(t_f) \sim e^{-\Lambda_u(t_f, t_1)} \; . \tag{6.99}$$

Next, we consider the prefactor $Q^*_{t_1}(t_f)$ and its derivative $Z^*_{t_1}(t_f)$ with respect to the final position. From our above discussion we know that the term proportional to $p^*_{t_1}(t)$ in the differential equation (6.33) for the prefactor can be neglected for sufficiently large times, and without loss of generality

$$\frac{d}{dt}\left[\dot{Q}^*(t) - 2Q^*(t)F'(x^*_{t_1}(t), t)\right] = 0 \tag{6.100}$$

is valid for all times $t > t_u$. The term in the squared brackets in equation (6.100) is therefore constant and

$$\dot{Q}^*(t) - 2Q^*(t)F'(x^*_{t_1}(t), t) = \dot{Q}^*(t_u) - 2Q^*(t_u)F'(x^*_{t_1}(t_u), t_u) =: c(t_u) \; . \tag{6.101}$$

The solution of (6.101) is readily found:

$$Q^*(t) = e^{2\Lambda_u(t, t_u)}\left[Q^*(t_u) - \frac{1}{2}c(t_u)I_u(t_u, t)\right] \; . \tag{6.102}$$

The term in the squared brackets in equation (6.102) converges according to equation (6.93) towards a finite value, and for large $t_f - t_1$ we find:

$$Q^*_{t_1}(t_f) \sim e^{2\Lambda_u(t_f, t_1)} \; . \tag{6.103}$$

---

[9] *Proof:* Consider two final times $t_f > t'_f$ and a fixed starting time t_1. The corresponding optimizing paths shall be denoted by $x^*_{t_1}(t|t'_f)$ and $x^*_{t_1}(t|t_f)$, respectively. Consider further the path $\tilde{x}(t)$ that equals $x^*_{t_1}(t|t'_f)$ for $t_1 \le t \le t'_f$ and $x_u(t)$ for $t'_f \le t \le t_f$. As the deterministic movement on the unstable orbit does not accumulate any action, the action of the path $\tilde{x}(t)$ equals that of $x^*_{t_1}(t|t'_f)$ which is, hence, an upper bound for the action of the path $x^*_{t_1}(t|t_f)$.

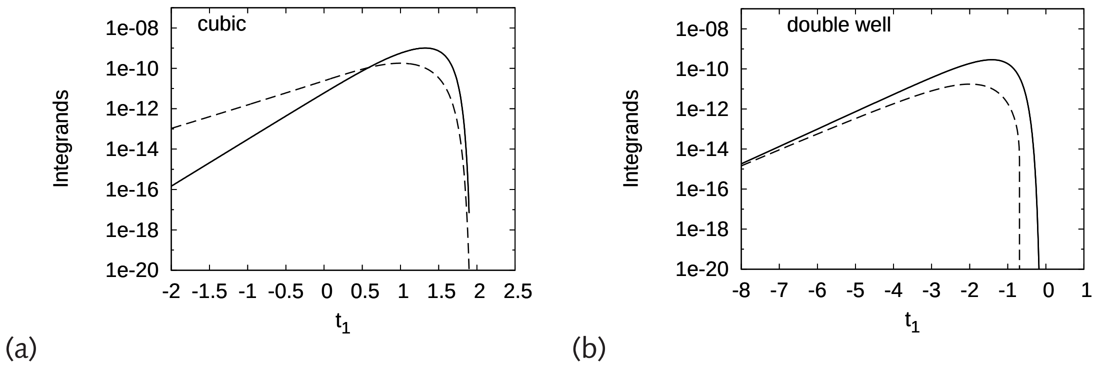

Figure 6.4: (a) Integrands of $\Gamma_0(t_f)$ (solid line) and $\Gamma_1(t_f)$ (dashed line) for a static cubic potential $V(x) = -a/3\,x^3 + b/2\,x^2$ with $a = 1.78$ and $b = 2.67$. The noise strength is $D = 0.05$, and the reference level is chosen as $x_1 = 0.75$. (b) The same for a double well potential $V(x) = a/4x^4 - b/2x^2$ with $a = 0.25$, $b = 1.0$, and $x_1 = -1.1$.

We mention that the quantities $c(t_u) = c(t_u|t_1, t_f)$ and $Q^*(t_u) = Q^*(t_u|t_1, t_f)$ in equation (6.102) depend on both, the initial and the final times. For a rigorous proof of (6.103) one therefore also has to show that $c(t_u|t_1 - n\mathcal{T}, t_f)$ and $Q^*(t_u|t_1 - n\mathcal{T}, t_f)$ converge for $n \to \infty$ towards a finite limit which will, in general, depend on t_1. Hence, in order to write the expression (6.103) in the limit $t_f - t_1 \to \infty$ as an equation, a t_1-periodic function has to be multiplied to the right-hand side.

From our above discussion the asymptotical behavior of the remaining quantity $Z^*_{t_1}(t_f)$ can be easily derived. For this purpose, we consider the differential equation (6.44, 6.45) which determines the derivative of the prefactor. Using the asymptotical behavior (6.103) of $Q^*_{t_1}(t_f)$ and the boundary condition $\mathcal{D}_x(t_f) = 1$, we see that the inhomogeneity $H(t)$, evaluated at the final time t_f, is dominated by an exponentially increasing factor $H(t_f) \sim \exp(2\Lambda_u(t_f, t_1))$. Considering $Z^*_{t_1}(t_f)$ for a fixed time t_f as a function of t_1, the left-hand side of the differential equation evaluated at t_f must grow in the same manner. As we are dealing with a linear differential equation with bounded coefficients (on the left-hand side), we can conclude that $Z^*_{t_1}(t_f)$ itself is dominated by the exponentially increasing factor $\exp(2\Lambda_u(t_f, t_1))$, hence

$$Z^*_{t_1}(t_f) \sim e^{2\Lambda_u(t_f,t_1)} \,. \tag{6.104}$$

An exception to this asymptotical behavior has to be expected for a static potential with $F''(x_u(t), t) = F''(x_{\max}) = 0$. In this case a closer inspection of equations (6.40,6.41) and (6.44, 6.45) reveals that $Z^*_{t_1}(t_f)$ only grows like $\exp(\Lambda_u(t_f, t_1))$.

Having now discussed the asymptotics of all quantities appearing in the approximation (6.54-6.56) for the instantaneous escape rate, we can turn to the integrands of the integrals in (6.55,6.56). Using relations (6.99,6.103), we infer that for large $t_f - t_1$ the integrand of the leading term $\Gamma_0(t_f)$ decreases like $\exp(-2\Lambda_u(t_f, t_1))$ and that of the first correction $\Gamma_1(t_f)$ as $\exp(-\Lambda_u(t_f,t_1))$. That means, the lower limits of both integrals in (6.55,6.56) can be replaced by some finite value. We can further infer that, for all *finite* noise strengths D, the integrand of $\Gamma_1(t_f)$ will be much larger than that of $\Gamma_0(t_f)$ for large $t_f - t_1$. This indicates that the first correction might significantly improve the approximation for finite values of the noise strength D. We, however, note that this is not in contradiction with the fact that $\Gamma_1(t_f)$ becomes negligible compared to $\Gamma_0(t_f)$ as $D \to 0$.

The asymptotical behavior of the integrands of $\Gamma_0(t_f)$ and $\Gamma_1(t_f)$ is illustrated in figure 6.4 for two static potentials. In the case of the cubic potential the integrands decrease in the above discussed way, whereas the static double well potential is one of the exceptions discussed below equation (6.104). As both, $F''(x_u(t)) = F''(0)$ and $\dot{x}_u(t)$ vanish, the derivative $Z^*_{t_1}(t_f)$ of the prefactor is dominated by the exponential factor $\exp(\lambda_u(t_f - t_1))$, and, hence, the integrand of $\Gamma_1(t_f)$ is dominated by the same exponentially decreasing factor $\exp(-2\lambda_u(t_f - t_1))$ as that of $\Gamma_0(t_f)$.

In equation (6.65) of section 6.4.2, we have neglected the term proportional $DZ^*_{t_0}(t_1)/Q^*_{t_0}(t_1)$. This could be done because for transitions from the stable orbit to the reference level x_1 this term is usually very small compared to $p^*_{t_0}(t_1)$. We desist from a rigorous proof, but give two arguments for this statement. Firstly, the momentum $p^*_{t_0}(t_1)$ of the optimizing path is not small at the moment it crosses the reference level. In contrast, $p^*_{t_1}(t_f)$ decreases exponentially with time $t_f - t_1$ [cf. equation (6.99)]. Secondly, proceeding as in equations (6.100-6.102), one can easily show that the prefactor of a path equals

$$Q^*_{t_0}(t_s) = I_s(t_s)/2 \qquad (6.105)$$

for all times t_s at which it is still the vicinity of the stable orbit. Hence, the prefactors corresponding to two neighboring paths are "exactly" the same as long as they are near the stable orbit. Differences can only be accumulated in the short time interval, needed to travel from the vicinity of the stable orbit to the reference level. Therefore, the ratio $Z^*_{t_0}(t_1)/Q^*_{t_0}(t_1)$ is in most cases very small itself.

6.4.5 Expansion around asymptotic paths

For reasons of computational efficiency [see also Sec. 6.4.6] we can further approximate the instantaneous escape rate and express all quantities appearing in equations (6.54-6.56) in terms of the path $x^\infty_{t_1}(t)$ which satisfies the boundary conditions

$$x^\infty_{t_1}(t_1) = x_1, \quad \lim_{t\to\infty} (x^\infty_{t_1}(t) - x_u(t)) = 0 \; . \qquad (6.106)$$

It can be inferred from our discussions in sections 6.3.3 and 6.4.4 that the paths which strongly deviate from $x^\infty_{t_1}(t)$ correspond to a large action $\Phi^*_{t_1}(t_f)$. Their contribution to the escape rate in equations (6.54-6.56) is exponentially suppressed by the term $\exp(-\Phi^*_{t_1}(t_f)/D)$.

We first point out that we can truncate the path $x^\infty_{t_1}(t)$ at any time t_f. As the resulting path obviously satisfies the Hamiltonian equations (6.28,6.29), it is still an optimizing path with initial point (x_1, t_1) and final point $(x_f = x_{t_1}^{\infty}(t_f), t_f)$. Hence, equations (6.35,6.42,6.47), determining the derivative of the action, of the momentum, and of the prefactor with respect to the final position, remain valid. Using the notation introduced in section 6.3.1, we get:

$$\begin{aligned} \frac{\partial}{\partial x_f}\Phi_{t_1}^{*}(x_{t_1}^{\infty}(t_f), t_f) &= p_{t_1}^{\infty}(t_f)\ , && (6.107)\\ \frac{\partial^2}{\partial x_f^2}\Phi_{t_1}^{*}(x_{t_1}^{\infty}(t_f), t_f) &= \frac{\partial}{\partial x_f}p_{t_1}^{\infty}(t_f) = \mathcal{D}_p^{\infty}(t_f)\ , && (6.108)\\ \frac{\partial}{\partial x_f}Q_{t_1}^{*}(x_{t_1}^{\infty}(t_f), t_f) &= Z_{t_1}^{\infty}(t_f)\ . && (6.109) \end{aligned}$$

These quantities can be calculated as described in section 6.3.2. Equations (6.107-6.109) can now be used to expand the action, momentum, and prefactor of the optimizing path $x_{t_1}^{*}(t)$, with boundary condition $x_{t_1}^{*}(t_f) = x_u(t_f)$, in powers of the distance $\Delta x_{t_1}^{\infty}(t_f) = x_{t_1}^{*}(t_f) - x_{t_1}^{\infty}(t_f)$ of the path $x_{t_1}^{\infty}(t)$ from the unstable orbit. For the action it follows:

$$\begin{aligned} \Phi_{t_1}^{*}(x_u(t_f), t_f) &= \Phi_{t_1}^{*}(x_{t_1}^{\infty}(t_f), t_f) + p_{t_1}^{\infty}(t_f)\Delta x_{t_1}^{\infty}(t_f)\\ &+ \frac{1}{2}\mathcal{D}_p^{\infty}(t_f)\Delta x_{t_1}^{\infty}(t_f)^2 + \dots\ . \qquad (6.110) \end{aligned}$$

The final momentum and prefactor can be expanded in the same way:

$$\begin{aligned} p_{t_1}^{*}(x_u(t_f), t_f) &= p_{t_1}^{\infty}(t_f) + \mathcal{D}_p^{\infty}(t_f)\Delta x_{t_1}^{\infty}(t_f) + \dots\ , && (6.111)\\ Q_{t_1}^{*}(x_u(t_f), t_f) &= Q_{t_1}^{*}(x_{t_1}^{\infty}(t_f), t_f) + Z_{t_1}^{\infty}(t_f)\Delta x_{t_1}^{\infty}(t_f) + \dots\ . && (6.112) \end{aligned}$$

While in equations (6.111,6.112) only the first order terms are kept, the second order term is included in the approximation (6.110) for the action for two reasons. Firstly, including this term does not “cost” anything. The derivative $\mathcal{D}_p^{\infty}(t_f)$ of the momentum is also needed elsewhere, e.g., in equation (6.111). Secondly, the action of the path enters approximation (6.54-6.56) for the escape rate via the term $\exp(-\Phi_{t_1}^{*}(t_f)/D)$. Hence, for small noise strengths D, even small errors in the approximation for the action are exponentially amplified. For the derivative of the prefactor $Q_{t_1}^{*}(t_f)$, appearing in equation (6.56), only the zeroth order approximation

$$Z_{t_1}^{*}(t_f) = Z_{t_1}^{\infty}(t_f) + \dots \qquad (6.113)$$

will be used. This is justified by the fact that $\Gamma_1(t_f)$ itself is a correction. The error resulting from neglecting the higher order terms will therefore be very small.

Equations (6.110-6.113), together with (6.54-6.56) and (6.77), are the third main result of this chapter. In the next section we discuss that these equations provide a computationally efficient approximation to the instantaneous escape rate for periodically modulated force fields.

6.4.6 Main steps for a practical application

We will now summarize the main steps which are necessary for an application of the approximation to a given force field $F(x,t)$. Except for some special cases like the piecewise parabolic potential, described in section 6.6.2, all these steps require numerical methods.

In a first step, the stable and unstable orbit $x_{s,u}(t)$ have to be determined. As the solution of the deterministic equation (6.5) converges to the stable orbit for any initial condition lying in the basin of attraction, the determination of $x_s(t)$ is quite easy. All that has to be done is to evolve the deterministic equation of motion "sufficiently long" forward in time. In practice, different initial conditions are used. After an "equilibration time" the solutions of the deterministic equation (6.5) become (approximately) independent of the initial condition and agree with the stable orbit. In the same way the unstable orbit $x_u(t)$ can be determined by evolving equation (6.5) backwards in time for some initial conditions $x(t_0) > x_s(t_0)$.

In a second step, the intermediate level x_1 has to be chosen. While equation (6.52) is valid for any level with $x_s(t) < x_1 < x_u(t)$ for all times t, the quality of the approximation usually depends on the explicit choice. This will be demonstrated for an example in section 6.6.4. As a guideline, x_1 should be chosen such that $|V(x_{s,u}(t),t) - V(x_1,t)|$ and $|F(x_1,t)|$ are as large as possible.

Then, the first passage time density $\Psi_{t_0}(x_1,t_1)$ can be approximated by equations (6.32,6.77). For the calculation of the quantities $\Phi^*_{t_0}(x_1,t_1), Q^*_{t_0}(x_1,t_1)$, and $\dot{x}^*_{t_0}(t_1)$, appearing in these formulas, a system of three coupled differential equations (6.28,6.29,6.33) with boundary conditions

$$\lim_{t\to-\infty} x^*_{t_0}(t) - x_s(t) = 0, \quad x^*_{t_0}(t_1) = x_1 \, , \tag{6.114}$$

$$\lim_{t\to-\infty} Q^*_{t_0}(t) = 0, \quad \lim_{t\to-\infty} \dot{Q}^*_{t_0}(t) = 1 \tag{6.115}$$

has to be solved. Not dealing with an initial-value problem, the solution of the differential equations, in general, requires more sophisticated numerical methods like shooting procedures or relaxation methods [PTVF92]. However, as we need the first passage time density $\Psi_{t_0}(x_1,t_1)$ for all times t_1, the following very simple method can be used: We first choose a small $\Delta x_s > 0$ for which the linearization (6.81) of the force field is justified for all $x^*_{t_0}(t) - x_s(t) < \Delta x_s$ and for all times t. Then, for some time t_s we set:

$$x^*_{t_0}(t_s) = x_s(t_s) + \Delta x_s, \quad p^*_{t_0}(t_s) = \Delta x_s / I_s(t_s), \tag{6.116}$$

$$Q^*_{t_0}(t_s) = I_s(t_s)/2, \quad \dot{Q}^*_{t_0}(t_s) = \dot{I}_s(t_s)/2 \, . \tag{6.117}$$

We know from our discussion in sections 6.4.3 and 6.4.4 that $(x^*_{t_0}(t_s), p^*_{t_0}(t_s))$ given by (6.116) corresponds to an optimizing path with the desired initial condition, and the prefactor in (6.117) is the solution of equation (6.33) with initial condition (6.115). Using equations (6.31,6.87,6.88,6.95), a short calculation yields the action of this path at time t_s:

$$\Phi^*_{t_0}(x^*(t_s), t_s) = \frac{1}{2} \frac{\Delta x_s^2}{I_s(t_s)} \ . \tag{6.118}$$

For the initial conditions (6.116,6.117), the set of differential equations can be evolved forward in time until the level x_1 is crossed at time t_1.[10] This time clearly depends on the chosen reference time t_s and on the distance to the stable orbit Δx_s, i.e., $t_1 = t_1(\Delta x_s, t_s)$. Using equations (6.31,6.118), the action of the path is

$$\Phi^*_{t_0}(x_1, t_1) = \frac{1}{2} \frac{\Delta x_s^2}{I_s(t_s)} + \int_{t_s}^{t_1} dt \ p^*_{t_0}(t)^2 \ . \tag{6.119}$$

Having determined all necessary quantities for the approximation of the first passage time density for this time, one can next vary either Δx_s or/and t_s and repeat the same procedure. In this way, the first passage time density $\Psi_{t_0}(x_1, t_1)$ can be calculated for sufficiently many times t_1. These cannot be fixed a priori, but, by using adaptive procedures for the variation of the parameter t_s (or Δx_s), the distance between these sampling points can be made arbitrarily small. Then, $\Psi_{t_0}(x_1, t_1)$ can be interpolated to arbitrary times. The first passage time densities for the cubic potential which are shown in figure 6.3 have been calculated in this way.

In a next step, $\partial/\partial x_f \rho(x_f, t_f | x_1, t_1)$ has to be determined according to equation (6.53). This can be done in two ways which are both similar to the procedure used to determine the first passage time density. We will later refer to the first method as the *full approximation*. The second method makes use of the expansion around the asymptotic paths, described in the previous section, and is for periodically modulated force fields computationally much more efficient.

For the full approximation, we first fix the final time t_f for which the instantaneous escape rate shall be calculated. We choose a small distance $\Delta x_u < 0$ and a reference time $t_u < t_f$ and set:

$$x^*_{t_1}(t_u) = x_u(t_u) + \Delta x_u, \quad p^*_{t_1}(t_u) = \Delta x_u / I_u(t_u, t_f) \ . \tag{6.120}$$

For this initial condition the differential equations for the optimizing paths are evolved backwards in time, until the level x_1 is crossed at time $t_1 = t_1(\Delta x_u, t_u)$ with momentum p_1. Then, the system of six differential equations (6.28,6.29,6.33,6.40,6.41,6.44) can be evolved forward in time to t_f with initial conditions

$$x^*_{t_1}(t_1) = x_1 \ , \quad p^*_{t_1}(t_1) = p_1 \ , \tag{6.121}$$

$$\mathcal{D}_x(t_1) = 0 \ , \quad \mathcal{D}_p(t_1) = p_0 \ , \tag{6.122}$$

$$Q^*_{t_1}(t_1) = 0 \ , \quad \dot{Q}^*_{t_1}(t_1) = 1 \ , \tag{6.123}$$

$$Z^*(t_1) = 0 \ , \quad \dot{Z}^*(t_1) = 0 \ . \tag{6.124}$$

---

[10] If the solution $Q^*_{t_0}(t)$ of the differential equation (6.33) becomes negative, $x^*_{t_0}(t)$ does for larger times no longer minimize the action, but rather corresponds to a saddle or a maximum. In this case, or if the level x_1 is not crossed, a different Δx_s and/or t_s has to be chosen.

Because of the linearity of the differential equations (6.40,6.41,6.44) and because of the initial condition (6.124) for the inhomogeneous equation, p_0 can be chosen arbitrarily, but the final solutions of both, $\mathcal{D}_p(t_f)$ and $Z^*(t_f)$, have to be divided by $\mathcal{D}_x(t_f)$. Again, by variation of either t_u or Δx_u, all quantities can be calculated for sufficiently many t_1. If one is interested in the instantaneous escape rate for different final times t_f, this part of the approximation is computationally very expensive.

The second approximation scheme is particularly suited for periodic force fields and allows to approximate $\partial/\partial x_f \rho(x_f, t_f|x_1, t_1)$ much more efficiently. In this approximation scheme we proceed as in the full approximation, but consider the limit $t_f \to \infty$, i.e., we determine the paths $x^\infty_{t_1}(t)$. For sufficiently many t_1 these paths and the values of the other quantities along these paths can be stored (in appropriate time steps). For a given final time t_f, all needed quantities can then be expressed in terms of these paths, as described in section 6.4.5. This method is computationally favorable because the differential equations have to be solved for a sufficient number of times t_1 only once. After that, for each time t_f just one integral has to be solved numerically to approximate the instantaneous escape rate $\Gamma(t_f)$ according to equations (6.54-6.56). We mention that the computational costs do not depend on the noise strength D. The optimizing paths, actions, and prefactors are independent of this quantity. The approximation is therefore particularly efficient if the escape rate shall be calculated for different noise strengths.

6.5 Adiabatically slowly modulated potentials

Before demonstrating our approximation scheme for different time-dependent force fields, we show that our approximation reduces to the well known Kramers result (2.19) for static or adiabatically slowly modulated potentials and weak noise strengths D.

Hence, let us consider a static potential $V(x)$ and a corresponding static force field $F(x) = -V'(x)$. The stable and unstable orbits are obviously the minimum of the potential $x_{\min}$ and maximum $x_{\max}$, respectively. Using equations (6.28,6.29) for the optimizing path, a short calculation shows

$$\frac{d}{dt}\left[\dot{x}^*(t)^2 - V'(x^*(t))^2\right] = 0 \;, \tag{6.125}$$

and therefore

$$\left[\dot{x}^*(t) - V'(x^*(t))\right]\left[\dot{x}^*(t) + V'(x^*(t))\right] = const \;, \tag{6.126}$$

with some constant $const$. Let us next consider the optimizing path $x^*_{t_0}(t)$, corresponding to the boundary conditions (6.114), and implicitly define the time $t_s = t_s(\epsilon) \ll t_1$ via $x^*_{t_0}(t_s) = x_{\min} + \epsilon$ with $\epsilon \ll x_1 - x_{\min}$. From our discussions in section 6.4.3 we know that $\dot{x}^*_{t_0}(t_s) = \mathcal{O}(\epsilon)$. As also $V'(x^*_{t_0}(t_s)) = \mathcal{O}(\epsilon)$, by taking the limit $\epsilon \to 0$ we can infer that $const = 0$ in equation (6.126). It thus follows that the optimizing path is given by

$$p^*_{t_0}(t) = \dot{x}^*_{t_0}(t) = V'(x^*_{t_0}(t)) \;. \tag{6.127}$$

That means, for a static potential the optimizing path with boundary conditions (6.114) is nothing but the time-reversed deterministic motion, and the action (6.31) is readily found to be the difference of the potential energy between initial and final point:

$$\Phi^*_{t_0}(t_1) = V(x_1) - V(x_{\min}) \, . \tag{6.128}$$

For the optimizing path (6.127), equation (6.33) for the prefactor reduces to

$$\ddot{Q}^*_{t_0}(t) = -2\dot{Q}^*_{t_0}(t) V''(x^*_{t_0}(t)) \, , \tag{6.129}$$

with the usual initial condition $Q^*_{t_0}(t_0) = 0$ and $\dot{Q}^*_{t_0}(t_0) = 1$. Its solution is formally given by

$$\begin{aligned} Q^*_{t_0}(t) &= Q^*_{t_0}(t_s) + \dot{Q}^*_{t_0}(t_s) \left[V'(x^*_{t_0}(t_s))\right]^2 \int_{t_s}^{t} dt' \, \frac{1}{\left[V'(x^*_{t_0}(t'))\right]^2} & (6.130) \\ &= Q^*_{t_0}(t_s) + \dot{Q}^*_{t_0}(t_s) \left[V'(x^*_{t_0}(t_s))\right]^2 \int_{x^*_{t_0}(t_s)}^{x^*_{t_0}(t)} dx \, \frac{1}{\left[V'(x)\right]^3} \, , & (6.131) \end{aligned}$$

where t_s is some reference time. Choosing, in particular, $t_s = t_s(\epsilon)$ as defined below equation (6.126) and $t = t_1$, we see that the main contribution to the integral in equation (6.131) stems from the x-values with $x \approx x^*_{t_0}(t_s) = x_{\min} + \epsilon$. We can therefore expand $V'(x)$ around $x = x_{\min}$ with the result:

$$\begin{aligned} Q^*_{t_0}(t_1) &\approx Q^*_{t_0}(t_s) + \dot{Q}^*_{t_0}(t_s) \left[V''(x_{\min})\epsilon\right]^2 \int_{x^*_{t_0}(t_s)}^{x_1} dx \, \frac{1}{\left[V''(x_{\min})(x - x_{\min})\right]^3} \\ &= Q^*_{t_0}(t_s) + \frac{\dot{Q}^*_{t_0}(t_s)}{2V''(x_{\min})} + \mathcal{O}(\epsilon) \, . & (6.132) \end{aligned}$$

Now, taking the limit $\epsilon \to 0$ and using the initial condition $Q^*_{t_0}(t_0) = 0$ and $\dot{Q}^*_{t_0}(t_0) = 1$ gives the prefactor $Q^*_{t_0}(t_1) = 1/(2V''(x_{\min}))$. Hence, the first passage time density through the level x_1 is approximately given by equations (6.32,6.77), yielding together with equations (6.127,6.128)

$$\Psi_{t_0}(t_1) = \Psi = \sqrt{\frac{V''(x_{\min})}{2\pi D}} V'(x_1) e^{-(V(x_1) - V(x_{\min}))/D} \, . \tag{6.133}$$

As already mentioned at the end of section 6.4.2, this approximation can also be obtained within the framework of transition state theory [HTB90].

We next turn to the optimizing path $x^*_{t_1}(t)$ with boundary conditions $x^*_{t_1}(t_1) = x_1$ and $x^*_{t_1}(t_f) = x_{\max}$. Due to the continuous time translation symmetry, all quantities depend on the initial and final time only via $t_f - t_1$. Now, the main idea is to follow the proceeding in section 6.4.5, and to express all quantities in the approximation for the transition probability $\rho(x_f, t_f | x_1, t_1)$ in terms of the asymptotic optimizing path

$x_{t_1}^{\infty}(t)$ corresponding to the boundary conditions (6.106). In full analogy to our above discussions, this path is easily found:

$$p_{t_1}^{\infty}(t) = \dot{x}_{t_1}^{\infty}(t) = V'(x_{t_1}^{\infty}(t)) \ . \tag{6.134}$$

Again, the action is the difference of the potential energy between initial and final point:

$$\Phi_{t_1}^{\infty} = \int_{t_1}^{\infty} dt \ \left[p_{t_1}^{\infty}(t)\right]^2 = V(x_{\max}) - V(x_1) \ . \tag{6.135}$$

The action corresponding to the path $x_{t_1}^{*}(t)$ can be approximated by equation (6.110). Neglecting in this equation terms of order $\Delta x_{t_1}^{\infty}(t_f)^2$ and using (6.31,6.91,6.135), a short calculation gives

$$\Phi_{t_1}^{*}(x_{\max}, t_f) \approx V(x_{\max}) - V(x_1) + \frac{1}{2}|V''(x_{\max})| \left(x_{\max} - x_{t_1}^{\infty}(t_f)\right)^2 \ , \tag{6.136}$$

where the dependence on the final position has been explicitely stated to avoid confusion with that of the truncated asymptotic path.

The prefactor $Q_{t_1}^{*}(x_{t_1}^{\infty}(t_f), t_f)$ of the truncated asymptotic path is given by the solution of equation (6.129) (cf. equation (6.130)):

$$\begin{aligned} Q_{t_1}^{*}(x_{t_1}^{\infty}(t_f), t_f) &= \left[V'(x_1)\right]^2 \int_{t_1}^{t_f} dt' \, \frac{1}{\left[V'(x_{t_1}^{\infty}(t'))\right]^2} && (6.137) \\ &\approx \frac{1}{2}\left(\frac{V'(x_1)}{V'(x_{t_1}^{\infty}(t_f))}\right)^2 \frac{1}{|V''(x_{\max})|} \ . && (6.138) \end{aligned}$$

In the limit $D \to 0$, we can neglect terms of order $\Delta x_{t_1}^{\infty}(t_f)$ in equations (6.111,6.112). As also the contribution $\Gamma_1(t_f)$ vanishes in this limit, we have everything at hand to approximate the escape rate. Substituting equations (6.133,6.134,6.136,6.138) into equation (6.55) yields

$$\begin{aligned} \Gamma_0(t_f) &= \frac{\sqrt{V''(x_{\min})|V''(x_{\max})|}}{2\pi D} e^{-\Delta V/D} && (6.139) \\ &\times \int_{-\infty}^{t_f} dt_1 \ \left[V'(x_{t_1}^{\infty}(t_f))\right]^2 \exp\left[-\frac{1}{2D}|V''(x_{\max})|(x_{\max} - x_{t_1}^{\infty}(t_f))^2\right] \ , \end{aligned}$$

with $\Delta V = V(x_{\max}) - V(x_{\min})$. Using the fact that $x_{t_1}^{\infty}(t_f)$ depends on both times only via their difference $t_f - t_1$, we can rewrite the integral in equation (6.139) as an integral over the coordinate by substituting $x = x_{t_1}^{\infty}(t_f)$. For small noise strengths D, the integrand of this integral is sharply peaked at the upper bound $x_{\max}$ of this integral. The factor $V'(x)$ in front of the exponential function can therefore be expanded around $x_{\max}$, up to first order in $x_{\max} - x$. Doing this, we finally get

$$\int_{-\infty}^{t_f} dt_1 \ \left[V'(x_{t_1}^{\infty}(t_f))\right]^2 \exp\left[-\frac{1}{2D}|V''(x_{\max})|(x_{\max} - x_{t_1}^{\infty}(t_f))^2\right] \approx D \ . \tag{6.140}$$

Inserting this result into equation (6.139) shows that, for static potentials in the limit $D \to 0$, the approximation of the escape rate reduces to

$$\Gamma_0(t_f) \approx \frac{\sqrt{V''(x_{\min})|V''(x_{\max})|}}{2\pi} e^{-\Delta V/D} \; . \qquad (6.141)$$

This is exactly the Kramers formula (2.19) for the dimensionless units used in this chapter.

We have, thus, shown that the approximation scheme for the first passage time density and the escape rate reduces to the well known results for static potentials. This will still hold for adiabatically slow modulations. In the limit of very fast modulations, meaning that the potential is modulated on time scales much shorter than the time scales of the deterministic motion, the potential and its derivatives, appearing in the equations for the optimizing path, can be replaced by their concomitant time-averaged versions. The escape rate is, hence, again given by equation (6.141).

6.6 Examples

We now illustrate the procedure on some examples. In sections 6.6.1 - 6.6.3 a piecewise parabolic potential is considered for which all quantities appearing in equations (6.54-6.56) can be calculated analytically. Only the integrals themselves have to be determined numerically. In section 6.6.4 a cubic potential is studied. Here all steps have do be done numerically, as described in section 6.4.6.

The approximated escape rates are compared to those obtained from solving the Fokker-Planck equation (6.11). For this purpose, standard numerical procedures can be used. We have used two different methods. For the first method the partial differential equation has to be discretized in space using finite differences. It is then evolved in time employing an implicit Cranck-Nicolson scheme [PTVF92]. The spatial discretization in the second method is performed using a Chebyshev collocation method. By the method of lines the partial differential equation is reduced to a system of ordinary differential equations which is then solved by standard methods. Whereas for the first scheme a self-written algorithm has been used, for the second method a commercial algorithm from the NAG (National Algorithms Group) library (routine *d03pdc*) has been employed [BD91]. Both methods yielded essentially the same results. The curves shown in this work have been calculated with the algorithm from the NAG library.

6.6.1 Piecewise parabolic potential: General case with time-dependent coefficients

Our first example is the piecewise parabolic potential jointed at $x = 0$. In its most general form, this is given by

$$\begin{aligned} V(x,t) &= U(x,t) - f(t)x \;, \qquad (6.142) \\ U(x,t) &= \frac{1}{2}\begin{cases} h_s(t)\lambda_s\left(\bar{x}_s^2(t) - (x - \bar{x}_s(t))^2\right) & \text{for } x \leq 0 \\ h_u(t)\lambda_u\left(\bar{x}_u^2(t) - (x - \bar{x}_u(t))^2\right) & \text{for } x > 0 \end{cases} , \end{aligned}$$

where

$$\bar{x}_s(t) < 0, \qquad h_s(t)\lambda_s < 0 \;, \tag{6.143}$$

$$\bar{x}_u(t) > 0, \qquad h_u(t)\lambda_u > 0 \;, \tag{6.144}$$

and where $h_{s,u}(t)$, $\bar{x}_{s,u}(t)$, and $f(t)$ are time-dependent functions. The force field $F(x,t) = -\partial/\partial x V(x,t)$ has to be continuous at $x = 0$. This requires

$$h_s(t)\lambda_s\bar{x}_s(t) = h_u(t)\lambda_u\bar{x}_u(t) \;. \tag{6.145}$$

Defining a new force $\tilde{f}(t) = f(t) - h_s(t)\lambda_s\bar{x}_s(t)$ thus allows us to rewrite $F(x,t)$ corresponding to (6.142) in the form

$$F(x,t) = \begin{cases} h_s(t)\lambda_s x + \tilde{f}(t) & \text{for } x \leq 0 \\ h_u(t)\lambda_u x + \tilde{f}(t) & \text{for } x > 0 \end{cases} , \tag{6.146}$$

where the three independent functions $h_{s,u}(t)$ and $\tilde{f}(t)$ are a priori arbitrary, with the only condition that the deterministic dynamics $\dot{x}(t) = F(x(t),t)$ exhibits a stable orbit $x_s(t) < 0$ and an unstable orbit $x_u(t) > 0$ (cf. section 6.2.1).

The particular form of the potential suggests to choose the intermediate level

$$x_1 = 0 \;. \tag{6.147}$$

With this choice the calculation of each of the needed quantities becomes quite easy.

We first determine the first passage time density $\Psi_{t_0}(t_1)$. As long as the optimizing path $x^*(t)$ has not crossed the intermediate level x_1, i.e., $x^*(t) \leq 0$, the linearization (6.81) of the force field $F(x,t)$ is exact. Consequently, also equations (6.82-6.88) and (6.94-6.96) are the exact solutions of the optimizing path.

It is convenient to choose the reference time in equations (6.94-6.96) as $t_s = t_1$. With this choice the optimal path becomes

$$x^*(t) = x_s(t) - x_s(t_1)e^{\Lambda_s(t_1,t)}\frac{I_s(t)}{I_s(t_1)} \;, \tag{6.148}$$

$$p^*(t) = -x_s(t_1)\frac{e^{\Lambda_s(t_1,t)}}{I_s(t_1)} \;, \tag{6.149}$$

and hence

$$\dot{x}^*_{t_0}(t_1) = -2\frac{x_s(t_1)}{I_s(t_1)} + \tilde{f}(t_1) \ . \tag{6.150}$$

From equations (6.31,6.88,6.96) and (6.149) the action of the path readily follows

$$\Phi^*_{t_0}(t_1) = \frac{1}{2}\frac{x_s(t_1)^2}{I_s(t_1)} \ , \tag{6.151}$$

and the prefactor is given by equation (6.105). Combing equations (6.32,6.77,6.148-6.151), the zeroth order approximation to the first passage time density is

$$\Psi_{t_0}(t_1) = \left(-\frac{2x_s(t_1)}{I_s(t_1)} + \tilde{f}(t_1)\right)\frac{1}{\sqrt{2\pi D I_s(t_1)}}e^{-x_s(t_1)^2/(2DI_s(t_1))} \ . \tag{6.152}$$

We note that this approximation is only valid if $\dot{x}^*_{t_0}(t_1)$ in equation (6.150) is strictly positive for all times, i.e., if the modulation of the potential is not too strong. Otherwise the path would have been in the region $x > 0$, where the linearization of the force field is different to that used in order to derive the expressions.

In full analogy we can determine the transition probability $\rho(x_f, t_f|x_1, t_1)$. As the reference time t_u in equations (6.90,6.91) for the optimizing path is arbitrary, one can, in particular, choose $t_u = t_1$ and integrate $p^*(t)^2$ from t_1 to t_f, yielding the action of the path:

$$\Phi^*_{t_1}(t_f) = -\frac{1}{2}\frac{x_u(t_1)^2}{I_u(t_1, t_f)} \ . \tag{6.153}$$

The prefactor follows from equation (6.102) with $t_u = t_1$ and the relation $I_u(t_f, t_1) = -\exp(2\Lambda_u(t_f, t_1))I_u(t_1, t_f)$:

$$Q^*_{t_1}(t_f) = I_u(t_f, t_1)/2 \ . \tag{6.154}$$

It depends solely on the initial and final times, but not on the initial and final coordinates x_1 and x_f, respectively. A direct consequence is that the derivative $Z^*_{t_1}(t_f)$ of the prefactor, and hence $\Gamma_1(t_f)$, vanish for all times. This can also be seen from equations (6.44-6.46) determining the derivative. For the piecewise parabolic potential, the right-hand side of the differential equation (6.45) vanishes in the whole regime $x > 0$. The differential equation is thus homogeneous, and the initial conditions (6.46) can only be satisfied by $Z^*(t) = 0$.

Finally, using equations (6.148-6.154), the instantaneous escape rate (6.55) is

$$\Gamma(t_f) \approx \frac{1}{2\pi D}\int_{-\infty}^{t_f} dt_1 \ \left(-\frac{2x_s(t_1)}{I_s(t_1)} + \tilde{f}(t_1)\right)\frac{x_u(t_1)e^{2\Lambda_u(t_1,t_f)}}{I_s(t_1)^{1/2}\left|I_u(t_1,t_f)\right|^{3/2}}\exp\left(-\frac{\Phi^*_{t_0}(t_1,t_f)}{D}\right) \ , \tag{6.155}$$

with the generalized action

$$\Phi^*_{t_0}(t_1, t_f) = \frac{1}{2}\left(\frac{x_s^2(t_1)}{I_s(t_1)} - \frac{x_u^2(t_1)}{I_u(t_1, t_f)}\right) \ . \tag{6.156}$$

For the explicit evaluation of the functions $I_{s,u}$ and Λ_u, defined via equations (6.87,6.88) and (6.96), usually numerical methods have to be employed.

We mention that the case $f(t) = 0$ and time-periodic $h_s(t) = h_u(t)$ was also treated in [BG04]. However, as already discussed at the end of section 6.4.1, their approach could not be directly generalized to other potentials.

6.6.2 The piecewise parabolic potential: Periodic tilting

Let us now consider the special case of a periodically tilted, piecewise parabolic potential $V(x,t)$. We start from equation (6.142) and choose a static contribution $U(x,t) = U(x)$ and a periodic function $f(t+\mathcal{T}) = f(t)$, resulting in

$$V(x,t) = \frac{1}{2}\begin{cases}\lambda_s\left(\bar{x}_s^2 - (x-\bar{x}_s)^2\right) - f(t)x & \text{for } x \le 0\\ \lambda_u\left(\bar{x}_u^2 - (x-\bar{x}_u)^2\right) - f(t)x & \text{for } x > 0\end{cases} . \tag{6.157}$$

Compared to equation (6.142), the functions $h_{s,u}(t)$ and $\bar{x}_{s,u}(t)$ are constant, and without loss of generality we can choose $h_{s,u}(t) = 1$. Furthermore, condition (6.145), guaranteeing that the force is continuous at $x = 0$, can be written in the form

$$\lambda_s\bar{x}_s = \lambda_u\bar{x}_u = \sqrt{\frac{2V_0\,|\lambda_s|\,\lambda_u}{\lambda_u + |\lambda_s|}} , \tag{6.158}$$

with barrier height $V_0 := V(x_{\max},t) - V(x_{\min},t)$ for $f(t) = 0$. The potential is, hence, determined by the three independent parameters λ_s, λ_u, and V_0.

For this special choice, the functions $\Lambda_{s,u}$ and $I_{s,u}$ can be easily calculated with the result:

$$\Lambda_{s,u}(t,\tilde{t}) = \lambda_{s,u}(t-\tilde{t}) , \tag{6.159}$$

$$I_s(t) = -1/\lambda_s , \tag{6.160}$$

$$I_u(t,\tilde{t}) = -\frac{1}{\lambda_u}\left(1 - e^{2\lambda_u(t-\tilde{t})}\right) . \tag{6.161}$$

The approximation (6.155,6.156) for the instantaneous escape rate can then be written in a form depending solely on the models parameters:

$$\Gamma(t_f) \approx \frac{\sqrt{|\lambda_s|\,\lambda_u}}{2\pi D}\int_{-\infty}^{t_f} dt_1\,\frac{(2\lambda_s x_s(t_1) - \lambda_s\bar{x}_s + f(t_1))\lambda_u x_u(t_1)e^{-2\lambda_u(t_f-t_1)}}{\left(1 - e^{-2\lambda_u(t_f-t_1)}\right)^{3/2}} \times \exp\left[\frac{1}{2D}\left(\lambda_s x_s(t_1)^2 - \frac{\lambda_u x_u(t_1)^2}{1 - e^{-2\lambda_u(t_f-t_1)}}\right)\right] . \tag{6.162}$$

This is still true for an arbitrary $f(t)$. The driving force enters the approximation (6.162) not only via the term in the numerator of the integrand, but also via the stable and unstable orbit $x_{s,u}(t)$. In order to give an explicit numerical example, we have to fix $f(t)$. Here we choose

$$f(t) = A\sin(\omega t) . \tag{6.163}$$

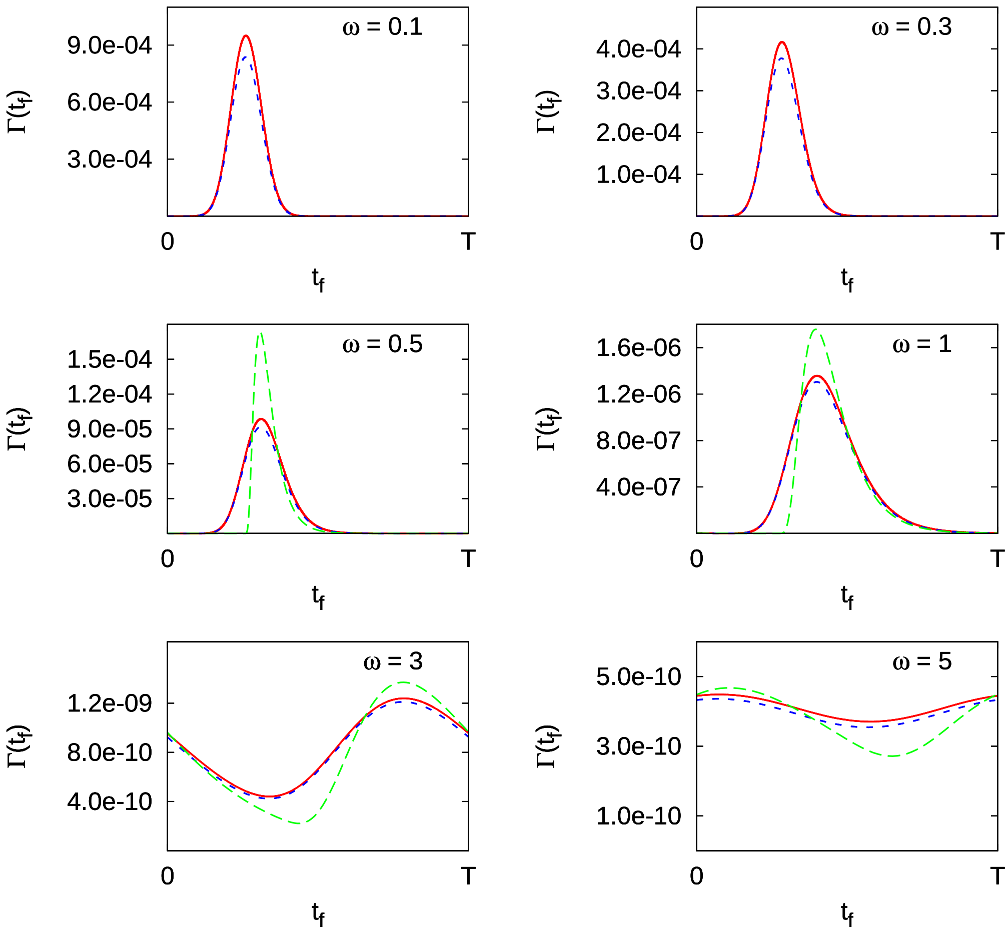

Figure 6.5: The instantaneous escape rate $\Gamma(t_f)$ for the piecewise parabolic potential (6.157) with driving force (6.163) for different driving frequencies ω. The parameters of the potential are $V_0 = 1$, $\lambda_s = -1$, $\lambda_u = 1$, $A = 0.5$, and the noise strength is $D = 0.05$. The escape rates, obtained from numerically solving the Fokker-Planck equation, are shown as red solid lines and the approximation (6.162) as blue, short-dashed lines. For the frequencies $\omega \geq 0.5$ the green, long-dashed lines show the approximations according to equations (6.168-6.175).

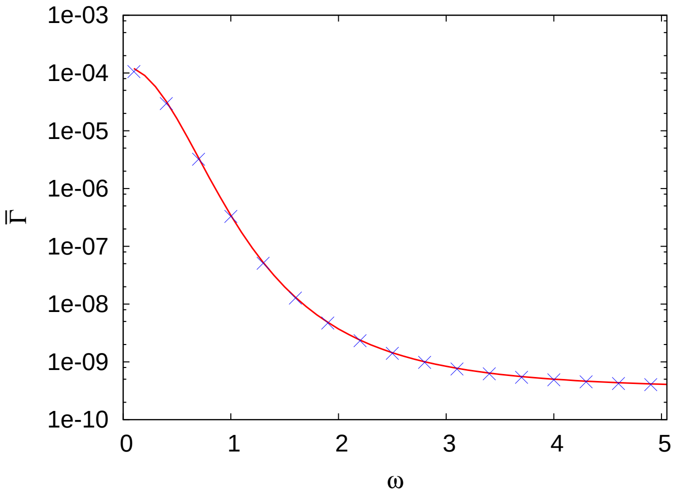

Figure 6.6: Time-averaged escape rate $\bar{\Gamma}$ for the piecewise parabolic potential (6.157) as a function of the driving frequency ω. The parameters are the same as in figure 6.5. The numerical solution of the Fokker-Planck equation is shown as the red, solid line and the approximation (6.162) as blue crosses.

For this driving term the periodic orbits are found to be:

$$x_{s,u}(t) = \bar{x}_{s,u} - \frac{A[\lambda_{s,u}\sin(\omega t) + \omega\cos(\omega t)]}{\lambda_{s,u}^2 + \omega^2} \,. \tag{6.164}$$

For various driving frequencies we have determined the instantaneous escape rates and compared them to approximation (6.162). The results are shown in figure 6.5. The approximation is very good for all these examples. For low frequencies, like $\omega = 0.1$, the escape rate strongly synchronizes with the driving force (6.163). We are in the adiabatic regime, and the peak of the escape rate has the same symmetry about its maximum as the driving force $f(t)$. With increasing ω the height of the peak shrinks more and more, and it is no longer synchronized with $f(t)$. For intermediate frequencies the peak is strongly asymmetric, and the escape rate (6.162) converges for $\omega \to \infty$ towards the escape rate of the un-driven potential, i.e., $f(t) = 0$.

In figures 6.6-6.8 the time-averaged escape rate (6.14) is depicted as a function of the driving frequency ω, amplitude A, and of the noise strength D. Again, the approximation (6.162) is very good, with a relative error that does not exceed a few percent for all shown combinations of parameters. It increases with increasing amplitude and noise strength and with decreasing driving frequency. The reason for this behavior is that the ratio Φ^*_{opt}/D of the globally minimal action and the noise strength – and thus the quality of the saddle point approximation – decreases in all these cases.

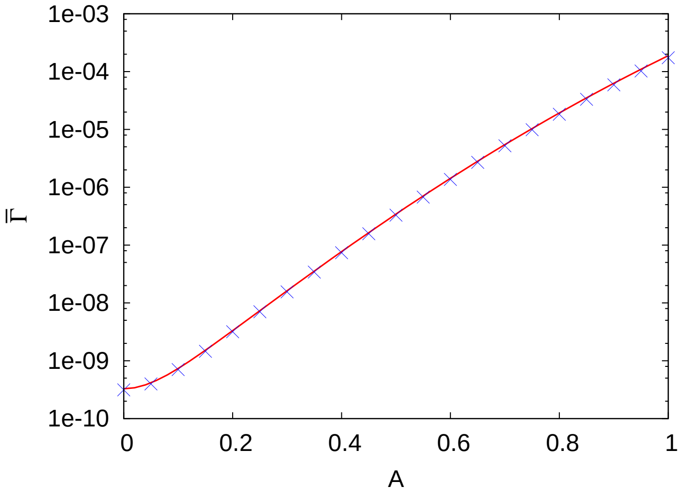

Figure 6.7: Time-averaged escape rate $\bar{\Gamma}$ for the piecewise parabolic potential (6.157) as a function of the amplitude A of the driving force (6.163) for a driving frequency $\omega = 1$. The remaining parameters are the same as in figure 6.5. The numerical solution of the Fokker-Planck equation is shown as the red, solid line and the approximation (6.162) as blue crosses.

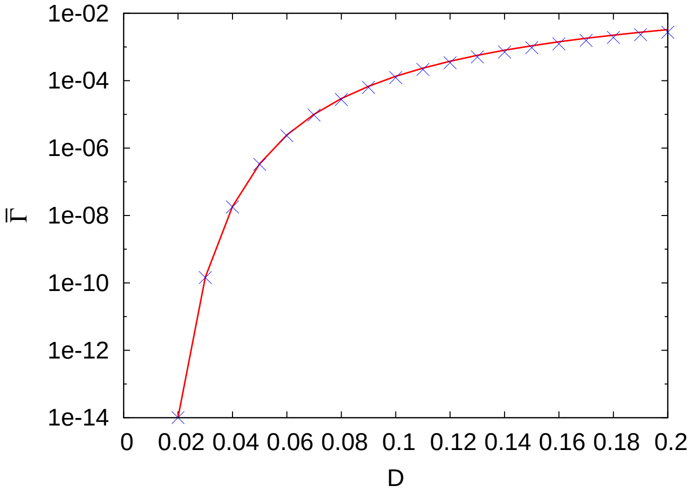

Figure 6.8: Time-averaged escape rate $\bar{\Gamma}$ for the piecewise parabolic potential (6.157) as a function of the noise strength D. The frequency of the driving term $f(t)$ is $\omega = 1$. The remaining parameters are the same as in figure 6.5. The numerical solution of the Fokker-Planck equation is shown as the red, solid line and the approximation (6.162) as blue crosses.

6.6.3 The piecewise parabolic potential: Moderately fast driving

For some limiting cases the instantaneous escape rate can be further approximated. As shown for a general potential in section 6.5, this approximation reduces to the Kramers formula (2.19) in the adiabatic and in the high frequency limit. For the piecewise parabolic potential, an alternative derivation of this result is given in appendix B.3, where we start from the integral in equation (6.162) and show that it can be further approximated in the limit of adiabatically slow driving. In this section we show that one recovers another known approximation [LRH00b] in the case of moderately strong and moderately fast driving.

We remind that the argument of the exponential function in equation (6.162) equals minus the total action $\Phi^*_{t_0}(t_1,t_f) = \Phi^*_{t_0}(t_1) + \Phi^*_{t_1}(t_f)$, divided by the noise strength D. We rewrite the total action for the potential (6.157) in the following form:

$$\Phi^*_{t_0}(t_1,t_f) = \Phi^{\mathrm{per}}_{t_0}(t_1) + \Delta\Phi_{t_0,t_f}(t_1)\ , \tag{6.165}$$

$$\Phi^{\mathrm{per}}_{t_0}(t_1) = \frac{1}{2}(\lambda_s x_s(t_1)^2 - \lambda_u x_u(t_1)^2)\ , \tag{6.166}$$

$$\Delta\Phi_{t_0,t_f}(t_1) = \frac{1}{2}\frac{e^{-2\lambda_u(t_f-t_1)}}{1-e^{-2\lambda_u(t_f-t_1)}}\lambda_u x_u(t_1)^2\ . \tag{6.167}$$

Obviously, $\Phi^{\mathrm{per}}_{t_0}(t_1)$ is periodic, i.e., $\Phi^{\mathrm{per}}_{t_0}(t_1+\mathcal{T}) = \Phi^{\mathrm{per}}_{t_0}(t_1)$, and $\Delta\Phi_{t_0,t_f}(t_1)$ vanishes for $t_f - t_1 \to \infty$. For moderately strong and moderately fast modulations, the periodic function $\Phi^{\mathrm{per}}_{t_0}(t_1)$ develops distinct minima at times $t^*_n = t^* + n\mathcal{T}$. For small noise strengths D, the integral (6.162) can then approximated by the Laplace method, yielding

$$\Gamma(t_f) \approx \sqrt{D}\gamma^{\mathrm{opt}} e^{-\Phi^{\mathrm{opt}}/D}\kappa(t_f)\ , \tag{6.168}$$

with

$$\Phi^{\mathrm{opt}} = \Phi^{\mathrm{per}}_{t_0}(t^*)\ , \tag{6.169}$$

$$\gamma^{\mathrm{opt}} = \frac{1}{\mathcal{T}}\sqrt{\frac{|\lambda_s\lambda_u|}{2\pi\ddot{\Phi}^{\mathrm{per}}_{t_0}(t^*)}}\dot{x}^*_{t_0}(t^*)\lambda_u x_u(t^*)\ , \tag{6.170}$$

$$\kappa(t_f) = \frac{\mathcal{T}}{D}\sum_{n=-\infty}^{N_{t_f}} \frac{e^{-2\lambda_u(t_f-t^*_n)}}{(1-e^{-2\lambda_u(t_f-t^*_n)})^{3/2}} e^{-\Delta\Phi_{t_0,t_f}(t^*_n)/D}\ . \tag{6.171}$$

Here N_{t_f} denotes the largest integer n for which $t^*_n < t_f$.

Approximation (6.168) is formally equivalent to that in [LRH00b]. Moreover, for the concrete choice (6.163) of the driving force, we can explicitly evaluate equations (6.168-6.171) and show that both approximations are not only formally equivalent, but coincide up to very small terms. The calculation is somehow lengthy and not very enlightening. As it is also straightforward, we omit the details here and just give the final result. The extrema of $\Phi^{\mathrm{per}}_{t_0}(t_1)$ are given by the relation

$$\tan(\omega t_1) = \frac{1}{\omega}\frac{\lambda_u\lambda_s - \omega^2}{\lambda_s + \lambda_u}\ , \tag{6.172}$$

for $\lambda_s \neq -\lambda_u$ [the equality can be treated as a limiting case]. This equation has two solutions in $[0, \mathcal{T})$, one corresponding to a maximum of the action, the other one to a minimum. We need the latter and denote it by t^*. Evaluating (6.166) at this time yields

$$\Phi^{\mathrm{opt}} = V_0 \left(1 - \left| \frac{A^2(|\lambda_s| + \lambda_u)\lambda_s\lambda_u}{2V_0\nu^4} \right|^{1/2} \right)^2 , \tag{6.173}$$

$$\nu^2 = \sqrt{(\lambda_s^s + \omega^2)(\lambda_u^2 + \omega^2)} \, . \tag{6.174}$$

The time-independent factor γ^{opt} is given by

$$\gamma^{\mathrm{opt}} = \frac{1}{\mathcal{T}\sqrt{\pi}} \frac{|\lambda_s|\,\lambda_u}{|\lambda_s| + \lambda_u} \sqrt{\Phi^{\mathrm{opt}} + \Phi^{\mathrm{opt}\;3/2} \frac{\nu^2}{|A|\,\omega^2} \sqrt{\frac{2\,|\lambda_s|\,\lambda_u}{|\lambda_s| + \lambda_u}}} \, , \tag{6.175}$$

and $\kappa(t_f)$ follows from equations (6.167,6.171) and (6.172). Figure 6.5 shows this approximation for various frequencies. For the intermediate and large ω it is relatively good. But with increasing $\mathcal{T}$ the deviations from the exact result rapidly grow.

We mention that by further approximating the denominators $(1 - e^{-2\lambda_u(t_f - t_n^*)})^\mu$ [$\mu = 1, 3/2$] in equations (6.167) and (6.171) by 1, the approximation exactly coincides with that from [LRH00b].

6.6.4 The cubic potential

Our second example is the linear-cubic potential:

$$V(x,t) = U(x) - A\sin(\omega t)x \, , \tag{6.176}$$

$$U(x) = -\frac{a}{3}x^3 + \frac{b}{2}x^2 \, , \tag{6.177}$$

with a, b some constants. The minima of the static potential $U(x)$ are located at

$$x_{\mathrm{min}} = 0 \, , \quad x_{\mathrm{max}} = b/a \, , \tag{6.178}$$

and the barrier hight is

$$V_0 = \Delta U = \frac{1}{6}\frac{b^3}{a^2} \, . \tag{6.179}$$

Alternatively to a, b one can thus also characterize the potential by the two parameters V_0 and $\Delta x = x_{\mathrm{max}} - x_{\mathrm{min}}$. The potential is point symmetric about its inflection point at $x_{\mathrm{inf}} = b/(2a)$. This suggests to place the reference level x_1 in this region.

We have already mentioned at the beginning of this section that all steps necessary for approximating the escape rate for the linear-cubic potential have to be accomplished numerically, as detailed in section 6.4.6. In figure 6.9 (a) we compare the contributions of the two terms, Γ_0 and Γ_1, to the approximation (6.54-6.56) for one

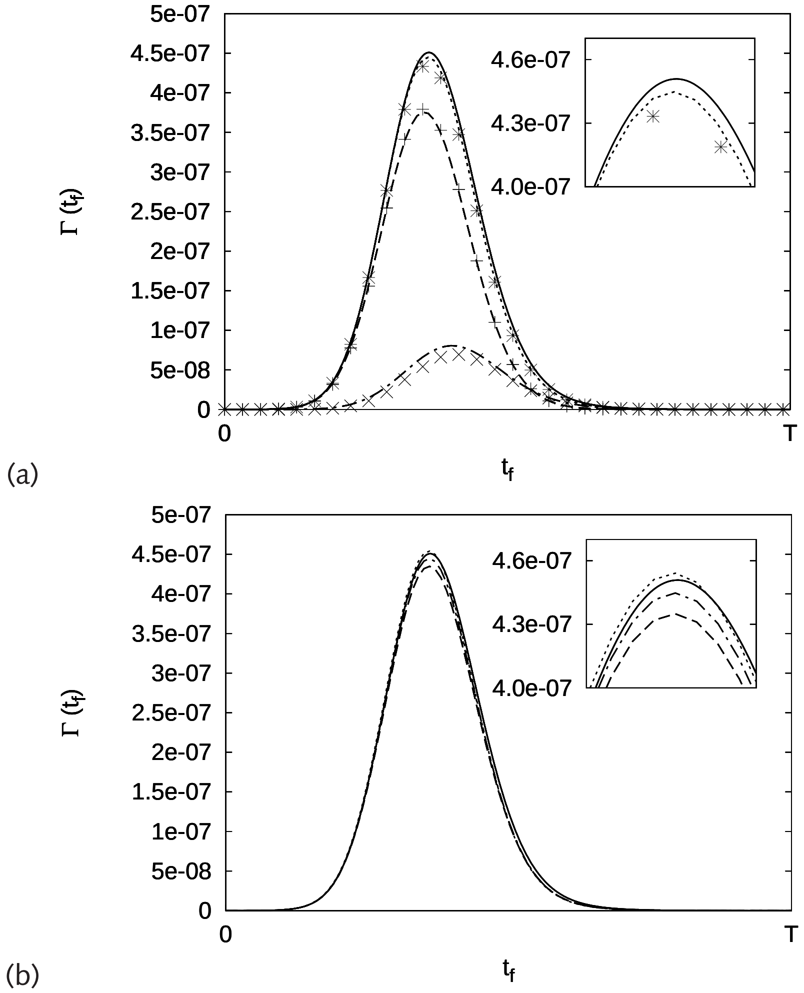

Figure 6.9: The instantaneous escape rate for the linear-cubic potential (6.176,6.177). The parameters of the potential are $V_0 = 1$, $\Delta x = 1.5$, $A = 0.3$, $\omega = 1$, and the noise strength is $D = 0.05$. In (a) the reference level is placed at the inflection point at $x_1 = 0.75$, and the different contributions to the approximation of the escape rate $\Gamma(t) = \Gamma_0(t) + \Gamma_1(t)$ are compared. The solid line shows the exact result, obtained from numerically solving the Fokker-Planck equation (6.11). The dashed line corresponds $\Gamma_0(t)$ as defined in equation (6.55) and the dashed-dotted line to the first-correction $\Gamma_1(t)$ from equation (6.56). The dotted line is the sum of these terms. The points correspond to the approximation in terms of the asymptotic paths, as described in section 6.4.6. In (b) the exact result (solid line) is compared to the approximations $\Gamma(t)$ obtained for different reference levels: $x_1 = 0.6$ (dotted), $x_1 = 0.75$ (dashed-dotted), and $x_1 = 0.9$ (dashed). In both figures the inset shows an amplification of the peak.

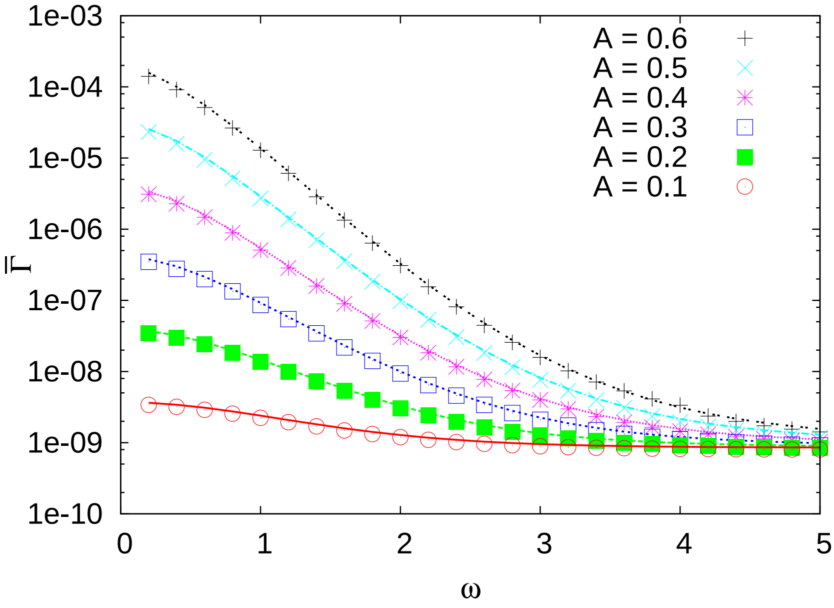

Figure 6.10: Time-averaged escape rate $\bar{\Gamma}$ for the linear-cubic potential (6.176,6.177) as a function of the driving frequency ω for different modulation amplitudes A. The parameters of the potential are $V_0 = 1$, $\Delta_x = 1.5$, and the noise strength is $D = 0.05$. The lines correspond to the exact result and the points to the approximation in terms of the asymptotic paths. The reference level was placed at $x_1 = 0.9$.

set of parameters. Although the noise strength $D = 0.05$ for this example is rather small compared to V_0, the first correction Γ_1 is still not negligible. For other sets of parameters and the same V_0/D, the situation is very similar. On the other hand, approximating the quantities further in terms of the asymptotic paths (cf. section 6.4.5) yields nearly the same result as the full approximation. In figure 6.9 (b) the influence of the reference level is examined. The dependence of the approximation on this choice is rather small as long as x_1 is not too close to either the stable or the unstable orbit. Again, the situation does not change much when approximating the quantities in terms of the asymptotic paths (data not shown).

In figure 6.6.4 we have determined the time-averaged escape rate (6.14) as a function of the driving frequency ω for various modulation amplitudes A. For the whole range of parameters the approximation in terms of the asymptotic paths is very good.

The approximation scheme was also tested for other potentials, like cosine or double-well potentials of the form $V(x,t) = ax^4 - bx^2 - f(t)x$. The results for these potentials are comparable to the results shown in this section for the linear-cubic potential.

6.7 Time-dependent temperatures

Let us again consider the Langevin equation (6.1) with a time-dependent noise strength $D(t) = Dg(t)$, i.e.,

$$\dot{x}(t) = F\left(x(t),t\right) + \sqrt{2Dg(t)}\xi(t) \ , \tag{6.180}$$

$$\lim_{t\to\infty} \frac{1}{t}\int_0^t dt\, g(t) = 1 \ , \quad g(t) > 0 \ . \tag{6.181}$$

In section 6.2.3 we have discussed that, by introducing an auxiliary time $\hat{t}$ and an auxiliary force $\tilde{F}$ via equations (6.17,6.19), this problem can be mapped to an equivalent problem (6.18) with a time-independent noise strength D. Then, the instantaneous rate $\tilde{\Gamma}(\hat{t})$ of escape from the auxiliary force field in the auxiliary time can be approximated as described in section 6.4, and the escape rate for the original problem (6.180) follows as $\Gamma(t) = g(t)\tilde{\Gamma}(\hat{t}(t))$, cf. equation (6.20).

That means, in order to approximate the escape rate, again, the differential equations (6.28,6.29,6.33,6.40,6.41,6.44) have to be solved, but now in the auxiliary time $\hat{t}$ and for the effective force field $\tilde{F}$. For practical purposes, it may, however, be more convenient to transform these equations back to the original time t and the original force F, so that the mapping $t \to \hat{t}$ does not have to be inverted. Doing so, the equations for the optimizing path read:

$$\dot{x}^*(t) \quad = 2g(t)p^*(t) + F(x^*(t),t) \ , \tag{6.182}$$

$$\dot{p}^*(t) \quad = -p^*(t)F'(x^*(t),t) \ , \tag{6.183}$$

with $x^*(t_0) = x_0$ and $x^*(t_f) = x_f$, and $\mathcal{D}_x, \mathcal{D}_p$ are determined by

$$\dot{\mathcal{D}}_x(t) \quad = \quad F'(t)\mathcal{D}_x(t) + 2g(t)\mathcal{D}_p(t) \ , \tag{6.184}$$

$$\dot{\mathcal{D}}_p(t) \quad = \quad -p^*(t)F''(t)\mathcal{D}_x(t) - F'(t)\mathcal{D}_p(t) \ , \tag{6.185}$$

with $\mathcal{D}_x(t_0) = 0$ and $\mathcal{D}_x(t_f) = 1$. The action along the optimizing path becomes

$$\Phi^*(x_f, t_f | x_0, t_0) = \int_{t_0}^{t_f} dt \; g(t) p^*(t)^2 \; . \qquad (6.186)$$

Analogously, we find the differential equation for the prefactor Q^*:

$$\frac{1}{2} \frac{d}{dt} \left[\frac{\dot{Q}^*(t)}{g(t)} \right] = \frac{d}{dt} \left[\frac{Q^*(t) F'(t)}{g(t)} \right] - Q^*(t) p^*(t) F''(t) \; , \qquad (6.187)$$

with

$$Q^*(t_0) = 0, \quad \dot{Q}^*(t_0) = g(t_0) \; , \qquad (6.188)$$

and the equation for its derivative Z^* with respect to the final position:

$$\frac{1}{2} \frac{d}{dt} \left[\frac{\dot{Z}^*(t) - 2F'(t) Z^*(t)}{g(t)} \right] + p^*(t) F''(t) Z^*(t) = H(t) \; , \qquad (6.189)$$

with

$$H(t) = \frac{d}{dt} \left[\frac{F''(t) Q^*(t) \mathcal{D}_x(t)}{g(t)} \right] - F''(t) Q^*(t) \mathcal{D}_p(t) - F'''(t) p^*(t) Q^*(t) \mathcal{D}_x(t) \; , \qquad (6.190)$$

and initial conditions

$$Z^*(t_0) = 0, \quad \dot{Z}^*(t_0) = 0 \; . \qquad (6.191)$$

Finally, the instantaneous escape rate follows according to equations (6.54-6.56) and (6.20) as:

$$\begin{aligned} \Gamma(t_f) &= \Gamma_0(t_f) + \Gamma_1(t_f) + \Gamma_0(t_f) * \mathcal{O}(D) \; , & (6.192) \\ \Gamma_0(t_f) &= g(t_f) \int_{t_0}^{t_f} dt_1 \; \Psi_{t_0}(t_1) \frac{p^*_{t_1}(t_f) e^{-\Phi^*_{t_1}(t_f)/D}}{\sqrt{4\pi D Q^*_{t_1}(t_f)}} \; , & (6.193) \\ \Gamma_1(t_f) &= g(t_f) \int_{t_0}^{t_f} dt_1 \; \Psi_{t_0}(t_1) \frac{D Z^*_{t_1}(t_f) e^{-\Phi^*_{t_1}(t_f)/D}}{2 Q^*_{t_1}(t_f) \sqrt{4\pi D Q^*_{t_1}(t_f)}} \; , & (6.194) \\ \Psi_{t_0}(t_1) &= \dot{x}^*_{t_0}(t_1) \frac{e^{-\Phi^*_{t_0}(t_1)/D}}{\sqrt{4\pi D Q^*_{t_0}(t_1)}} \; . & (6.195) \end{aligned}$$

Examples for the escape of Brownian particles from static potentials in a time-dependent thermal environment will be discussed in the next chapter.

7 Escape from time-dependent systems with multiple metastable states: Suppression of thermally activated escape by heating

In the previous chapter we have considered Brownian particles in a force field with a single metastable state. Both, the thermal environment, modeled by a Gaussian white noise and a friction force, and the force field were allowed to be time-dependent. We have worked out an approximation scheme for the instantaneous escape rate and shown that it deviates strongly from the Kramers rate for fast modulations. In this chapter we extend this discussion to potentials with multiple metastable states. Particular attention will be paid to Brownian particles in a static potential under the influence of a time-dependent thermal environment [LCH97, ER04a, IW08, LHL08]. While for small, constant noise strengths always the energetically lowest metastable state is preferentially occupied, we show that this situation may change for time-dependent temperatures. Especially, the effective escape rate from a potential with several metastable states may *decrease* upon temporally *increasing* the temperature. Indeed, given that thermal noise is indispensable to escape, one would expect that an "extra dose" of noise should always enhance escape. The result is thus unexpected and counter-intuitive. Similar previous findings were always obtained for quite different types of systems: Dissipative quantum tunneling in the deep cold [GZC92], models without a barrier against deterministic escape [MS96b, Rei96], or non-dynamical systems [VR01].

7.1 Model

7.1.1 Dynamics

Let us consider a Brownian particle in a potential $V(x,t)$ which should depend on time solely via a multiplicative, strictly positive function $h(t)$, i.e.,

$$F(x,t) = -V'(x,t) = -h(t)U'(x) \ . \tag{7.1}$$

Experimentally, such a situation may be realized by colloidal particles in a suitably designed potential landscape. This can be achieved by exploiting light [ADBC86, BSPB04, LLPG05, BRB07], dielectrophoretic [RSAP94, FL95], or magnetic [HW00,

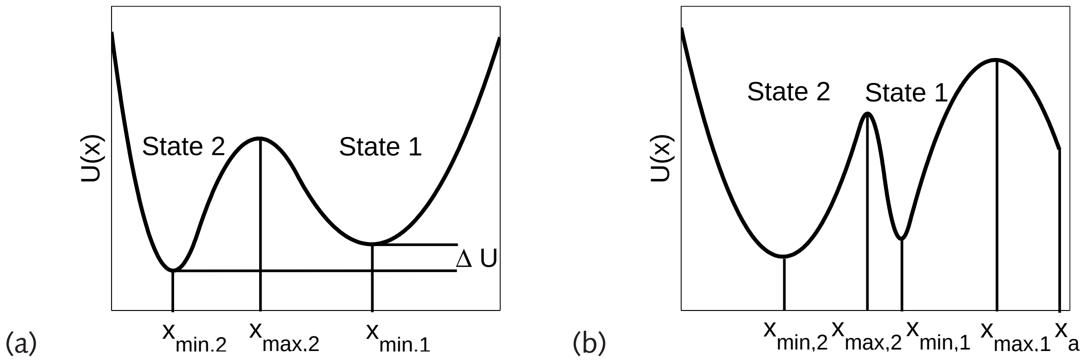

Figure 7.1: (a) Schematic sketch of a potential with two metastable states. The potential in (b) has an additional potential barrier and an absorbing boundary. Both potentials were built up of jointed parabolas.

EMRJ03, ER04b, Gij04, Pam06] forces. The potential $U(x)$ is assumed to have $N \geq 2$ minima $x_{\min,i}$, $i = 1 \ldots N$. We will distinguish the cases that (i) the potential is confining with $N-1$ maxima $x_{\max,i}$, $i = 2 \ldots N$, and:

$$x_{\min,N} \leq x_{\max,N} \leq x_{\min,N-1} \leq \cdots \leq x_{\max,2} \leq x_{\min,1} \ , \quad \text{(case 1)} \ , \tag{7.2}$$

and that (ii) the potential has an additional maximum $x_{\max,1}$ and an absorbing boundary at $x_a > x_{\max,1}$, with

$$x_{\min,N} \leq x_{\max,N} \leq \cdots \leq x_{\min,1} \leq x_{\max,1} \leq x_a \ , \quad \text{(case 2)} \ . \tag{7.3}$$

Examples for the two cases with $N = 2$ are shown in figure 7.1. Due to the chosen form of the time-dependence of the potential, the minima correspond to stable orbits of the deterministic dynamics and the maxima to unstable orbits. We can, therefore, define N distinct basins of attraction:

$$\mathcal{A}_1 := \begin{cases} \{x \in \mathbb{R} \mid x > x_{\max,2}\} \ , & \text{(case 1)} \\ \{x \in \mathbb{R} \mid x_{\max,2} < x < x_{\max,1}\} \ , & \text{(case 2)} \end{cases} \ , \tag{7.4}$$

$$\mathcal{A}_i := \{x \in \mathbb{R} \mid x_{\max,i+1} < x < x_{\max,i}\} \ , \quad i = 2 \ldots N-1 \ , \tag{7.5}$$

$$\mathcal{A}_N := \{x \in \mathbb{R} \mid x < x_{\max,N}\} \ , \tag{7.6}$$

and we will say that the system is in state i if $x \in \mathcal{A}_i$ (cf. figure 7.1).

The dynamics of the Brownian particle in a time-dependent (spatially homogeneous) thermal environment can be modeled by equations (6.180,7.1), i.e.,

$$\dot{x}(t) = -h(t)U'(x(t)) + \sqrt{2Dg(t)}\xi(t) \ , \tag{7.7}$$

with Gaussian white noise $\xi(t)$ or, as discussed in sections 2.3 and 6.2, equivalently by the Fokker-Planck equation (6.11). We will assume in the following that $h(t)$ and

$g(t)$ are time-periodic with a common period $\mathcal{T}$. In presence of the fluctuation force $\sqrt{2Dg(t)}\xi(t)$, transitions between states i and $i \pm 1$ are allowed. If these transitions are rare events, the dynamics can alternatively also be described by a one-step master equation:

$$\begin{aligned}
\dot{n}_1(t) &= \begin{cases} -\Gamma_{1,2}(t)n_1(t) + \Gamma_{2,1}(t)n_2(t) \ , & \text{(case 1)} \\ -(\Gamma_{1,2}(t) + \Gamma_{1,0}(t))n_1(t) + \Gamma_{2,1}(t)n_2(t) \ , & \text{(case 2)} \end{cases} \ , && (7.8) \\
\dot{n}_i(t) &= -(\Gamma_{i,i-1}(t) + \Gamma_{i,i+1}(t))n_i(t) + \Gamma_{i-1,i}(t)n_{i-1}(t) && (7.9) \\
&\quad +\Gamma_{i+1,i}(t)n_{i+1}(t) \ , \quad i = 2 \ldots N-1 \ , \\
\dot{n}_N(t) &= -\Gamma_{N,N-1}(t)n_N(t) + \Gamma_{N-1,N}(t)n_{N-1}(t) \ , && (7.10)
\end{aligned}$$

where $n_i(t)$ denotes the probability to find the system in state i at time t, $\Gamma_{i,j}(t)$, $i, j \geq 1$, the instantaneous transition rate from state i to state j, and $\Gamma_{1,0}(t)$ the instantaneous escape rate from state 1 over the potential barrier at $x_{\max,1}$. These rates can be approximated as described in chapter 6. In the following, we will write equations (7.8-7.10) in the form

$$\dot{\mathbf{n}}(t) = -\mathbf{G}(t)\mathbf{n}(\mathbf{t}) \ , \tag{7.11}$$

where $\mathbf{n}(t) = (n_1(t), \ldots, n_N(t))$ is an N-dimensional vector and $\mathbf{G}(t)$ a tridiagonal $N \times N$ matrix.

If $\int_0^{\mathcal{T}} dt \ \Gamma_{i,j}(t) \ll 1$ for all i, j, the rates in equations (7.8-7.10) may also be replaced by the concomitant time-averaged rates $\bar{\Gamma}_{i,j} = 1/\mathcal{T} \int_0^{\mathcal{T}} dt \ \Gamma_{i,j}(t)$, and the probabilities by the averaged probabilities $\bar{n}_i(t) = 1/\mathcal{T} \int_{t-\mathcal{T}/2}^{t+\mathcal{T}/2} dt' \ n_i(t')$, leading to the following dynamics:

$$\dot{\bar{\mathbf{n}}}(t) = -\bar{\mathbf{G}}\bar{\mathbf{n}}(\mathbf{t}) \ , \tag{7.12}$$

where $\bar{\mathbf{G}}$ corresponds to the matrix $\mathbf{G}(t)$ in equation (7.11).

7.1.2 Case 1: Equilibrium condition

Let us first study case 1 of a confining potential [cf. figure 7.1(a)]. Obviously, the probability

$$n(t) := \sum_{i=1}^{N} n_i(t) \ , \tag{7.13}$$

to find the particle in any of the N states is 1 for all times. However, for time-dependent functions $h(t)$ and $g(t)$, in general, no stationary solution $\mathbf{n}(\mathbf{t})$ of equation (7.11) exists. This situation changes when considering the time-averaged dynamics (7.12). Then, one can show that $\bar{\mathbf{n}}(\mathbf{t})$ equilibrates to a stationary distribution $\mathbf{n_{eq}} = (n_{eq,1}, \ldots, n_{eq,N})$, independently of the initial condition. As can be easily seen from the dynamics, this stationary distribution obeys detailed balance:

$$\bar{\Gamma}_{i,i+1}n_{eq,i} = \bar{\Gamma}_{i+1,i}n_{eq,i+1} \ , \quad i = 1, \ldots, N-1 \ . \tag{7.14}$$

For time-independent potentials and noise strengths, i.e., $h(t) = g(t) = 1$, the single transition rates are given by the Kramers rate (2.19). Denoting the stationary distribution for this case by $\mathbf{n_{stat}}$, equation (7.14) becomes

$$\frac{n_{stat,i}}{n_{stat,j}} = \sqrt{\frac{U''(x_{\min,j})}{U''(x_{\min,i})}} \exp(-(U(x_{\min,i}) - U(x_{\min,j}))/D) \ , \tag{7.15}$$

showing that with decreasing noise strength D and temperature, respectively, preferentially the energetically lowest state is occupied. Making further use of the normalization of $\mathbf{n_{stat}}$, one gets

$$n_{stat,k} = \frac{1}{\sum_{i=1}^{N} \sqrt{\frac{U''(x_{\min,k})}{U''(x_{\min,i})}} \exp(-(U(x_{\min,i}) - U(x_{\min,k}))/D)} \ , \tag{7.16}$$

for all $k = 1, \ldots, N$.

7.1.3 Case 2: Effective escape rate

If the potential has an additional maximum at $x_{\max,1}$ and an absorbing boundary at x_a, the total probability $n(t)$ is a monotonically decreasing function of time. However, if the potential barrier at $x_{\max,1}$ is the dominant one, i.e., $U(x_{\max,1})$ much larger than all other $U(x_{\max,i})$, the time-averaged distribution $\bar{\mathbf{n}}(t)$ will at first relax to a quasi-stationary distribution $\mathbf{n_{eq}}(t)$, which approximately obeys detailed balance (7.14). Then, the effective time-averaged escape rate from the potential can be defined as

$$\bar{\Gamma} := \frac{n_{eq,1}(t)}{n(t)} \bar{\Gamma}_{1,0} \ , \tag{7.17}$$

where $n_{eq,1}(t)/n(t)$ is, according to our above assumption, time-independent for sufficiently large times t. Alternatively, if $U(x_{\max,1})$ is not much higher than the other maxima (but still the highest), the time needed to reach the quasi-equilibrium state can be of similar order as the typical time $1/\bar{\Gamma}_{1,0}$, which a particle starting in state 1 needs to escape over the potential barrier $x_{\max,1}$ if transitions to other states are prohibited. Then, depending on the initial distribution $\mathbf{n}(t_0)$, it can take a very long time for the right-hand side of equation (7.17) to become time-independent. In this case, it is advantageous to define the effective time-averaged escape rate as the lowest eigenvalue of the matrix $\bar{\mathbf{G}}$, i.e.,

$$\bar{\Gamma} := \min(\mathrm{Eig}(\bar{\mathbf{G}})) \ , \tag{7.18}$$

and the quasi equilibrium distribution $\mathbf{n_{eq}}(t)$ as the corresponding eigenvector (with time-dependent normalization constant). If the barrier at $x_{\max,1}$ is the dominant one, this definition becomes equivalent to (7.17) so that in the following definition (7.18) will be used.

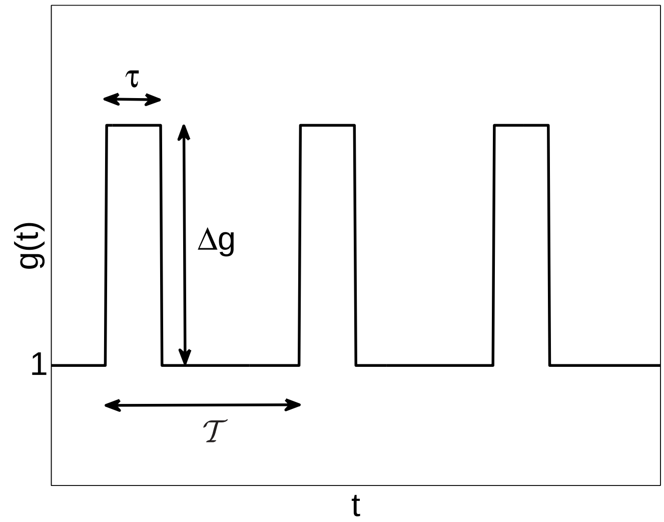

Figure 7.2: Time-dependence of the noise strength $D(t) = Dg(t)$.

For time-independent noise strengths and potentials, the Kramers approximation (2.19) and equation (7.16) can be used again, and if $x_{\max,1}$ is the dominant barrier, equation (7.17) becomes

$$\bar{\Gamma} = \frac{\sqrt{|U''(x_{\max,1})|}}{2\pi} \frac{\exp(-U(x_{\max,1})/D)}{\sum_{i=1}^{N} \sqrt{\frac{1}{U''(x_{\min,i})}} \exp(-U(x_{\min,i})/D)} \,. \tag{7.19}$$

Hence, in the time-independent case the effective escape rate is an increasing function of the noise strength and temperature, respectively.

7.1.4 Temperature modulations

In section 6.2.3 we have discussed that the problem of an overdamped particle in a fluctuating potential is equivalent to that of an overdamped particle in a static potential with an effective time-dependent noise strength $D(t) = Dg(t)$. We can, therefore, without loss of generality, restrict our discussions to the case of a static potential, i.e., $h(t) = 1$ in equation (7.1). Furthermore, from a practical point of view, this situation can be realized more easily in real experiments. One may, for example, think of short laser pulses which heat the neighborhood of the particle. If the period between the laser pulses is sufficiently large, the heat can dissipate to the environment after switching off the laser, so that the original temperature (or noise strength) is reached before the next laser pulse. Another possible realization is a second heat bath which can be temporarily switched on.[1] This bath can be a "magnetic bath" where a random magnetic field interacts with a paramagnetic particle or an "acoustomechanical bath" generated by piezo elements [CSJG07], to name only two possibilities.

In this chapter we consider a rectangular variation of the noise strength where $g(t)$ periodically switches between the values 1 and $1+\Delta g$ (see figure 7.2):

$$g(t) = 1 + \Delta g \; \Theta(\tau - (t \mod \mathcal{T})) \; , \tag{7.20}$$

with $\Theta(\cdot)$ the Heaviside step function and $\mod$ the modulus-function. The pulse strength is denoted by Δg and the pulse length by τ which should be shorter than the period $\mathcal{T}$.

7.1.5 Model potential

For the calculations in this chapter we use a potential of jointed parabolas (for an example see figure 7.1). Assuming that the force is continuous, we have discussed in section 6.6.1 (for $N = 1$) that such a potential is uniquely characterized by the values of the potential $U(x_{\mathrm{min,max},i})$ at the extrema and by the values of curvature $\lambda_{s,u,i} = -U''(x_{\mathrm{min,max},i})$ at these points. This choice has the advantage that, up to a simple numerical integration, all calculations can be done analytically.

7.2 Transition rate

Next, we will derive approximations for the transition rates $\Gamma_{i,i\pm1}(t)$ and $\bar{\Gamma}_{i,i\pm1}$, respectively. As already discussed, for sufficiently small noise strengths (meaning that the potential barrier is large compared to $Dg(t)$ for all times), these rates can be approximated as described in chapter 6 (particularly in section 6.7). Considering only period lengths $\mathcal{T} \gg \tau$ and $\mathcal{T} \gg \tau_R$, we can focus on a single pulse

$$g_s(t) = 1 + \Delta g \; \Theta(t) \; \Theta(\tau - t) \; . \tag{7.21}$$

The transition rates for the single pulse will be denoted by $\Gamma^s_{i,i\pm1}(t)$ and $\bar{\Gamma}^s_{i,i\pm1}$, respectively. The rates for our original time-periodic problem are then approximately

$$\begin{aligned} \Gamma_{i,i\pm1}(t) &= \Gamma^s_{i,i\pm1}(t \mod \mathcal{T}) \; , && (7.22) \\ \bar{\Gamma}_{i,i\pm1} &= \bar{\Gamma}^s_{i,i\pm1} = \frac{1}{\mathcal{T}} \int_0^{\mathcal{T}} dt \; \Gamma^s_{i,i\pm1}(t) \; . && (7.23) \end{aligned}$$

Without loss of generality, we can restrict our discussions to transitions from state i to state $i-1$, i.e., from a minimum at $x_{\mathrm{min,i}}$ over a barrier of height $\Delta U_{i,i} = U(x_{\mathrm{max,i}}) -$

---

[1] Two heat bathes at different temperatures, with fluctuation forces modeled by Gaussian white noises, can be replaced by an effective heat bath with an effective temperature.

$U(x_{\mathrm{min,i}})$ at $x_{\mathrm{max,i}}$.[2] The condition that the force is everywhere continuous requires that the parabolas are jointed at q_i with [cf. equation (6.158)]

$$\lambda_{s,i}(x_{\mathrm{min,i}} - q_i) = \lambda_{u,i}(x_{\mathrm{max,i}} - q_i) = \sqrt{\frac{2\Delta U_{i,i}|\lambda_{s,i}|\lambda_{u,i}}{|\lambda_{s,i}| + \lambda_{u,i}}} \; . \tag{7.24}$$

Having now completely specified the problem, the transition rate can be approximated by solving the set of differential equations given in section 6.7. Again, if $|U(q_i) - U(x_{\mathrm{min,max},i})|$ is sufficiently large compared to the noise strength, the reference level $x_1 = q_i$ can be chosen. For this choice a straightforward calculation shows that the solutions for the optimal path, action, and the prefactor have the same functional form as in equations (6.148-6.151,6.153,6.154) for the case of a time-dependent potential with a constant noise strength (section 6.6.1). The only difference is that $x_{s,u}(t_1)$ in these equations have to be replaced by $x_{\mathrm{min,i}} - q_i$ and $x_{\mathrm{max,i}} - q_i$, respectively, and that the functions $I_{s,u} = I_{s,u,i}$ have a slightly different definition, namely

$$\begin{aligned} I_{s,i}(t) &:= 2\int_{-\infty}^{t} dt'\, g(t') e^{2\Lambda_{s,i}(t,t')} \; , &(7.25)\\ I_{u,i}(t,\tilde{t}) &:= 2\int_{\tilde{t}}^{t} dt'\, g(t') e^{2\Lambda_{u,i}(t,t')} \; , &(7.26)\\ \Lambda_{s,u,i}(t,\tilde{t}) &:= \lambda_{s,u,i}(t-\tilde{t}) \; , &(7.27)\end{aligned}$$

As in the case of a time-independent noise strength, the derivative $Z^*_{t_1}(t_f)$ of the prefactor vanishes, and together with equations (6.182,6.193,6.195) we arrive at the following approximation for the transition rate:

$$\begin{aligned} \Gamma_{i,i-1}(t) &= -\frac{g(t)(x_{\mathrm{min,i}} - q_i)(x_{\mathrm{max,i}} - q_i)}{2\pi D} &(7.28)\\ &\quad \times \int_{-\infty}^{t} dt_1 \left[\frac{2g(t_1)}{I_{s,i}(t_1)} + \lambda_{s,i}\right] \frac{e^{-2\lambda_{u,i}(t-t_1)}}{\sqrt{|I_{s,i}(t_1) I^3_{u,i}(t_1,t)|}} e^{-\Phi^*_{t_0}(t_1,t)/D} \; , \\ \Phi^*_{t_0}(t_1,t) &= \frac{1}{2}\left(\frac{(x_{\mathrm{min,i}} - q_i)^2}{I_{s,i}(t_1)} - \frac{(x_{\mathrm{max,i}} - q_i)^2}{I_{u,i}(t_1,t)}\right) \; . &(7.29)\end{aligned}$$

Hence, the instantaneous transition rate (7.28) is the product of a continuous function in t (the integral) and the discontinuous $g(t)$ and is hence discontinuous itself. Furthermore, for the special choice (7.21) for $g(t)$ the functions $I_{s,i}(t)$ and $I_{u,i}(t,\tilde{t})$ can be explicitely evaluated with the result:

$$I_{s,i}(t_1) = -\frac{1}{\lambda_{s,i}} \begin{cases} 1 & \text{if } t_1 \le 0 \\ 1 + \Delta g - \Delta g\, e^{2\lambda_{s,i} t_1} & \text{if } 0 < t_1 \le \tau \\ 1 + \Delta g\, e^{2\lambda_{s,i} t_1}(e^{-2\lambda_{s,i}\tau} - 1) & \text{else} \end{cases} \tag{7.30}$$

---

[2] The transition rate from state i to a state $i+1$ follows from considering the potential $U(-x)$.

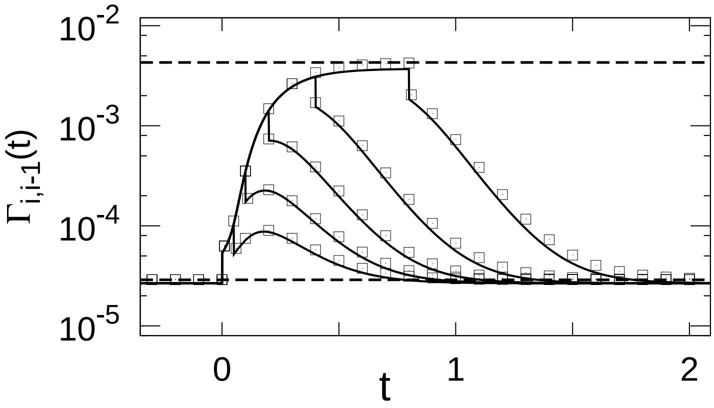

Figure 7.3: Time-dependent transition rates for a piecewise parabolic potential with a well at $x_{\rm min,i} = 0$, a barrier at $x_{\rm max,i} = 1$, curvatures $\lambda_{s,i} = -4$, $\lambda_{u,i} = 4$, and barrier height $\Delta U_{i,i} = 1$. The escape rates were calculated for $D = \Delta g D = 0.1$, and $\tau = 0.05$, $\tau = 0.1$, $\tau = 0.2$, $\tau = 0.4$, $\tau = 0.8$ (bottom up). Squares: Precise numerical solutions obtained from numerically solving the Fokker-Planck equation. Solid lines: Analytical approximation (7.28-7.31). Dashed lines: Kramers rates (2.19) for D (bottom) and $(1 + \Delta g)D$ (top).

and

$$I_{u,i}(t_1,t) = -\frac{1-e^{-2\lambda_{u,i}(t-t_1)}}{\lambda_{u,i}} - \frac{\Delta g}{\lambda_{u,i}} \begin{cases} e^{2\lambda_{u,i}t_1}(1-e^{-2\lambda_{u,i}t}) & \text{if } t_1 \le 0 < t \le \tau \\ e^{2\lambda_{u,i}t_1}(1-e^{-2\lambda_{u,i}\tau}) & \text{if } t_1 \le 0 < \tau < t \\ 1-e^{-2\lambda_{u,i}(t-t_1)} & \text{if } 0 < t_1 < t \le \tau \\ 1-e^{-2\lambda_{u,i}(\tau-t_1)} & \text{if } 0 < t_1 < \tau \le t \\ 0 & \text{else} \end{cases} . \quad (7.31)$$

The remaining integrals for the instantaneous transition rate in equation (7.28) and for the time-averaged rate in equation (7.23) have to be calculated numerically.

As an example, we consider the piecewise parabolic potential with a well at $x_{\rm min,i} = 0$, a barrier at $x_{\rm max,i} = 1$, curvatures $\lambda_{s,i} = -4$, $\lambda_{u,i} = 4$, and barrier height $\Delta U_{i,i} = 1$. Already for the moderately small noise strength used in figure 7.3, the accuracy of the analytical approximation (7.28-7.31) is quite good. We found that it quickly improves even further upon decreasing temperatures. Up to small errors, the Kramers rate is recovered until the temperature pulse sets in at $t = 0$. Then, the rate rapidly increases and approaches the Kramers rate corresponding to $(1+\Delta g)D$, provided the pulse lasts sufficiently long. Finally, an analogous relaxation back to the original Kramers rate follows. While the initial transients are well understood [Shn97, BDKA99, SSLM01], to the best of our knowledge no previously existing analytical approximation would be able to faithfully describe the "perturbed and interfering transients" for largely arbitrary pulses and pulse-sequences.

The discontinuity of the rates at the beginning and at the end of the pulses, which has been discussed below equation (7.29), can be observed for all pulse lengths, for both, the approximation and the exact solution obtained from solving the Fokker-Planck equation (for reasons of better visibility only a few points are depicted). In the case of very short pulses (e.g. $\tau = 0.1$), the instantaneous rate increases again after this sudden drop at the end of the pulse, resulting in the spikes which can also be observed in the exact solution. At first glance these peaks might appear unnatural, but the physical mechanism behind them is clear. A particle can benefit most from the additional energy provided by the pulse if it is during the pulse in the region of the steepest slope of the potential (the largest repulsive force). There, most of the action is accumulated. Such a particle following the optimal path reaches the maximum after the end of the pulse. Hence, the probability to find the particle at the unstable orbit is a continuous function of time. But also the noise, which determines the average absolute value of the velocity, enters the expression for the transition rate. This function is by choice not continuous. The rate is thus the product of a term which reaches its maximum value after the pulse and a term which suddenly drops at the end of the pulse, resulting in the observed time-dependence for small τ.

We note that the analogous case of a time-independent noise strength and a fluctuating potential can be treated in the same way. The resulting formulas and approximations are derived in appendix C.

7.3 The quasi-stationary distribution

Having discussed how the transition rates between the single states can be approximated for a piecewise parabolic potential in presence of a fluctuating noise strength, we now study how the (quasi) stationary distribution $\mathbf{n_{eq}}$, introduced in section 7.1.2, depends on the pulse length τ, the pulse strength Δg, and the un-modulated noise strength D.

Let us consider the potential shown in figure 7.4(a) with just two metastable states, i.e., $N = 2$. As discussed above, this potential is fully specified by the values of the potential at the extrema: $U(x_{\min,2}) = 0$, $U(x_{\max,2}) = 1$, and $U(x_{\min,1}) = 0.2$ and by the values of the curvature: $(\lambda_{s,2}, \lambda_{u,2}, \lambda_{s,1}) = (-5, 5, -1)$. In figure 7.4(b) the instantaneous transition rates are depicted for a pulse strength $\Delta g = 1.0$, a pulse length $\tau = 4$, and $D = 0.05$. As a consequence of the smaller noise strength, the error of the approximation is smaller than that in figure 7.3 [data not shown]. After "switching on" the additional noise, the time scales on which the single rates converge to the Kramers rate corresponding to the noise strength $(1 + \Delta g)D$ are quite different for the two transitions. $\Gamma_{2,1}(t)$ initially increases much faster than $\Gamma_{1,2}(t)$ and reaches accordingly the final value faster. This can be understood by considering the intrinsic time scales of the potential for the two transitions. These are $-1/\lambda_{s,1}$ and $1/\lambda_{u,2}$ for the transition from state 1 to state 2, and $-1/\lambda_{s,2}$ and $1/\lambda_{u,2}$ for the transition from state 2 to state 1. A comparison with equations (7.28-7.31) shows that these are indeed the relevant time scales which enter the approximation of the instantaneous

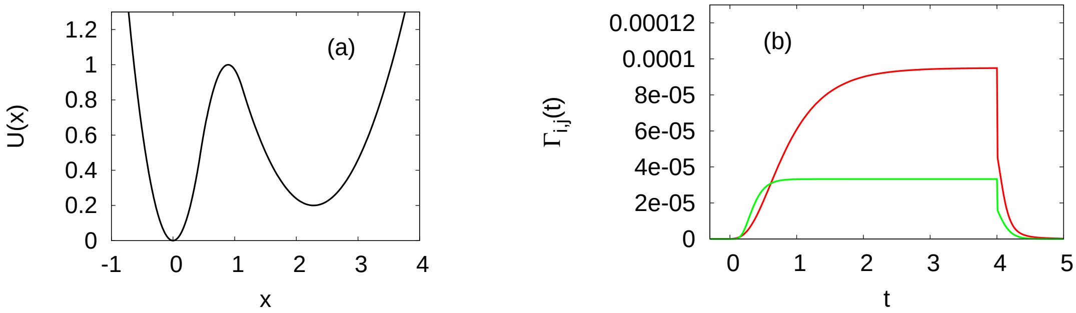

Figure 7.4: (a) The piecewise parabolic potential is specified by the values of the potential at the extrema: $U(x_{\min,2}) = 0$, $U(x_{\max,2}) = 1$, and $U(x_{\min,1}) = 0.2$ and by the values of the curvature: $(\lambda_{s,2}, \lambda_{u,2}, \lambda_{s,1}) = (-5, 5, -1)$. (b) The instantaneous transition rates between the two states of the potential have been calculated according to equation (7.28). $\Gamma_{1,2}(t)$ is shown in red and $\Gamma_{2,1}(t)$ in green. The pulse length was $\tau = 4$, the noise strength $D = 0.05$, and the pulse strength $\Delta g = 1$.

escape rate. Hence, as $-1/\lambda_{s,2} < -1/\lambda_{s,1}$ it is intuitively clear that $\Gamma_{2,1}(t)$ converges faster than $\Gamma_{1,2}(t)$.

Furthermore, for times $t \in [0.15; 0.6]$, $\Gamma_{2,1}(t)$ is even larger than $\Gamma_{1,2}(t)$. Consequently, for small pulse lengths τ also the time-averaged rate $\bar{\Gamma}_{2,1}$ from state 2 to state 1 is larger than the reverse rate, despite the fact that state 2 is energetically favorable. As the quasi equilibrium distribution $\mathbf{n_{eq}}$ is determined by relation (7.14), for these pulse lengths state 1 is preferentially occupied, contrarily to what one would intuitively expect.

In figure 7.5(a) the ratio $n_{eq,1}/n_{eq,2} = \bar{\Gamma}_{2,1}/\bar{\Gamma}_{1,2}$ is plotted as a function of the pulse length τ for various pulse strengths Δg for a fixed $D = 0.05$ and a fixed period $\mathcal{T} = 20$. While in the un-modulated case, $\Delta g = 0$ (and $\tau = 0$, respectively), nearly the whole probability is accumulated in state 2 ($n_{eq,1}/n_{eq,2} \approx 0.05$), this ratio shifts towards larger values when applying the noise pulses. Naively, one would think that this ratio should always be smaller than the ratio (7.15) of the Kramers rates for the stationary noise strength $(1+\Delta g)D$. This is, however, not the case. For strong pulses this ratio, considered as a function of the pulse length τ, has a prominent maximum at small τ values. In figure 7.5(b) the pulse strength $\Delta g = 0.9$ was held fixed, but the noise strength D was varied. For small D the ratio $n_{eq,1}/n_{eq,2}$ again shows a distinct maximum at small pulse length. Furthermore, it is a non-monotonic function of the noise strength D (for a fixed pulse length and pulse strength), in contrast to the case of a stationary noise strength discussed below equation (7.15). In particular, for $\tau \approx 0.35$ the probability to find the system in the energetically unfavorable state 1 increases with decreasing noise strength (and temperature, respectively). This is not in contradiction to the laws of thermodynamics. As we are dealing with a systems far from equilibrium, these laws are not applicable to our system.

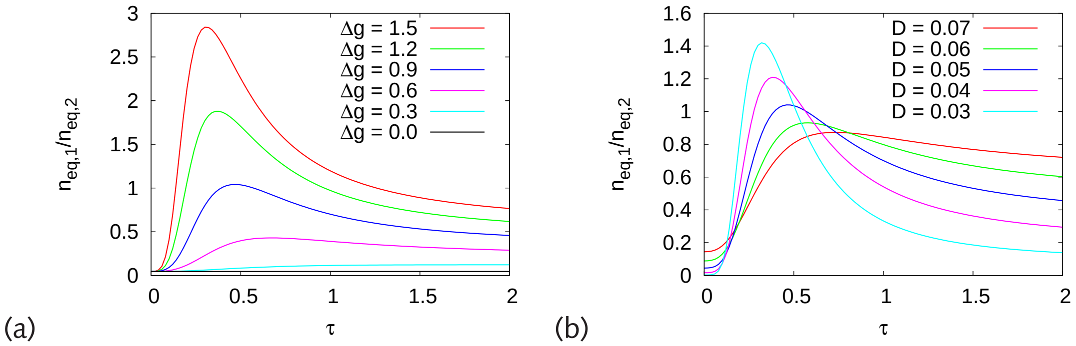

Figure 7.5: (a) Ratio of the probabilities to find the system in the single states in the (quasi) stationary distribution as a function of the pulse length τ for different pulse strengths Δg. The potential was the same as in figure 7.4. The ratio has been calculated according to equations (7.14,7.22,7.23,7.28). For all curves a noise strength $D = 0.05$ and a period $\mathcal{T} = 20$ was used. (b) The same for different noise strengths D for a fixed pulse strength $\Delta g = 0.9$.

In summary, for small noise strengths D, short but strong temperature pulses can significantly alter the quasi equilibrium distribution $\mathbf{n_{eq}}$ if the intrinsic time scales of the potential are different for the metastable states. Then, a particle which escapes from a state with a fast time scale can use the additional energy, provided by the short temperature pulse, better than a particle which escapes from a state with a slow time scale. We note that these temperature pulses cannot only be used to shift the quasi equilibrium distribution $\mathbf{n_{eq}}$ towards an energetically unfavorable state, but also to nearly completely empty a state. Examples for this will be given in the next section.

7.4 Non-equilibrium stabilization by heating

Let us now study the second case of a non-confining potential and restrict our discussion, again, to just two metastable states. The particular example shown in figure 7.6(a) is specified by the values of the potential at the extrema $(U(x_{\min,2}),\ U(x_{\max,2}),\ U(x_{\min,1}),\ U(x_{\max,1})) = (0,\ 1,\ 0.1,\ 1.1)$ and by the values of the curvature $(\lambda_{s,2},\ \lambda_{u,2},\ \lambda_{s,1},\ \lambda_{u,1}) = (-1,\ 10,\ -10,\ 1)$. When applying the noise pulses (7.21) (with $\Delta g > 0$), all single transition rates $\bar{\Gamma}_{i,i\pm1}$ increase. For a fixed pulse strength, period, and noise strength D, the time-averaged rates as a function of the pulse length are depicted in figure 7.6(b). The comparison to the result obtained from solving the Fokker-Planck equation shows that our approximation is again very good, but does not preserve the invariance of the time-averaged rates under a supersymmetric transformation [MSZ88, Jun93, Jun96]. The latter can be deduced from the results for the rates $\bar{\Gamma}_{2,1}$ and $\bar{\Gamma}_{1,0}$. These are slightly different for the approximation, while the exact rates

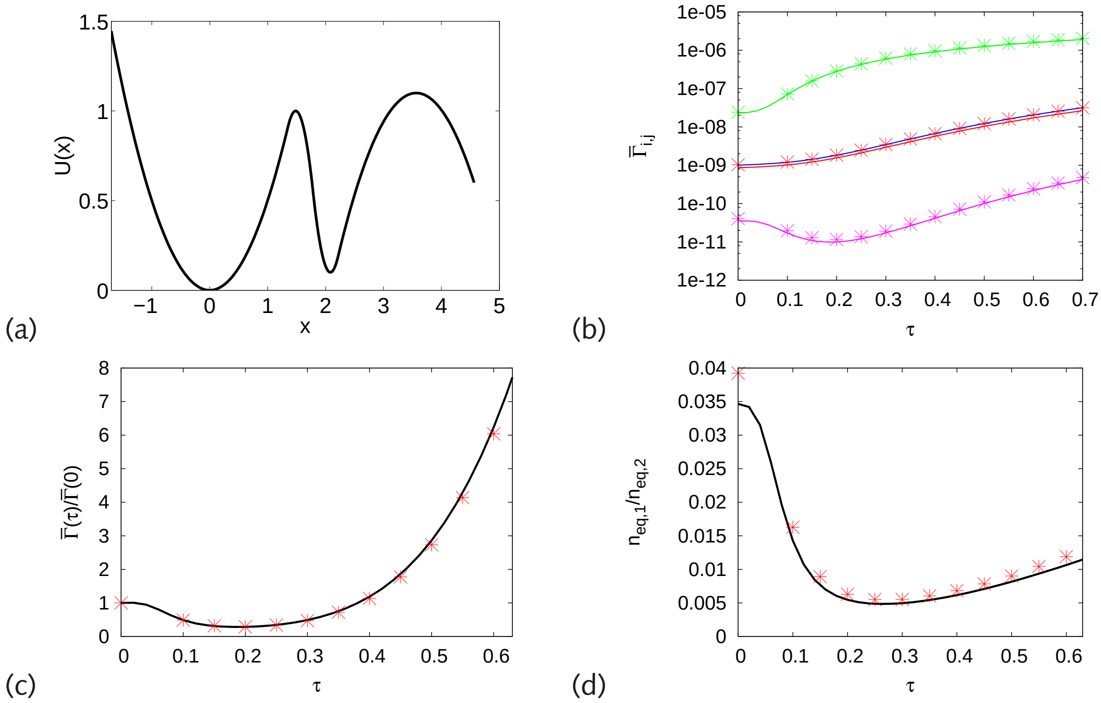

Figure 7.6: (a) The piecewise parabolic potential is specified by the values of the potential at the extrema: $(U(x_{\min,2}), U(x_{\max,2}), U(x_{\min,1}), U(x_{\max,1})) = (0,\ 1,\ 0.1,\ 1.1)$ and by the values of the curvature: $(\lambda_{s,2},\ \lambda_{u,2},\ \lambda_{s,1},\ \lambda_{u,1}) = (-1,\ 10,\ -10,\ 1)$. (b) The time-averaged transition rates between the single states ($\bar{\Gamma}_{1,2}$ green, $\bar{\Gamma}_{2,1}$ red, $\bar{\Gamma}_{1,0}$ blue) as a function of the pulse length τ have been calculated according to equation (7.28) (solid lines) and by solving the Fokker-Planck equation (points). The results for $\bar{\Gamma}_{2,1}$ and $\bar{\Gamma}_{1,0}$, obtained from solving the Fokker-Planck equation, are identical up to very small numerical errors. The effective escape rate $\bar{\Gamma}$ (pink) was calculated employing equation (7.18). The pulse strength was $\Delta g = 1$, the period length $\mathcal{T} = 20$, and the noise strength $D = 0.05$. The ratio of the effective escape rate $\bar{\Gamma} = \bar{\Gamma}(\tau)$ as a function of τ to the effective escape rate for the un-modulated noise strength $\bar{\Gamma}(0)$ is shown in (c) and the ratio of the occupation probabilities $n_{eq,i}$ in (d).

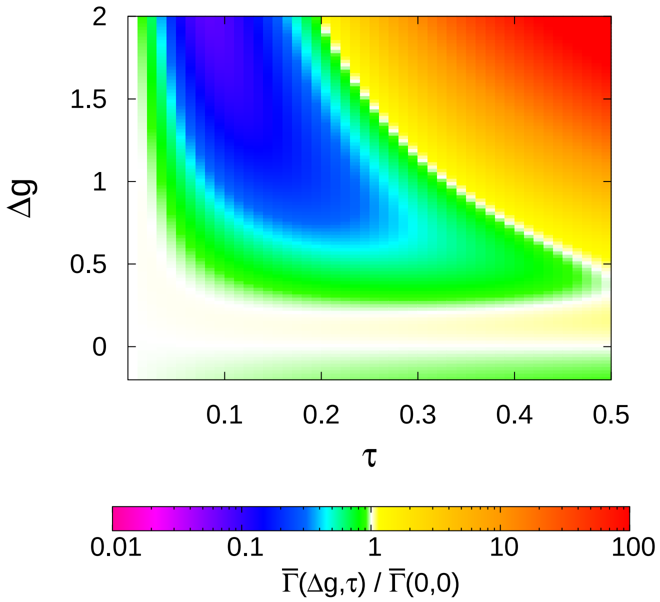

Figure 7.7: The effective escape rate $\bar{\Gamma} = \bar{\Gamma}(\Delta g, \tau)$ as a function of the pulse strength Δg and of the pulse length τ was calculated according to equations (7.20,7.28) for the same potential, period, and noise strength D as in figure 7.6.

are identical.[3]

Also shown in figure 7.6(b) and (c) is the effective escape rate $\bar{\Gamma}$ which has been calculated according to equation (7.18). It is a non-monotonic function of the pulse length τ. Furthermore, for small τ it is even smaller than the escape rate in the un-modulated case. That means, by temporarily heating the system, the metastable potential becomes more stable, in contrast to what one expects and in contrast to equation (7.19) which holds for an adiabatically slow modulation of the noise strength. The physical origin of this effect is the same as that of the effect described in the previous section. Different intrinsic time scales of the potential are involved in the transitions from one state to a neighboring one and in the backward transition. After switching on the additional noise of strength $D\Delta g$, the instantaneous transition rates converge to the new "equilibrium" values on different time scales [cf. figure 7.4(b)]. The result is the observed dependence of the time-averaged transition rates on the pulse length [see 7.6(b)]. $\bar{\Gamma}_{1,2}$ increases for small τ much faster than the other two

---

[3] The problem studied here is equivalent to the escape from a fluctuating potential $V(x,t)$ for a time-independent noise strength. It is well known that the time-averaged (but *not* the instantaneous) escape rate from this potential is identical to that from the supersymmetric partner $-V(-x,-t)$ [MSZ88, Jun93, Jun96]. As the escape rates $\bar{\Gamma}_{2,1}$ and $\bar{\Gamma}_{1,0}$ correspond to such a supersymmetric pair of potentials, the observation is clear.

transition rates because only the short time scales $1/\lambda_{u,2}$ and $-1/\lambda_{s,1}$ are involved in this transition. This results in a reduced probability $n_{eq,1}$ to find the system in state 1 [figure 7.6(d)]. However, a reduced probability $n_{eq,1}$ is necessary for the effective escape rate to decrease, but not sufficient. This probability, considered as a function of the pulse length, has to decrease faster than the transition rate $\bar{\Gamma}_{1,0}$ increases. This can be seen by comparing figures 7.6(c) and (d). In the whole shown range of τ values, the probability to find the system in state 1 is lower than in the un-modulated case. For the effective escape rate this is only true for short pulses with $\tau \lesssim 0.4$. We verified that for these pulse lengths already a single temperature pulse indeed yields an analogous reduction of escapes events. For longer pulses the escape rate rapidly increases.

In figure 7.7 the dependence of the effective escape rate on both, the pulse strength and the pulse length, is shown. In the whole green and blue parameter region a particle in the potential is stabilized by the pulses, while yellow and red indicate an increased escape rate. One sees that a larger reduction of the rate is possible for strong pulses, but at the same time the pulses have to be shorter. Our numerical calculations showed that the "stabilization effect" rapidly vanishes, when lowering the height of the intermediate barrier, while keeping the temperature pulses the same. It appears again, when using stronger and shorter pulses, or when going over to lower temperatures [data not shown]. Furthermore, the example from figure 7.7 suggests that for each Δg there exists an $\epsilon > 0$ such that $\bar{\Gamma}(\Delta g, \tau)$ is a monotonically increasing function of the pulse length τ in $[0; \epsilon]$, but until now we were not able to mathematically rigorously prove it.

In figure 7.8 the same has been done for two other potentials. The potential in (a) differs from the potential used in figures 7.6 and 7.7, only in that the values of the potential at the two minima have been exchanged so that $x_{\min,1}$ is now the minimum with the lowest energy. The effective escape rate shows qualitatively the same dependence on the pulse length and the pulse strength as that in figure 7.7. In view of the fact that for an adiabatically slow modulation of the potential and low temperatures the minimum at $x_{\min,2}$ has little influence on the escape process, this finding might be even more surprising than that for the potential from figure 7.6. For the potential in (b) the time scales (i.e. the curvatures), corresponding to the two minima, have been exchanged. The result of this exchange of time scales is that the stabilization effect does not occur which is in full agreement with our above discussion. Now, for small pulse lengths the transition rate from state 2 to state 1 increases much faster than the other rates, so that preferentially state 1 is occupied. The result is that now the effective escape rate is even larger than the rate from a potential with no intermediate barrier at $x_{\max,2}$.

Hence, the response of the escape rate from a potential with several metastable states to noise pulses depends strongly on the details of the potential, the noise strength, the pulse length, and the pulse strength. The system can be stabilized by the pulses if the noise strength D is sufficiently small and if the pulses are strong, but short. The potential barriers between the single metastable states have to be of

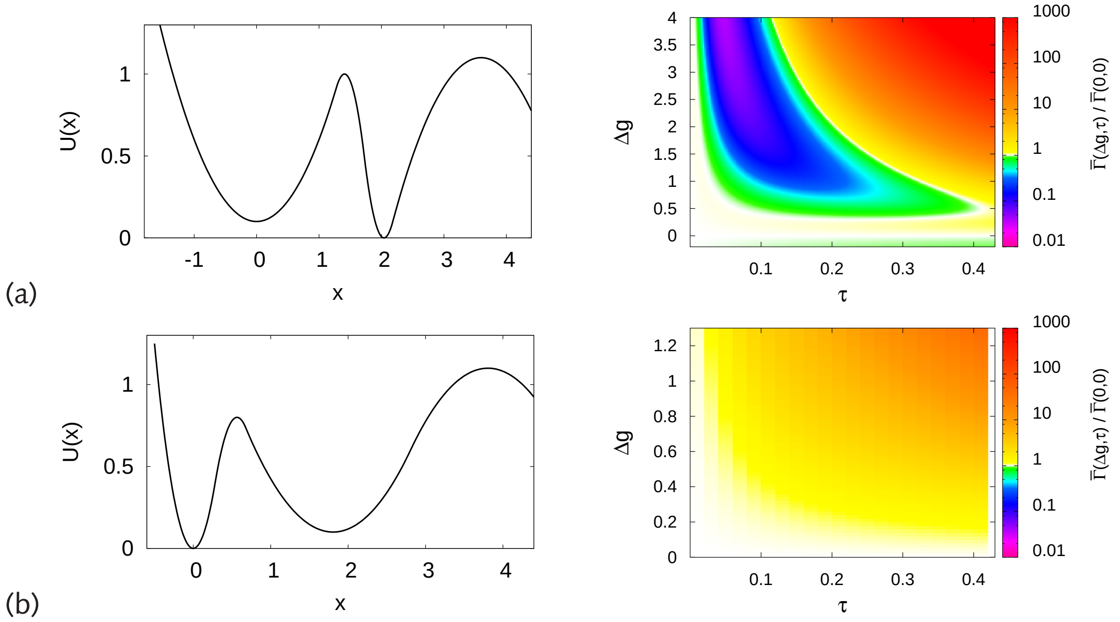

Figure 7.8: The effective escape rate $\bar{\Gamma}(\Delta g, \tau)$ as a function of the pulse strength Δg and of the pulse length τ for different potentials. The piecewise parabolic potential in (a) is specified by $(U(x_{\mathrm{min},2}), U(x_{\mathrm{max},2}), U(x_{\mathrm{min},1}), U(x_{\mathrm{max},1})) = (0.1, 1.0, 0, 1.1)$ and by $(\lambda_{s,2}, \lambda_{u,2}, \lambda_{s,1}, \lambda_{u,1}) = (-1, 10, -10, 1)$. That in (b) by $(U(x_{\mathrm{min},2}), U(x_{\mathrm{max},2}), U(x_{\mathrm{min},1}), U(x_{\mathrm{max},1})) = (0, 0.8, 0.1, 1.1)$ and by $(\lambda_{s,2}, \lambda_{u,2}, \lambda_{s,1}, \lambda_{u,1}) = (-10, 10, -1, 1)$. The remaining parameters are the same as in figures 7.6 and 7.7.

similar height as the potential barrier against escape from the potential. The most important requirement is, however, that the fastest intrinsic time scales of the potential correspond to transitions from a metastable state to a “deeper” bound state, i.e., to a bound state which is further away from the relevant barrier against escape at $x_{\mathrm{max},1}$.

7.5 Discussion

In this chapter we have considered particles in potentials with multiple metastable states under non-equilibrium conditions which are generated by fluctuations of the potential or the noise strength, i.e., by variations of the temperature of the thermal environment. The (quasi) stationary distributions, resulting from these non-equilibrium conditions, do not have the same restrictions as the equilibrium distributions.

We have demonstrated that, by applying short temperature pulses, the probability to find the system in some of its metastable states can be significantly increased compared to the equilibrium case, even if these states are energetically unfavorable. A similar effect was studied by Millonas and Chialvo in [MC96]. They considered the eight-state linear Bezanilla-Peroso-Stefani model [BPS94] for Shaker K^+ ion channels. Each state corresponds to a conformation of the channel. In this model only transitions between two neighboring states are allowed, and the transition rates are controlled by the membrane potential. Millonas and Chialvo have argued that this model is equivalent to the dynamics of an overdamped particle in a one-dimensional potential with eight metastable states and, hence, to the systems studied in this chapter. They approximated the potential by a piecewise linear one and applied an additional time-dependent voltage in the form of a telegraph noise which resulted in a random tilting of the potential. By this (random) driving force the channel could be focused in one of the eight conformational states. In comparison to the un-driven case, the probability to find the system in this state increased by a factor of 25. This effect, which Millonas and Chialvo called "*non-equilibrium kinetic focusing*", was recently observed experimentally in [KK08]. However, the physical origin of the effect is different to the effect discussed in this chapter. We have discussed the case of a fluctuating potential or noise strength, where the instantaneous energy barriers are large compared to the instantaneous noise strength at every time. The tilting forces used by Millonas and Chialvo had to be so large that some of the barriers temporarily disappear.

The other closely related effect, which has been discussed in this chapter, is the reduction of the escape rate from a potential with several metastable states by applying short temperature pulses. Potentials of this kind are ubiquitous in the context of chemical reactions and play, e.g., a role for reactions which proceed in two or more steps via one or more intermediate states (cf. chapter 5.5). An example for such a system might be a complex of two or more (macro) molecules[4] which can exist in different metastable states. Temperature pulses could be generated as described in section 7.1.4. Most realistic are short laser pulses [NVBG07], whose basic effects (on the reacting molecules *and* their environment) may still be roughly modeled by a temperature pulse. We expect that our finding will be qualitatively robust against various modifications of the pulsed perturbation. Depending on the details of the potential landscape, these perturbations might result in the focusing of the complex in one of its metastable states and in a reduced effective dissociation rate. The requirement for the appearance of the effect is that the time scale of the perturbations is similar to the internal relaxation times of the complex in the single metastable states. Furthermore, the fastest intrinsic time scales of the potential have to correspond to transitions from a metastable state to a "deeper" bound state (see the discussion at the end of the previous section). Whether this is the case or not, cannot be influenced. In general, it is not even known, before subjecting the system to these perturbations. On the other hand, from the response of the system to the perturbations one might learn something about the intrinsic time scales of the complex. We note that the noise pulses are completely non-local. Hence, the macromolecules themselves do not have to be manipulated in order to conduct such an experiment.

---

[4] The ion channels discussed by Millonas are proteins and hence also macromolecules.

The systems discussed here are just two examples where effects of this kind might play a role. There exist a number of other systems which are described within the same framework and where the “method” proposed in this chapter is applicable to. For example, the manipulation of colloidal particles in a suitably designed potential landscape, as discussed in section 7.1.1, may serve as a model system for which the above described effects can be demonstrated.

Finally, we note that it is well known that chemical reactions can be controlled by applying properly shaped femtosecond laser pulses [NVBG07]. This is, however, a pure quantum mechanical effect which takes place on different time scales. For the quantum control femtosecond laser pulses are needed, whereas the effect described in this chapter has a completely different physical origin, and one can expect that the laser pulses can be substantially longer.

8 Summary and outlook

The leitmotif of this thesis was thermally activated escape from a metastable state far from thermal equilibrium. In the first part of this work, we have addressed the problem of theoretically modeling and interpreting single-molecule force spectroscopy experiments. Under the specific conditions given in these kinds of experiments the instantaneous escape rate is very well approximated by the Kramers rate from the frozen potential. The second part of this work dealt with the case that either the potential or the temperature of the thermal bath is modulated on time scales comparable to the time scale of the internal relaxation processes. Here, Kramers' approximation does not apply, and finding appropriate approximations to the escape rate is a technically challenging task. In the following, the results from each part of the work shall be treated separately.

8.1 Single-molecule force spectroscopy

It is well accepted that the rupture of chemical bonds under application of external forces is a thermally activated process that can be described within the general framework of Kramers' rate theory. Nevertheless, the interpretation of experimental rupture force data, as for example obtained from single-molecule force spectroscopy by AFM, is still a challenging task. This problem has been addressed in chapters 4 and 5 of this thesis.

In a first step, we have considered the case that an appropriate model is given which can satisfactorily explain the experimental data. Then, the maximum likelihood estimator is an extremely simple and general method if one wishes to extract the values of the model parameters $\boldsymbol{\mu}$ from a (large) set of rupture force data. The inferred parameters are, on the average, closer to the "true" model parameters than for any other estimator. This has been mathematically rigorously shown and demonstrated for different examples. Compared to the commonly used methods for parameter estimation in the field of single-molecule force spectroscopy, the maximum likelihood method has two further advantages. Firstly, no binning of the rupture force data to histograms is needed. The estimates do, therefore, not depend on the somewhat arbitrary choice of the bin-width. Secondly, the statistical uncertainties are readily available once the parameters are estimated. For Bell's model, even analytical expressions for these uncertainties could be derived.

Employing the method proposed by Raible et al. [RER⁺04], it can be checked whether the experimentally obtained rupture force distributions are compatible to a one-step rate description. However, even if this is the case, one cannot reconstruct the full potential landscape. Instead, one usually adopts some functional form for the force-dependence of the escape rate and the potential landscape, respectively, and estimates the involved model parameters, e.g., by the maximum likelihood method. For a quite general such functional form, we have demonstrated that, even under idealized conditions, no more than three model parameters can be extracted reliably from single-molecule force spectroscopy experiments. A fourth parameter, which specifies the exact dependence of the barrier height on the applied force, was found to be largely arbitrary. As a consequence, the inferred value for the barrier height in absence of force can strongly deviate from the "true" height of the potential barrier. Therefore, without having further information, this quantity cannot be determined reliably by single-molecule force spectroscopy as proposed by some authors.

In a second step, we have considered real experimental data. The rupture force distributions from all experiments studied by us and almost all published experimental rupture force distributions are incompatible to the one-step rate description. Different models, which might explain these findings, have been discussed. The most general and promising explanation was the heterogeneous bond model originally introduced by Raible et al. [REB$^+$06]. Here this discussion has been put forward. Indeed, there exist experimental hints for variations of the pulling geometry, and we have discussed that these variations are, amongst others, possible physical sources of the proposed heterogeneity. For a particular example, we have demonstrated that a randomization of the energy barrier height as well as a randomization of the dissociation length can explain the experimental findings. Furthermore, the theoretical rupture force distribution does not critically depend on details of the distribution of model parameters. These findings argue for the heterogeneous bond model. Any kind of variation in the experimental conditions results in qualitatively the same rupture force distributions and the same velocity dependence of the $-v\ln(n(f|v,f_{\mathrm{min}}))$ functions as experimentally observed. At the same time, this makes it even more difficult to extract quantitative information in the form of model parameters, or distributions of them, from a single-molecule force spectroscopy experiment.

Because of the fascinating possibility of single-molecule force spectroscopy to study interactions of biomolecules at the single-molecule level, it is likely that also in the next years a lot of experimental and theoretical efforts will be spent in order to gain further insight into the forced rupture of chemical bonds. For example, specially designed experiments can possibly help to identify some sources for the proposed heterogeneity to play an important role, while others can be discarded as unimportant. Based on such experiments a detailed theoretical modeling of the heterogeneity might be possible.

8.2 Escape rates far from thermal equilibrium

In chapters 6 and 7 the case of fast driven systems was considered. Either the potential or the temperature was allowed to be modulated on time scales comparable to the time scale of the internal relaxation processes. An approximation scheme to the instantaneous escape rate in the framework of path integrals has been worked out (chapter 6). A comparison to high precision numerical results showed for various examples, from periodically tilted potentials (section 6.6) to static potentials with a pulsed temperature (sections 7.2-7.4), that the resulting errors of the approximation are, in fact, very small. To the best of our knowledge, no previously existing approximation would be applicable to such largely arbitrary potentials and perturbations.

We have, furthermore, discussed several properties of the approximation. In particular, for adiabatically slow modulations Kramers' rate is recovered. For a piecewise parabolic potential an explicit expression for the escape rate could be derived. The integrals appearing in this approximation can be very efficiently solved numerically. For other potentials the escape rate is also given by an integral, but the integrand is only determined as the solution of a set of ordinary differential equations, making the approximation computationally more expensive than for the piecewise parabolic potential. However, for time-periodic modulations, an efficient approximation scheme was proposed and demonstrated. Especially for very low noise strengths this scheme is computationally favorable compared to solving the Fokker-Planck equation. Furthermore, our approximation may serve as the starting point for future works.

Finally, in chapter 7 this approximation was applied to systems with two metastable states and a pulsed temperature. As such a system is far from thermal equilibrium, the physics is not restricted by the second law of thermodynamics, and interesting effects can occur. Here, two of these effects have been demonstrated. For a potential with several metastable states short temperature pulses can be employed to "focus" the system in one of the metastable states. Depending on the intrinsic time scales of the system, this is *not* necessarily the ground state, but may correspond to a local minimum with a considerably higher energy. In the same line, these short temperature pulses may lead to a reduction of the effective escape rate from the potential.

Different systems in which these effects can occur have been identified. While colloidal particles in suitably designed fields of force may serve to give a proof of principle, it is possible that these effects can also lead to interesting applications in the field of biophysics. For example, by subjecting it to short laser pulses, a bond between two biomolecules may be stabilized, or a protein may be focused in another conformational state than the ground state. As these effects depend critically on the intrinsic time scales of the relevant potential landscape, they do not occur in each system. But from the response of the system to such fast perturbations, it may be possible to draw conclusions about the underlying energy landscape of the system.

Appendices

Appendix A

Supplements to chapter 4

A.1 Asymptotic distribution of the maximum likelihood estimate

In this section we prove the second main conclusion from section 4.1.2, namely that the distribution of the maximum likelihood estimate $\boldsymbol{\mu}^*$ is Gaussian and looks, apart from the peak position, the same as the likelihood (4.9) for one given data set $\mathbf{f}$.

To keep things as simple as possible, we assume that there exist (small) integers n_β for each of the Z pulling velocities v_β so that $n_\beta/n_\gamma = \rho_\beta/\rho_\gamma$. Denoting by n the sum of all n_β, the total number of rupture forces can be written as $N = N'n$ and the set of N rupture forces $\mathbf{f}$ can be divided into N' subsets $\mathbf{f}^k = \{f^k_{i,\beta}\}$ where for fixed k, $f^k_{i,\beta}$ is one out of the n_β rupture forces sampled at pulling velocity v_β.

Having introduced this notation, we define N' new random variables

$$\mathbf{X}^k = \mathbf{X}^k(\mathbf{f}^k) = \frac{1}{n}\sum_{\beta=1}^{Z}\sum_{i=1}^{n_\beta} H^{-1}\partial/\partial\boldsymbol{\mu}\ln p_1(f^k_{i,\beta}|\boldsymbol{\mu}_0, v_\beta)\ . \tag{A.1}$$

We know already from our discussion in section 4.1.2 that these random variables have an expectation value zero and a covariance matrix

$$\langle\mathbf{X}\,\mathbf{X}^\dagger\rangle = \frac{1}{n}H^{-1}\ . \tag{A.2}$$

Then, from the central limit theorem [Cra46] it follows that

$$\boldsymbol{\mu}^* - \boldsymbol{\mu}_0 = \frac{1}{N'}\sum_{k=1}^{N'}\mathbf{X}^k \tag{A.3}$$

is Gaussian distributed with zero mean and covariance matrix

$$\langle[\boldsymbol{\mu}^* - \boldsymbol{\mu}_0]\,[\boldsymbol{\mu}^* - \boldsymbol{\mu}_0]^\dagger\rangle = \frac{1}{nN'}H^{-1} = \frac{1}{N}H^{-1}\ . \tag{A.4}$$

A.2 Statistical uncertainties for Bell's model

In order to determine the covariance matrix of the maximum likelihood estimate for Bell's model, in section 4.2.1 the quantity $s(\boldsymbol{\mu})$ as defined in (4.5) had to be calculated. Details of this calculation are given below.

We first calculate

$$E(\alpha) := \langle e^{\alpha f}\rangle_1 = \int_0^\infty df\ e^{\alpha f} p_1(f|\boldsymbol{\mu}_0, v) \tag{A.5}$$
$$= \int_0^\infty df e^{\alpha f} \frac{e^{\lambda_0+\alpha_0 f}}{r} \exp\left(-\frac{e^{\lambda_0}}{r}\frac{e^{\alpha_0 f}-1}{\alpha_0}\right)$$

for an arbitrary loading rate $r = \kappa v$ and $\alpha > -\alpha_0$. It is convenient to rewrite equation (A.5) using the dimensionless quantities $\tau := e^{\lambda_0}/(r\alpha_0)$ and $\eta = \alpha/\alpha_0$ and to substitute $t = \tau\exp(\alpha_0 f)$, yielding

$$E(\alpha) = \tau^{-\eta} e^{\tau} \int_\tau^\infty dt\ t^\eta e^{-t}\ . \tag{A.6}$$

Using that $\tau \ll 1$ in typical AFM pulling experiments, we derive at

$$E(\alpha) = \tau^{-\eta}\Gamma(\eta+1) + \mathcal{O}(\tau)\ , \tag{A.7}$$

where $\Gamma(\cdot)$ denotes the Gamma function. Equation (A.7) directly gives the expected rupture force:

$$\langle f\rangle_1 = \frac{\partial}{\partial\alpha}E(\alpha=0) = -\frac{1}{\alpha_0}\left(\mathcal{C} + \ln\tau\right) + \mathcal{O}(\tau)\ , \tag{A.8}$$

with $\mathcal{C} \approx 0.577$ the Euler constant. Using equations (A.7,A.8) and the linearity of the expectation value we obtain:

$$-\langle \ln p_1(f|\boldsymbol{\mu}, r)\rangle_1 =$$
$$-\lambda + \ln(\kappa v) + \eta(\mathcal{C} + \ln\tau) + \frac{e^\lambda}{\kappa v\alpha}\frac{1}{\tau^\eta}\Gamma(\eta+1)\ . \tag{A.9}$$

Finally, equation (A.9) together with the definition of the quantity $s(\boldsymbol{\mu})$ yields the desired result (4.18).

A.3 Optimal bin-width for histograms

Let p_1 be a probability density function with two continuous and bounded derivatives. For a sample of size N the histogram estimate $\hat{p}_1$ of p_1 is defined as

$$\hat{p}_1(f) = \frac{\Lambda_N(f)}{N h_N}\ , \tag{A.10}$$

with $\Lambda_N(f)$ the number of values falling into the bin of width h_N around f. Then one can show [Sco79, Rud82] that for large sample sizes the integrated mean squared error

$$IMSE = \int df\ \langle(\hat{p}_1(f) - p_1(f))^2\rangle_1\ , \tag{A.11}$$

considered as a function of the bin-width, is minimized by

$$h_N^* = \left(\frac{6}{\int df \; (p_1'(f))^2} \right)^{1/3} N^{-1/3} \; . \tag{A.12}$$

Following the same lines as in Appendix A.2, we obtain for Bell's model:

$$\int df (p_1'(f|\boldsymbol{\mu}, v))^2 = \frac{1}{8}\alpha^3 \left(1 + \mathcal{O}\left(\frac{2e^\lambda}{\kappa v \alpha} \right) \right) \; . \tag{A.13}$$

Inserting (A.13) into (A.12) yields the optimal bin-width:

$$h_N^* \approx 3.63 \frac{1}{\alpha N^{1/3}} \; . \tag{A.14}$$

It should be noted that in the limit $\frac{2e^\lambda}{\kappa v \alpha} \ll 1$, the optimal bin-width depends solely on the sample size N and on the parameter α which determines the width of the distribution, but neither on the force-free dissociation rate $k_0 = \exp(\lambda)$ nor on the pulling velocity v.

If one wishes to determine the optimal bin-width prior to parameter estimation, one may make use of the well known result $\langle (f - \langle f \rangle_1)^2 \rangle_1 \approx \pi^2/(6\alpha^2)$ and choose

$$h_N = 2.83 s_N N^{-1/3} \; , \tag{A.15}$$

where s_N denotes the standard deviation of the measured rupture forces. This estimate is pretty close to the optimal bin-width $h_{N,Gauss} \approx 3.49 s_N N^{-1/3}$ of a Gaussian distribution [Sco79].

Appendix B

Supplements to chapter 6

B.1 Limit of the integral (6.71)

In section 6.4.2 we have considered the integral

$$I(y,\delta) = \int\limits_{t'-\delta'}^{t'} ds\ \tilde{\Psi}_{t_0}(x_1,s) \frac{y - \tilde{X}_s(t')}{t'-s} \frac{e^{-\frac{(y-\tilde{X}_s(t'))^2}{2(t'-s)}}}{\sqrt{2\pi(t'-s)}} \ , \tag{B.1}$$

where $\tilde{X}_s(t')$ is the solution of the deterministic motion (6.5) in the rescaled time $t' = 2Dt$ with initial condition $\tilde{X}_s(s) = x_1$. Hence, $\tilde{X}_s(t') \approx x_1 + \tilde{F}(x_1,s)\ (t'-s)$ for small $(t'-s)$, where $\tilde{F}(x_1,s) := F(x_1,s/2D)/(2D)$. In this appendix we will consider the limit $y \searrow x_1$ and $t \searrow 0$ of $I(y,\delta)$. The result, given in equation (6.72), was previously derived in [DW92].

Let us first rewrite equation (B.1) as:

$$I(y,\delta) := \int\limits_{t'-\delta'}^{t'} ds\ \tilde{\Psi}_{t_0}(x_1,s) \left[\frac{y-x_1}{t'-s} + A(s,t')\right] \frac{e^{-\frac{(y-x_1)^2}{2(t'-s)}+B(s,t',y)}}{\sqrt{2\pi(t'-s)}} \ , \tag{B.2}$$

with

$$A(s,t') = \frac{x_1 - \tilde{X}_s(t')}{t'-s} = \tilde{F}(x_1,s) + \mathcal{O}(\delta') \ , \tag{B.3}$$

$$B(s,t',y) = \frac{1}{2}A(s,t')(\tilde{X}_s(t') + x_1 - 2y) \ . \tag{B.4}$$

Obviously, $B(s,t',y)$ is a continuous function in s and y with $B(t',t',x_1) = 0$. Furthermore, one can easily convince oneself that

$$\frac{y-x_1}{t'-s} \frac{e^{-\frac{(y-x_1)^2}{2(t'-s)}}}{\sqrt{2\pi(t'-s)}} \tag{B.5}$$

converges for $y \searrow x_1$ towards the delta distribution $\delta(t'-s)$ (the function is normalized and sharply peaked at $t'^{(-)}$). In this limit equation (B.1) therefore becomes:

$$\lim_{y\searrow x_1} I(y,\delta) = \tilde{\Psi}_{t_0}(x_1,t') + \lim_{y\searrow x_1} \int\limits_{t'-\delta'}^{t'} ds\ \tilde{\Psi}_{t_0}(x_1,s) A(s,t') \frac{e^{-\frac{(y-x_1)^2}{2(t'-s)}+B(s,t',y)}}{\sqrt{2\pi(t'-s)}} \ . \tag{B.6}$$

The integrand of the remaining integral is now bounded from above by $K(t'-s)^{-1/2}$ where K is some constant. Hence, this integral vanishes for $\delta \searrow 0$ and equation (6.72) holds.

B.2 Series expansion of the first passage time density for a piecewise linear potential

In this appendix we derive an upper bound for the error made by approximating the first passage time density for a piecewise linear potential by the first n terms of the series (6.76). Here, piecewise linear means that the potential is linear in a sufficiently large interval around x_1.

For this special potential

$$F(X_{t_1}(s), s) = F(x_1, s) \tag{B.7}$$

holds for all considered times in the integral (6.74) and for all $t_1 \leq s \leq t$, and consequently:

$$\begin{aligned} X_{t_1}(t) &= x_1 + \int_{t_1}^{t} ds\, F(x_1, s)\,, & \text{(B.8)} \\ \sigma^2_{t_1}(t) &= 2(t - t_1)\,. & \text{(B.9)} \end{aligned}$$

We now assume that the potential is modulated continuously and that the temporal derivative $\dot{F}(x_1, s)$ is finite for all times. Its maximum absolute value is denoted by $\dot{F}_{\max}$. Under this assumption one can estimate

$$\left|\frac{2(X_{t_1}(t) - x_1)}{\sigma^2_{t_1}(t)} - F(x_1, t)\right| = \left|\frac{\int_{t_1}^{t} ds\, (F(x_1, s) - F(x_1, t))}{t - t_1}\right| \leq \frac{1}{2}\dot{F}_{\max}(t - t_1)\,. \tag{B.10}$$

As in section 6.4.2, we will furthermore assume that the potential is not modulated *too violently*, but here this statement is quantified by the assumption that a constant $C > 0$ exists such that for all times t and t_1

$$\frac{\left[\int_{t_1}^{t} ds\, F(x_1, s)\right]^2}{4(t - t_1)} - \Delta\Phi^*(t, t_1) > C(t - t_1)\,. \tag{B.11}$$

Combining equations (6.78-6.80,B.7-B.11), the following upper bound for the first correction to the first passage time density follows:

$$\begin{aligned} \left|\Psi^1_{t_0}(x_1, t)\right| &\leq \dot{x}^*_{t_0,max}\sqrt{\frac{Q^*_{t_0,max}}{Q^*_{t_0,min}}}\frac{\dot{F}_{\max}}{2\sqrt{4\pi D}}\rho(x_1, t|x_0, t_0)\int_{t-\tau_R}^{t} dt_1\, \sqrt{t - t_1}e^{-C(t-t_1)/D} \\ &\leq \dot{x}^*_{t_0,max}\left[\sqrt{\frac{Q^*_{t_0,max}}{Q^*_{t_0,min}}}\frac{\dot{F}_{\max}D\Gamma(3/2)}{4\sqrt{\pi}C^{3/2}}\right]\rho(x_1, t|x_0, t_0)\,, & \text{(B.12)} \end{aligned}$$

where $\Gamma(\cdot)$ denotes the Gamma-function and $\dot{x}^*_{t_0,max}$ the maximum value of $\dot{x}^*_{t_0}(t_1)$.

Similarly, one can show that the higher order terms are bounded by:

$$\left|\Psi^n_{t_0}(x_1,t)\right| \le \dot{x}^*_{t_0,max}\left[\sqrt{\frac{Q^*_{t_0,max}}{Q^*_{t_0,min}}}\frac{\dot{F}_{\max}D\Gamma(3/2)}{4\sqrt{\pi}C^{3/2}}\right]^n \rho(x_1,t|x_0,t_0)\;. \tag{B.13}$$

Using equations (6.76,B.13), we can conclude:

$$\Psi_{t_0}(x_1,t) = \dot{x}^*_{t_0}(t)\rho(x_1,t|x_0,t_0)\left[1+\mathcal{O}(D)\right]\;. \tag{B.14}$$

The errors which result from neglecting the integral in equation (6.74) are therefore of the same order of magnitude as the terms already neglected in the saddle point approximation (6.32).

Although the error bounds derived in this appendix do strictly apply only to the special case of a piecewise linear potential, we can assume that the error is of a similar order of magnitude for potentials where equation (B.7) holds approximately for all relevant times t_1 in the integral (6.74).

B.3 Escape rate for an adiabatically slowly driven, piecewise parabolic potential

In section 6.5 we have shown that, in the limit of small noise strengths D and adiabatically slow modulations of the potential, approximation (6.55) for the instantaneous escape rate reduces to the Kramers formula (2.19). In this section an alternative derivation is presented for the piecewise parabolic potential.

With "slow modulation" we mean that the period $\mathcal{T}$ of the driving force is much larger than the other relevant time scales $\tau_{s,u} = 1/|\lambda_{s,u}|$. Then, for all t_1 contributing significantly to the integral in equation (6.162) we can approximate:

$$\begin{aligned} x_{s,u}(t_1) &\approx x_{\min,\max}(t_f) = \bar{x}_{s,u} - f(t_f)/\lambda_{s,u}\;, && \text{(B.15)}\\ f(t_1) &\approx f(t_f)\;. && \text{(B.16)} \end{aligned}$$

Inserting (B.15,B.16) into (6.162) yields:

$$\begin{aligned} \Gamma(t_f) &= -\frac{|\lambda_s\lambda_u|^{3/2}\,x_s(t_f)x_u(t_f)}{2\pi D}e^{\frac{\lambda_s x_s(t_f)^2}{(2D)}}R(t_f)\;, && \text{(B.17)}\\ R(t_f) &= \int_{-\infty}^{t_f} dt_1\,\frac{e^{2\lambda_u(t_f-t_1)}}{(1-e^{2\lambda_u(t_f-t_1)})^{3/2}}e^{-\frac{1}{2D}\frac{\lambda_u x_u(t_f)^2}{1-e^{2\lambda_u(t_f-t_1)}}}\;. && \text{(B.18)} \end{aligned}$$

For convenience we define $\alpha := \lambda_u x_u(t_f)^2/2D$. Substituting $s = 1/(1-e^{2\lambda_u(t_f-t_1)})$ in equation (B.18) gives:

$$R(t_f) = \frac{1}{2\lambda_u}\int_1^\infty ds\,\frac{1}{\sqrt{s}}e^{-\alpha s} = \frac{1}{2\lambda_u}\sqrt{\frac{\pi}{\alpha}}[1-\mathrm{erf}(\sqrt{\alpha})]\;, \tag{B.19}$$

where $\mathrm{erf}(x) = 2\pi^{-1/2} \int_0^x dy e^{-y^2}$ is the error function. For large arguments this can be approximated by:

$$\mathrm{erf}(x) \approx 1 - \frac{e^{-x^2}}{\sqrt{\pi} x} \ , \tag{B.20}$$

with an error smaller than $e^{-x^2}/(2\sqrt{\pi}x^3)$ [AS65]. As for small noise strengths D the argument $\sqrt{\alpha}$ of the error function will become large, we can use equation (B.20) to approximate $R(t_f)$ in equation (B.19):

$$R(t_f) = \frac{D}{\lambda_u^2 x_u(t_f)^2} e^{-\frac{\lambda_u x_u(t_f)^2}{2D}} \left[1 + \mathcal{O}(D)\right] . \tag{B.21}$$

Inserting equation (B.21) into (B.17) and using (6.158) finally yields

$$\Gamma(t_f) \approx \frac{\sqrt{|\lambda_s \lambda_u|}}{2\pi} e^{-\frac{\Delta V(t_f)}{D}} \ , \tag{B.22}$$

with $\Delta V(t_f) = V(x_{\max}(t_f), t_f) - V(x_{\min}(t_f), t_f)$ the potential barrier of the quasi-static potential at time t_f. This is, however, exactly the Kramers formula (2.19).

In the opposite limit, $\mathcal{T}$ much smaller than all other relevant time scales, one can replace $x_{s,u}(t_1)$ and $f(t_1)$ in the integral (6.162) by the concomitant time-averaged versions and proceed in full analogy to the adiabatic limit, also recovering the Kramers formula.

Appendix C

Escape rate from a piecewise parabolic potential: Rectangular pulse

In section 6.6.1 approximation (6.155,6.156) for the instantaneous escape rate from a piecewise parabolic potential with time-dependent coefficients (and a time-independent noise strength) has been derived. In this appendix we consider the special case of a fluctuating potential (6.142) specified by:

$$h_s(t) = h_u(t) = 1 + \Delta h \; \Theta(t) \; \Theta(\tau - t) \; , \tag{C.1}$$

$$\bar{x}_s(t) = \bar{x}_s < 0 \; , \quad \bar{x}_u(t) = \bar{x}_u > 0 \; , \tag{C.2}$$

with some constant $\tau > 0$, called the pulse length. That means, in the interval $[0;\tau]$ the potential barrier V_0 is lowered or increased by $\Delta h \, V_0$ (depending on the sign of Δh). Obviously, the stable and unstable orbits are $x_{s,u}(t) = \bar{x}_{s,u}$. For this special choice the functions $\Lambda_{s,u}$ and $I_{s,u}$ defined in equations (6.87,6.88,6.96) can be explicitely evaluated with the result:

$$\Lambda_{s,u}(t,\tilde{t}) = \lambda_{s,u}(t-\tilde{t}) + \lambda_{s,u}\Delta h \begin{cases} t & \text{if } \tilde{t} < 0 < t < \tau \\ t-\tilde{t} & \text{if } 0 \leq \tilde{t} < t < \tau \\ \tau & \text{if } \tilde{t} < 0 < \tau < t \\ \tau - \tilde{t} & \text{if } 0 \leq \tilde{t} \leq \tau < t \\ 0 & \text{else} \end{cases} \; , \tag{C.3}$$

$$I_s(t_1) = -\frac{1}{\lambda_s} \begin{cases} 1 & \text{if } t_1 < 0 \\ \frac{1}{1+\Delta h}(1 + \Delta h \, e^{2\lambda_s(1+\Delta h)t_1}) & \text{if } 0 \leq t_1 < \tau \\ 1 + \frac{\Delta h}{1+\Delta h} e^{2\lambda_s t_1}(e^{-2\lambda_s \tau} - e^{-2\lambda_s \Delta h \, \tau}) & \text{else} \end{cases} \; , \tag{C.4}$$

and

$$I_u(t_1,t) = -\frac{1}{\lambda_u}\begin{cases} 1-\frac{e^{2\lambda_u t_1}}{1+\Delta h}\left[\Delta h + e^{-2\lambda_u(1+\Delta h)t}\right] & \text{if } t_1 < 0 < t < \tau \\ \frac{1}{1+\Delta h}\left[1-e^{-2\lambda_u(1+\Delta h)(t-t_1)}\right] & \text{if } 0 \le t_1 < t < \tau \\ 1+e^{2\lambda_u t_1} & \\ \times\left[-\frac{\Delta h}{1+\Delta h}+\frac{\Delta h}{1+\Delta h}e^{-2\lambda_u(1+\Delta h)\tau}-e^{-2\lambda_u(t+\Delta h\,\tau)}\right] & \text{if } t_1 < 0 < \tau \le t \\ \frac{1}{1+\Delta h}+e^{2\lambda_u(1+\Delta h)t_1} & \\ \qquad\qquad \times\left[\frac{\Delta h}{1+\Delta h}e^{-2\lambda_u(1+\Delta h)\tau}-e^{-2\lambda_u(t+\Delta h\,\tau)}\right] & \text{if } 0 \le t_1 < \tau \le t \\ 1-e^{2\lambda_u(t_1-t)} & \text{else} \end{cases} . \tag{C.5}$$

The corresponding approximation for a static potential with a fluctuating noise strength is derived and discussed in section 7.2.

Bibliography

[ADBC86] A. Ashkin, J. M. Dziedzic, J. E. Bjorkholm, and S. Chu. Observation of a single-beam gradient force optical trap for dielectric particles. *Opt. Lett.*, 11:288–290, 1986.

[AdJM$^+$04] T. Auletta, M. R. de Jong, A. Mulder, F. C. J. M. van Veggel, J. Huskens, D. N. Reinhoudt, S. Zou, S. Zapotoczny, H. Schönherr, G. J. Vancso, and L. Kuipers. β-Cyclodextrin Host-Guest Complexes Probed under Thermodynamic Equilibrium: Thermodynamics and AFM Force Spectroscopy. *J. Am. Chem. Soc.*, 126:1577–1584, 2004.

[AJL$^+$08] B. Alberts, A. Johnson, J. Lewis, M. Raff, K. Roberts, and P. Walter. *Molecular Biology of the Cell*. Garland Science, New York, 2008.

[AL98] S. Antoci and D. E. Liebscher. Wentzel's Path Integrals. *Int. J. Theor. Phys.*, 37:531–535, 1998.

[AS65] M. Abramowitz and I. A. Stegun. *Handbook of mathematical functions with formulas, graphs, and mathematical tables*. Dover Publications, New York, 1965.

[Ast06] R. D. Astumian. The unreasonable effectiveness of equilibrium theory for interpreting nonequilibrium experiments. *Am. J. Phys.*, 74:683–688, 2006.

[BBA$^+$03] F. W. Bartels, B. Baumgarth, D. Anselmetti, R. Ros, and A. Becker. Specific binding of the regulatory protein ExpG to promoter regions of the galactoglucan biosynthesis gene cluster of *Sinorhizobium meliloti* - a combined molecular biology and force spectroscopy investigation. *J. Struct. Biol.*, 143:145–152, 2003.

[BBA$^+$05] B. Baumgarth, F. W. Bartels, D. Anselmetti, A. Becker, and R. Ros. Detailed studies of the binding mechanism of the *Sinorhizobium meliloti* transcriptional activator ExpG to DNA. *Microbiology*, 151:259–268, 2005.

[BBLD07] B. Brotherson, L. A. Bottomley, P. Ludovice, and Y. Deng. Cationic Polyacrylamide Conformation on Mica Studied by Single Molecule "Pulling" with Scanning Probe Microscopy. *Macromolecules*, 40:4561–4567, 2007.

[BD91] M. Berzins and P. M. Dew. Algorithm 690: Chebyshev Polynomial Software for Elliptic-Parabolic Systems of PDEs. *ACM Trans. Math. Software*, 17:178–206, 1991.

[BDA02] D. Bartolo, I. Derényi, and A. Ajdari. Dynamic response of adhesion complexes: Beyond the single-path picture. *Phys. Rev. E*, 65:051910–1–4, 2002.

[BDKA99] M. Bier, I. Derényi, M. Kostur, and R. D. Astumian. Intrawell relaxation of overdamped Brownian particles. *Phys. Rev. E*, 59:6422–6432, 1999.

[Bel78] G. I. Bell. Models for the Specific Adhesion of Cells to Cells. *Science*, 200:618–627, 1978.

[BG02] N. Berglund and B. Gentz. Beyond the Fokker-Planck equation: pathwise control of noisy bistable systems. *J. Phys. A: Math. Gen.*, 35:2057–2091, 2002.

[BG04] N. Berglund and B. Gentz. On the Noise-Induced Passage through an Unstable Periodic Orbit I: Two-Level Model. *J. Stat. Phys.*, 114:1577–1618, 2004.

[BG05] N. Berglund and B. Gentz. Universality of first-passage- and residence-time distributions in non-adiabatic stochastic resonance. *EPL (Europhysics Letters)*, 70:1–7, 2005.

[BKB$^+$05] B. Bonanni, A. S. M. Kamruzzahan, A. R. Bizzarri, C. Rankl, H. J. Gruber, P. Hinterdorfer, and S. Cannistraro. Single Molecule Recognition between Cytochrome C 551 and Gold-Immobilized Azurin by Force Spectroscopy. *Biophys. J.*, 89:2783–2791, 2005.

[BMF$^+$07] F. W. Bartels, M. McIntosh, A. Fuhrmann, C. Metzendorf, P. Plattner, N. Sewald, D. Anselmetti, R. Ros, and A. Becker. Effector-Stimulated Single Molecule Protein-DNA Interactions of a Quorum-Sensing System in *Sinorhizobium meliloti*. *Biophys. J.*, 92:4391–4400, 2007.

[BML$^+$05] S. Beri, R. Mannella, D. G. Luchinsky, A. N. Silchenko, and P. V. E. McClintock. Solution of the boundary value problem for optimal escape in continuous stochastic systems and maps. *Phys. Rev. E*, 72:036131–1–16, 2005.

[BPHD08] R. B. Best, E. Paci, G. Hummer, and O. K. Dudko. Pulling Direction as a Reaction Coordinate for the Mechanical Unfolding of Single Molecules. *J. Phys. Chem. B*, 112:5968–5976, 2008.

[BPS94] F. Bezanilla, E. Perozo, and E. Stefani. Gating of *Shaker* K^+ Channels: II. The Components of Gating Currents and a Model of Channel Activation. *Biophys. J.*, 66:1011–1021, 1994.

[BPZ$^+$03] D. J. Brockwell, E. Paci, R. C. Zinober, G. S. Beddard, P. D. Olmsted, D. A. Smith, R. N. Perham, and S. E. Radford. Pulling geometry defines the mechanical resistance of a β-sheet protein. *Nat. Struct. Biol.*, 10:731–737, 2003.

[BQG86] G. Binnig, C. F. Quate, and Ch. Gerber. Atomic Force Microscope. *Phys. Rev. Lett.*, 56:930–933, 1986.

[BR82] G. Binnig and H. Rohrer. Scanning tunneling microscopy. *Helv. Phys. Acta*, 55:726–735, 1982.

[BRB07] S. Bleil, P. Reimann, and C. Bechinger. Directing Brownian motion by oscillating barriers. *Phys. Rev. E*, 75:031117–1–5, 2007.

[BRGW82] G. Binnig, H. Rohrer, Ch. Gerber, and E. Weibel. Tunneling through a controllable vacuum gap. *Appl. Phys. Lett.*, 40:178–180, 1982.

[BS05] O. Braun and U. Seifert. Force spectroscopy of single multidomain biopolymers: A master equation approach. *Eur. Phys. J. E*, 18:1–13, 2005.

[BSPB04] D. Babic, C. Schmitt, I. Poberaj, and C. Bechinger. Stochastic resonance in colloidal systems. *EPL (Europhysics Letters)*, 67:158–164, 2004.

[CCR81] B. Caroli, C. Caroli, and B. Roulet. Diffusion in a Bistable Potential: The Functional Integral Approach. *J. Stat. Phys.*, 26:83–111, 1981.

[Col79] S. Coleman. The Uses of Instantons. In A. Zichichi, editor, *The whys of subnuclear physics*, pages 805–941. Plenum, New York, 1979.

[Cra46] H. Cramér. *Mathematical Methods of Statistics*. Princeton University Press, Princeton, 1946.

[CSJG07] G. Coupier, M. Saint Jean, and C. Guthmann. Single file diffusion enhancement in a fluctuating modulated quasi-1D channel. *EPL (Europhysics Letters)*, 77:60001–1–6, 2007.

[CT91] T. M. Cover and J. A. Thomas. *Elements of Information Theory*. Wiley, New York, 1991.

[CVLL^{+}03] M. Carrion-Vazquez, H. Li, H. Lu, P. E. Marszalek, A. F. Oberhauser, and J. M. Fernandez. The mechanical stability of ubiquitin is linkage dependent. *Nat. Struct. Biol.*, 10:738–743, 2003.

[CW51] H. B. Callen and T. A. Welton. Irreversibility and Generalized Noise. *Phys. Rev.*, 83:34–40, 1951.

[D'A03] G. D'Agostini. Bayesian inference in processing experimental data: principles and basic applications. *Rep. Prog. Phys*, 66:1383–1419, 2003.

[DBA04] I. Derényi, D. Bartolo, and A. Ajdari. Effects of Intermediate Bound States in Dynamic Force Spectroscopy. *Biophys. J.*, 86:1263–1269, 2004.

[DBBR06] H. Dietz, F. Berkemeier, M. Bertz, and M. Rief. Anisotropic deformation response of single protein molecules. *Proc. Natl. Acad. Sci. USA*, 103:12724–12728, 2006.

[DFKU03] O. K. Dudko, A. E. Filippov, J. Klafter, and M. Urbakh. Beyond the conventional description of dynamic force spectroscopy of adhesion bonds. *Proc. Natl. Acad. Sci. USA*, 100:11378–11381, 2003.

[DHS06] O. K. Dudko, G. Hummer, and A. Szabo. Intrinsic Rates and Activation Free Energies from Single-Molecule Pulling Experiments. *Phys. Rev. Lett.*, 96:108101–1–4, 2006.

[DMS$^+$07] O. K. Dudko, J. Mathé, A. Szabo, A. Meller, and G. Hummer. Extracting Kinetics from Single-Molecule Force Spectroscopy: Nanopore Unzipping of DNA Hairpins. *Biophys. J.*, 92:4188–4195, 2007.

[Dos03] V. Dose. Bayesian inference in physics: case studies. *Rep. Prog. Phys*, 66:1421–1461, 2003.

[Dro95] A. N. Drozdov. Power Series Expansion for the Time Evolution Operator with a Harmonic-Oscillator Reference System. *Phys. Rev. Lett.*, 75:4342–4345, 1995.

[Dur85] J. Durbin. The First-Passage Density of a Continuous Gaussian Process to a General Boundary. *J. Appl. Prob.*, 22:99–122, 1985.

[DW92] J. Durbin and D. Williams. The First-Passage Density of the Brownian Motion Process to a Curved Boundary. *J. Appl. Prob.*, 29:291–304, 1992.

[Ein05] A. Einstein. Über die von der molekularkinetischen Theorie der Wärme geforderte Bewegung von in ruhenden Flüssigkeiten suspendierten Teilchen. *Ann. Phys.*, 17:549–560, 1905.

[EMRJ03] A. Engel, H. W. Müller, P. Reimann, and A. Jung. Ferrofluids as Thermal Ratchets. *Phys. Rev. Lett.*, 91:060602–1–4, 2003.

[EPNS08] T. Erdmann, S. Pierrat, P. Nassoy, and U. S. Schwarz. Dynamic force spectroscopy on multiple bonds: Experiments and model. *EPL (Europhysics Letters)*, 81:48001–1–6, 2008.

[ER97] E. Evans and K. Ritchie. Dynamic Strength of Molecular Adhesion Bonds. *Biophys. J.*, 72:1541–1555, 1997.

[ER03] M. Evstigneev and P. Reimann. Dynamic force spectroscopy: Optimized data analysis. *Phys. Rev. E*, 68:045103–1–4, 2003.

[ER04a] R. Eichhorn and P. Reimann. Paradoxical nonlinear response of a Brownian particle. *Phys. Rev. E*, 70:035106–1–4, 2004.

[ER04b] A. Engel and P. Reimann. Thermal ratchet effects in ferrofluids. *Phys. Rev. E*, 70:051107–1–15, 2004.

[ERCdB05] R. Eichhorn, P. Reimann, B. Cleuren, and C. Van den Broeck. Moving backward noisily. *Chaos*, 15:026113–1–9, 2005.

[ESJ^{+}06] M. Evstigneev, A. Schirmeisen, L. Jansen, H. Fuchs, and P. Reimann. Force Dependence of Transition Rates in Atomic Friction. *Phys. Rev. Lett.*, 97:240601–1–4, 2006.

[ET93] B. Efron and R. J. Tibshirani. *An introduction to the bootstrap*. Chapman & Hall, New York, 1993.

[Eva01] E. Evans. Probing the relation between force – lifetime – and chemistry in single molecular bonds. *Annu. Rev. Biophys. Biomol. Struct.*, 30:105–128, 2001.

[Evs08] M. Evstigneev. Statistics of forced thermally activated escape events out of a metastable state: Most probable escape force and escape-force moments. *Phys. Rev. E*, 78:011118–1–6, 2008.

[EWB^{+}05] R. Eckel, S. D. Wilking, A. Becker, N. Sewald, R. Ros, and D. Anselmetti. Single-Molecule Experiments in Synthetic Biology: An Approach to the Affinity Ranking of DNA-Binding Peptides. *Angew. Chem. Int. Ed.*, 44:3921–3924, 2005.

[FAR^{+}08] A. Fuhrmann, D. Anselmetti, R. Ros, S. Getfert, and P. Reimann. Refined procedure of evaluating experimental single-molecule force spectroscopy data. *Phys. Rev. E*, 77:031912–1–10, 2008.

[FD74] T. A. Fulton and L. N. Dunkleberger. Lifetime of the zero-voltage state in Josephson tunnel junctions. *Phys. Rev. B*, 9:4760–4768, 1974.

[Fis94] E. Fischer. Einfluss der Configuration auf die Wirkung der Enzyme. *Ber. Dtsch. Chem. Ges.*, 27:2985–2993, 1894.

[FL95] L. P. Faucheux and A. Libchaber. Selection of Brownian Particles. *J. Chem. Soc. Faraday Trans.*, 91:3163–3166, 1995.

[Fok14] A. D. Fokker. Die mittlere Energie rotierender elektrischer Dipole im Strahlungsfeld. *Ann. Phys.*, 43:810–820, 1914.

[FSA^{+}09] A. Fuhrmann, J. C. Schoening, D. Anselmetti, D. Staiger, and R. Ros. Quantitative Analysis of Single-Molecule RNA-Protein Interaction. *Biophys. J.*, 96:5030–5039, 2009.

[FW] A. Fuhrmann and V. Walhorn. Private communication.

[FW98] M. I. Freidlin and A. D. Wentzell. *Random Perturbations of Dynamical Systems*. A Series of Comprehensive Studies in Mathematics/260, Springer, New York, 1998.

[FWKG03] C. Friedsam, A. K. Wehle, F. Kühner, and H. E. Gaub. Dynamic single-molecule force spectroscopy: bond rupture analysis with variable spacer length. *J. Phys.: Condens. Matter*, 15:S1709–S1723, 2003.

[Gar95] A. Garg. Escape-field distribution for escape from a metastable potential well subject to a steadily increasing bias field. *Phys. Rev. B*, 51:15592–15595, 1995.

[GER09] S. Getfert, M. Evstigneev, and P. Reimann. Single-molecule force spectroscopy: Practical limitations beyond Bell's model. *Phys. A*, 388:1120–1132, 2009.

[GHJM98] L. Gammaitoni, P. Hänggi, P. Jung, and F. Marchesoni. Stochastic resonance. *Rev. Mod. Phys.*, 70:223–287, 1998.

[GHT80] H. Grabert, P. Hänggi, and P. Talkner. Microdynamics and Nonlinear Stochastic Processes of Gross Variables. *J. Stat. Phys.*, 22:537–552, 1980.

[Gie03] F. J. Giessibl. Advances in atomic force microscopy. *Rev. Mod. Phys.*, 75:949–983, 2003.

[Gij04] M. A. M. Gijs. Magnetic bead handling on-chip: new opportunities for analytical applications. *Microfluid. Nanofluid.*, 1:22–40, 2004.

[GPS02] H. Goldstein, C. Poole, and J. Safko. *Classical mechanics*. Addison-Wesley, New York, 2002.

[GR07] S. Getfert and P. Reimann. Optimal evaluation of single-molecule force spectroscopy experiments. *Phys. Rev. E*, 76:052901–1–4, 2007.

[Gre52] M. S. Green. Markoff Random Processes and the Statistical Mechanics of Time-Dependent Phenomena. *J. Chem. Phys.*, 20:1281–1295, 1952.

[GRK$^+$08] S. Guo, C. Ray, A. Kirkpatrick, N. Lad, and B. B. Akhremitchev. Effects of Multiple-Bond Ruptures on Kinetic Parameters Extracted from Force Spectroscopy Measurements: Revisiting Biotin-Streptavidin Interactions. *Biophys. J.*, 95:3964–3976, 2008.

[GW93] M. Gitterman and G. H. Weiss. Small-noise approximations to the solution of the Smoluchowski equation. *Phys. Rev. E*, 47:976–980, 1993.

[GZC92] B. Golding, N. M. Zimmerman, and S. N. Coppersmith. Dissipative Quantum Tunneling of a Single Microscopic Defect in a Mesoscopic Metal. *Phys. Rev. Lett.*, 68:998–1001, 1992.

[HB93] J. L. Hutter and J. Bechhoefer. Calibration of atomic-force microscope tips. *Rev. Sci. Instrum.*, 64:1868–1873, 1993.

[HBG$^+$96] P. Hinterdorfer, W. Baumgartner, H. J. Gruber, K. Schilcher, and H. Schindler. Detection and localization of individual antibody-antigen recognition events by atomic force microscopy. *Proc. Natl. Acad. Sci. USA*, 93:3477–3481, 1996.

[HD06] P. Hinterdorfer and Y. F. Dufrêne. Detection and localization of single molecular recognition events using atomic force microscopy. *Nat. Methods*, 3:347–355, 2006.

[HG00] B. Heymann and H. Grubmüller. Dynamic Force Spectroscopy of Molecular Adhesion Bonds. *Phys. Rev. Lett.*, 84:6126–6129, 2000.

[HH05] E. Hershkovits and R. Hernandez. Chemical reaction dynamics within anisotropic solvents in time-dependent fields. *J. Chem. Phys.*, 122:014509–1–12, 2005.

[HK06] F. Hanke and H. J. Kreuzer. Breaking bonds in the atomic force microscope: Theory and analysis. *Phys. Rev. E*, 74:031909–1–5, 2006.

[HO07] V. Heinrich and C. Ounkomol. Force versus Axial Deflection of Pipette-Aspirated Closed Membranes. *Biophys. J.*, 93:363–372, 2007.

[HP08] J. Husson and F. Pincet. Analyzing single-bond experiments: Influence of the shape of the energy landscape and universal law between the width, depth, and force spectrum of the bond. *Phys. Rev. E*, 77:026108–1–14, 2008.

[HS03] G. Hummer and A. Szabo. Kinetics from Nonequilibrium Single-Molecule Pulling Experiments. *Biophys. J.*, 85:5–15, 2003.

[HTB90] P. Hänggi, P. Talkner, and M. Borkovec. Reaction-rate theory: fifty years after Kramers. *Rev. Mod. Phys.*, 62:251–342, 1990.

[HW00] C. Haber and D. Wirtz. Magnetic tweezers for DNA micromanipulation. *Rev. Sci. Instrum.*, 71:4561–4570, 2000.

[HZV$^+$07] J. Hanne, G. Zocchi, N. K. Voulgarakis, A. R. Bishop, and K. Ø . Rasmussen. Opening rates of DNA hairpins: Experiment and model. *Phys. Rev. E*, 76:011909–1–8, 2007.

[IP04] A. Imparato and L. Peliti. Kinetic barriers in RNA unzipping. *Eur. Phys. J. B*, 39:357–363, 2004.

[ISB$^+$97] S. Izrailev, S. Stepaniants, M. Balsera, Y. Oono, and K. Schulten. Molecular Dynamics Study of Unbinding of the Avidin-Biotin Complex. *Biophys. J.*, 72:1568–1581, 1997.

[IW08] J. Iwaniszewski and A. Wozinski. Resonant activation: Potential vs. temperature fluctuations. *EPL (Europhysics Letters)*, 82:50004–1–5, 2008.

[Jam06] F. James. *Statistical Methods in Experimental Physics*. World Scientific Publishing Co.Pte.Ltd., Singapore, 2006.

[JB03] E. T. Jaynes and G. L. Bretthorst. *Probability Theory: The Logic of Science*. Cambridge University Press, Cambridge, 2003.

[Jun93] P. Jung. Periodically driven stochastic systems. *Phys. Rep.*, 234:175–295, 1993.

[Jun96] G. Junker. *Supersymmetric Methods in Quantum and Statisitcal Physics*. Springer, Berlin, 1996.

[JWK$^+$01] C. Jeppesen, J. Y. Wong, T. L. Kuhl, J. N. Israelachvili, N. Mullah, S. Zalipsky, and C. M. Marques. Impact of Polymer Tether Length on Multiple Ligand-Receptor Bond Formation. *Science*, 293:465–468, 2001.

[Kam03] N. G. van Kampen. *Stochastic Processes in Physics and Chemistry*. Elsevier, Amsterdam, 2003.

[KCB$^+$04] F. Kühner, L. T. Costa, P. M. Bisch, S. Thalhammer, W. M. Heckl, and H. E. Gaub. LexA-DNA Bond Strength by Single Molecule Force Spectroscopy. *Biophys. J.*, 87:2683–2690, 2004.

[KEG06] F. Kühner, M. Erdmann, and H. E. Gaub. Scaling Exponent and Kuhn Length of Pinned Polymers by Single Molecule Force Spectroscopy. *Phys. Rev. Lett.*, 97:218301–1–4, 2006.

[KJHM05] M. Kuhn, H. Janovjak, M. Hubain, and D. J. Müller. Automated alignment and pattern recognition of single-molecule force spectroscopy data. *J. Microsc.*, 218:125–132, 2005.

[KK08] A. Kargol and K. Kabza. Test of the nonequilibrium kinetic focusing of voltage-gated ion channels. *Phys. Biol.*, 5:026003–1–7, 2008.

[Kra40] H. A. Kramers. Brownian motion in a field of force and the diffusion model of chemical reactions. *Physica*, 7:284–304, 1940.

[KT04] L. N. Kantorovich and T. Trevethan. General Theory of Microscopic Dynamical Response in Surface Probe Microscopy: From Imaging to Dissipation. *Phys. Rev. Lett.*, 93:236102–1–4, 2004.

[Kur72] J. Kurkijärvi. Intrinsic Fluctuations in a Superconducting Ring Closed with a Josephson Junction. *Phys. Rev. B*, 6:832–835, 1972.

[Kuy97] F. Kuypers. *Klassische Mechanik*. Wiley-vch, Weinheim, 1997.

[KW03] S. J. Koch and M. D. Wang. Dynamic Force Spectroscopy of Protein-DNA Interactions by Unzipping DNA. *Phys. Rev. Lett.*, 91:028103–1–4, 2003.

[Lan08] P. Langevin. Sur la théorie du mouvement brownien. *C. R. Acad. Sci. Paris*, 146:530–533, 1908.

[LCH97] J. Łuczka, T. Czernik, and P. Hänggi. Symmetric white noise can induce directed current in ratchets. *Phys. Rev. E*, 56:3968–3975, 1997.

[LG97] D. S. Lemons and A. Gythiel. Paul Langevin's 1908 paper "On the Theory of Brownian Motion". *Am. J. Phys.*, 65:1079–1081, 1997.

[LHL08] N. Li, P. Hänggi, and B. Li. Ratcheting heat flux against a thermal bias. *EPL (Europhysics Letters)*, 84:40009–1–5, 2008.

[LLA$^+$02] R. Lavery, A. Lebrun, J. Allemand, D. Bensimon, and V. Croquette. Structure and mechanics of single biomolecules: experiment and simulation. *J. Phys.: Condens. Matter*, 14:R383–R414, 2002.

[LLPG05] S. H. Lee, K. Ladavac, M. Polin, and D. G. Grier. Observation of Flux Reversal in a Symmetric Optical Thermal Ratchet. *Phys. Rev. Lett.*, 94:110601–1–4, 2005.

[LOR$^+$01] H. Li, A. F. Oberhauser, S. D. Redick, M. Carrion-Vazquez, H. P. Erickson, and J. M. Fernandez. Multiple conformations of PEVK proteins detected by single-molecule techniques. *Proc. Natl. Acad. Sci. USA*, 98:10682–10686, 2001.

[LOYI06] F. Liu, Z. Ou-Yang, and M. Iwamoto. Dynamic disorder in receptor-ligand forced dissociation experiments. *Phys. Rev. E*, 73:1–1–4, 2006.

[LRH00a] J. Lehmann, P. Reimann, and P. Hänggi. Surmounting Oscillating Barriers. *Phys. Rev. Lett.*, 84:1639–1642, 2000.

[LRH00b] J. Lehmann, P. Reimann, and P. Hänggi. Surmounting oscillating barriers: Path-integral approach for weak noise. *Phys. Rev. E*, 62:6282–6303, 2000.

[LRT82] F. Langouche, D. Roekaerts, and E. Tirapegui. *Functional Integration and Semiclassical Expansions*. Mathematics and Its Applications/10, Reidel, Dordrecht, 1982.

[Lud75] D. Ludwig. Persistence of Dynamical Systems under Random Perturbations. *SIAM Rev.*, 17:605–640, 1975.

[LYZL06] S. Lü, Z. Ye, C. Zhu, and M. Long. Quantifying the effects of contact duration, loading rate, and approach velocity on P-selectin-PSGL-1 interactions using AFM. *Polymer*, 47:2539–2547, 2006.

[MA88] G. Meyer and N. M. Amer. Novel optical approach to atomic force microscopy. *Appl. Phys. Lett.*, 53:1045–1047, 1988.

[MBZ$^+$07] J. Morfill, K. Blank, C. Zahnd, B. Luginbühl, F. Kühner, K. E. Gottschalk, A. Plückthun, and H. E. Gaub. Affinity-Matured Recombinant Antibody Fragments Analyzed by Single-Molecule Force Spectroscopy. *Biophys. J.*, 93:3583–3590, 2007.

[MC96] M. M. Millonas and D. R. Chialvo. Control of Voltage-Dependent Biomolecules via Nonequilibrium Kinetic Focusing. *Phys. Rev. Lett.*, 76:550–553, 1996.

[Mer01] R. Merkel. Force spectroscopy on single passive biomolecules and single biomolecular bonds. *Phys. Rep.*, 346:343–385, 2001.

[Mil83] W. H. Miller. Reaction-path dynamics for polyatomic systems. *J. Phys. Chem.*, 87:3811–3819, 1983.

[ML06] C. E. Maloney and D. J. Lacks. Energy barrier scalings in driven systems. *Phys. Rev. E*, 73:061106–1–5, 2006.

[MNL$^+$99] R. Merkel, P. Nassoy, A. Leung, K. Ritchie, and E. Evans. Energy landscape of receptor-ligand bonds explored with dynamic force spectroscopy. *Nature*, 397:50–53, 1999.

[MS96a] R. S. Maier and D. L. Stein. Oscillatory Behavior of the Rate of Escape through an Unstable Limit Cycle. *Phys. Rev. Lett.*, 77:4860–4863, 1996.

[MS96b] R. N. Mantegna and B. Spagnolo. Noise Enhanced Stability in an Unstable System. *Phys. Rev. Lett.*, 76:563–566, 1996.

[MS01] R. S. Maier and D. L. Stein. Noise-Activated Escape from a Sloshing Potential Well. *Phys. Rev. Lett.*, 86:3942–3945, 2001.

[MSL$^+$05] B. T. Marshall, K. K. Sarangapani, J. Lou, R. P. McEver, and C. Zhu. Force History Dependence of Receptor-Ligand Dissociation. *Biophys. J.*, 88:1458–1466, 2005.

[MSZ88] F. Marchesoni, P. Sodano, and M. Zannetti. Supersymmetry and Bistable Soft Potentials. *Phys. Rev. Lett.*, 61:1143–1146, 1988.

[MVV$^+$04] J. Mathé, H. Visram, V. Viasnoff, Y. Rabin, and A. Meller. Nanopore Unzipping of Individual DNA Hairpin Molecules. *Biophys. J.*, 87:3205–3212, 2004.

[MWS07] Y. Murayama, H. Wada, and M. Sano. Dynamic force spectroscopy of a single condensed DNA. *EPL (Europhysics Letters)*, 79:58001–1–6, 2007.

[NAPG06] G. Neuert, C. Albrecht, E. Pamir, and H. E. Gaub. Dynamic force spectroscopy of the digoxigenin-antibody complex. *FEBS Lett.*, 580:505–509, 2006.

[NDKM03] M. Nguyen-Duong, K. W. Koch, and R. Merkel. Surface anchoring reduces the lifetime of single specific bonds. *EPL (Europhysics Letters)*, 61:845–851, 2003.

[NSK$^+$03] R. Nevo, C. Stroh, F. Kienberger, D. Kaftan, V. Brumfeld, M. Elbaum, Z. Reich, and P. Hinterdorfer. A molecular switch between alternative conformational states in the complex of Ran and importin $\beta1$. *Nat. Struct. Biol.*, 10:553–557, 2003.

[NVBG07] P. Nuernberger, G. Vogt, T. Brixner, and G. Gerber. Femtosecond quantum control of molecular dynamics in the condensed phase. *Phys. Chem. Chem. Phys.*, 9:2470–2497, 2007.

[Pam06] N. Pamme. Magnetism and microfluidics. *Lab Chip*, 6:24–38, 2006.

[PD40] L. Pauling and M. Delbrück. The Nature of the Intermolecular Forces Operative in Biological Processes. *Science*, 92:77–79, 1940.

[PH05] F. Pincet and J. Husson. The Solution to the Streptavidin-Biotin Paradox: The Influence of History on the Strength of Single Molecular Bonds. *Biophys. J.*, 89:4374–4381, 2005.

[PKRB05] M. Panhorst, P. Kamp, G. Reiss, and H. Brückl. Sensitive bondforce measurements of ligand-receptor pairs with magnetic beads. *Biosens. Bioelectron.*, 20:1685–1689, 2005.

[PPF$^+$05] Y. V. Pereverzev, O. V. Prezhdo, M. Forero, E. V. Sokurenko, and W. E. Thomas. The Two-Pathway Model for the Catch-Slip Transition in Biological Adhesion. *Biophys. J.*, 89:1446–1454, 2005.

[PT05] E. Pollak and P. Talkner. Reaction rate theory: What it was, where is it today, and where is it going? *Choas*, 15:026116–1–11, 2005.

[PTVF92] W. H. Press, S. A. Teukolsky, W. T. Vetterling, and B. P. Flannery. *Numerical Recipes in C. The Art of Scientific Computing*. Cambridge: University Press, Cambridge, 1992.

[RBA07] C. Ray, J. R. Brown, and B. B. Akhremitchev. Correction of Systematic Errors in Single-Molecule Force Spectroscopy with Polymeric Tethers by Atomic Force Microscopy. *J. Phys. Chem. B*, 111:1963–1974, 2007.

[RD05] D. Ryvkine and M. I. Dykman. Noise-induced escape of periodically modulated systems: From weak to strong modulation. *Phys. Rev. E*, 72:011110–1–15, 2005.

[RD06] D. Ryvkine and M. I. Dykman. Pathways of activated escape in periodically modulated systems. *Phys. Rev. E*, 73:061109–1–11, 2006.

[REB+06] M. Raible, M. Evstigneev, F. W. Bartels, R. Eckel, M. Nguyen-Duong, R. Merkel, R. Ros, D. Anselmetti, and P. Reimann. Theoretical Analysis of Single-Molecule Force Spectroscopy Experiments: Heterogeneity of Chemical Bonds. *Biophys. J.*, 90:3851–3864, 2006.

[Red01] S. Redner. *A Guide to First-Passage Processes*. Cambridge University Press, Cambridge, 2001.

[Rei96] P. Reimann. Noisy One-Dimensional Maps Near a Crisis. I. Weak Gaussian White and Colored Noise. *J. Stat. Phys.*, 82:1467–1501, 1996.

[Rei01] P. Reimann. A uniqueness-theorem for "linear" thermal baths. *Chem. Phys.*, 268:337–346, 2001.

[Rei02] P. Reimann. Brownian motors: noisy transport far from equilibrium. *Phys. Rep.*, 361:57–265, 2002.

[RER+04] M. Raible, M. Evstigneev, P. Reimann, F. W. Bartels, and R. Ros. Theoretical analysis of dynamic force spectroscopy experiments on ligand-receptor complexes. *J. Biotechnol.*, 112:13–23, 2004.

[RGB+03] E. Riedo, E. Gnecco, R. Bennewitz, E. Meyer, and H. Brune. Interaction Potential and Hopping Dynamics Governing Sliding Friction. *Phys. Rev. Lett.*, 91:084502–1–4, 2003.

[Ris89] H. Risken. *The Fokker-Planck Equation. Methods of Solution and Applications*. Springer, Berlin, 1989.

[Rit06] F. Ritort. Single-molecule experiments in biological physics: methods and applications. *J. Phys.: Condens. Matter*, 18:R531–R583, 2006.

[RRL+06] T. V. Ratto, R. E. Rudd, K. C. Langry, R. L. Balhorn, and M. W. McElfresh. Nonlinearly Additive Forces in Multivalent Ligand Binding to a Single Protein Revealed with Force Spectroscopy. *Langmuir*, 22:1749–1757, 2006.

[RSA+98] R. Ros, F. Schwesinger, D. Anselmetti, M. Kubon, R. Schäfer, A. Plückthun, and L. Tiefenauer. Antigen binding forces of individually addressed single-chain Fv antibody molecules. *Proc. Natl. Acad. Sci. USA*, 95:7402–7405, 1998.

[RSAP94] J. Rousselet, L. Salome, A. Ajdari, and J. Prost. Directional motion of browninan particles induced by a periodic asymmetric potential. *Nature*, 370:446–448, 1994.

[Rud82] M. Rudemo. Empirical Choice of Histograms and Kernel Density Estimators. *Scand. J. Statist.*, 9:65–78, 1982.

[RY99] D. Revuz and M. Yor. *Continous Martingales and Brownian Motion*. A Series of Comprehensive Studies in Mathematics/293, Springer, Berlin, 1999.

[Sch81] L. S. Schulman. *Techniques and Applications of Path Integration*. Wiley, New York, 1981.

[Sco79] D. W. Scott. On Optimal and Data-Based Histograms. *Biometrika*, 66:605–610, 1979.

[SDG99] V. N. Smelyanskiy, M. I. Dykman, and B. Golding. Time Oscillations of Escape Rates in Periodically Driven Systems. *Phys. Rev. Lett.*, 82:3193–3197, 1999.

[Sei00] U. Seifert. Rupture of Multiple Parallel Molecular Bonds under Dynamic Loading. *Phys. Rev. Lett.*, 84:2750–2753, 2000.

[Shn97] V. A. Shneidman. Transient solution of the Kramers problem in the weak noise limit. *Phys. Rev. E*, 56:5257–5264, 1997.

[Siv96] D. S. Sivia. *Data Analysis - A Bayesian Tutorial*. Clarendon Press, Oxford, 1996.

[SJF05] A. Schirmeisen, L. Jansen, and H. Fuchs. Tip-jump statistics of stick-slip friction. *Phys. Rev. B*, 71:245403–1–7, 2005.

[SL07] H. Shang and G. U. Lee. Magnetic Tweezers Measurement of the Bond Lifetime – Force Behavior of the IgG–Protein A Specific Molecular Interaction. *J. Am. Chem. Soc.*, 129:6640–6646, 2007.

[Smo15] M. v. Smoluchowski. Über Brownsche Molekularbewegung unter Einwirkung äußerer Kräfte und deren Zusammenhang mit der verallgemeinerten Diffusionsgleichung. *Ann. Phys.*, 48:1103–1112, 1915.

[SO03] S. Sills and R. M. Overney. Creeping Friction Dynamics and Molecular Dissipation Mechanisms in Glassy Polymers. *Phys. Rev. Lett.*, 91:095501–1–4, 2003.

[SOS$^+$00] T. Strunz, K. Oroszlan, I. Schumakovitch, H.-J. Güntherodt, and M. Hegner. Model Energy Landscapes and the Force-Induced Dissociation of Ligand-Receptor Bonds. *Biophys. J.*, 79:1206–1212, 2000.

[SPA$^+$07] Y. Sugimoto, P. Pou, M. Abe, P. Jelinek, R. Pérez, S. Morita, and Ó. Custance. Chemical identification of individual surface atoms by atomic force microscopy. *Nature*, 446:64–67, 2007.

[SR06] M. Schlierf and M. Rief. Single-Molecule Unfolding Force Distributions Reveal a Funnel-Shaped Energy Landscape. *Biophys. J.*, 90:L33–L35, 2006.

[SSHM99] D. A. Simson, M. Strigl, M. Hohenadl, and R. Merkel. Statistical Breakage of Single Protein A-IgG Bonds Reveals Crossover from Spontaneous to Force-Induced Bond Dissociation. *Phys. Rev. Lett.*, 83:652–655, 1999.

[SSLM01] S. M. Soskin, V. I. Sheka, T. L. Linnik, and R. Mannella. Short Time Scales in the Kramers Problem: A Stepwise Growth of the Escape Flux. *Phys. Rev. Lett.*, 86:1665–1669, 2001.

[STH04] M. Schindler, P. Talkner, and P. Hänggi. Firing Time Statistics for Driven Neuron Models: Analytic Expressions versus Numerics. *Phys. Rev. Lett.*, 93:048102–1–4, 2004.

[STH05] M. Schindler, P. Talkner, and P. Hänggi. Escape rates in periodically driven Markov processes. *Physica A*, 351:40–50, 2005.

[Str95] L. Stryer. *Biochemistry*. Freeman, New York, 1995.

[Tal99] P. Talkner. Stochastic resonance in the semiadiabatic limit. *New J. Phys.*, 1:4.1–4.25, 1999.

[TNELG04] S. F. Tolic-Norrelykke, A. M. Engh, R. Landick, and J. Gelles. Diversity in the Rates of Transcript Elongation by Single RNA Polymerase Molecules. *J. Biol. Chem.*, 279:3292–3299, 2004.

[VL01] R. A. Vijayendran and D. E. Leckband. A Quantitative Assessment of Heterogeneity for Surface-Immobilized Proteins. *Anal. Chem.*, 73:471–480, 2001.

[VR01] J. M. G. Vilar and J. M. Rubí. Noise Suppression by Noise. *Phys. Rev. Lett.*, 86:950–953, 2001.

[VSWS05] C. Veigel, S. Schmitz, F. Wang, and J. R. Sellers. Load-dependent kinetics of myosin-V can explain its high processivity. *Nat. Cell Biol.*, 7:861–869, 2005.

[Wen24] G. Wentzel. Zur Quantenoptik. *Z. Phys.*, 22:193–199, 1924.

[WH80] U. Weiss and W. Häffner. The Uses of Instantons for Diffusion in Bistable Potentials. In J. P. Antoine and E. Tirapegui, editors, *Functional Integration*, pages 311–331. Plenum, New York, 1980.

[Wie94] R. Wiesendanger. *Scanning Probe Microscopy and Spectroscopy - Methods and Applications*. Cambridge University Press, Cambrigde, 1994.

[Wil03] P. M. Williams. Analytical descriptions of dynamic force spectroscopy: behaviour of multiple connections. *Anal. Chim. Acta*, 479:107–115, 2003.

[WOH$^+$97] W. Wernsdorfer, E. B. Orozco, K. Hasselbach, A. Benoit, B. Barbara, N. Demoncy, A. Loiseau, H. Pascard, and D. Mailly. Experimental Evidence of the Néel-Brown Model of Magnetization Reversal. *Phys. Rev. Lett.*, 78:1791–1794, 1997.

[ZLCB02] C. Zhu, M. Long, S. E. Chesla, and P. Bongrand. Measuring Receptor/Ligand Interaction at the Single-Bond Level: Experimental and Interpretative Issues. *Ann. Biomed. Eng.*, 30:305–314, 2002.

[ZLM05] C. Zhu, J. Lou, and R. P. McEver. Catch bonds: Physical models, structural bases, biological function and rheological relevance. *Biorheology*, 42:443–462, 2005.

[Zwa61] R. Zwanzig. Memory Effects in Irreversible Thermodynamics. *Phys. Rev.*, 124:983–992, 1961.

Acknowledgments/Danksagung

I wish to thank: / Ich bedanke mich bei:

An erster Stelle möchte ich mich ganz herzlich bei Prof. Dr. Peter Reimann bedanken: für die interessante Themenstellung, für die stets hervorragende Betreuung und für das angenehme Arbeitsklima.

Prof. Dr. Dario Anselmetti danke ich dafür, dass er sich bereit erklärt hat, diese Arbeit zu begutachten.

Prof. Dr. Robert Ros und Alexander Fuhrmann für die gute Zusammenarbeit, die vielen fruchtbaren Diskussionen und den netten Aufenthalt in Phoenix.

Der Arbeitsgruppe "Experimentelle Biophysik und angewandte Nanowissenschaften" von Prof. Dr. Dario Anselmetti, die ich durch die Zusammenarbeit mit Prof. Dr. Robert Ros, Alexander Fuhrmann und später auch mit Volker Walhorn näher kennen gelernt habe und die mir die in dieser Arbeit verwendeten experimentellen Daten bereitgestellt hat.

Allen Doktoranden, Diplomanden und sonstigen Kollegen auf E5 für die angenehme Atmosphäre, auch außerhalb der Arbeit.

Bei Hannelore Litschewsky für die Hilfe bei allen organisatorischen Arbeiten.

Besonders bedanken möchte ich mich auch bei Beate West, die bei allen Computerproblemen stets schnell geholfen hat.

Bei Thorsten Bogner und Jörg Ummethum für das sorfältige Korrekturlesen.

Der Deutschen Forschungsgemeinschaft für die Finanzierung meiner Stelle innerhalb des SFBs 613.

Christina und Inga danke ich einfach dafür, dass sie da sind.

Schließlich möchte ich mich bei meiner Familie, insbesondere bei meinen Eltern, dafür bedanken, dass sie mich stets untersützt haben.

Erklärung

Hiermit versichere ich, dass ich die vorliegende Arbeit selbstständig und ohne unerlaubte Hilfsmittel erstellt und außer den angegebenen Quellen keine weiteren Hilfsmittel verwendet habe.

Sebastian Getfert　　　　Bielefeld, 6. Juli 2009